Connecting Metal-Support Interaction and Electrochemical Promotion Phenomena for Nano-structured Catalysts

Holly Dole

Thesis submitted to the

Faculty of Graduate and Postdoctoral Studies

in partial fulfillment of the requirements for the

degree of Doctor of Philosophy

In

Department of Chemical and Biological Engineering

Faculty of Engineering

University of Ottawa

Abstract

Air pollutants can cause poor air quality; however, the use of heterogeneous catalytic oxidation has been shown to be an efficient and cost-effective removal method. Some examples of commercial application of such catalysts include catalytic convertors in automobiles and industrial process exhausts. Research with regards to improving these technologies has included using less-expensive catalyst materials, increasing catalytic performance, and achieving higher efficiency.

The concept of metal-support interaction (MSI) is one method of altering catalytic performance through changing the properties of the metal catalyst due to the interaction with the support material. Similarly, the phenomenon of electrochemical promotion of catalysis (EPOC) has also been shown to enhance the catalytic activity, however, through the application of a small electrical stimulus to a catalyst-working electrode deposited on a solid electrolyte (e.g. yttria-stablized zirconia). The properties of the metal catalyst are altered due to the movement of ions (in this case, O^{2-}) from the electrolyte. Since its discovery, several factors were identified that are preventing EPOC from being commercialized, including the use of thick film catalysts. Implementing nano-catalysts makes this method competitive with typical heterogeneous catalysts; however, it has not been studied by many research groups. Furthermore, many heterogeneous catalytic studies have been performed separately for each of these phenomena; however, a connection between EPOC and MSI has yet to be fully understood.

The overall objective of this project is to study the concept of EPOC over highly-dispersed nano-catalysts and determine how MSI relates to the change in catalytic activity. Supported nano-catalysts were synthesized, characterized, and evaluated for catalytic performance using model reactions. A reactor was designed to carry out the electrochemical studies, where the EPOC concept was successfully implemented and a relationship with MSI established. Furthermore, additional studies were conducted to determine the role of the O^{2-} in the catalyst support and its relationship to MSI.

Résumé

Les polluants atmosphériques peuvent entraîner une mauvaise qualité de l'air; cependant, l'oxydation catalytique hétérogène a été démontrée comme étant une méthode d'élimination efficace et rentable. Quelques exemples d'application commerciale de ces catalyseurs comprennent les convertisseurs catalytiques dans les automobiles et les gaz d'échappement de procédés industriels. La recherche concernant l'amélioration de ces technologies inclut l'utilisation de matériaux moins coûteux, l'augmentation de la performance catalytique, et l'atteinte d'une plus grande efficacité.

Le concept d'interaction métal-support (metal-support interaction, MSI) est une méthode permettant d'altérer la performance catalytique en modifiant les propriétés du catalyseur métallique due à l'interaction avec le matériel de support. De même, le phénomène de promotion électrochimique de la catalyse (electrochemical promotion of catalysis, EPOC) a également été démontré comme étant capable d'augmenter l'activité catalytique, toutefois, grâce à l'application d'une petite impulsion électrique à une électrode de travail-catalyseur déposée sur un électrolyte solide (par exemple zircone yttriée). Les propriétés du catalyseur métallique sont modifiées en raison du mouvement d'ions (dans ce cas, O^{2-}) à partir de l'électrolyte. Depuis sa découverte, plusieurs facteurs qui empêchent la commercialisation d'EPOC ont été identifiés, incluant l'utilisation de catalyseurs à couche épaisse. L'implémentation de nano-catalyseurs rend cette méthode compétitive en comparaison aux catalyseurs hétérogènes typiques; cependant, cela n'a pas été étudié par de nombreux groupes de recherche. En outre, de nombreuses études catalytiques hétérogènes ont été effectuées séparément pour chacun de ces phénomènes; toutefois, le lien entre EPOC et MSI n'a pas été encore pleinement compris.

L'objectif global de ce projet est d'étudier le concept d'EPOC sur nano-catalyseurs hautement dispersées et de déterminer comment MSI se rapporte au changement d'activité catalytique. Des nano-cata lyseurs supportés ont été synthétisés, caractérisés, et évalués pour une performance catalytique utilisant des modèles réactionnels. Un réacteur a été conçu pour réaliser les études électrochimiques, où le concept d'EPOC a été implémenté avec succès et la relation avec MSI a été établie. De plus, des études supplémentaires ont été menées afin de déterminer le rôle des ions O^{2-} dans le support du catalyseur et de sa relation avec MSI.

Statement of Contributions of Collaborators

I hereby declare that I am the sole author of this thesis. I have performed the experimental studies and subsequent data analysis. I have written all chapters contained in this thesis.

My supervisor, Dr. Elena Baranova provided continual support and guidance throughout this work. In addition, some of the work was done in collaboration with Dr. Philippe Vernoux, Dr. Leonardo Lizarraga, and Dr. Foteini M. Sapountzi from Université de Lyon. They contributed with many helpful editorial comments and corrections.

The synthesized catalysts for Chapter 4 and Chapter 5 were done by Jong M. Kim and Rima J. Isaifan, respectively. Experiments related to the papers presented in Chapter 6 and Chapter 7 were performed with the assistance of undergraduate students, Luis F. Safady and Ana C.G.S.A. Costa.

TEM images for Chapter 4 were carried out by Daniel Aubert and Agnes Princivalle from Ceramic Synthesis and Functionalization Laboratory in Saint-Gobain, France. X-ray photoelectron spectroscopy measurements shown in Chapter 7 were performed and analyzed by Dr. Spyridon Ntais. Dr. Martin Couillard (National Research Council Canada) performed and analyzed the transmission electron spectroscopy images shown in Chapter 7-9.

Acknowledgements

First and foremost, I would like to thank my supervisor, Dr. Elena Baranova, for the support and guidance that she has given me throughout my graduate studies; in addition, for giving me the opportunity to work in a lab abroad at the Université de Lyon as well as being able to attend conferences in several different places.

It is with great appreciation that I thank Dr. Philippe Vernoux for also giving me the opportunity to work in his research group at the Université de Lyon. I would also like to acknowledge the other graduate students and post-docs that assisted me with my project while I was there.

Thank you also goes to Dr. Spyridon Ntais and Dr. Martin Coulliard for performing the characterization of my nano-catalysts; also, for the insightful discussions and support of my research.

I would like to thank the National Science and Engineering Research Council for their financial support of this project through a Discovery Grant as well as my Master's and PhD Graduate Scholarship.

Much of this project also would not have been accomplished without the help of the undergraduate students, Luis Safady and Ana Costa. Additionally, thanks to my fellow colleagues in the Lab of Electrochemical Engineering for assisting with the project, whether through discussions or running the equipment.

I would also like to recognize the great technical support in the Department of Chemical and Biological Engineering, Louis Tremblay, Franco Ziroldo and Gérard Nina. From building to problem solving errors, my experimental setup would not be what it is without the skills of these three gentlemen.

Finally, I would greatly like to thank my friends and family for their continuous support over the many years of studying. In particularly, I could have not done this without the love and encouragement from my parents, Shelley and Murray Dole, and my brothers, David and Andrew (and Tianna). Thanks to all my friends who supported me daily and made my graduate studies enjoyable.

Table of Contents

List of Figures

List of Tables

Nomenclature

ADF	annular dark-field
BE	binding energy
CE	counter electrode
CGO	$Ce_{0.9}Gd_{0.1}O_{2-\delta}$
EDX	energy dispersive X-ray
EMSI	electronic metal-support interaction
EO	ethylene oxide
EPOC	electrochemical promotion of catalysis
E-R	Eley-Rideal
ESD	electrostatic spray deposition
FWHM	full-width at half maximum
FW¾M	full-width at ¾ maximum
HAADF	high-angle annular dark-field
ICP-OES	inductively-coupled plasma optical emission spectroscopy
IMP	impregnation
LPRD	liquid phase reduction deposition
LSCF/GDC	$La_{0.6}Sr_{0.4}Co_{0.2}Fe_{0.8}O_{3-\delta}Gd_{0.1}O_{1.95}$
LSM	$La_{0.7}Sr_{0.3}MnO_3$
MEPR	monolithic electrochemically promoted reactor
MIEC	mixed ionic-electronic conducting
MSI	metal-support interaction
MVK	Mars van Krevelen
NEMCA	non-Faradaic electrochemical modification of catalytic activity
NP	nanoparticle
OSC	oxygen storage capacity
P-EPOC	permanent electrochemical promotion of catalysis
PF	plug flow
PVP	polyvinylpyrrolidone
RE	reference electrode
RWGS	reverse water-gas shift

SCCR	single-chamber capsule reactor
SDC	samarium-doped ceria
SEM	scanning electron microscopy
SMSI	strong metal-support interaction
STEM	scanning transmission electron microscopy
TCD	thermal conductivity detector
TD	thermally-decomposed
TEM	transmission electron microscopy
TGA	thermogravimetric analysis
TOF	turnover frequency
tpb	three-phase boundary
UHV	ultra-high vacuum
VOC	volatile organic compound
VPO	vanadium phosphate
WE	working electrode
XPS	X-ray photoelectron spectroscopy
XRD	X-ray diffraction
YSZ	yttria-stablized zirconia

List of Symbols

A	pre-exponential factor
a_{Au}	surface area of one Au atom
a_{Pt}	surface area of one Pt atom
D	dispersion
d_{avg}	average particle size
E_a	activation energy
F	Faraday`s constant
I	current
i	current density
I_o	exchange current
i_o	exchange current density
MW_i	molecular weight of component i
N_a	Avogadro`s number
N_G	moles of active metal sites
n_{cell}	equivalent number of galvanic cells
p_i	partial pressure of component i
R	universal gas constant
r	closed circuit catalytic rate; catalytic rate of promoted catalyst
r_o	open circuit catalytic rate; catalytic rate of unpromoted catalyst
r'_o	open circuit catalytic rate normalized for mass of metal
r_p	permanently promoted catalytic rate
T	reactor temperature
T_{20}	temperature at which 20% conversion occurs
T_{50}	temperature at which 50% conversion occurs
U_{cell}	cell potential
U_{wr}	catalyst-working electrode potential
$[i]_{IN}$	inlet concentration of component i
$[j]_{OUT}$	outlet concentration of component j

γ	permanent rate enhancement ratio
δ^+	image charge
ρ	rate enhancement ratio
ρ_{Au}	density of Au
ρ_{MSI}	promotional (metal-support interaction)
ρ_{Pt}	density of Pt
Λ	Faradaic efficiency
Λ_{MSI}	self-induced Faradaic efficiency
φ	work function
Φ_j	work function of component j

Chapter 1: Introduction

1.1 Brief Background and Motivation

Several studies have shown that air pollutants causing poor air quality can affect the human respiratory and cardiovascular system resulting in disability or even mortality [1–6]. Volatile organic compounds (VOCs) are a group of carbon-based chemicals that are among these air pollutants. There are several methods that have been demonstrated to reduce VOC emissions; however, the use of heterogeneous catalytic oxidation shows to be efficient and cost-effective. Many different catalysts and supports have been studied for this purpose, including metal oxides [7], noble metals supported by metal oxides or carbon [8], and noble metals supported by a mixture of metal oxides [9]. Some examples of commercial application of such catalysts include catalytic convertors found in automobiles and industrial process exhausts. Research with regards to improving these technologies has included using less-expensive catalyst materials (conventionally, noble metal catalysts are used), increasing catalytic performance and achieving higher efficiency [10–13]. The current studies aim to reduce the amount of expensive metal catalyst being used, while enhancing the catalytic activity of the catalyst to remain as effective.

One method of enhancing the activity of a catalyst is through the concept of promotion. This concept involves adding a chemical species, referred to as a promoter, to the catalyst to change its catalytic behaviour. There are two main methods that exist in order to introduce promoters to the catalyst – chemical (classical) promotion and electrochemical promotion [14]. Chemical promotion involves adding a promoter species to the catalyst during the preparation procedure [14–18]. The addition of such species can result in a change in the electronic or crystal structure of the catalyst which improves its catalytic performance and selectivity for the desired chemical reaction. Similarly, electrochemical promotion of catalysis (EPOC) is carried out by the application of a small current or potential to a catalyst-working electrode, resulting in the modification of its electronic properties; however, compared to classical promotion, the addition of ionic promoter species (e.g., $O^{\delta-}$) is done in-situ and can be controlled depending on specified reaction conditions [14,15,19–28]. These promoter species consequently alter the adsorption strength of the reaction components

resulting in a distinct change in catalytic performance [14]. Since its discovery, there have been several factors identified that are preventing this method from being commercialized [29], including the use of thick film catalysts. Implementing highly-dispersed nano-catalysts (as illustrated in Figure 1-1) makes this method competitive with typical high activity heterogeneous catalysts; however, it has not been studied by many research groups due to the difficulty in establishing an electrical connection between the nanoparticles for the purpose of a working electrode.

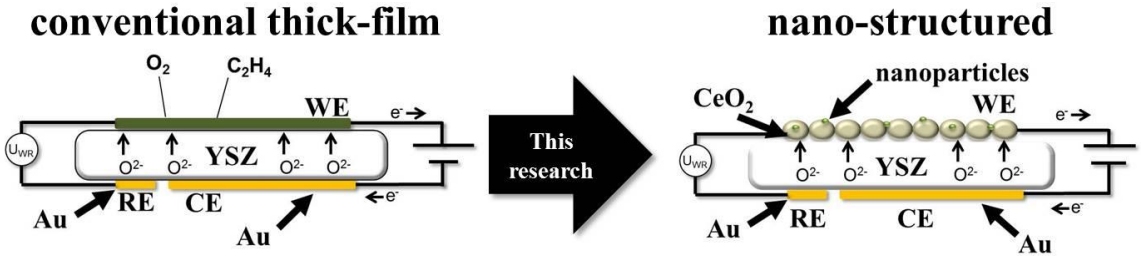

Figure 1-1: Applying the concept of EPOC to highly-dispersed nano-catalysts.

A related phenomenon to EPOC is referred to as metal-support interaction (MSI), where the support plays a key role in changing the properties of the catalyst due the interaction of between the two materials, usually resulting in higher catalytic activity. More specifically, the concept of strong metal-support interaction (SMSI) was introduced where it was shown that the presence of TiO_2 significantly alters the catalyst properties of the supported metal [30,31]. Many heterogeneous catalytic studies have been carried out with regards to this concept; however, a connection between EPOC and MSI has yet to be fully understood. It has been said that EPOC and MSI are closely related (as depicted in Figure 1-2 for the complete oxidation of ethylene), and the difference is only operational and not functional [32]. Further details of these concepts, as well as the current state of the research done in this field are summarized in Chapter 2.

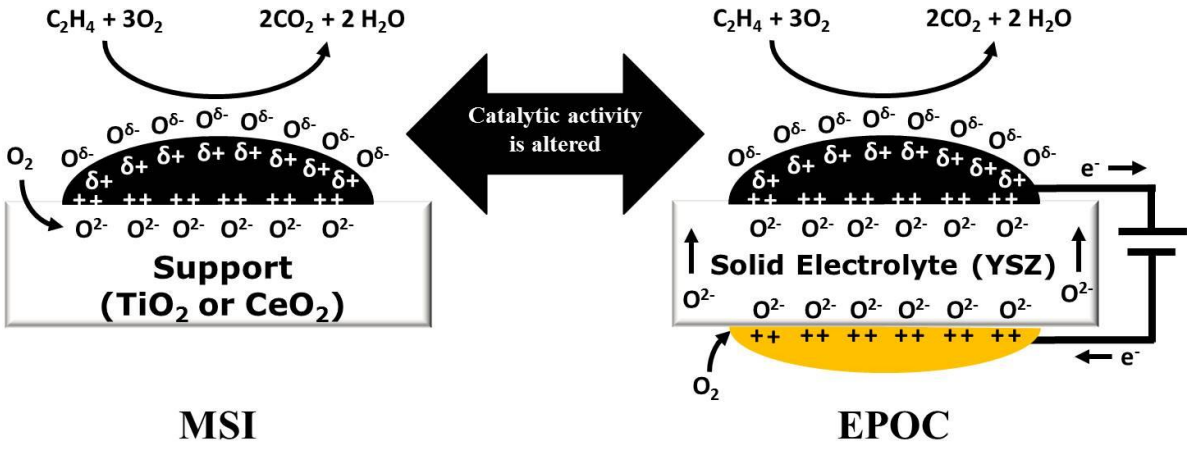

Figure 1-2: Connection between MSI and EPOC.

More recently, the concept of electronic metal-support interaction (EMSI)[33–37] has been discussed as an explanation for the different electronic interactions at the interface of the metals and supports. It is suggested that the d-band center plays an important role in this interaction, influencing the ability for a surface to bond to an adsorbate, resulting in changes in the catalytic activity. Three properties that have been identified as contributing factors include the position of the d-band centers, degree of filling of the d-bands, and coupling matrix element between the adsorbate states and metal d-states [37]. This concept is fairly new in the catalysis field and, more specifically, with regards to metal-support interaction.

1.2 Overview of Project Objectives

The overall objective for the proposed project was to study the concept of MSI (including EMSI) and how it relates to the phenomenon of electrochemical promotion for highly-dispersed nano-catalysts in the instance of the oxidation of volatile organic compounds (VOCs). First, each concept was studied separately, and then a connection was established in the final studies. In order to achieve this overall objective, several sub-objectives were executed as follows:

1) Synthesize nanoparticle catalysts having an average particle size in the range of less than 10 nm, including gold (Au), platinum (Pt), ruthenium (Ru), iridium (Ir) as well as a bimetallic catalyst, platinum-tin (PtSn).

2) Characterize physical and chemical properties of the nano-catalysts using various characterization techniques, including transmission electron microroscopy (TEM), X-ray diffraction (XRD), and X-ray photoelectron spectroscopy (XPS).

3) Evaluate the catalytic performance, with regards to MSI, of the nano-catalysts supported on an ionically conducting (i.e., yttria-stabilized zirconia, or YSZ), mixed ionic-electronic conducting (MIEC) (i.e., ceria, or CeO_2), and non-ionic conducting (i.e., gamma-alumina, γ-Al_2O_3) materials for different VOC oxidation reactions.

4) Develop a reactor design and corresponding electrochemical cell for the efficient evaluation of the nano-catalysts for EPOC.

5) Apply the phenomenon of EPOC to the highly-dispersed nano-catalysts and achieve enhancement in the catalytic activity for the complete oxidation of a VOC.

6) Assess the relationship between EPOC and MSI with regards to the role of using an "active" catalyst support or adding a second metal catalyst.

7) Examine the role of the CeO_2 oxygen storage capability and its influence on the interaction with the supported metal catalysts.

1.3 Thesis Structure

The overall objective of this project was achieved through the progression from each study outlined in Chapters 2-8. After providing a literature review on EPOC and MSI (Chapter 1), the concept of MSI was first examined in Chapters 3 and 4 for supported metal nano-catalysts. Next, in order to move to evaluating the nano-catalysts electrochemically, a new reactor design was required, as shown in Chapter 5. This led to the investigation of the phenomenon of EPOC over highly-dispersed nano-catalysts in Chapter 6. From this study, it was determined that the enhancement in the catalytic activity was related to a resulting stronger metal-support interaction caused by the polarization of the electrochemical cell. Further investigation into this relationship between MSI and EPOC was then carried out, as discussed in Chapter 7, by connecting the electrochemical and catalytic behaviours of the catalysts. As a result of the studies shown in Chapters 6 and 7, it was deemed that CeO_2

plays an important role in this relationship; therefore, an additional study was conducted to show the significant influence that this MIEC material has on the catalytic performance of the supported nano-catalysts.

Overall, it was hypothesized that the type of support, especially non-active versus active, will show a significant effect on the metal-support interaction, influencing the catalytic performance. Furthermore, it will be challenging to achieve EPOC with the nano-catalysts, since, conventionally, thick, continuous films have been used which allows for more efficient current distribution during polarization. Longer polarization duration, as well as higher potentials are expected to be required for the nano-catalysts. A connection between the two phenomena will be achieved through a deeper understanding of the movement of O^{2-} ions in the active support. The presence of these lattice oxygens in CeO_2 are expected to play a significant role in the interaction between the metal nanoparticles and support material.

The first sub-objective was achieved by synthesizing free-standing metal catalysts using a polyol method, then supporting them on various support materials. Chapter 3 discusses the synthesis of Au nanoparticles supported on YSZ, an ionically conductive support, and γ-Al_2O_3, a non-ionically conductive support. It should be noted that the Au nano-catalysts were not further studied due to unsuccessful trials in obtaining particle sizes less than 10 nm. Similarly, Pt nanoparticles supported on YSZ and γ-Al_2O_3 were synthesized for the study in Chapter 4. It was determined that in order to continue on to the electrochemical studies, YSZ or γ-Al_2O_3 would not be sufficient support materials for a catalyst-working electrode due to their lack of electronic conductivity. Therefore, CeO_2, a MIEC material, was chosen as a support material for the rest of the project. Chapters 5-8 include the synthesis of Ru nanoparticles supported on CeO_2, a mixed ionic-electronic conductive support, with a comparison shown in Chapter 6 to a thermally-decomposed synthesized Ru catalyst on CeO_2. CeO_2-supported Pt, $Pt_{50}Sn_{50}$, and Ir catalysts were also synthesized for the studies shown in Chapters 7 and 8. These chapters include the use of freestanding Pt, Ru and Ir catalysts as well. All synthesized catalysts and corresponding characterization data is shown in Table 1-1.

Table 1-1: Synthesized nano-catalysts.

Type of Nano-Catalyst	Reducing/ Stabilizing Agent	Support	Pretreatment	Metal Loading (%)	Average Colloidal Particle Size (nm)	Average Supported Particle size (nm)	*Corresponding Chapter*
Pt	0.08 M NaOH	YSZ	untreated	1.1[a]	2.5[c]	2.7[d]	4
Pt		YSZ		0.8[a]	2.5[c]	3.0[d]	4
Pt		YSZ		0.4[a]	2.5[c]	2.7[d]	4
Pt		γ-Al_2O_3		0.7[a]	2.5[c]	2.3[d]	4
Pt	0.06 M NaOH	CeO_2		1[b]	3.8[c]		7
Pt				5[b]	3.8[c]		7
Pt	0.2 M NaOH	CeO_2		1[b]	1.0[c]		7
Pt				5[b]	1.0[c]		7
$Pt_{50}Sn_{50}$	0.08 M NaOH	CeO_2		1[b]	3.1[c]	1.9[d]	7
Ru				1[b]	1.9[d]	1.1[d]	5, 6,7, 8
Ir				1[b]	1.0[d]	1.0[d]	8
Au	1:3, Au:PVP	YSZ	calcined at 300°C	1[b]	N/A	8.4[c]	3
Au	1:10, Au:PVP			1[b]		6.3[c]	3
Au	1:3, Au:PVP			1[b]		12.8[c]	3
Au	1:3, Au:PVP		calcined at 600°C	1[b]		17.1[c]	3
Au	1:10, Au:PVP			1[b]		13.1[c]	3

[a]measured by ICP-OES; [b]nomina; [c]determined by XRD; [d]determined by TEM
N/A: not applicable since the nano-catalyst catalyst is synthesized directly on the support

Several characterization techniques were used throughout this project to achieve the second sub-objective. For all of the nano-catalysts, TEM was used to determine the catalyst particle size distribution (Chapters 3-8), as well as the dispersion, in some cases (Chapters 3, 4 and 8). Similarly, XRD was used to calculate the crystallite size of the metal nanoparticles (Chapters 3, 4 and 7) and determine possible alloy formation (Chapter 7). These two techniques were the main measurements made throughout all studies in order to characterize the synthesized nano-catalysts.

The synthesis of the Au nanoparticles in Chapter 3 involved the addition of a stabilizing polymer which inhibits the catalytic activity; therefore, needed to be removed after the synthesis. Temperature-programmed gravimetric analysis (TGA) was used to assess the appropriate temperature for the effective removal of this polymer.

Each catalyst synthesized was supported at a desired weight percent; considered the nominal metal loading. To obtain the actual metal loading on the catalyst support, in Chapter 4, inductively-coupled plasma optical emission spectroscopy (ICP-OES) was used. Knowing the actual loading, the effect of metal loading was evaluated.

Chapter 6 discusses findings that the CeO_2 support was possibly partially reduced. Therefore, in order to compare the oxidation state of the ceria support before and after the polarization measurements, XPS was employed.

When evaluating the catalytic performance of the nano-catalysts, three different VOC oxidation reactions were used as model reactions. These included carbon monoxide (CO) (Chapter 3), toluene (C_7H_8) (Chapter 4), ethylene (C_2H_4) (Chapters 5 - 8) oxidation at atmospheric conditions. Ethylene oxidation was chosen for the latter studies due to its simple nature compared to toluene; however, being more complex for modelling VOCs compared to CO. It is also commonly used in many EPOC studies found in literature.

Some important factors that were considered when developing the reactor design (Chapter 5) included ease of assembly, effective current collection, and comparable performance to other conventional reactor designs. The main concern for the electrochemical cell design was that the catalyst-working electrode was electrically conductive; thus leading to the use of a MIEC material as a catalyst support.

Both Chapters 5 and 6 summarize results for the application of EPOC to the highly-dispersed Ru/CeO_2 nano-catalysts. The effect of applied current/potential, application duration (i.e., presence of permanent EPOC), and reaction conditions were evaluated. Through the calculation of the rate enhancement ratio (ρ), permanent rate enhancement ratio (γ), and Faradaic efficiency (Λ), the enhancement in the catalytic activity as well as the presence of the EPOC phenomenon ($|\Lambda| > 1$) was determined. In addition to the successful application of this phenomenon to highly-dispersed nano-catalysts, it was established that the enhanced activity may be caused by the partial reduction of CeO_2, resulting in a stronger interaction with the metal nanoparticles.

In order to elucidate this close relationship between EPOC and MSI, steady-state polarization curves were performed in Chapter 7; comparing open circuit catalytic rates of the nano-catalysts and their corresponding exchange current densities. The effect of particle size, temperature, the presence of CeO_2, as a MIEC support, and the addition of a second metal (i.e., Sn) were evaluated. The adoption of a previously proposed MSI rate enhancement ratio (ρ_{MSI}) was used to evaluate the effect of the presence of CeO_2 in the supported metal

catalysts compared to the free-standing metal nanoparticles. Moreover, a MSI Faradaic efficiency (Λ_{MSI}) was introduced in order to establish a preliminary relationship between MSI and EPOC.

Finally, due to the significant effect on the electrochemical and catalytic behaviour observed in the presence of CeO_2, a further study (Chapter 8) was conducted in order to evaluate the influence that CeO_2 has on the interaction with the supported metal catalysts (i.e., Pt, Ru, Ir). This study was achieved by observing the catalytic behaviour for ethylene oxidation in the presence and absence of both oxygen and ethylene. The different behaviours of the supported and free-standing nanoparticles were discussed.

Chapter 2: Literature Review

Adapted from "H.A.E. Dole and E.A. Baranova, Implementation of Nanostructured Catalysts in the Electrochemical Promotion of Catalysis" in the Handbook of Nanoelectrochemistry (2016) Springer International Publishing Switzerland, DOI 10.1007/978-3-319-15207-3_29-1.

2.1 Introduction

2.1.1 Heterogeneous Catalysis: Nanoparticles, Promotion, and Metal-Support Interaction

The form of catalysis where the reactants are in a different phase as the catalyst itself is referred to as heterogeneous catalysis [38]. The steps carried out during a heterogeneous catalytic reaction are first diffusion of the reactants to the catalyst surface then intraparticle diffusion of the reactants through the catalyst pores to the active sites. The reactants adsorb on the active sites and a surface reaction occurs. The products then desorb from the catalyst sites, intraparticle diffusion of the products occurs, and, finally, there is diffusion of the products away from the catalyst [38].

In heterogeneous catalysis, only the surface atoms are considered active for catalytic reactions; that is, for bulk material, most of the material is not being used (i.e., low volume-to-surface area ratio). The introduction of nanostructured catalysts changed the catalytic ability in heterogeneous catalysis research areas, giving an approach to optimize this volume-to-surface area ratio. To be considered "nano," the catalyst is defined as having at least one dimension in the range of 1–100 nm. There are several methods that have been developed to prepare such nanostructured catalysts. For instance, nano-films can be prepared through techniques such as physical vapor deposition [39,40], chemical vapor deposition [41,42], and atomic layer deposition [43,44], while nanoparticles can be prepared by impregnation [45–49], deposition–precipitation [45,50–54], coprecipitation [55–59], sol–gel [60–63], and polyol [64–72] as summarized in Table 2-1. The nanoparticle catalysts can be supported on two different types of supports, those considered non-active (i.e., γ-Al_2O_3, SiO_2, activated carbon) or active (i.e., TiO_2, CeO_2, YSZ, SDC).

Table 2-1: Selected representation of preparation methods for nanoparticles.

Method	Synthesized catalyst	Ref.
Impregnation	Au/TiO_2	[45]
	Fe_2O_3/SiO_2	[46]
	Ru/SnO_2, Ru/CeO_2, Ru/ZrO_2, $Ru/\gamma\text{-}Al_2O_3$	[47]
	Pt/YSZ	[48]
	$Pt\text{-}Ir/TiO_2$ nanotubes	[49]
Deposition-precipitation	Au/TiO_2	[45]
	$Au/\gamma\text{-}Al_2O_3$	[50]
	Au/TiO_2, Au/CeO_2, Au/Al_2O_3, Au/SiO_2	[51]
	$Au\text{-}Ag/TiO_2$	[52]
	Ag/SiO_2	[53]
	Ag/TiO_2, $Au\text{-}Ag/TiO_2$	[54]
Coprecipitation	Pd-doped CeO_2	[55]
	Fe_3O_4	[56]
	Pd/Al_2O_3	[57]
	$Co_{0.5-x}Mn_xZn_{0.5}Fe_2O_4$	[58]
	$LiFePO_4/C$	[59]
Sol-gel	ZnO, CuO, Cu0.05Zn0.95O	[60]
	$CoFe_2O_4$	[61]
	SnO_2	[62]
	$Ni_{0.7-x}Mg_xCu_{0.3}Fe_2O_4$	[63]
Polyol	Pt	[67]
	Pt	[72]
	PtRu	[65]
	PtRu	[70]
	Pt_7Sn_3	[71]
	FePt	[64]
	Ru, Pt	[68,73]
	Ag	[66]
	Cu	[69]

An important factor related to the type of support is the dispersion of the catalyst which is defined as the ratio of the number of gas-exposed surface atoms to the total number of catalyst atoms. In general, dispersion increases with decreasing particle size and theoretically approaches 100 % for particles with diameter in the range of 1 nm. It has been shown that, typically, higher dispersion leads to higher catalytic activity due to the presence of more active sites [47,74–76]. This trend has been shown for the same support material (i.e., SiO_2) synthesized with different surface areas [74]. Moreover, the catalytic activity of supported metal or metal oxide nanoparticles can be further enhanced or stabilized by using catalyst promoters or through the metal–support interaction (MSI) phenomenon.

Enhancing the activity of a catalyst through the concept of promotion involves adding a chemical species, referred to as a promoter, during the catalyst preparation procedure to the

catalyst in order to change its catalytic behavior. The discovery of this concept was first employed through what is referred to as chemical promotion [14–18]. The addition of such species can result in a change in the electronic and/or crystal structure of the catalyst which improves its catalytic performance, stability, and selectivity for the desired chemical reaction.

In general, promoters can be divided into two categories – structural and electronic promoters [14,77]. Structural promoters (e.g., Al_2O_3) enhance and stabilize the active phase while not participating in the catalytic reaction itself. Contrary to this, electronic promoters (e.g., alkali metal atoms) have a role in the catalytic reaction; they enhance the catalytic properties of the active phase by altering its chemisorptive properties, with respect to bond strength, of the reactants and intermediate species. The focus of this discussion will be on electronic promoters since they are a common factor between chemical and electrochemical promotion, as will be discussed later.

Table 2-2 summarizes some of the different types of electronic promoters and corresponding applications. The most commonly used electronic promoters include potassium [78–81] and sodium [82–86]. Other chemical promoters include other alkali metals (i.e., Cs) [79,87], alkaline earth metals (i.e., Mg, Ba) [79,88,89], and some transition metals (i.e., Co, Cr, Mo) [90].

Table 2-2: Summary of the type and use of some electronic promoting species.

Promoting species	Catalyst	Reaction	Ref.
Potassium (K)	Fe(111), Fe(100)	Adsorption of N_2	[78]
	Ru/Zeolite-X (Ru-KX)	NH_3 synthesis	[79]
	Fe_3O_4(111), A-Fe_2O_3(0001)	Dehydrogenation of ethylbenzene to styrene	[80]
	K-Fe (S6-20) BASF	Dehydrogenation of ethylbenzene to styrene	[81]
Sodium (Na)	Pd/YSZ	NO_x reduction by C_3H_6	[82]
	Pt/γ-Al_2O_3	NO_x reduction by C_3H_6	[83]
	Pt/γ-Al_2O_3	NO_x reduction by C_3H_6 and CO	[84]
	Rh/YSZ	NO_x reduction by CO	[85]
	Pt/YSZ	C_2H_4 oxidation	[86]
Cesium (Cs)	Ru/CsX	NH_3 synthesis	[79]
Cesium (Cs), chlorine (Cl)	Ag_2O	Epoxidation of C_2H_4	[87]
Barium (Ba)	Pt/γ-Al_2O_3	NO_x reduction by C_3H_6	[88]
Magnesium (Mg), barium (Ba)	Ru/BaX, Ru/MgX	NH_3 synthesis	[79]
Magnesium (Mg), barium (Ba), calcium (Ca), strontium (Sr)	Au/Al_2O_3	Partial oxidation of methanol to H_2	[89]
Cobalt (Co), chromium (Cr), molybdenum (Mo)	VPO/TiO_2, VPO/γ-Al_2O_3	Ammoxidation of 2-chloro benzaldehyde to 2-chloro benzonitrile	[90]
Carbon monoxide (CO)	Au(111)	Methanol oxidation	[91]

Potassium, as a chemical promoter, has been used for a variety of chemical reactions and fundamental chemistry studies [78,79]. A fundamental study was done on a single crystal of Fe(111) and Fe(100) showing a pronounced electron transfer from K to the Fe surfaces; this is attributed to the lowering of the "local" work function near where the potassium atoms are adsorbed [78]. Bécue et al. [79] demonstrated the effect of K promoters on the surface of a zeolite-X-supported Ru catalyst (2 wt%) for the synthesis of ammonia. It was found that the presence of K promoters increases the activity by approximately 70 % for optimal potassium coverage. For coverage higher than the optimal amount of potassium, it was observed that the activity did not increase; instead, a decrease in activity was attributed to the blocking of active sites due to excess potassium coverage.

More recently, chemical promotion has been shown using other alkali metals such as cesium or alkaline earth metals and transition metals. A recent review on the epoxidation of ethylene to ethylene oxide (EO) over a silver catalyst demonstrated the industrial application of using cesium and chlorine as promoters for the selectivity of EO [87]. It was found that the

unpromoted metallic silver catalyst had an EO selectivity around 50 %, while, with the addition of the promoters, the selectivity was enhanced to as high as 90 %. It is proposed that the Cl blocks the nonselective sites and promotes the active oxygen while Cs acts as a structural promoter. It is said that the Cl promoters weaken the Ag–O bond creating more reactive oxygen to enhance the EO isomerization. On the other hand, Cs interacts with the Ag_2O surface and subsurface oxygen resulting in CsO_x-type complexes.

The use of alkaline earth metals (i.e., Mg, Ca, Sr, Ba) as promoters was shown in one study to enhance both the activity and selectivity of supported gold catalysts (Au/Al_2O_3) in the partial oxidation of methanol to H_2 [89]. It was found that H_2 selectivity increased with increasing basicity of the promoting oxide species (i.e., unpromoted < MgO < CaO < SrO < BaO); however, the opposite trend was observed for the selectivity toward CO and CH_4. Similarly, the effect of transition metal additives on the catalytic properties of a vanadium phosphate (VPO) catalyst was studied for the selective ammoxidation of 2-chloro benzaldehyde to 2-chloro benzonitrile [90]. To observe the effect of such promoters, Co, Mo, and Cr were added to the VPO structure and supported on two different oxide supports – TiO_2 and γ-Al_2O_3. It was observed that a significant improvement in both selectivity and activity existed compared to the bulk VPO catalyst. More specifically, in the case of TiO_2-supported VPO, the addition of Cr exhibited the best performance followed by Mo. From these results, it was also found that the ability of the promoter appears to depend on the nature of the support and its interaction with the catalyst.

Furthermore, traditionally, it has been observed that electropositive species usually promote catalytic reactions while electronegative species poison the catalyst surface. One electronegative species, CO, has been well known to act as a poison for many metal catalysts; however, recent studies have shown a promotional effect of this species [91,92]. Rodriguez et al. [91] have demonstrated the promotional effect of adsorbed carbon monoxide for the oxidation of alcohols over a gold catalyst. It was proposed that neighboring adsorbed CO enhances the OH bond on the surface of the catalyst in addition to promoting the breaking of the C–H bond of the alcohol molecules, thus increasing catalytic activity.

A related phenomenon to the promotion of catalytic activity is referred to as metal–support interaction (MSI), where the support plays a key role in changing the properties of the

catalyst due the interaction between the two materials, usually resulting in higher catalytic activity [93,94]. It should be noted that despite the vast amount of MSI studies reported up-to-date, the mechanism and appearance of this effect are still under discussion. Both fundamental and catalytic reaction studies with regard to metal–support interaction are summarized in Table 2-3.

Table 2-3: Summary of selected metal-support interaction studies.

Metal catalyst	Support	Reaction	Ref.
Ru, Pd, OS, Ir, Pt	TiO_2	H_2, CO sorption	[30]
Pt	WO_3/C, TiO_2/C, C	Not applicable (XPS study)	[95]
Pt	YSZ	Not applicable (XPS study)	[96]
Au	SiO_2, TiO_2	CO oxidation	[74]
Pt	Al_2O_3, TiO_2 (P25, rutile, anatase), CeO_2, SiO_3, MgO	CO oxidation	[76]
PdO	CeO_2, TiO_2, Co_3O_4, Mn_2O_3, SnO_2	CO oxidation	[97]
Pt, Ni	YSZ, γ-Al_2O_3, TiO_2, CeO_2	CO oxidation	[98]
Cu	YSZ, γ-Al_2O_3	CO oxidation	[99–101]
Pt	YSZ, γ-Al_2O_3, C	CO oxidation	[102]
Pt	YSZ, CeO_2, Sm-doped CeO_2, C, γ-Al_2O_3	CO oxidation, C_2H_4 oxidation	[103]
Au	CeO_2/TiO_2	CO oxidation, water-gas shift reaction	[104]
Pd	CeO_2/YSZ	CH_4 oxidation	[105]
Pt	YSZ, TiO_2, SiO_2	C_3H_8 oxidation	[106]
Pt	YSZ, γ-Al_2O_3	Toluene oxidation	[107]

Overbury et al. [74] showed that for equally sized Au nanoparticles supported on SiO_2 (lower surface area) and TiO_2 (higher surface area), the catalytic activity was higher for the TiO_2-supported catalysts due to stronger metal–support interaction. Similarly, Kimura et al. [76] demonstrated that for the same loading of metal catalysts deposited on Al_2O_3 and TiO_2, a lower dispersion was obtained for the particles supported on Al_2O_3 compared to TiO_2 indicating aggregation of the metal particles. This was attributed as a stronger metal–support interaction between Pt and TiO_2 compared to Pt and Al_2O_3. It is especially noted that the smaller the nanoparticle, the stronger the interactions are with the support, therefore, increasing the effect of the support used [108].

A more specific term, strong metal–support interaction (SMSI), was first introduced in 1978 to describe the significant change in the chemisorptive properties of group VIII noble metals when they were supported on TiO_2 [30,31]. It was shown that these metals, both unsupported

and supported on common materials such as Al_2O_3, chemisorb one hydrogen atom per metal atom; however, in the case of TiO_2, the ability to chemisorb H_2 was either decreased or disappeared completely. It was suggested that SMSI is due to TiO_x migration to the catalyst surface. Among other theories, the possibility of d-orbital overlap between the Ti^{4+} cations and supported metal atoms was suggested [31]. More recently, Lewera et al. [95] carried out a study to further understand the change in electronic properties of nano-sized metals when deposited on TiO_2 through the analysis of X-ray photoelectron spectroscopy (XPS) data. Pt nanoparticles with an average size of 2 nm were deposited on a composite of TiO_2/C. A downshift in binding energy of the Pt $4f_{7/2}$ peak was observed which indicated a local charge density change due to the interaction between the metal and TiO_2. In addition, the presence of an additional (O 1s) peak for the Pt/TiO_2/C spectrum, compared to Pt/C and TiO_2/C, is attributed to oxygen bonded to Ti alloyed with Pt indicating the interaction between the two materials. The analysis of the Ti 2p peak also showed a downshift in binding energy for the supported Pt sample suggesting a new electronic state of Ti. Similarly, Ntais et al., [96] conducted an XPS study for YSZ-supported Pt nanoparticles which also showed a downshift.

Several recent studies have studied the MSI phenomenon, not only using TiO_2-supported metals but employing other ionic and mixed ionic–electronic conducting materials as well. High catalytic activity toward the water–gas shift reactions was shown for a Au/CeO_x/TiO_2(110) catalyst [104]. The high catalytic activity was attributed to the chemical properties of Ce_2O_3, which was formed through the interaction with TiO_2 and its effect at the ceria–gold interfaces. Similarly, Jiménez-Borja et al. [105] demonstrated a strong interaction between Pd and CeO_2 for a Pd/CeO_2/YSZ catalyst for the oxidation of methane. It was observed that the presence of ceria caused a decrease in the size of Pd^0 particles (from 280 to 103 nm) and an increase in the size of PdO particles. This is attributed to the oxygen storage properties of CeO_2 which seems to play a key role in the formation of PdO. Higher catalytic activity was observed for the catalysts containing more PdO compared to Pd. Furthermore, Pd catalysts supported on highly ordered mesoporous metal oxides (i.e., CeO_2, TiO_2, Co_3O_4, Mn_2O_3, and SnO_2) for the oxidation of CO were carried out to demonstrate the interaction between the metal and metal oxide supports [97]. It was found from XPS results that the binding energy of the Pd $3d_{5/2}$ peak for Pd/meso-CeO_2, Pd/meso-SnO_2, and Pd/meso-TiO_2 catalysts shifted more than that for Pd/meso-Co_3O_4 and Pd/meso-Mn_2O_3 indicating that the

former catalysts have more surface interactions with the Pd metal. From the catalytic experiments, the bare supports and supported Pd catalysts showed high catalytic activity in the order of Co_3O_4 > Mn_2O_3 > CeO_2 > SnO_2 > TiO_2; however, the increase in catalytic activity from bare support to supported Pd catalyst was the highest for the Pd/meso-CeO_2, Pd/meso-SnO_2, and Pd/meso-TiO_2 catalysts indicating the significant role of the support.

Ionically conductive supports or solid electrolytes have emmerged as a class of very promising catalyst supports due to their high ionic conductivity, and chemical and mechanical stability [109]. For a material to be ionically conductive, it must possess the structure that allows for either ions to transfer through a series of interstitial sites (i.e., Frenkel defects) or ions to transfer through vacancies in the crystal structure (i.e., Schottky defects) [14,110,111]. Some examples include yttria-stabilized zirconia (YSZ) (O^{2-} conductor), K-β'Al_2O_3 (K^+ conductor), and Na-β"Al_2O_3 (Na^+ conductor). As an extension, mixed ionic–electronic materials not only possess ionic conductive capabilities but electronic conductive properties as well [112,113]. Ion transfer in such materials occurs through structure defects as discussed; however, electronic conductivity occurs through delocalized states in the conduction or valence band or through localized states by a thermally assisted hopping mechanism. It should be noted that the reason for these properties is independent of each other – ion conductance depends on crystal structure while electronic conductance depends on electronic bandgap corresponding to the properties of the constituent ions [112]. Examples of mixed ionic–electronic conducting materials include ceria (CeO_2), titania (TiO_2), and perovskite-type materials in a form of $La_{1-x}A_xCo_{1-y}B_yO_{3-\delta}$ (where A = Sr, Ba, Ca, and B = Fe, Cu, Ni) [113,114].

Initially, the concept of MSI was attributed to an electronic effect; however, further studies have shown an effect of oxygen vacancies in metal oxides as well. Metcalfe and Sundaresan [98] demonstrated this concept for CO oxidation over Pt and Ni catalysts supported on YSZ, γ-Al_2O_3, TiO_2, and CeO_2. It was found that catalytic activity for the Pt catalysts ranged from Pt/TiO_2 > Pt/YSZ > Pt/γ-Al_2O_3. The most interesting results are those for the Ni catalysts, where Ni/TiO_2, Ni/YSZ, TiO_2, and YSZ showed significant catalytic activity, with the supported Ni catalyst showing higher activity than their corresponding pure supports. The difference in the activity of Ni/TiO_2 and pure TiO_2 could be attributed to only the electronic

effects of TiO_2; however, after observing higher activity for Ni/YSZ compared to pure YSZ, it was proposed that oxygen ion transfer between the metal and support also plays a role in enhancing the catalytic activity. A similar conclusion was found for studies of a copper catalyst supported on γ-Al_2O_3 and YSZ [99–101]. The higher catalytic activity was attributed to the presence of Cu^+ due to the interaction between the copper oxide on the surface of the YSZ and the nearby oxygen vacancies. Vernoux et al. [115] also observed such migration of ionic species from the support to the surface of the nano-catalyst, referring to it as self-induced electrochemical promotion. This concept has been suggested as an explanation for higher catalytic activity for the oxidation of CO over YSZ-supported Pt nanoparticles [72,102]. It was shown that the catalyst was active for a temperature as low as 40°C. This high catalytic activity was attributed to the migration of O^{2-} species species to the surface which may lead to alterations in the catalytic properties of the Pt nanoparticles. This phenomenon has also been observed for both propane oxidation [115] and toluene oxidation [107] over a Pt/YSZ catalyst. Most recently, Isaifan and Baranova [103] also demonstrated the role of ionic and mixed ionic–electronic supports and the mobility of O^{2-} from these supports for the oxidation of CO and C_2H_4 in an oxygen-free environment. It was found that Pt/YSZ, Pt/CeO_2, and Pt/Sm-doped CeO_2(SDC) have high catalytic activity for CO and C_2H_4 oxidation while Pt/C and Pt/γ-Al_2O_3 as well as the blank supports show no catalytic activity in the absence of gaseous O_2. These results imply that O^{2-} from the support reacts with CO and C_2H_4 in an electrochemical reaction at the three phase boundary and the mechanism of nano-galvanic cells was proposed [116].

2.2 Electrochemical Promotion of Catalysis

Discovered in the 1980s [117], the phenomenon of electrochemical promotion of catalysis (EPOC), also referred to as non-Faradaic electrochemical modification of catalytic activity (NEMCA), demonstrated a new approach to enhancing the catalytic activity and opened up a new class of promoters previously unknown in heterogeneous catalysis (e.g., O^{2-}, H^+, OH^-, H^+). By applying an electrical current or potential between the catalyst-working electrode and a counter electrode deposited on a solid electrolyte, it was found that the catalytic activity and selectivity can be significantly altered due to modifications of the electronic properties of the catalyst. Consequently, the adsorption strength of the reaction components is altered resulting in a distinct change in catalytic performance [14]. Compared to chemical

promotion, the addition of promoter species is done in situ and can be controlled depending on specified reaction conditions [14,15,19–24,26–28,118]. This also implies that promoters with short lifetimes can still effectively be utilized as its coverage on the catalyst surface can be fixed through the application of a current or potential. Therefore, it is said that there is an operational and not a functional difference between chemical and electrochemical promotions [14,20,29,77,85,119]. Currently, EPOC has been studied for more than 100 catalytic systems and does not appear to be limited to any specific type of catalytic reaction, metal catalyst, or solid electrolyte. Since the discovery of EPOC, several comprehensive reviews [18,24,29,118,120–132], book chapters [133–137], and a book [14] have been published to describe this phenomenon; the authors invite the reader to consult these works for comprehensive reading on the EPOC phenomenon. Here, a short overview of the principles, a common experimental setup and reactors, as well as some examples of EPOC with thick, low dispersion film catalysts will be discussed followed by recent studies using nanostructured catalysts.

The concept behind EPOC is that, initially, before current or potential is applied, the catalyst surface is covered by chemisorbed reactants (e.g., O_2 and C_2H_4) in an equilibrated state. Depending on the concentration of the species, there may be more or less of each species adsorbed on the catalyst surface. By applying a current or potential, ions (i.e., O^{2-} in the case of YSZ) from the solid electrolyte either back-spillover (i.e., move to the surface of the catalyst) or spillover (i.e., move from the surface of the catalysts) depending whether the electrochemical cell is positively or negatively polarized, respectively. In the case of back-spillover of the O^{2-} species, it is said that these species form a strong bond on the catalyst surface. The mechanism of this transformation can be seen in the following reaction (Eq. 2-1) [14]:

$$O^{2-}(YSZ) \rightarrow \left[O^{\delta-} - \delta +\right](catalyst) + 2e^{-} \qquad \textbf{2-1}$$

where $O^{\delta-}$ is the general form of the back-spillover species corresponding to its image charge $\delta+$, indicating that the back-spillover species is overall neutral. The formation of this layer is referred to as an effective double layer. Due to this back-spillover, the oxygen reactant from the gas phase is forced into a weakly bonded state resulting in a more reactive chemisorbed

species. Therefore, it is observed that the catalytic rate increases until a new steady-state is reached through the equilibrium of the strongly and weakly bonded oxygen species [14]. The opposite effect is observed for the spillover of the O^{2-} species.

In general, the property of a solid surface that dictates its chemisorptive and catalytic properties is its work function (Φ). By definition, the work function is the minimum energy required for an electron to move from the Fermi level of the solid to an outer point, a few μm outside the surface [14,138]. Depending on the type of species adsorbed or spilled over onto the catalyst surface, the work function can be altered accordingly. An electron donor species (e.g., C_2H_4) will cause the work function to decrease, while an electron acceptor species (e.g., O_2) will cause the work function to increase. Four different types of reaction behaviors, in regard to the presence of these species, have been established to classify the relationship between work function and catalytic rate (r) for EPOC studies – electrophobic ($\delta r/\delta\Phi > 0$), electrophilic ($\delta r/\delta\Phi < 0$), volcano type (exhibits a minimum), and inverted volcano type (exhibits a maximum).

More specifically, to evaluate the performance of the catalyst in terms of electrochemical promotion, there are two main parameters that are calculated – rate enhancement ratio (ρ), and Faradaic efficiency (Λ) [14]. The rate enhancement ratio (Eq. 2-2) is defined as,

$$\rho = r/r_0 \qquad \textbf{2-2}$$

where r_0 is the open circuit oxidation of reactant species ($mol \cdot s^{-1}$) and r is the oxidation rate ($mol \cdot s^{-1}$) for an applied current/potential. The Faradaic efficiency (Eq. 2-3), for an O^{2-} conducting system, is defined as the following:

$$\Lambda = (r - r_0)/(I/2F) \qquad \textbf{2-3}$$

where I is the current measured across the cell (A) and F is Faraday's constant (96 485 $C \cdot mol^{-1}$). It should be noted that the enhancement is considered to be the effect of electrochemical promotion only when $|\Lambda| > 1$, which indicates non-Faradaic enhancement [14].

First discovered by Comninellis and coworkers [139], another important aspect that is considered in EPOC studies is what is referred to as “permanent” electrochemical promotion of catalysis (P-EPOC). It has been shown that the reversibility of EPOC strongly depends on the duration of polarization and magnitude of applied current or potential. With P-EPOC, after current interruption, the catalytic rate remains higher than the initial open circuit value. In the case of P-EPOC, the permanent rate enhancement can be evaluated using Eq. 2-4 [139]:

$$\gamma = r_p / r_0 \qquad \textbf{2-4}$$

where γ is the permanent rate enhancement ratio and r_p is the catalytic rate ($mol \cdot s^{-1}$) at the new steady-state value after current interruption.

Two types of experimental reactors exist to carry out conventional EPOC studies – a fuel cell type reactor and single-chamber type reactor [14]. The fuel cell type reactor (Figure 2-1a) consists of two chambers, one in which the catalyst-working electrode is exposed to the reactants and products, while the other chamber contains the counter and reference electrodes which are exposed to a reference gas only. Contrary to this, the single-chamber type reactor (cell configuration in Figure 2-1b and typical experimental setup in Figure 2-1c) consists of all electrodes exposed to the same reactants and products. The important consideration with this type of reactor is that the reference electrodes must be made of an inert material with respect to the reactants (in most cases, gold is used) to ensure no contribution to the catalytic rate. Conventional EPOC studies were carried out using metal (deposited with metallic paste) catalyst films, typically, of a thickness in the range of 5–10 μm [20,140] and a metal dispersion less than 0.1 % [141]. Typical solid electrolytes include YSZ (O^{2-} conductor), β’-Al_2O_3 (Na^+ conductor), or β”-Al_2O_3 (K^+ conductor).

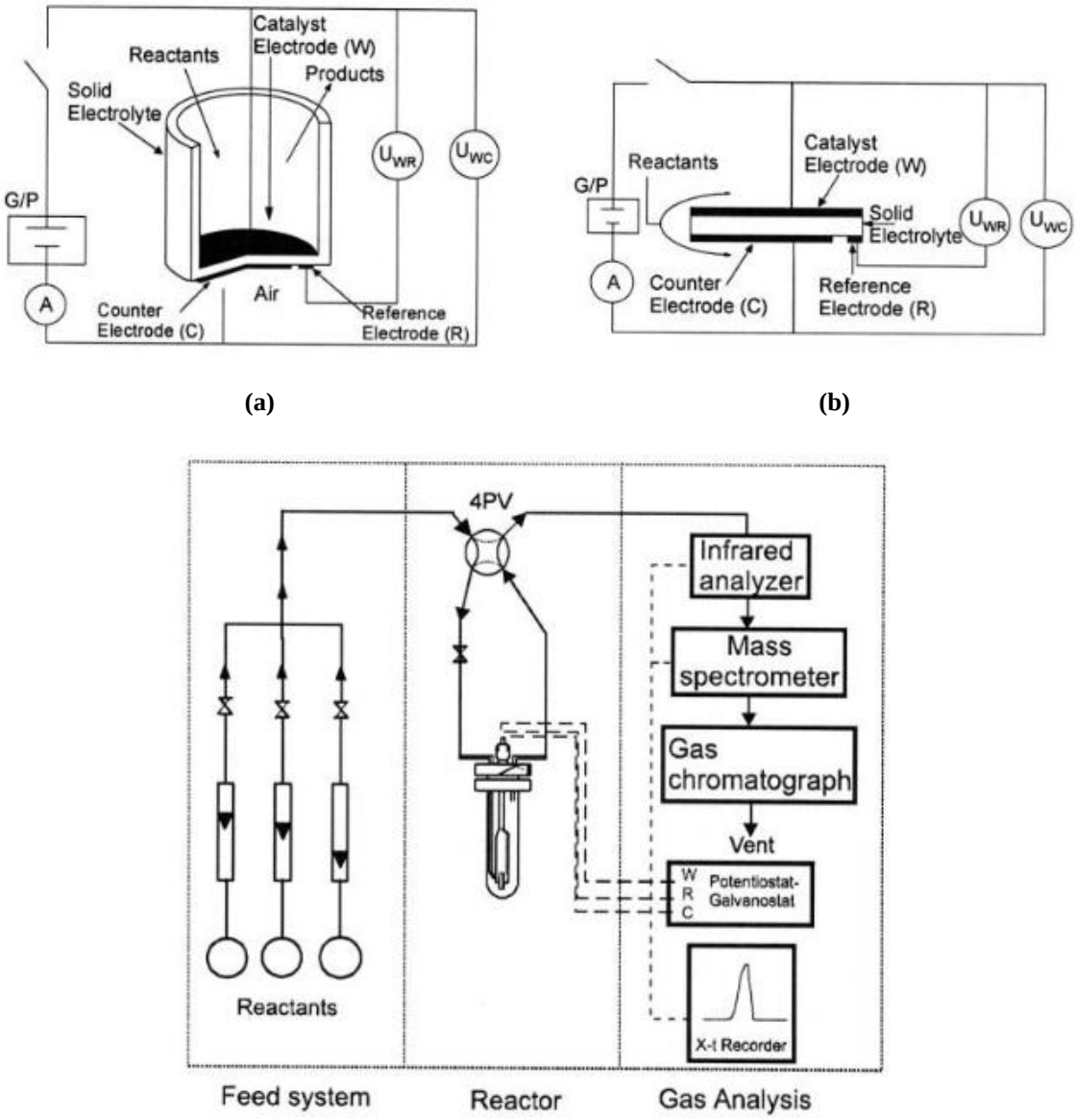

(a) **(b)**

(c)

Figure 2-1 Schematic of the (a) fuel cell type reactor, (b) single-chamber type reactor, and (c) typical gas flow experimental arrangement using the single-chamber type reactor (Reproduced from Vayenas et al. [14]**)**

The EPOC phenomenon has been shown to be effective for various reactions; however, the most common model reaction used in conventional EPOC studies is the complete oxidation of ethylene (Table 2-4) [20,24,117,140–149]. This was the reaction under observation over a porous Ag film when it was first discovered that pumping and removing oxygen ions from the surface of the catalyst through an applied current can alter the catalytic rate and selectivity [117]. It was then later demonstrated that this effect is not specific to any type of

reaction system, although the most significant enhancement (i.e., tenfold increase, Λ up to 15 000) was shown for the oxidation of C_2H_4 over a Pt catalyst [20,140].

Table 2-4: Electrochemical promotion of ethylene oxidation for various catalytic systems.

Catalyst	Solid electrolyte	Temperature (°C)	Promotion Parameters ρ_{max}	$\Lambda_{max/min}$	Ref.
Ag	YSZ	320-420	-	< 300	[117]
Pt	YSZ	260-420	-	< 15 000	[140]
Pt	YSZ	300-450	-	74 000	[20]
Pt	YSZ	375	300	289	[141]
Pt	YSZ	510	-	144	[142]
Rh	YSZ	320-450	1.4	123	[143]
IrO_2	YSZ	380	-	200	[144]
IrO_2	YSZ	380	13	~100	[145]
IrO_2	YSZ	380	2.5	2000	[146]
Pd	YSZ, β"Al_2O_3	300-400	-	3000	
Pt	TiO_2	500	21	1880	[147]
	Gd-doped $BaPrO_3$				
Pt	Y-doped $BaZrO_3$	400-600	1.3	-	[148]
Pt	$La_{0.99}Sr_{0.01}NbO_{4-\delta}$	350-450	1.4	-100	[149]

Enhancement in catalytic activity through this phenomenon for C_2H_4 oxidation has been shown over Pt catalysts supported on YSZ and TiO_2, O^{2-} conducting supports [147]. Further studies for IrO_2 film catalysts supporting on a YSZ electrolyte showed an enhancement in catalytic activity through an applied positive potential (i.e., oxygen ions migrate to the surface of the catalyst) [144–146]. Permanent promotion was also observed for this system which was attributed to the formation of a higher coordinated oxide at the catalyst/solid interface [145]. Moreover, Koutsodontis et al. [141] demonstrated that the catalyst film thickness for a Pt/YSZ cell is an important factor that affects the magnitude of electrochemical promotion as well, showing that the catalytic rate increases with the increase in film thickness. In addition to O^{2-} conducting electrolytes, positive ion (i.e., Na [147,150–153], K [154], and H [147–149,155]) conducting electrolytes have been employed. The electronic effect of these types of promoters is the opposite of that for oxygen ions; that is, by pumping positive ions to the catalyst surface, the work function decreases. In studies involving Na^+ promoters, Na-β"Al_2O_3 is used as a solid electrolyte. In general, it has been found that catalytic activity, for CO [150] or C_2H_4 [147] oxidation and NO reduction by hydrocarbons [151–153], is increased with low Na coverage, while as Na coverage increases, this leads to poisoning of the catalyst surface. Similar observations were found in the case of

potassium promoters from a K-β'Al_2O_3 electrolyte for CO oxidation over a Pt catalyst [154]. With regard to the use of H^+ promoters, several different electrolytes have been studied (e.g., Nafion [147,155], Gd-doped $BaPrO_3$ [148], Y-doped $BaZrO_3$ [148], and $La_{0.99}Sr_{0.01}NbO_{4-\delta}$ [149]). Compared to Na and K, H^+ promoters do not seem to have a significant enhancement of the catalytic activity [148,149], in addition to a weak non-Faradaic effect [149].

Although much research has been performed regarding this technology, limitations have been identified that prevent its commercialization. These include eliminating the conventionally used thick film catalysts which have low surface areas and high material costs and moving from theoretical to more practical reactor designs [29]. Overall, the objective is to be able to apply the concept of EPOC to high dispersion heterogeneous catalysts.

2.3 Application of Nanostructured Catalysts for EPOC

2.3.1 Highly Dispersed Nano-Catalyst Preparation

In heterogeneous catalysis, dispersion of a catalyst has been shown to be an important factor in terms of catalytic performance; the higher the dispersion, the more available the active sites, typically resulting in higher catalytic activity. Dispersion is one aspect of commonly used electrochemical promotion catalysts that has been recognized as an important factor that requires improvement in order to be competitive with the state-of-the-art commercial heterogeneous catalysts. To address the limitation of low metal dispersion found for the catalyst-working electrodes of conventional electrochemical promotion systems, several deposition techniques have been studied (Table 2-5).

Table 2-5: Preparation methods of highly dispersed nano-catalysts.

Method	Catalyst	Dispersion/loading	Particle size	Film thickness	Ref.
Impregnation	Pt	0.2 or higher	-	-	[156]
	Pd	4.9%	2.6 nm	-	[157]
	Ag	1%	100 nm	-	[158]
	Ru	3 mg Ru	-	4 μm	[159]
	RuO_2	1.72 g RuO_2/m^2	-	-	[160]
	Pt	34, 40, 42%	3.5, 3.0 nm	-	[106]
Metal sputtering	Pt	-	40 nm	-	[161,162]
	Pt	-	-	30, 90 nm	[163]
	Pt	2.2, 32 μg Pt/cm^2	-	2, 22 nm	[164]
	Pt	-	-	150 nm	[165]
	Pt	5%	50 nm	-	[166,167]
	Pt	40%	-	40 nm	[168]
	Rh	10%	-	40 nm	[169]
	Rh, Pt	13-40%	-	40 nm	[170]
	Rh, Pt	> 10%	-	40 nm	[171]
	Rh-Pt	> 15%	-	40 nm	[172]
Electroless deposition	Pd	5 mg Pd	-	-	[173]
Electrostatic spray deposition (ESD)	Pt	250 μg Pt	9 nm	65	[174]
		320 μg Pt	9 nm	85	
		420 μg Pt	23.2 nm	110	

The first technique that has been used in recent electrochemical promotion studies that results in near-nanometric or porous films is wet or dry impregnation 156–160]. In general, this type of technique employs a precursor salt of the desired metal dissolved in the solution. The solution is dried on the solid electrolyte, calcined, and reduced in H_2. For example, Marwood and Vayenas [156] dissolved H_2PtCl_6 in water, dried at 80°C (catalyst 1) and 90°C (catalyst 2), calcined in air at 450°C for 1 h, and reduced in 2% H_2 in helium at 250°C for 2 h. Using the CO titration technique [175] to determine dispersion, it was found that catalyst 2 had a dispersion of D = 21 % while for catalyst 1, which had a similar mass as catalyst 2 but a surface area of a factor of 5 higher, the dispersion was estimated to be approximately D ≈ 100%. A similar procedure was carried out by Jiménez-Borja et al. [157] using a 0.1 M $Pd(NH_3)_4(NO_3)_2$ aqueous solution which resulted in a Pd metal dispersion of 4.9% for 0.85 mg of Pd deposited. Even though not in the nanometric scale, other groups have demonstrated a decrease in metal required through porous micrometric films, as shown by Theleritis et al. [159] who deposited a porous film of thickness ~4 μm for a loading of approximately 3 mg of catalyst. In addition, Li and Gaillard [158] demonstrated the use of a less expensive metal, Ag, for working electrode films that was of a micrometric thickness of 1.8 and 3.9 μm, and an average crystallite size of approximately 100 nm.

Another common deposition technique that has been employed by many research groups [161–172] to increase catalyst dispersion is metal sputtering, in which the solid electrolyte substrate is placed inside a vacuum chamber in close proximity to the desired metal to be deposited. The desired metal is bombarded with ionized gas molecules in order to displace the metal in small quantities and slowly deposit a thin, nanometric layer on the substrate. This technique has been used by several groups to deposit Rh [169–171], Pt [161–168], or Rh–Pt bimetallic [172] thin-film catalysts. Both Balomenou et al. [170,171] and Baranova et al. [169,176,177] have achieved a film thickness of approximately 40 nm and a dispersion of approximately 13-40% and 10%, respectively. Other groups have also shown sputter deposition of Pt that achieves a thickness ranging from 30 to 150 nm, corresponding to dispersions from 5 % to 40 % [161–163,165–168]. Uniquely, Karoum et al. [164] sputter deposited a thin layer of Pt (~2 nm) on an 80 nm LSM ($La_{0.7}Sr_{0.3}MnO_3$) interlayer where the Pt layer did not necessarily cover the entire surface; however, it was shown to be viable for electrochemical promotion and electronically conductive due to the LSM interlayer. Finally, co-deposition of both Rh and Pt (atomic ratio, 1:1) was performed by Koutsodontis et al. [172] which resulted in an approximate thickness of 40 nm and a total active metal surface area of 1.9×10^{-5} mol metal.

Other research groups have also employed alternative, less common techniques such as electroless deposition [173] and electrostatic spray deposition (ESD) [174]. Lintanf [174] describes the ESD method as using less material compared to conventionally used paste deposition and being fully reproducible. It was reported that three different types of films can be produced – reticulated, dense, and dense – with particles corresponding to film thicknesses of 110, 65, and 85 nm, respectively. The average crystallite size was found to be 23.2 nm for the reticulated film and 9.0 nm for both dense films. Also, an approximate dispersion of 40 % was reported.

2.3.2 Cell Configurations and Reactor Design

Another factor that has been identified and discussed in previous reviews [29,128] which is preventing commercial application of electrochemical promotion from being achieved is the configuration of the cell and design of the reactor. In a recent comprehensive review, Tsiplakides and Balomenou [29] summarized the considerations taken to address the need

for cell configurations that can accommodate thin films and nanoscale catalysts along with designing a more compact reactor that has efficient current collection. The development of electrocatalysts, new configurations such as bipolar or monolithic, and concept of "wireless" EPOC is discussed in this review.

As alluded to in the previous section, the simplest modification to the conventionally used electro chemical promotion cell is to deposit less metal for the working electrode. An important factor to consider, though, is that the metal deposited as a working electrode must remain electronically connected; otherwise, some of the film will not be polarized. Lintanf's [174] description includes a gold mesh on the working electrode side of the cell in order to ensure electronic connectivity for their thin (65-110 nm) Pt catalyst films deposited by ESD. These details are not indicated in other studies [157,159,165–167,178]; however, electrochemical promotion using the conventional cell configuration was observed for catalyst films exhibiting dispersions ranging from 5 %to 80 %demonstrating the presence of at least some electrical connectivity. Similarly, another approach to establish electrical connectivity involves introducing a mixed ionic–electronic conductive (MIEC) interlayer between the nanostructured catalyst and solid electrolyte. Some examples of MIEC interlayer materials that have been used in recent studies include TiO_2 [163,169,177], LSM ($La_{0.7}Sr_{0.3}MnO_3$) [164], CeO_2 [179], and LSCF/GDC ($La_{0.6}Sr_{0.4}Co_{0.2}Fe_{0.8}O_{3-\delta}Gd_{0.1}O_{1.95}$) composite (30% GDC) [180]. Several methods were used to introduce these interlayers. Baranova et al. [169,177] deposit TiO_2(~5 μm thickness) on a YSZ pellet by applying a solution of 20 % TiO_2 in EtOH:H_2O (1:1), evaporating at 60°C for 10 min, and thermal treatment at 450°C for 30 min in air; following this deposition, Rh is sputter deposited overlaying the TiO_2. Alternatively, another study showed the use of sputter depositing for both the TiO_2 interlayers (~90 nm thickness) along with the deposition of Pt (~30 nm thickness) [163]. Figure 2-2 shows SEM micrographs of the deposited layers on the YSZ pellet. It was noted that the YSZ pellet is not fully covered by the TiO_2 interlayer (Figure 2-2b)

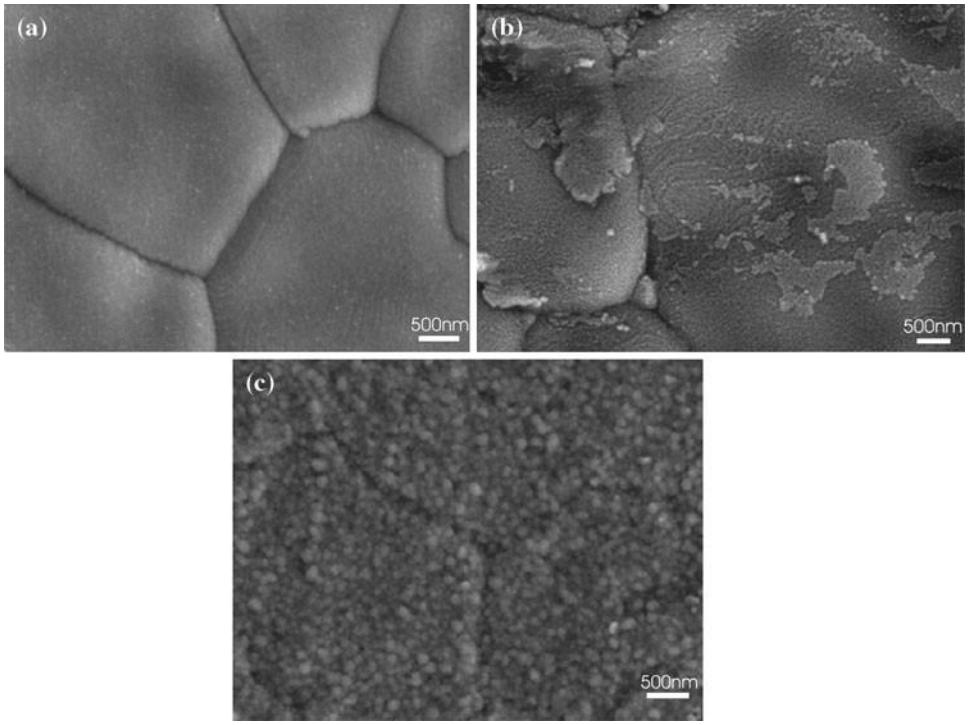

Figure 2-2: SEM micrographs of (a) YSZ surface, (b) sputter-deposited TiO_2 on YSZ surface, and (c) sputter-deposited Pt on TiO_2/YSZ surface (Reproduced from Papaioannou et al. [163]**)**

Both interlayer (LSM) and Pt catalyst were also sputter deposited in a study performed by Karoum et al. [164]; however, interesting to note, the use of a CGO ($Ce_{0.9}Gd_{0.1}O_{2-\delta}$) pellet was shown to be an alternative to using YSZ. For a temperature range of 200-400°C, the ionic conductivity of the CGO pellet was shown to be at least 10 times higher than that of the YSZ pellet. Finally, as described by Kambolis et al. [180], the electronic conductivity of the catalyst electrode in their EPOC cell was not ensured by the impregnated Pt nanoparticles but by the MIEC interlayer of LSCF/GDC which was deposited through screen printing on a GDC pellet.

The first step toward a modified cell configuration is shown in Figure 2-3, proposed by Marwood [181] in the 1990s, in which the catalyst is not used as an electrode as in the conventional EPOC, but rather it is instead electronically isolated with current passing between two gold electrodes. This pioneering work showed that Pt was deposited using the commonly used paste to determine whether a direct electrical connection between the catalyst and counter electrode was necessary to observe the effect of electrochemical promotion [181].

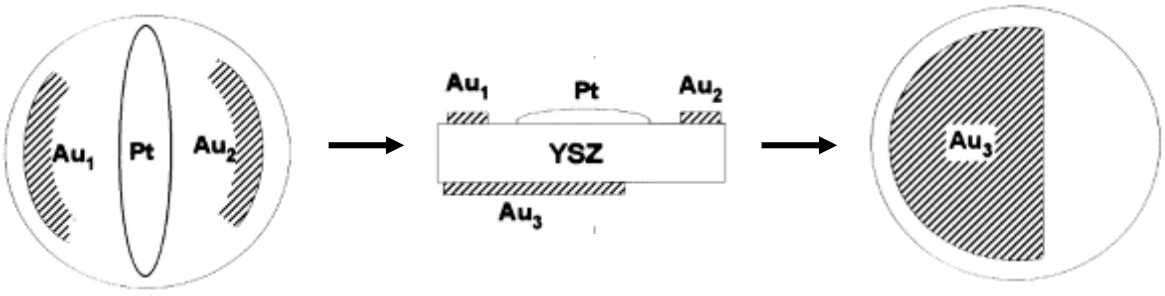

Figure 2-3: Schematic of first proposed bipolar configuration, Pt catalyst and Au working (Au_1), counter (Au_2), and reference (Au_3) electrodes (Reproduced from Marwood[181]**)**

Similarly, a preceding study demonstrated the use of highly dispersed impregnated Pt (~5 nm) nanoparticles [156]; however, they were deposited on a gold working electrode. From this study, it was shown that direct contact between the catalyst and the solid electrolyte was not necessary as well. In addition, it was also not necessary for the catalyst to be continuous to observe the effects of electrochemical promotion.

Various other cell designs have been proposed and tested by other research groups which fall under the bipolar configuration category. These include depositing Pt metal paste in the forms of stripes or dots between two gold electrodes [182], coating glass beads with Rh and placing them inside a YSZ tube that is coated with two gold electrodes on the outer surface [119], and sputtering Pt between the comb-like gold electrode structures (distance of 2 mm between electrodes) [161]. Figure 2-4 depicts a bipolar cell configuration presented by Xia et al. [162]. As shown in the figure, it was proposed that upon application of an electrical field, the dispersed Pt nanoparticles form partially or completely polarized galvanic cells, one side being positively polarized and the other negatively polarized.

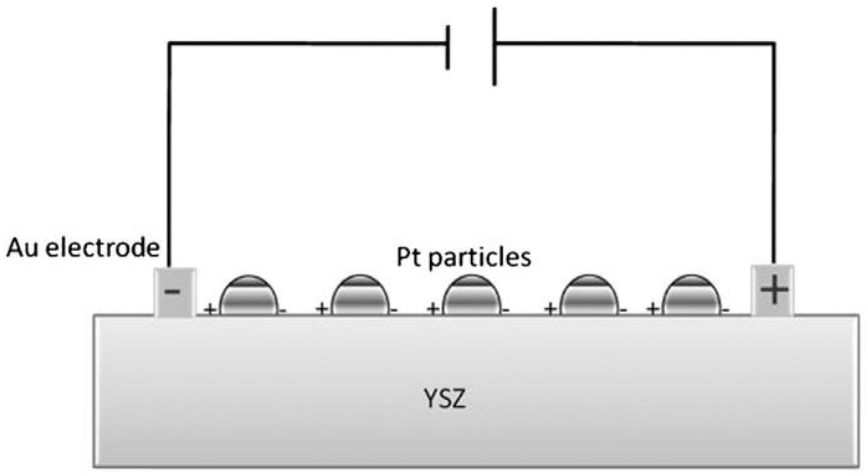

Figure 2-4: Schematic of bipolar configuration of electrochemical cell, consisting of two Au electrodes and polarized Pt particles deposited on YSZ solid electrolyte (Reproduced from Xia et al. [162]**)**

Further cell modifications were first proposed by Wodiunig et al. [160] through the use of a cylindrical YSZ solid electrolyte monolith. A RuO_2 catalyst was deposited through thermal decomposition (i.e., impregnation) inside the channels of the monolith, while two gold electrodes were deposited symmetrically on the outside of the cylinder. A similar honeycomb monolith was used in a previous study where dispersed Pd particles were introduced into the channels by electroless deposition; however, instead of both electrodes deposited on the outside of the cylinder, a gold working electrode was deposited on the entire outside surface, while a continuous Pd film was deposited (as a counter electrode) on the center channel of the monolith [173]. Furthermore, using this concept of a monolithic reactor and in regard to both the desire for efficient current collection and a compact reactor design, the monolithic electrochemically promoted reactor (MEPR) was proposed by Balomenou et al. [170,171]. Details of the design and construction of this reactor are well outlined, describing that the main advantage is that it can be assembled and dismantled easily and the plates can be replaced as necessary [170]. This type of reactor has also been employed by Koutsodontis et al. [172] who describe the design as a hybrid between the classical honeycomb monolith and a flat- or ribbed-plate solid oxide fuel cell; a feasible solution in order to minimize electrical connections.

A more recent concept that has been related to the electrochemical promotion phenomenon is that of self-induced electrochemical promotion. One of the main advantages of this type of

catalytic cell is that there is no electrical contacts required which, in turn, means no external circuit. It has also been a suggestion in order to overcome the limitation of the electrical connectivity of nano-catalysts. This concept has been demonstrated for the oxidation of CO over YSZ-supported Pt nanoparticles [72,102] as well as for propane oxidation over a Pt/YSZ catalyst [115]. Similarly, the concept of a wireless configuration has been studied as well which involves a concentration driving force that causes the migration of promoting ion species from the support toward the surface of the nanostructured catalyst [183–185]. These studies were also performed for a Pt catalyst deposited on a MIEC support (or membrane). The cell is placed inside a dual chamber reactor which consists of a reaction side (i.e., catalyst, reaction gases) and a sweep side (i.e., catalyst, sweep gas). In this case, open circuit conditions correspond to using the same reaction mixture on each side. To induce backspillover (i.e., pushing oxygen toward the surface of the reaction side catalyst), oxygen was introduced on the sweep side. This creates an oxygen chemical potential difference across the membrane driving the oxygen toward the reaction side. Furthermore, spillover (i.e., removing oxygen from the surface of the reaction side catalyst) was induced by sweeping hydrogen on the sweep side creating a driving force in the opposite direction [183–185]. It should be noted that the same in situ control of catalytic activity as EPOC can be achieved with this type of wireless configuration by altering the oxygen concentration difference across the membrane.

2.3.3 Electrochemical Promotion of Nanostructured Catalysts

Several model reactions have been used to evaluate and investigate the viability of electrochemical promotion for the nano-catalyst systems (as shown in Table 2-6). These include complete oxidation of ethylene [160,163,169,170,176,177,181,182] and propane [164,165,167,180], combustion of CO [161,162,166] and natural gas [157,173,179], reduction of NO in the presence of hydrocarbons [119,171,172,174,178], and, more uniquely, SO_2 oxidation [168] and the reverse water-gas shift (RWGS) reaction [159]. Each study has shown promising results for electrochemical promotion over nano-catalysts for different cell configurations and reactor designs which prove to be furthering this technology toward commercialization.

Table 2-6: Electrochemical promotion of nano-catalytic systems.

Reaction	Catalyst	Solid electrolyte	Temperature (°C)	Promotion parameters		Ref.
				ρ_{max}	$\Lambda_{max/min}$	
C_2H_4 oxidation	Pt	YSZ	353	1.38	688	[181]
	Pt	YSZ	400	3.8	-	[182]
	Pt	YSZ	280	67	188	[163]
		TiO_2/YSZ		168	753	
	Pt, Rh	YSZ	300-380	1.45	77	[170]
	Rh	YSZ	300-420	60	1400	[169,176,177]
		TiO_2/YSZ		78	1791	
	RuO_2	YSZ	360	-	90	[160]
C_3H_8 oxidation	Pt	YSZ	350	5.6	330	[165]
	Pt	YSZ	150-500	22.4	480	[167]
	Pt	$Ce_{0.9}Gd_{0.1}O_{2-\delta}$	170-250	1.3	6	[164]
	Pt	$Ce_{0.9}Gd_{0.1}O_{0.95}$	267-338	1.38	85	[180]
CO oxidation	Pt	YSZ	300	500	1.5	[161,162]
	Pt	YSZ	250	4	530	[166]
CH_4 oxidation	Pd	YSZ	400	-	47	[173]
	Pd	YSZ	120-500	3.65	-	[157]
	Pd	CeO_2/YSZ	480	5.6	764	[179]
NO_x reduction	Pt	YSZ	300-510	2.3	48	[174]
	Pt, Rh	YSZ	290-305	14	900	[171]
	Pt-Rh	YSZ	335-380	6.46	13.75	[172]
	Rh	YSZ	275-450	6	5	[119]
	Rh	YSZ	370	220	1207	[178]
SO oxidation	Pt	YSZ	330-370	2	30	[168]
RWGS	Ru	YSZ	200-300	2.5	1000	[159]

In general, it has been concluded that the reaction rate of ethylene oxidation is significantly increased when a positive polarization is applied [160,163,169,170,176,177,181,182]. The introduction of a MIEC interlayer, especially TiO_2, was shown to enhance the catalytic activity even more [163,169]. Baranova et al. [169] discuss that this enhancement due to the addition of the TiO_2 interlayer is attributed to the higher surface area of the catalyst deposited on TiO_2 layer, under polarization, acts as a catalyst in transforming the gaseous O_2 to promoter O^{2-} species at the Pt/gas interface [163]. Figure 2-5 shows a comparison of the catalytic performance of the Pt catalyst with and without the incorporation of a TiO_2 interlayer. Some of the observations discussed from these results include that there is an increase in U_{WR} for Pt/TiO_2/YSZ catalyst which implies an increase in work function indicating a higher coverage of promoting O^{2-} species on the catalyst surface resulting in greater enhancement in activity; also, a new steady state, upon positive polarization, was achieved significantly faster for the Pt/TiO_2/YSZ catalyst compared to the Pt/YSZ catalyst.

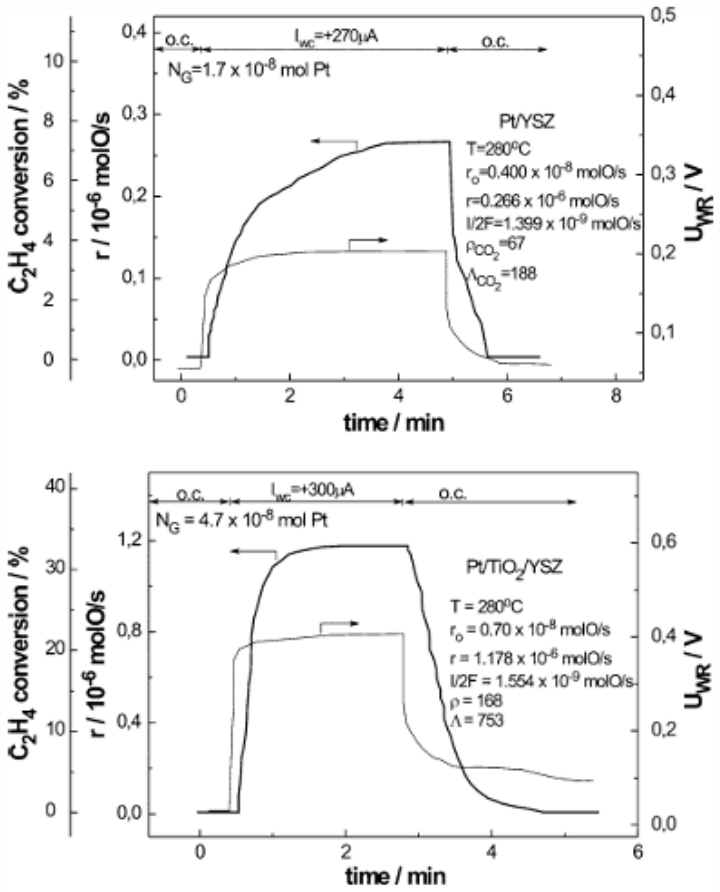

Figure 2-5: Transient effect of applied constant current on the rate of C_2H_4 oxidation: (top) Pt/YSZ catalyst, (bottom) Pt/TiO_2/YSZ catalyst (Reproduced from Papaioannou et al. [163]**).**

Similar results were found using the bipolar configuration by both Marwood [181] and Balomenou et al. [182]; however, it was observed that the magnitude of electrochemical promotion (in terms of rate enhancement ratio and Faradaic efficiency) was factors lower than that observed for the conventional configuration. Both groups attributed this to two effects, current bypass and individual bipolar electrodes. Current bypass involves the possibility of current passing through the bulk of the YSZ without affecting the Pt catalyst. Some possible solutions in order to obtain similar catalytic performance include applying much larger currents, or using a thinner YSZ pellet or appropriate electrode geometry to lessen the loss of current. The concept of individual bipolar electrodes means that each individual Pt nanoparticle catalyst behaves as a bipolar electrode; one side is positively charged, and the other side is negatively charged. This causes a nonuniform work function, contrary to that of a conventional electrode configuration; therefore, the resulting effect is a

combination of catalytic activity due to both positive and negative polarizations. It has been suggested that this can be overcome by using this type of configuration for reactions that exhibit both electrophobic and electrophilic behavior.

A similar limitation (i.e., underestimation of promotion parameters) was found by Kambolis et al. [180] for the oxidation of propane over Pt/LSCF-GDC/GDC catalyst. It was stated that a minor part of the applied current between the LSCF/GDC electrode and the counter electrode passes over the Pt nanoparticles resulting in an underestimation of the Faradaic efficiency values. These results are shown in Figure 2-6, summarizing the effect of positive polarization at three different temperatures. It can be seen that at 267°C, a two-step increase of propane conversion was observed. This was attributed to the fact that the LSCF/GDC electrode conductivity is quite low at such a temperature indicating that the movement of oxygen ions requires some time to be delocalized from the bulk of the electrode; the opposite is observed when the current is interrupted [180].

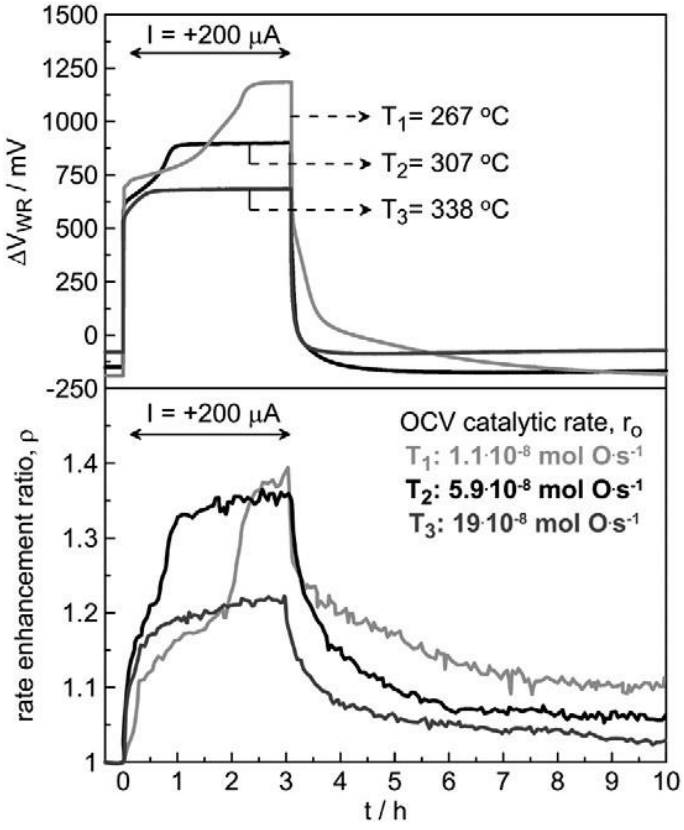

Figure 2-6: Transient effect of applied constant current on the rate of C_3H_8 oxidation for T_1, 267°C; T_2, 307°C; and T_3, 338°C (Reproduced from Kambolis et al. [180]**)**

Xia et al. have attempted to quantify this difference in promotion parameters compared to the conventional equations, taking into account that when the catalyst is highly dispersed and not directly electronically connected, it acts as individual, isolated galvanic cells during polarization [162]. They proposed a new technique where a galvanostatic step is applied to a system in the presence of $C^{16}O$ and isotope $^{18}O_2$ under high vacuum conditions. The formation of $C^{18}O_2$ *Faradaic reaction; ^{16}O from YSZ) and $C^{16}O^{18}O$ (non-Faradaic reaction; ^{18}O from $^{18}O_2$) is observed, and the number of galvanic cells is quantified, thus, resulting in the following modified equation (Eq. 2-5) for rate enhancement ratio being proposed:

$$\rho = \left(r_{C^{16}O_2} + r_{C^{16}O^{18}O}\right)/r^0_{C^{16}O^{18}O} \qquad \textbf{2-5}$$

where $r_{C^{16}O_2}$ is the rate of Faradaic formation of $C^{16}O_2$, $r_{C^{16}O^{18}O}$ is the rate of non-Faradaic formation of $C^{16}O^{18}O$, and $r^0_{C^{16}O^{18}O}$ is the initial open circuit catalytic rate. In addition, an adjustment to the equation (Eq. 2-6) for Faradaic efficiency was shown to be,

$$\Lambda = \left(r_{C^{16}O_2} + \Delta r_{C^{16}O^{18}O}\right)/r_{C^{16}O_2} \qquad \textbf{2-6}$$

or in the more conventional form (Eq. 2-7); however, accounting for the equivalent number of galvanic cells (n_{cell}),

$$\Lambda = (2F)/(I \cdot n_{cell}) \cdot \left(r_{C^{16}O_2} + \Delta r_{C^{16}O^{18}O}\right) \qquad \textbf{2-7}$$

where $\Delta r_{C^{16}O^{18}O}$ is the enhancement of the catalytic rate of $C^{16}O^{18}O$ during polarization.

From this discussion, it is evident that some limitations still exist with regard to the application of nanostructured catalysts and the corresponding modified cell configurations and reactor designs; however, these have been identified and are being investigated for possible solutions and explanations. Further fundamental research with regard to these new designs would prove to be beneficial in the understanding of the behavior of these nanostructured catalysts compared to the commonly known systems. In addition, adjusting the reaction environment to more practical operation conditions would make it possible to evaluate the nanostructured catalysts for commercial applications.

2.4 Conclusion

Recent progress in the implementation of nanostructured catalysts to overcome the commercial limitations of conventional electrochemical promotion systems and to gain a better understanding of the related MSI phenomenon was presented. These limitations for practical application include the low metal dispersion, high metal loading of expensive metals, and inefficient cell configuration and reactor design. It was shown that metal dispersion can be increased (by a factor of 10–100) through catalyst preparation techniques such as impregnation, sputter depositing, electroless deposition, and electrostatics spray deposition. In addition, adjustments to the cell configuration to accommodate these nanostructured catalysts, such as using the bipolar configuration or incorporating a mixed ionic–electronic conducting interlayer, have been studied along with new reactor designs, such as the monolithic electrochemical promotion reactor. These modifications have been shown to be the potential solutions to progressing toward commercial applications of electrochemical promotion. However, some of the limitations identified for these new designs include current bypass and individual bipolar electrodes, which cause an underestimation of conventional promotion parameters.

Chapter 3: Catalytic CO Oxidation over Au Nanoparticles Supported on Yttria-Stabilized Zirconia

*Dole, H.A.E., Kim, J.M., Lizarraga, L., Vernoux, P., Baranova, E.A. ECS Transaction, **45** 265-274 (2012).*

Gold nanoparticles supported on yttria-stabilized zirconia (YSZ) were synthesized using a modified alcohol method which involves the stabilizing agent, polyvinylpyrrolidone (PVP). Two different average sizes (Au2: 13.1 nm; Au1: 17.1 nm) of Au nanoparticles were synthesized. These catalysts were tested for gas phase CO oxidation. Since PVP is known to block the active Au sites, the catalysts were calcined at 300°C and 600°C in order to remove the PVP. Overall, higher catalytic activity was found for the smaller Au nanoparticles. It was also found that calcination is required in order to achieve activity, even though the particle size increases with this treatment. The effect of calcination temperature did not prove to be significant. It is demonstrated that O^{2-} ionically conductive YSZ is a promising catalyst support that can finely disperse and stabilize Au nanoparticles for CO oxidation.

3.1 Introduction

For many years, gold has been disregarded as an active catalyst in its bulk state due to its chemically inert property. It was not until Haruta [186–188] discovered that when gold particles with diameters smaller than 10 nm are supported on metal oxides, they tend to be very catalytic active for many reactions. However, this discovery came with the challenge of achieving small Au nanoparticles as Haruta stated, due to quantum size-effects, the smaller the Au nanoparticle, the lower the boiling point which results in significant agglomeration during calcination [186]. Recently, research has been focused on determining the effect of size and pretreatment conditions (i.e., calcination temperature). It has been found that Au nanoparticles less than 5 nm show a significant increase in catalytic activity [189,190]. Others have also shown that calcination causes agglomeration and that as the temperature is increased the gold phase changes from gold oxide to metallic gold which shows to influence the catalytic activity [191,192]. The effect of the support material has been shown to have less of an influence on the activity [190] which could allow for flexibility depending on the desired application.

The Au nanoparticles used in this study were supported on yttria-stabilized zirconia (YSZ), a metal oxide support. YSZ is known to be an O^{2-} conductor due to the presence of oxygen vacancies inside its crystallographic structure. This oxide has been extensively studied as a material for oxygen sensors and fuel cells [193]. Recently, YSZ has received attention as a catalytic support especially in studies of Electrochemical Promotion of Catalysis (EPOC); also called the NEMCA (Non Faradaic Electrochemical Modification of the Catalytic Activity) effect [14]. Vayenas et al. [14] were the first to show that the migration of ionic species from a solid electrolyte to the catalyst surface induced by electrical polarizations can improve catalytic performances. Vayenas et al. [25] have described EPOC as an electrically controlled strong metal support interaction (SMSI). Recently it was shown that YSZ is an attractive catalyst support for nanoparticle stabilization and activation for the reaction of CO oxidation over Pt/YSZ nanoparticles [72,102,115]. It was found that O^{2-} ionic species from YSZ can significantly promote the catalytic activity of Pt nanoparticles due to the thermally induced O^{2-} backspillover from YSZ over Pt catalyst in agreement with the electrochemical promotion mechanism. It was also found that observed effect becomes more pronounced with decreasing the particle size [102].

In this work, gold nanoparticles supported on YSZ (Au/YSZ) are investigated for the first time in the reaction of CO oxidation. To this end, Au nanoparticles with two different average sizes (13.1 and 17.1 nm) were synthesized using a modified alcohol method. This method was modified to achieve polyvinylpyrrolidone(PVP)-stabilized Au nanoparticles supported on YSZ. The variation in nanoparticle size was achieved by adjusting the ratio of Au to PVP in the synthesis solution [194–196]. The particle sizes of these catalysts were studied using x-ray diffraction (XRD). Surface properties were also characterized using transmission electron microscopy (TEM). An effective calcination temperature was also determined for the removal of PVP using a thermogravimetric analysis (TGA). The PVP-stabilized Au/YSZ nanoparticles were tested using the model reaction of CO oxidation. The effect of the Au particle size and calcination temperature on the catalytic activity was investigated.

3.2 Experimental

3.2.1 Synthesis of Au Nanoparticles

Gold nanoparticles (Au), deposited on YSZ powder (Au/YSZ) were synthesized using a similar method to the colloidal methods using alcohol as a reducing agent [197–199]; however, the procedure was modified to achieve supported Au/YSZ. Gold (III) chloride (Aldrich, 99.999%) precursor salt was dissolved in a mixture of nanopure water (18 MΩ cm) and ethanol (Fischer, 99%) with a ratio of water to ethanol of 1:1, in the presence of PVP (Sigma, 10,000 average molecular weight) and YSZ powder (TOSOH, 8% YSZ, with average crystallite size of 25 nm, 0.6 μm particle size and bulk density of 1.3 $g \cdot cm^{-3}$). The molar ratio of PVP to gold was 3:1 (Au1) and 10:1 (Au2) for the samples tested. The desired gold loading was 1 wt. % on YSZ. The obtained mixture was stirred for 30 minutes at room temperature then refluxed at 100°C for 2 h, followed by extensive washing with nanopure (18 MΩ·cm) water and drying in the air at 70°C. The initial color of the cloudy mixture appears yellow. After about 30 minutes, the colour of the mixture turns pink or purple, depending on the concentration of PVP. Upon drying, the synthesized 1 wt. % Au nanocatalysts on YSZ powder have a pink to purple color.

PVP is used as a polymer protective agent in order to achieve small nanoparticles by stabilizing the Au ions during the synthesis [194–196]. It is believed that the Au nanoparticles are stabilized through the reduction of van der Waals interaction between colliding colloidal particles [194]. Before testing the performance of the catalysts, the PVP must be removed as it known to inhibit the catalytic activity [200,201]. This was done by calcining the Au/YSZ catalyst at 300 or 600°C for 2 h in air.

3.2.2 Transmission Electron Microscopy

Transmission electron microscopy (TEM) images were taken for the Au/YSZ catalysts tested (JEOL 2010 LaB6) in order to obtain a higher resolution so that the morphology and size of Au particles may be better investigated. An extraction replica technique was used for sample preparation [202]. The catalyst was dispersed in ethanol, deposited on a mica film and covered with a carbon layer. The YSZ support and film of mica were then dissolved in hydrogen fluoride solution for 24 hours resulting in Au particles being fixed on the carbon

film. These particles were directly observed by TEM. The use of ImageJ software allowed for the determination of Au particle size distribution.

3.2.3 X-ray Diffraction

X-ray diffraction (XRD) patterns of the Au/YSZ nanoparticles were collected using RigakuUltima IV diffractometer using Cu Kα source. The experiments were run in the focused beam geometry with a divergence slit of 2/3 degree, a scan speed of 0.17 degree·min^{-1} and a scan step of 0.06 degree for all experiments. The diffractograms were collected between 30 and 55°2θ. The average particle diameter was determined using the Scherrer equation and the full widths at half maximum (FWHM) of the (111) plane of gold at 38° 2θ.

3.2.4 Thermogravimetric Analysis

Thermogravimetric analysis (TGA) (2960 SDT V3.0F) was carried out to determine an optimum temperature range at which the synthesized Au/YSZ samples are to be calcined in order to completely remove the PVP stabilizing agent. The temperature range should be high enough to decompose the carbons and other volatile compounds in the PVP polymer, but also, the temperature should be low enough that sintering and formation of agglomerates of Au nanoparticles are minimized. In order to determine the proper calcination temperature, TGA is run to establish the temperature range at which carbon decomposes. The sample is heated at a rate of 1.2°C·min^{-1} from room temperature to 580°C.

3.2.5 Catalytic Activity Measurements

The catalytic activity measurements of the Au/YSZ catalysts were carried out at atmospheric pressure in a continuous flow quartz reactor. The reaction gases were CO (Linde, 1.02% CO in He) combined with pure O_2 (Linde, pure O_2), and pure He (Linde, pure He) as a carrier gas. The gas compositions were controlled by mass flow controllers (Brooks, 5850 TR Series and MKS electronic mass flow controllers) and were the following: 760-780 ppm CO with 4.3-4.5% O_2 and He balance for CO oxidation. The overall flow rate was held constant at 4.3 L·h^{-1}, resulting in a space velocity of approximately 19 000 h^{-1}. The product gases for the oxidation of CO were analyzed with an on-line micro-chromatograph (μGC-R3000 SRA instruments) which contained two separate columns; one to separate O_2, N_2 and CO at a

temperature of 90°C and the other to separate CO_2 at a temperature of 100°C. CO_2 concentration in the product gas of the reactor was also monitored by an infrared (IR) analyzer (Horiba, VA-3000). A K-type thermocouple was attached to the reactor at the catalyst bed in order to monitor the temperature during the heat-up period. The entire reactor was placed in a furnace, which was attached to a temperature controller. The sample was heated from 25 to 250°C at a rate of $3°C \cdot min^{-1}$. For each catalyst, three heating cycles were performed to observe the stability of the catalyst.

3.3 Results and Discussion

3.3.1 Characterization of Au Catalysts

Figure 3-1 shows TEM images of Au2 which was untreated and calcined at 600°C. This image shows that the Au nanoparticles are uniformly distributed over the YSZ support. From the corresponding histograms, an average particle diameter was found to be 9.1 and 11.7 nm, respectively. These results show that calcination does have an effect on the particle size.

The XRD spectrum for each Au/YSZ catalysts is shown in Figure 3-2. The crystallite size for each sample was determined from the Au (111) peak using the Scherrer equation. These values are summarized in Table 3-1. It is evident that the size of the crystallite increased (approximately double) with calcination. Similar trends have been found in past studies (6, 7) where it is shown that calcination causes the gold nanoparticles to agglomerate as the melting temperature of the gold decreases with decreasing particle size.

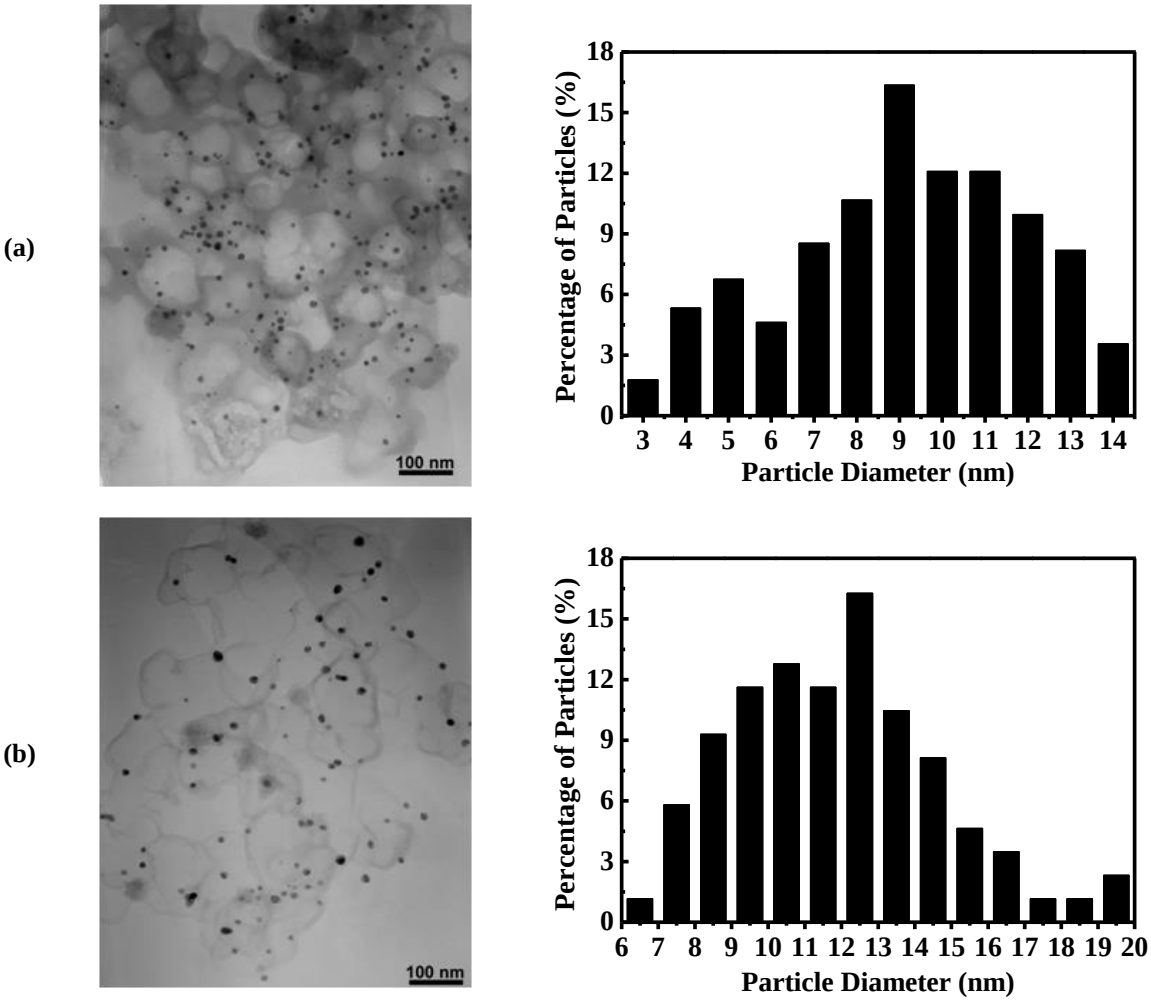

Figure 3-1: TEM images (left) and corresponding histograms (right) of Au2 (a) untreated; and (b) calcined at 600°C.

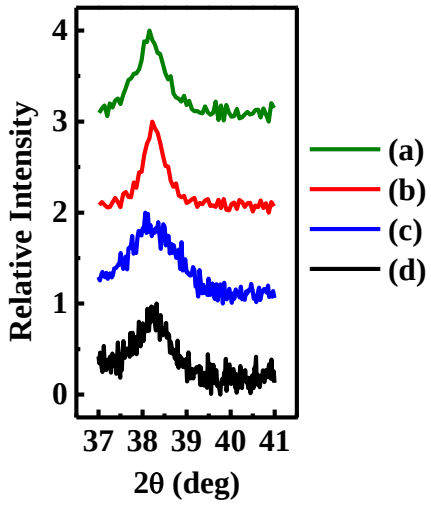

Figure 3-2: XRD spectra of Au (111) peak of Au/YSZ catalysts (a) Au2 calcined at 600°C; (b) Au1 calcined at 600°C; (c) Au2 untreated; and (d) Au1 untreated.

Dispersion calculations were performed for both Au/YSZ catalysts using the average particle diameter from the XRD measurements and the following equation[203],

$$dispersion\ (\%) = (MW_{Au} \cdot 600)/(\rho_{Au} d_{avg} a_{Au} N_a) \qquad \textbf{3-1}$$

where MW_{Au} is the molecular weight of Au (196.97 g·mol^{-1}), ρ_{Au} is the density of Au (19.32 g·cm^{-3}), d_{avg} is the average particle size, a_{Au} is the surface area of one Au atom (2.29 x 10^{-19} m^2·atom^{-1}), and N_a is Avogadro's number (6.022 x 10^{23} atom·mol^{-1}). It is evident that since the crystallite size changes between untreated and calcined catalysts (approximately doubled), the dispersion also changes. However, these differences in dispersion do not appear to influence the catalytic activity as Au2 has lower dispersion but higher activity than Au1 (Figure 3-3). Table 3-1 summarizes these dispersion values as well as the particle sizes for each catalyst.

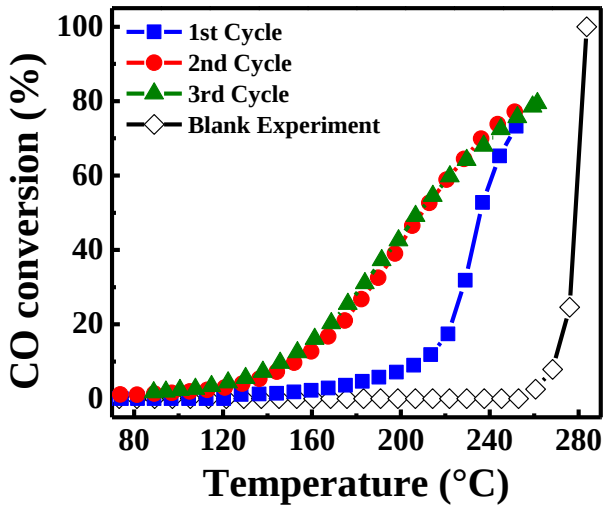

Figure 3-3: Catalytic performance for CO oxidation of Au2, calcined at 600°C.

Table 3-1: Summary of Au/YSZ catalysts prepared and corresponding characterization data.

Catalyst	Pre-treatment	Avg. Particle Diameter d_{avg} (nm)*	Dispersion (%)	CO Oxidation		
				Turnover Frequency, TOF (s^{-1}) (x 10^{-3})		Activation Energy, E_a (kJ·mol^{-1})
				100°C	200°C	
Au1	untreated	8.4	7.1	0	0	77.0
Au1	calcined at 300°C	-	-		-	56.1
Au1	calcined at 600°C	17.1	3.4	0	78.7	63.6
Au2	untreated	6.3	5.3	0	0.25	93.2
Au2	calcined at 600°C	13.1	2.6	8.45	181.74	24.1

*from XRD measurements

The result from the TGA of Au1 is shown in Figure 3-4. The first mass loss of 11.9 % is related to water evaporation and the second mass loss of 1.4 % is related to polymer decomposition. There is a slight loss of mass just below 600°C, likely being a partial removal of oxygen from YSZ. In order to evaluate the effect of all these losses detected from TGA, 300°C (removal of PVP only) and 600°C (removal of all species) selected to be the suitable temperature for calcination.

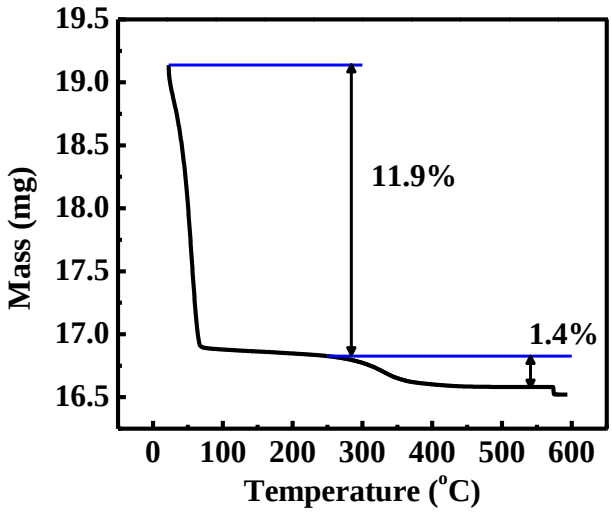

Figure 3-4: Thermogravimetric analysis of Au1.

3.3.2 Catalytic Performance for CO Oxidation

To study the catalytic performance of the Au/YSZ catalysts, the oxidation of CO was used as a model reaction. This reaction has been widely studied due to its environmental and industrial significance[204–207]. For each catalyst, the catalytic oxidation of CO was repeated for three successive heating ramps between 25 and 250°C. Figure 3-3 shows the catalytic activity of Au2 calcined at 600°C.

The results showed that the catalyst exhibits stable performance after the first cycle where the activity is observed from around 65°C. It is observed that the first cycle shows lower catalytic activity compared to the successive cycles. Similar multi-cycle performance has been observed by other research groups[45,208,209]; however, the opposite performance has also been observed[210,211]. This observation was explained by the dependence of the pretreatment conditions. In a previous study, it was determined that when catalysts were pre-oxidized, the catalytic activity of the first heating cycle was lower[210]. It was explained that

when the catalyst is exposed to a reducing species such as CO, the catalyst is activated which is shown by the higher catalytic activity in the successive runs. Another explanation could be the result of residual PVP even after calcination. It is possible that during the first cycle, there is PVP inhibiting the reaction, and it is only after the first cycle that the remaining PVP is removed.

3.3.3 Effect of Particle Size

Figure 3-5 shows the effect of Au particle size on the catalytic performance for CO oxidation. Two different ratios of PVP:Au were used to control the size of the particles which has also been shown in previous studies [196,201]. It was explained that the PVP can slow the diffusion of the gold ions within the solution, preventing them from coagulating; therefore, more PVP creates less diffusion. However, it has been shown that there is a limit to the amount of PVP that can influence the particle size [196]. From this study, it is clear that the smaller gold nanoparticles (Au2) synthesized using a ratio of 10:1 (PVP:Au) have the highest catalytic activity.

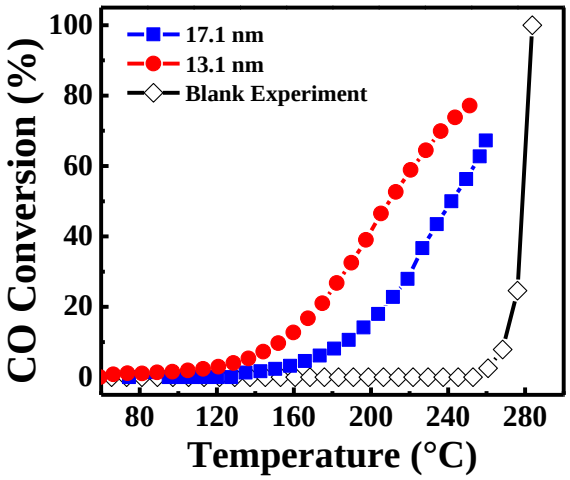

Figure 3-5: Comparison of catalytic performance for CO oxidation of Au/YSZ catalysts, calcined at 600°C with two different average particle size.

3.3.4 Effect of Calcination Temperature

Since PVP is known to inhibit catalytic reactions [200,201], the prepared Au/YSZ catalysts were pretreated by calcining at elevated temperatures to remove this stabilizing polymer. However, calcination can also have a negative effect on the performance of the catalysts. It has been previously shown that higher calcinations temperatures cause agglomeration of the

nanoparticles [191,192]. Since smaller nanoparticles are desired for greater activity, the amount of PVP and calcination temperature must be optimized to achieve the best performance.

Figure 3-6 shows a comparison of Au1 that was untreated, calcined at 300°C and calcined at 600°C with respect to a blank experiment (i.e. reactor without any catalyst). From the figure, it is evident that there is a significant effect on the catalytic activity between the untreated and calcined samples; however, the difference between calcinations temperatures does not appear to have such a significant effect. These results show that PVP does indeed inhibit the reaction. Since the PVP is used to stabilize the Au nanoparticles, it is said to be surrounding the nanoparticles. This in turn prevents the surface of the Au nanoparticles to be exposed resulting in lower catalytic activity. Therefore, it is important to sufficiently remove the PVP without causing significant agglomeration of the nanoparticles.

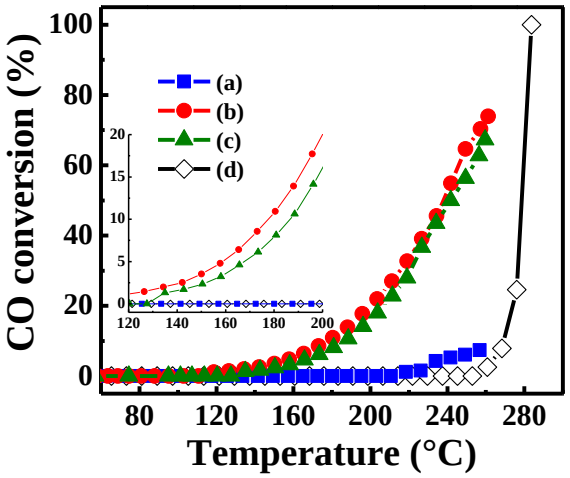

Figure 3-6: Effect of calcination temperature on the catalytic activity for CO oxidation of Au1 (a) untreated; (b) calcined at 300°C; (c) calcined at 600°C; and compared to a (d) blank experiment.

3.4 Conclusion

It is demonstrated that YSZ is a promising catalyst support for Au nanoparticles for the reaction of CO oxidation. Au nano-catalysts of two average sizes were synthesized using a modified alcohol method with a PVP stabilizer. The size of the particles depended on the amount of PVP used – more PVP made smaller particles. The catalytic performance of the untreated and calcined catalysts was evaluated for the model reaction of CO oxidation. It was found that calcination had an effect by increasing the particle size by approximately double; however, this treatment was necessary to remove the PVP stabilizer which is known to inhibit the reaction. This was evident by the better performance of the calcined catalyst compared to the untreated catalyst. The most important factor proved to be the size of the particle, where the smaller nanoparticle (Au2) showed the highest catalytic activity for CO oxidation. This catalyst showed catalytic activity beginning around 90°C. In order to improve this catalytic activity, the size of the Au nanoparticles will need to be decreased in further studies.

Chapter 4: Low Temperature Toluene Oxidation over Pt Nanoparticles Supported on Yttria-Stabilized Zirconia

Dole, H.A.E., Isaifan, R.J., Sapountzi, F.M., Lizarraga, L., Aubert, D., Princivalle, A., Vernoux, P., Baranova, E.A. Catalysis Letters, ***143,*** *996-1002 (2013).*

Toluene oxidation was measured over Pt nanoparticles synthesized using a modified polyol reduction method and deposited on ionically conductive yttria-stabilized zirconia (Pt/YSZ) for three different loadings (1.1%, 0.8%, 0.4%), and non-ionically conductive γ-alumina (Pt/γ-Al_2O_3) supports, as a comparison (metal loading 0.7%). It was found that nanoparticles supported on YSZ, tested as a support for the first time for toluene oxidation, have greater catalytic activity compared to a conventional γ-Al_2O_3 support in spite of a lower specific area and Pt dispersion. This could be explained by the stronger metal-support interactions between Pt and YSZ due to the ionic conductivity of YSZ and presence of oxygen vacancies.

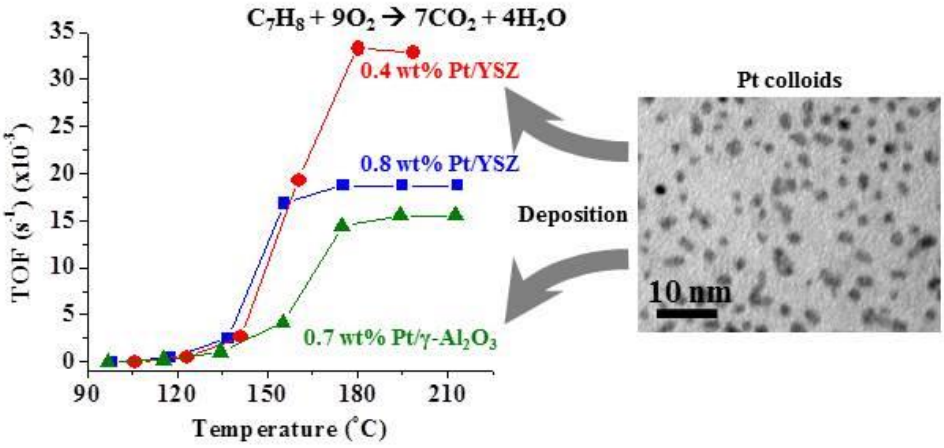

4 Introduction

A growing global concern about air pollution has sparked the interests of many research groups around the world. Volatile organic compounds (VOCs) are carbon-based chemicals that are among the pollutants that can cause environmental and health problems. There are several methods that have been demonstrated to control VOC emissions; however, the use of catalytic oxidation is found to be efficient and cost-effective. Many different catalysts and supports have been studied for this purpose, including metal oxides [7], and noble metals supported by metal oxides or carbon [212] or a mixture of metal oxides [9].

Yttria-stabilized zirconia (YSZ), a metal oxide support, is known to be an O^{2-} conductor due to the presence of oxygen vacancies inside its crystallographic structure. This oxide has been extensively studied as a material for oxygen sensors and fuel cells [193]. In the last twenty-five years, YSZ has received attention as a catalytic support due to its ionic conductivity properties especially in studies of Electrochemical Promotion of Catalysis (EPOC); also called the NEMCA (Non Faradaic Electrochemical Modification of the Catalytic Activity) effect [14]. Vayenas and collaborators [14] were the first to show that the migration of ionic species from a solid electrolyte to the gas exposed catalyst surface induced by electrical polarizations can improve catalytic performances. Vayenas et al. [25] have described EPOC as an electrically controlled strong metal support interaction (SMSI). In addition, it was found that ionic oxygen species can thermally migrate without any electrical polarization on nanoparticles of metallic catalysts supported on ionically conducting ceramics, such as YSZ [115]. Recently, Masui et al. have shown that the mobility of oxygen in the near surface region at the Pt nanoparticles dispersed on $Ce_{0.64}Zr_{0.15}Bi_{0.21}O_{0.1895}$ can promote the oxidation activity of toluene [213]. This phenomenon adds to the appeal of using YSZ as an alternative support in the catalytic removal of harmful pollutants such as VOCs.

Among the large variety of VOCs, toluene can be considered a representative of aromatic hydrocarbons and its oxidation at low temperatures has a significant practical interest. In this work, platinum nanoparticles with an average colloidal size of 2.5 ± 0.5 nm and narrow size distribution were synthesized using a modified polyol method. As-prepared colloids were deposited on YSZ and γ-Al_2O_3 (conventional support used in heterogeneous catalysis [214]) and tested for toluene oxidation. The effect of metal loading and support nature on the catalytic activity was investigated.

4.1 Experimental

4.1.1 Preparation and Characterization of Pt Nanoparticles

Platinum nanoparticles deposited on YSZ and γ-Al_2O_3 were synthesized using a modified polyol reduction method [68,70]. First, Pt nanoparticles in the form of colloids were synthesized in ethylene glycol (anhydrous 99.8%, Sigma Aldrich) at 160°C, starting from $PtCl_4$ (Alfa Aesar, 99.9% metals basis) precursor salt using a sodium hydroxide (EM Science, ACS grade) concentration of 0.08 M as described previously [72]. The resulting

dark brown colloidal solution was deposited on 8 mol% Y_2O_3-stabilized ZrO_2 (YSZ) (Tosoh, specific surface area ~13 $m^2 \cdot g^{-1}$), and γ-Al_2O_3 (Alfa-Aesar, specific surface area 120 $m^2 \cdot g^{-1}$) supports. The supported nanoparticles were extensively washed with deionized water (18 MΩ·cm) and separated by centrifugation (YSZ), then dried in air at 60°C.

The supported Pt nanoparticles were characterized by transmission electron microscopy (TEM) using JEOL 2010 LaB6. The size distribution and mean particle size were determined using the imaging software ImageJ by measuring 100-200 nanoparticles from the TEM images. X-ray diffraction (XRD, Rigaku Ultima IV diffractometer using Cu Kα source) in the focused beam geometry with a divergence slit of 2/3 degree, a scan speed of 0.17 degree·min^{-1} and a scan step of 0.06 degrees between 30 and 50° 2θ, was also used to determine the crystallite size of the Pt nanoparticles for comparison with TEM results. The supported Pt nanoparticles were characterized by TEM (JEOL 2010 LaB6) using a replica technique [202]. The use of Image J software allowed for the determination of Pt particles size distribution through measuring at least 200 nanoparticles from the TEM images. Preparation of these TEM samples is described in details previously [72].

Dispersion of platinum was determined for the supported Pt nanoparticles using the H_2-pulse chemisorption technique [48]. The resulting values were compared with dispersion calculations from the TEM images using the following equation [203],

$$dispersion\ (\%) = (MW_{Pt} \cdot 600)/(\rho_{Pt} \cdot d_{avg} \cdot a_{Pt} \cdot N_A) \qquad \textbf{4-1}$$

where MW_{Pt} is the molecular weight of Pt (195.08 g·mol^{-1}), ρ_{Pt} is the density of Pt (21.09 g·cm^{-3}), d_{avg} is the average particle diameter (from TEM images), a_{Pt} is the surface area of one Pt atom (8.06 x 10^{-20} m^2·$atom^{-1}$), and N_A is Avogadro's number. Table 4-1 summarizes the results of the characterization of each catalyst.

Table 4-1: Summary of catalyst characterization and catalytic performance parameters.

Samples	Average Colloidal Particle Size (XRD) (nm)	Average Supported Particle Size (TEM) (nm)	Pt Loading (wt %)	TOF (s^{-1}) ($x10^{-3}$)		E_a ($kJ \cdot mol^{-1}$)	T_{20} (°C)	T_{50} (°C)	Dispersion (%)	
				120°C	140°C				Calculated from TEM (Eq. 4-1)	Pulse H_2
Pt/YSZ1	2.5 ± 0.5	2.72	1.1[a]	0.93	4.9	123±7	135	147	42	26
Pt/YSZ2	2.5 ± 0.5	2.96	0.8[a]	0.68	4.8	137±4	139	147	39	-
Pt/YSZ3	2.5 ± 0.5	2.70	0.4[a]	0.49	2.6	119±16	145	157	42	-
Pt/γ-Al_2O_3	2.5 ± 0.5	2.34	0.7[a]	0.42	1.9	107±2	153	162	49	52
Pt/γ-Al_2O_3 [212]	1.7		0.9[b]	-	-	-	135	170	66[b]	
SBA-15 [215]	-		1.0[b]	-	-	-	140	168	5[b]	
Pt/CeO_2-ZrO_2-Bi_2O_3/γ-Al_2O_3 [213]	-		5[b]	-	-	-	105	110	-	
Pt/TiO_2 (IMP[c]) [216]	5.4		0.8[b]	-	-	-	200	230	19[b]	
Pt/TiO_2 (LPRD[d]) [216]	3.6		1.1b	-	-	-	100	120	28[b]	
Pt/γ-Al_2O_3 [217]	-		-	-	-	-	210	235	-	

[a]determined from ICP measurements
[b]from literature
[c]IMP – impregnation
[d]LPRD – liquid phase reduction deposition

4.1.2 Catalytic Activity Measurements

The catalytic activity measurements of the Pt nanocatalysts deposited on YSZ and γ-Al_2O_3 were carried out at atmospheric pressure in a continuous flow U-shaped quartz reactor. Approximately 50 mg of catalyst was placed into the reactor. The reactive mixture was composed of toluene vapour (Alfa Aesar, 99.8%), O_2 (Air Liquid, 99.995% purity) and He (Air Liquid, 99.995% purity) as a carrier gas. In order to adjust the VOC concentration, two He streams were employed: the first one was introduced into a regulated saturator to maintain a constant flow rate of toluene vapour and the other one balanced the overall concentration. Further details of this setup are described by Benard et al. [212]. The reactant and product gases were analyzed by an on-line gas chromatograph (Perkin Elmer Clarus 500) equipped with a thermal conductivity detector (TCD) and several columns (Shin Carbon ST, Q PLOT, 2 OV101 and molecular sieve) to quantify toluene, O_2, CO_2 and CO. The detection limit was 2 ppmv for carbon dioxide and no other product was detected. From the outlet concentrations of toluene ($[C_7H_8]_{OUT}$) and CO_2 ($[CO_2]_{OUT}$), and the inlet concentration of toluene ($[C_7H_8]_{IN}$), the toluene conversion, catalytic rate (r) and the turnover frequency (TOF) was calculated with the respective equations:

$$C_7H_8\ Conversion\ (\%) = [CO_2]_{OUT}/(7 \cdot [C_7H_8]_{OUT} + [CO_2]_{OUT}) \times 100\% \qquad \textbf{4-2}$$

$$r = Total\ Gas\ Flow\ (L/s) \times \left[\frac{1\ mol}{22.4\ L} \times \frac{273\ K}{298\ K}\right] \times \frac{[C_7H_8]_{IN}}{10^6\ ppm} \times \frac{C_7H_8\ Conversion\ (\%)}{100\%} \quad \textbf{4-3}$$

$$TOF = r/N_G \quad \textbf{4-4}$$

where N_G is the moles of active metal sites (mol) (calculated from the dispersion values determined from Eq. 4-1).

A PC with a dedicated program controlled the valve injection system, data acquisition and integration of chromatographic peaks. Blank experiments have shown that the quartz reactor was catalytically inert at least up to 600°C. The gas compositions were controlled by mass flow controllers (Brooks, 5850 TR Series) and were the following: 300 ppm C_7H_8 with approximately 20% O_2 and He balance. The overall flow rate was held constant at 4 $L \cdot h^{-1}$, resulting in a space velocity of approximately 16 000 h^{-1}. A K-type thermocouple was attached to the reactor at the catalyst bed in order to monitor the temperature during the heat-up period. The entire reactor was placed in a cylindrical furnace, which was attached to a temperature controller (Eurotherm). The sample was heated from 25 to 250°C at a rate of 2°C$\cdot min^{-1}$. The temperature was held constant at 250°C for 5 min and then decreased to room temperature. Three heating cycles were performed for each catalyst to observe the stability of the catalyst. A carbon balance was performed for each cycle (shown in Appendix A-3, Table A-1) in order to determine whether carbon deposition or other intermediates were being formed.

4.2 Results and Discussion

TEM characterization was carried out for the supported Pt nanoparticles. Figure 4-1 shows representative TEM micrographs and corresponding size distributions for the Pt nanoparticles supported on YSZ (0.8% metal loading) and γ-Al_2O_3 (0.7% metal loading).

The TEM images show that the Pt nanoparticles are homogeneously dispersed. From these images, an average Pt particle size was found to be 2.96 and 2.34 nm, for Pt/YSZ and Pt/γ-Al_2O_3, respectively. This is comparable to the average particle size determined from XRD for the corresponding colloid, which suggests that the modified polyol reduction method is

effective in achieving finely dispersed metallic particles. The Pt dispersion value of the Pt/γ-Al_2O_3 catalyst, measured by H_2-pulse chemisorption, is similar to that estimated from TEM images (Eq. 4-1 and Table 4-1). This confirms the good homogeneity of the sample. However, on YSZ, the Pt dispersion measured by H_2-pulse chemisorption is much smaller than that estimated from TEM. This statistic determination of the mean diameter is not accurate in that case, probably due to the low specific surface area of the sample. A few large Pt particles are most likely present on the sample; therefore, suggesting the TEM images are not representative of the entire Pt/YSZ sample.

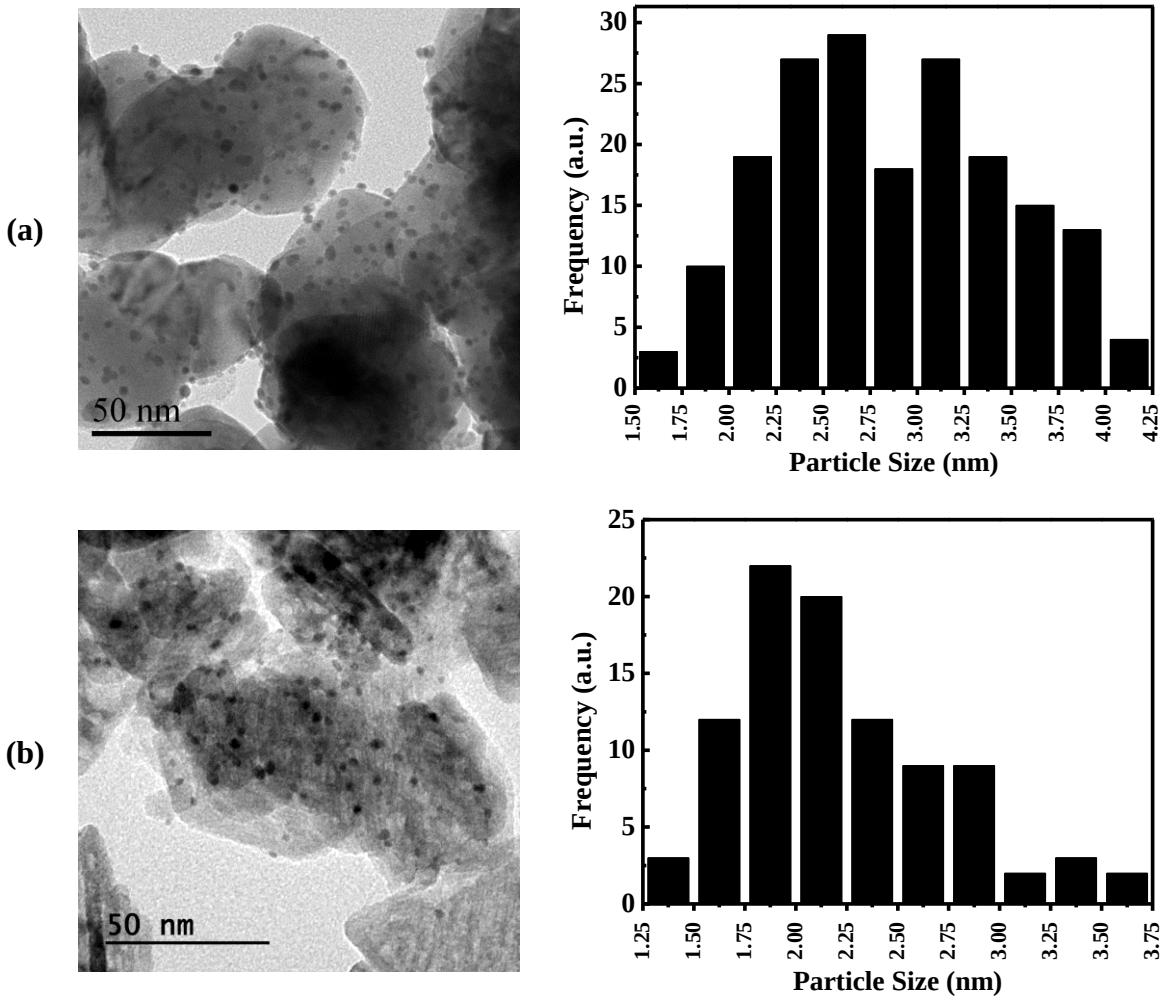

Figure 4-1: TEM images (left) and corresponding histograms (right) of Pt nanoparticles prepared with 0.08 M NaOH: (a) supported on YSZ; (b) supported on γ-Al_2O_3.

Catalytic oxidation of toluene was used as a model reaction, representing aromatic hydrocarbons, in order to evaluate the performance of the Pt nano-catalysts. Figure 4-2

shows the toluene conversion as a function of the temperature achieved from the Pt/YSZ2 catalyst for three cycles.

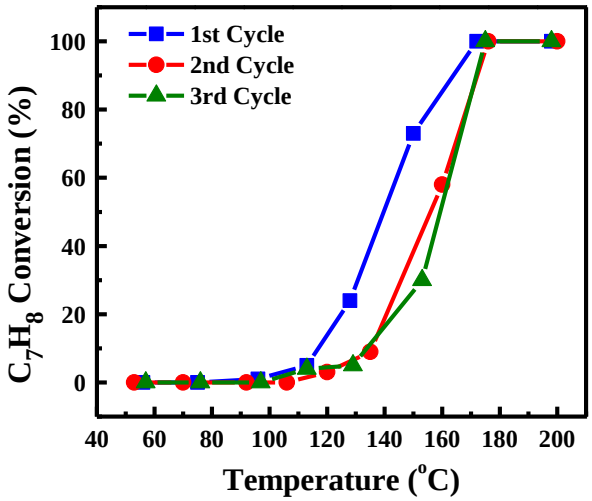

Figure 4-2: Toluene conversion as a function of temperature for Pt/YSZ2 (metal loading: 0.8 wt%) for three consecutive cycles.

Toluene conversion starts from around 100°C and reaches 100% at 180°C. The performance of each catalyst is relatively stable after the first cycle as the results during the second and third cycle are similar. This slight deactivation of the catalyst between the first and second cycle can be attributed to sintering of the Pt nanoparticles since they are heated on-stream for the first time to 250°C.

Figure 4-3 evaluates the effect of metal loading of Pt nanoparticles deposited on YSZ.

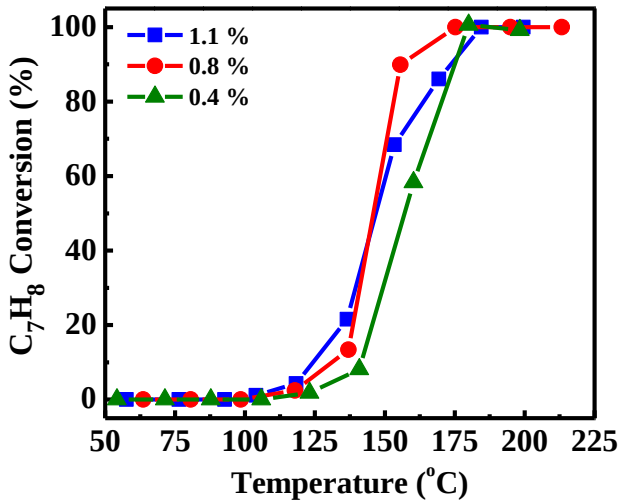

Figure 4-3: Effect of metal loading on catalytic activity of Pt/YSZ catalysts (*second cycle* is shown).

It is evident that metal loading has a slight effect on catalytic performance with, overall, a higher loading corresponding to higher catalytic performance at low temperatures (i.e., lower than 140°C). A similar trend was shown in a previous study where 1.5, 0.9 and 0.56% Pt was deposited on Al_2O_3 was evaluated for toluene and propene oxidation [217]. This trend was explained that with higher metal loading, lower dispersion is apparent, meaning that the particle size is relatively larger. With larger particles, the Pt-O bond strength decreases, causing more reactive oxygen species adsorbed on the Pt sites to react with the adsorbed toluene species. However, in this study, different metal loadings on YSZ did not show a significant difference in dispersion or average particle size which could explain the slight effect observed.

The effect of the support on the catalytic activity in terms of toluene conversion, turnover frequency, and intrinsic activity of the Pt nanoparticles deposited on YSZ (metal loading of 0.8 an 0.4%) and γ-Al_2O_3 (metal loading of 0.7%) are shown in Figure 4-4.

It is evident that for similar metal loadings, the catalytic activity of the Pt nanoparticles supported on YSZ is slightly higher or comparable to those supported on γ-Al_2O_3. This trend is more obvious when the catalytic rate is normalized for the active surface area (i.e., turnover frequency); whereby, Pt/YSZ had a lower active surface area compared to Pt/γ-Al_2O_3 resulting in higher TOF values with increasing temperature. More specifically, the TOF values at both 120 and 140°C are shown in Table 4-1. Overall, for both temperatures, the TOF value is higher for Pt/YSZ compared to Pt/γ-Al_2O_3. Additionally, the same trend was observed when the catalytic rate was normalized for mass of Pt where the metal loading and amount of catalyst employed for each test was accounted for.

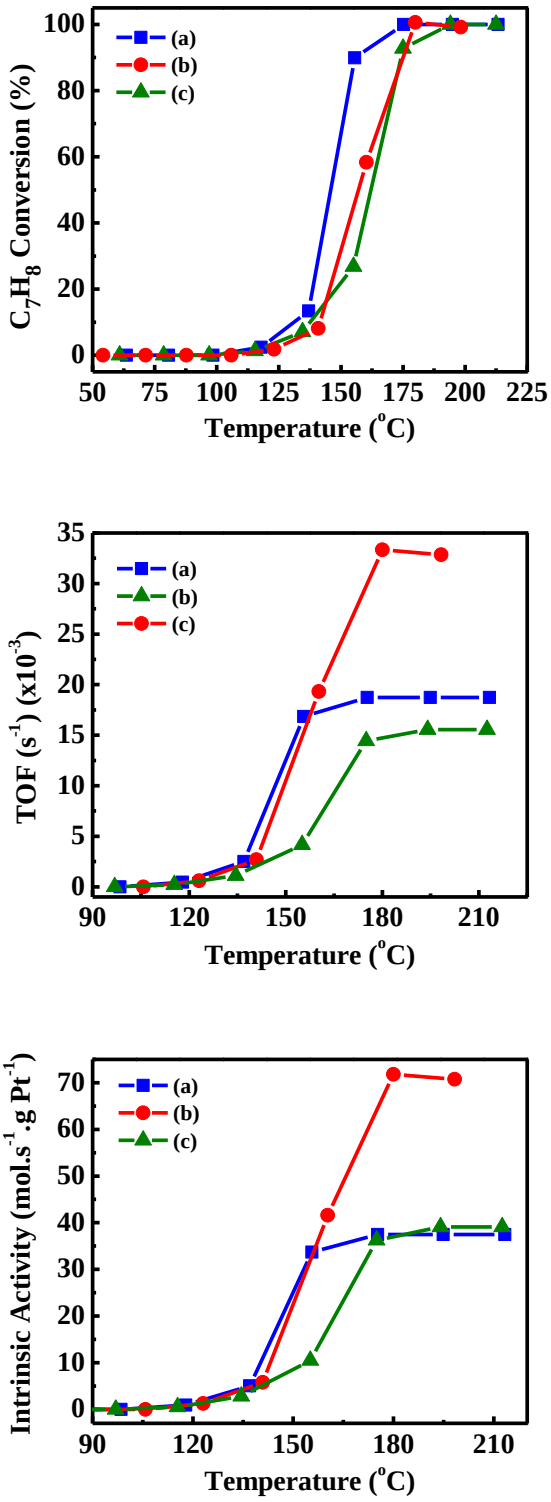

Figure 4-4: Comparison of catalytic performance of Pt supported on (a) YSZ2 (0.8 wt%); (b) YSZ3 (0.4 wt%); and (c) γ-Al_2O_3 (0.7 wt%) (*second cycle* is shown).

Table 4-1 summarizes the performances of the Pt/YSZ and Pt/γ-Al_2O_3 catalysts along with other similar catalysts evaluated in the literature for toluene oxidation [212,213,215,216,218]. Each catalyst from literature, containing similar Pt loadings and reaction conditions, was compared to those evaluated in the current study in terms of T_{20} and T_{50} (i.e., temperature at which 20 and 50% conversion occur, respectively). In general, the Pt/YSZ catalyst appears to have conversion at a lower temperature compared to the other findings. However, Masui et al. [213] found for a much higher Pt loading (5 wt%) that toluene conversion was achieved at slightly lower temperatures. Similarly, Santos et al. [215] found conversion at lower temperatures for a similar Pt loading but using a different synthesis method and TiO_2 as a support, as well as a high concentration of toluene, i.e. 4 g carbon·m^{-3} instead of 1.09 g carbon·m^{-3} in our study.

It is apparent that the catalytic performance of the Pt/YSZ catalyst, for a similar loading, is similar in terms of light-off temperature, to that of the Pt/γ-Al_2O_3 catalyst. This trend is also shown through the activation energy for toluene conversions of less than 20% for each catalyst that was determined using the following Arrhenius relationship.

$$\ln r = -E_a/(RT) + \ln A \qquad \textbf{4-6}$$

where r is the toluene oxidation rate (mol·s^{-1}), E_a is the apparent activation energy (J·mol^{-1}), R is the universal gas constant (J·mol^{-1}·K^{-1}), T is the reactor temperature (K), and A is the pre-exponential factor. Plots of *ln r* versus *1/T* were constructed, and the activation energies were calculated for each catalyst from the slope of a linear fit. Table 4-1 shows that Pt/YSZ, for a similar loading, has a similar activation energy to that of Pt/γ-Al_2O_3. Radic et al. [219] have interpreted the toluene oxidation on Pt using Mars van Krevelen (MVK) or Eley-Rideal (E-R) mechanisms. The MVK model has been widely reported for hydrocarbons oxidation [220,221]. In both cases (MVK and E-R), the reaction rate is controlled by two steps: the oxygen chemisorption on Pt and the surface reaction between oxidized hydrocarbons intermediate and adsorbed oxygen. Radic et al. [219] have calculated that the activation energy value for the surface reaction is around 73 kJ·mol^{-1} and is not affected by the Pt particle size. On the other hand, the activation energy value for oxygen chemisorptions decreases from 122 kJ·mol^{-1} to 108 kJ·mol^{-1} when the Pt particle size increases from 1 to 15

nm. These latter values are in good agreement with the apparent activation values found in the current study, i.e., 107-137 $kJ \cdot mol^{-1}$, considering Pt particles of 2.5 ± 0.5 nm. Therefore, it is suggested that the rate-determining step of the toluene oxidation, in the current experimental conditions, is the oxygen chemisorption on Pt. This indicates that more reactive oxygen species may exist on Pt/YSZ compared to that on Pt/γ-Al_2O_3 which could explain the slightly higher catalytic activity of toluene oxidation.

It is well established in the literature that the use of oxygen conducting supports (e.g. YSZ) can promote the catalytic activity of metallic nanoparticles, due to the phenomenon of metal-support interactions (MSI) [102,103,109,222]. In addition these supports present surface oxygen vacancies able to chemisorb reactants. Even though the origin of MSI is not fully clarified up to date, several studies have demonstrated a mechanistic equivalence between the phenomena of MSI and EPOC [14,115,139,144,146,220,223]. Both phenomena can be explained by a similar process, which is the back spillover of O^{2-} ionic species onto the metallic particles. This decoration of the metal particles by oxygen ions can be self-driven (for the case of MSI) or due to electrical polarization (for the case of EPOC) and results to alterations in the chemisorptive properties of the catalysts, which finally affect catalytic activity. In order for this process to be effective, the support material must possess sufficient ionic conductivity. The self-driven EPOC mechanism [14], recently confirmed using $^{18}O_2$ isotopic tracer experiments [170,221] which describes the electrochemical promotion of the catalytic activity of a metallic nanoparticle in contact with grain of ionically conducting support, without any electrical polarization, finally merges EPOC and MSI at the nm level [180].

It thus appears from this study that YSZ is a more promising support for toluene oxidation compared to γ-Al_2O_3, since it can act as a reservoir supplying promoting oxygen species to the catalyst, while spent oxygen in YSZ can be continuously replenished by gaseous oxygen.

4.3 Conclusion

Nanoparticles of Pt, synthesized by the modified polyol reduction method and supported on YSZ and γ-Al_2O_3, showed high catalytic activity towards toluene oxidation. Due to the lower specific surface area of YSZ, slightly larger Pt particles (2.96 nm) of smaller dispersion formed on the YSZ support compared to Pt on γ-Al_2O_3 (2.34 nm) starting from the same precursor colloids. Despite the lower dispersion, Pt/YSZ showed a slightly higher reaction rate per, both, active surface area and mass of Pt for toluene oxidation. This is attributed to stronger metal-support interactions between Pt and YSZ due to the ionic conductivity of YSZ and presence of oxygen vacancies suggesting that YSZ is a promising alternative support for toluene oxidation.

Chapter 5: Improved Catalytic Reactor for the Electrochemical Promotion of Highly Dispersed Ru Nanoparticles with CeO_2 Support

*Dole, H.A.E., Safady, L.F., Ntais, S., Couillard, M., Baranova, E.A. ECS Transactions, **61**, 65-74 (2014).*

An improved design for a catalytic reactor for electrochemical promotion of highly dispersed catalysts was presented and compared to that of a plug flow-type reactor for the model reaction of ethylene oxidation. Electrochemical cells were prepared with low particle size (1.1 nm) Ru nanoparticles (RuNPs) which were supported on a mixed ionic-electronic conductor, CeO_2, with a low metal loading (1 wt%), interfaced with a YSZ electrolyte. Comparable catalytic performance between the two reactors was observed for both open-circuits measurements. However, the rate enhancement ratio in the single-chamber capsule (SCC) reactor was found to be 1.6 compared to 1.4 for the plug flow-type reactor for an applied current of -5 μA. These results were attributed to better electrical contact to the isolated RuNPs. Furthermore, the SCC reactor is simple to assemble and provides an intimate contact between the RuNPs/CeO_2 catalyst and the current collector (i.e., gold mesh).

5.1 Introduction

Electrochemical promotion of catalysis (EPOC), also referred to as non-Faradaic electrochemical modification of catalytic activity (NEMCA), is a promising method for enhancing catalytic activity through the application of a small current or potential between the catalyst-working and counter electrode deposited on a solid electrolyte [14]. By applying such an electrical stimulus, the catalytic activity and selectivity can be altered due to modifications of the electronic properties of the catalyst. In the case of yttria-stabilized zirconia (YSZ) as a solid electrolyte, the addition or removal of O^{2-} species on the catalyst surface can be controlled in-situ depending on the specified reaction conditions. Fully reversible and "permanent" or "persistent" EPOC has been reported for more than 70 various catalytic systems[14]. In reversible EPOC experiments, the reaction rate returns to its initial value after the electrical stimulus is interrupted. For permanent EPOC (P-EPOC), the reaction rate remains at a higher value than the initial open circuit value [145,224].

Despite receiving much attention, this phenomenon has not yet reached commercial application. Two of the main technical factors preventing such development are the use of thick film catalysts with low surface areas and high material costs, and inefficient cell and

reactor designs, especially in the case of employing highly dispersed catalysts[29]. To address the limitation of low metal dispersion found for the catalyst-working electrodes of conventional electrochemical promotion systems, various deposition techniques have been developed and used. The most common methods include wet or dry impregnation [119,156,158–160], and metal sputtering [161,162,166,167,169,170]. The first step towards an alternative cell to accommodate high surface area catalysts was pioneered by Marwood, in the 1990s, where it was proposed that EPOC could be achieved through an isolated catalyst surrounded by two gold electrodes between which current passed [156,181]. Since then, several studies have expanded on this idea of a bipolar configuration, for example, sputtering a Pt catalyst between a comb-like gold electrode configuration [161,162].

Conventional EPOC studies have been, in general, carried out using two different types of experimental reactors – a fuel cell type reactor and single-chamber type reactor [14]. Since then, several new configurations have been introduced such as the plug flow-type[225] and monolithic reactors [160,171,226], both initially used for continuous-film catalysts. More recently, the plug flow-type reactor was used to demonstrate the feasibility of electropromoting a highly dispersed (~15%) Pt nanoparticle (average size = 8 nm) catalyst for the oxidation of propane was demonstrated. A 38% enhancement of the catalytic rate was observed with apparent Faradaic efficiency values up to 85. This study also demonstrated the benefits of employing a mixed ionic-electronic conductor (MIEC) support. It was found that using a MIEC can ensure electrical connectively between highly dispersed nanoparticle catalysts [180].

The design of an improved catalytic reactor (referred to as a single-chamber capsule (SCC) reactor) for the electrochemical promotion of highly dispersed catalysts is presented in this work. To determine the feasibility of the new design, the effects of the partial pressure of ethylene with constant partial pressure of oxygen, and applied negative current on the catalytic activity of the RuNPs/CeO_2 catalyst are presented and compared to that obtained using the plug flow-type reactor which was presented earlier by Vernoux's group [225].

To this end, ceria (CeO_2) as a MIEC, was used to support low particle size (average size = 1.1 nm) Ru nanoparticles for the electrochemical enhancement of the complete oxidation of ethylene. CeO_2 is a known conductor of O^{2-} ions due to the oxygen vacancies in the

crystallographic structure in addition to conducting electrons at elevated temperatures. Furthermore, due to its non-stoichiometry, CeO_2 has the ability to undergo conversion between Ce^{4+} and Ce^{3+} quite easily[227]. The highly dispersed RuNPs/CeO_2 catalyst powder was supported on a YSZ solid electrolyte in order to apply polarization.

5.2 Experimental

5.2.1 Synthesis of Ceria-Supported Ru Nanoparticles

Ruthenium nanoparticles deposited on CeO_2 (RuNPs/CeO_2) were synthesized using a modified polyol reduction method [68]. A colloid of Ru nanoparticles was synthesized in ethylene glycol (anhydrous 99.8% Sigma Aldrich), starting from $RuCl_3$ (Alfa Aesar, 99.99% metals basis) precursor salt and adding 0.08 M NaOH (EM Science, ACS grade). The salt solution was stirred for 30 minutes at room temperature and subsequently refluxed for 3 hours at 160°C. The resulting colloidal solution is deposited on CeO_2 (Alfa Aesar, specific surface area ~30-40 $m^2 \cdot g^{-1}$) for a desired metal loading of 1 wt%. The supported nanoparticles were extensively washed with deionized water (18 MΩ·cm) and separated by centrifugation, then dried in air at 40-60°C for 48 hours.

5.2.2 Preparation of Electrochemical Cell

To prepare the electrochemical cell, RuNPs/CeO_2 was deposited on one side of the YSZ disk as the working electrode (WE) along with inert gold counter (CE) and reference (RE) electrodes on the opposite side (as shown in Figure 5-1a). YSZ powder (TOSOH, specific surface area ~13 $m^2 \cdot g^{-1}$, average size of 0.3 μm) containing 8 mol% yttria was used to form electrolyte disks (18 mm diameter and 1 mm thickness) by a known procedure [228]. The counter and reference electrodes were deposited by applying gold paste (C2090428D4, Gwent Group, CAS: 98-55-5) followed by annealing at 500°C for 1 h.

In order to deposit the RuNPs/CeO_2 catalyst-working electrode, a solution of 1 wt% RuNPs/CeO_2 powder and ethanol was prepared. Approximately 0.2 g of RuNPs/CeO_2 was dispersed in 2 mL of ethanol. The solution was then deposited until the desired loading was obtained (0.10 mg Ru·cm^{-2}), drying at 60°C for 30 minutes between depositions. Finally, the catalyst was calcined in air at 350°C for 1 hour.

5.2.3 Catalyst Characterization

The colloidal and ceria-supported Ru nanoparticle catalysts were characterized by transmission electron microscopy (TEM) to determine the size distribution of the Ru nanoparticles. To obtain the TEM micrographs, the ceria-supported Ru catalyst powder was dispersed in ethanol then deposited dropwise on a TEM support grid, and the unsupported colloidal Ru nanoparticles were deposited directly on a carbon film (Ted Pella, ultrathin Carbon film on a holey carbon film). The analysis was performed on a FEI Titan^3 80 - 300 microscope operated at 300 kV and equipped with a CEOS aberration corrector for the probe forming lens, a monochromated field-emission gun, and an EDAX energy dispersive X-ray (EDX) spectrometer. To determine the particle size distribution, ImageJ software was used, measuring at least 750 particles.

5.2.4 Electrochemical Characterization of Single-Chamber Capsule Reactor

In order to determine the electrochemical response of the electrochemical cell containing the RuNPs/CeO_2 catalyst-working electrode in the single-chamber capsule reactor, polarization curves were obtained for an applied current between -15 and +15 μA (holding 30 minutes at each current setting) at temperatures of 350, 375 and 400°C and partial pressures of ethylene and oxygen of 0.012 kPa and 3 kPa, respectively (helium balance). Both the catalyst-working electrode potential (U_{WR}), and the cell potential (U_{cell}) were recorded.

5.2.5 Catalytic Measurements

Catalytic studies were carried out at atmospheric pressure in two different types of reactors – a plug flow-type (PF-type) reactor [225] and the single-chamber capsule (SCC) reactor (shown in Figure 5-1b). The electrochemical cell was placed in contact with gold current collectors allowing the gas flow to pass over the catalyst. A potentiostat (PARSTAT 2263) was used to polarize the cell for a desired duration and constant current. The reaction gases were C_2H_4 (Linde, 0.5% C_2H_4 in He), O_2 (Linde, 20.9% O_2 in He), and pure He (Linde, 99.997% He) as a carrier gas. The gas composition of 0.005 – 0.03 kPa C_2H_4, 3 kPa O_2 and He balance was controlled by mass flow controllers (MKS, 1259C and 1261C Series). The overall flow rate was held constant at 6 $L \cdot h^{-1}$. The product gases were analyzed with an on-line CO_2 gas analyzer (Horiba, VA-3000).

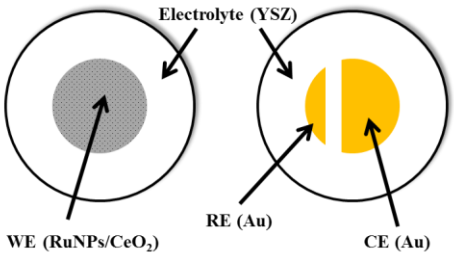

(a)

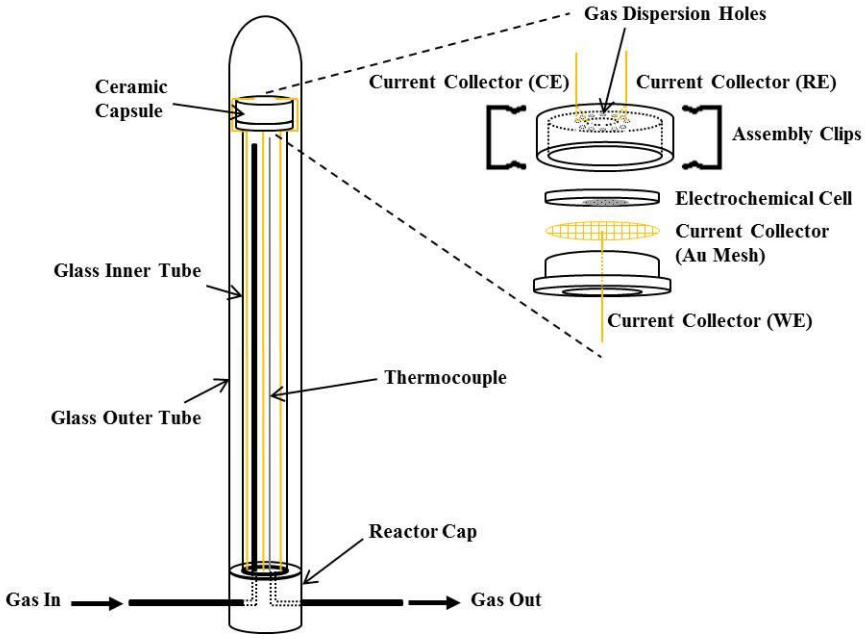

(b)

Figure 5-1: Schematic of the (a) electrochemical cell configuration; and (b) single-chamber capsule (SCC) reactor.

As shown in Figure 5-1b, the electrochemical cell (catalyst-working electrode facing down) is enclosed in a tight-fit ceramic (McMaster-Carr, Mycalex) capsule that is held together with two metal clamps (Omega Engineering, Nichrome wire, Ni80/Cr20). Both the ceramic capsule and metal clamps are mechanically stable and chemically inert in the temperature range of interest. Once assembled, the capsule sits on top of a glass inner tube where the Au current collectors, enclosed in YSZ tubes (to ensure no electrical contact between the wires), are fed to the base of the reactor. Similarly, a thermocouple is inserted through the base of the reactor to a point as close as possible to the capsule. It should be noted that the inner tube

also has gas dispersion holes in order to allow for circulation of the gas throughout the entire chamber. The complete assembly is enclosed by an outer glass tube and clamped to the reactor cap (stainless steel).

This SCC design allows for easy assembly and disassembly. Only the capsule requires assembly and disassembly when inserting a new electrochemical cell. Additionally, the current collector to the RuNPs is achieved by using a gold mesh in contact with the RuNPs/CeO_2 catalyst powder in comparison to the plug flow-type reactor where gold paste was painted on a quartz frit which extends up the sides of the walls of the reactor.

5.3 Results and Discussion

5.3.1 Characterization

TEM characterization was carried out for the colloidal Ru nanoparticles. A representative TEM micrograph is shown in Figure 5-2. It is evident that well-defined and fairly uniformly sized Ru nanoparticles were achieved. An average Ru particle size was determined to be 1.1 nm.

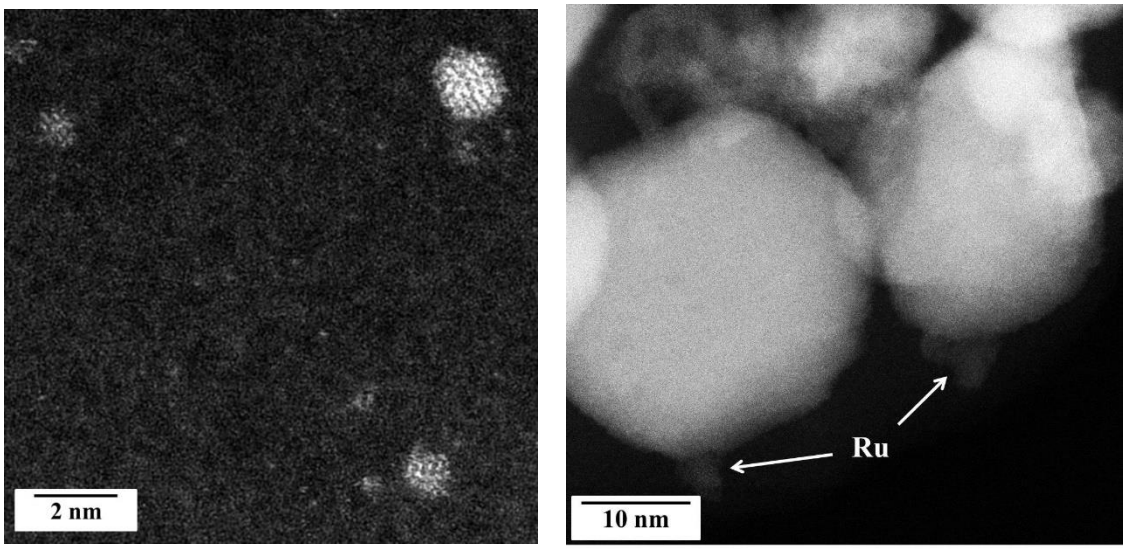

(a) **(b)**

Figure 5-2: TEM images of (a) colloidal Ru nanoparticles; and (b) ceria-supported Ru nanoparticles.

5.3.2 Electrochemical Characterization of Single-Chamber Capsule Reactor

The electrochemical response of the electrochemical cell in the single-chamber capsule reactor was determined through the application of currents from -15 to +15 μA while

measuring the catalyst-working electrode potential (U_{WR}) and cell potential (U_{cell}). These results are shown in the polarization curves shown in Figure 5-3.

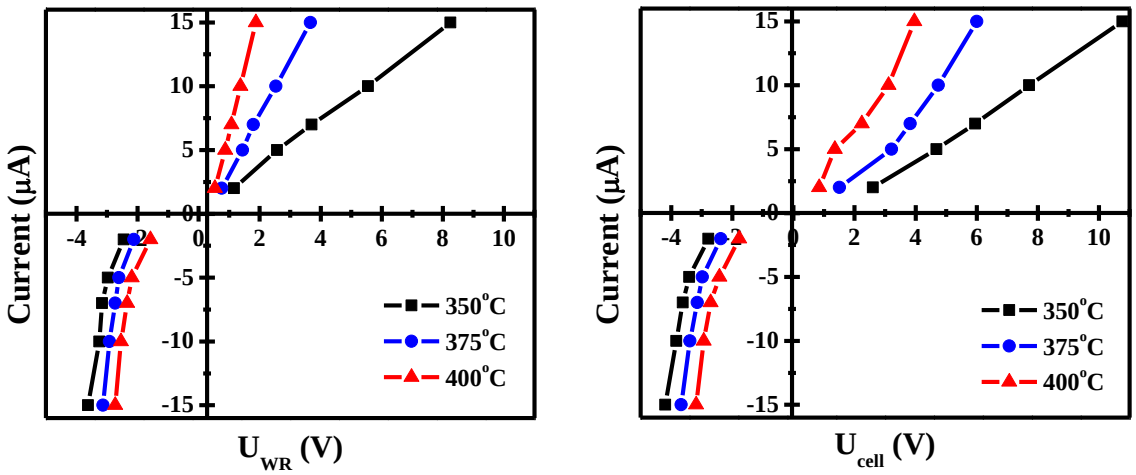

Figure 5-3: Steady-state polarization curves of the applied current (held 30 minutes) versus (a) catalyst-working electrode potential (U_{WR}); and (b) cell potential (U_{cell}) for the single-chamber capsule reactor (0.012 kPa C_2H_4 and 3 kPa O_2).

It is evident that it is possible to polarize the electrochemical cell in the single-chamber capsule reactor. Furthermore, as the temperature was increased, the electrolyte resistance decreased; this is as expected due to the increase in the ionic conductivity of the YSZ electrolyte with increasing temperature. It should be noted that such polarization curves could not be obtained for the plug flow-type reactor for the catalyst studied due to the poor electrical contact which was evident from the high aspect of noise to signal of the measured catalyst-working electrode potential as well as the cell potential exceeding 20 V for all conditions studied.

Additionally, as can be seen, anodic and cathodic curves are assymetrical. Under anodic polarization Ru oxidation, O_2 evolution, and C_2H_4 electrooxidation are occurring, whereas under negative polarization RuO_x, CeO_2, and O_2 reduction are taking place.

5.3.3 Open Circuit Measurements

The model reaction of complete oxidation of ethylene was chosen to carry out the following studies. Before polarizing the cells, the catalytic performance under open-circuit conditions was determined for both the plug flow-type reactor and the single-chamber capsule reactor.

For a constant partial pressure of oxygen (3 kPa), a forward (i.e., increasing partial pressure of ethylene) scan (0.009 kPa – 0.03 kPa) was carried out at 350°C (Figure 5-4).

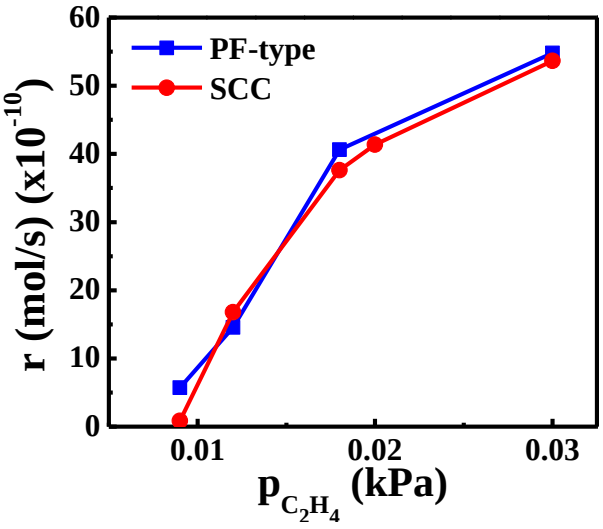

Figure 5-4: Catalytic performance of complete oxidation of ethylene over the RuNPs/CeO_2 catalyst employed in both the plug flow-type (PF-type) and single-chamber capsule (SCC) reactor (T = 350°C, P_{O2} = 3 kPa).

As expected, the catalytic activity of the RuNPs/CeO_2 catalyst is comparable between both the plug flow-type reactor and the single-chamber capsule reactor. From these results, a partial pressure of 0.012 kPa of C_2H_4, corresponding to a conversion <30%, was chosen to carry out the polarization study.

5.3.4 Effect of Polarization

As shown in a previous study [229], positive polarization of RuNPs/CeO_2 does not provide an increase in the catalytic activity for C_2H_4 oxidation. Contrary to this, the effect of cathodic polarization is significant. The effect of negative polarization for the RuNPs/CeO_2 catalyst was determined through the application of -5 μA at a partial pressure of 0.012 kPa at 350°C. An enhancement in the catalytic activity was observed for the RuNPs/CeO_2 catalyst using both reactors (Figure 5-5).

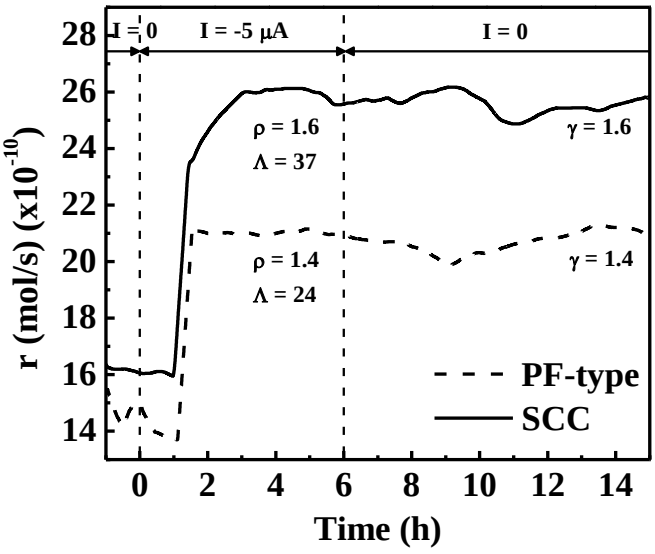

Figure 5-5: Transient effect of current application for C_2H_4 oxidation over RuNPs/CeO_2 on YSZ electrolyte at 350°C for an applied current of -5 μA for 6 hours (0.012 kPa C_2H_4) using both the plug flow-type (PF-type) reactor and single-chamber capsule (SCC) reactor.

A rate enhancement ratio (ρ) of 1.4 and 1.6 was observed for the plug flow-type reactor and single-chamber capsule reactor, respectively. In both cases, the Faradaic efficiency (Λ) was greater than 1, indicating that the activity is higher than predicted by Faraday's law. It is worth noting that the current application resulted in an initial slow increase in the reaction rate followed by an abrupt increase after approximately 1 hour. These results indicate that there is a delay between the electrochemical and catalytic process. Furthermore, the slow reaction response is likely due to relatively low ionic conductivity of CeO_2 and YSZ at 350°C [230].

It was also observed that the catalytic rate remained in the enhanced state, for both reactors, even after current interruption. As described in more detail in a previous study[229], it was proposed that partial reduction of CeO_2 might be responsible for the observed enhancement in the reaction rate. Through the application of a negative polarization, Ce^{4+} is electroreduced to a lower valence state due to the removal of oxygen species from its structure; thus creating more oxygen vacancies. These vacancies cause a stronger metal-support interaction in the RuNPs/CeO_2 system, resulting in an increase in the catalytic activity of Ru nanoparticles.

5.4 Conclusion

In the present work, an improved catalytic reactor for the electrochemical promotion of highly-dispersed catalysts was presented and compared to the operation of a plug flow-type reactor which was developed earlier for continuous thin film catalyst-working electrodes [225]. The design of the single-chamber capsule reactor allows for easy assembly and disassembly as well as improved current collection in comparison to the plug flow-type reactor for highly dispersed catalysts. The electrochemical cells consisted of Ru nanoparticles that were supported on CeO_2, a MIEC (1 wt% RuNPs/CeO_2) and interfaced with YSZ, an O^{2-} conductor. The single-chamber capsule reactor ensured good electrical contact to the RuNPs/CeO_2 catalyst and performed similarly to that of the plug flow-type reactor in both open-circuit experiments; however, a higher rate enhancement ratio was achieved using the SCC reactor compared to that of the PF-type reactor. The application of negative polarization (-5 μA) at 350°C showed a pronounced effect on the catalytic rate of the RuNPs/CeO_2 catalysts. The catalytic enhancement was attributed to the partial electroreduction of CeO_2. Partially reduced CeO_{2-x} and Ru nanoparticles are said to form a stronger metal-support interaction resulting in higher catalytic activity. The reduction process of ceria was observed to be slow due to the low O^{2-} diffusion rates from ceria to YSZ solid-electrolyte, causing a delay in the catalytic response. Once electrochemically promoted, a "permanent" or "persistent" catalytic rate enhancement was observed. Overall, this study shows the feasibility of the new reactor design and the application of the concept of electrochemical promotion to highly-dispersed heterogeneous catalysts.

Chapter 6: Electrochemically enhanced metal-support interaction of highly dispersed Ru nanoparticles with a CeO_2 support

Dole, H.A.E., Safady, L.F., Ntais, S., Couillard, M., Baranova, E.A. Journal of Catalysis, ***318,*** *85-94 (2014).*

Small particle size (1.1 nm) Ru nanoparticles were supported on a mixed ionic-electronic conductor, CeO_2, with a low metal loading (1 wt%), interfaced with a YSZ electrolyte. A pronounced enhancement (up to about 2.5 times) of the catalytic rate for the complete oxidation of ethylene was observed for negative polarization. The opposite effect was observed for positive polarization. Apparent Faradaic efficiencies up to 96 were determined, indicating a non-Faradaic effect. The modification of the cerium oxidation state (i.e., reduction from Ce^{4+} to Ce^{3+}) is proposed to enhance the catalytic performance of the Ru nanoparticles. XPS analysis was performed to confirm this reduction of ceria. The enhancement of catalytic activity is attributed to the presence of more oxygen vacancies in the ceria interlayer causing a stronger metal-support interaction. Results demonstrate the feasibility of in-situ modification of the metal support-interaction between Ru nanoparticles and CeO_2 catalytic support by a small current (-2 μA) application.

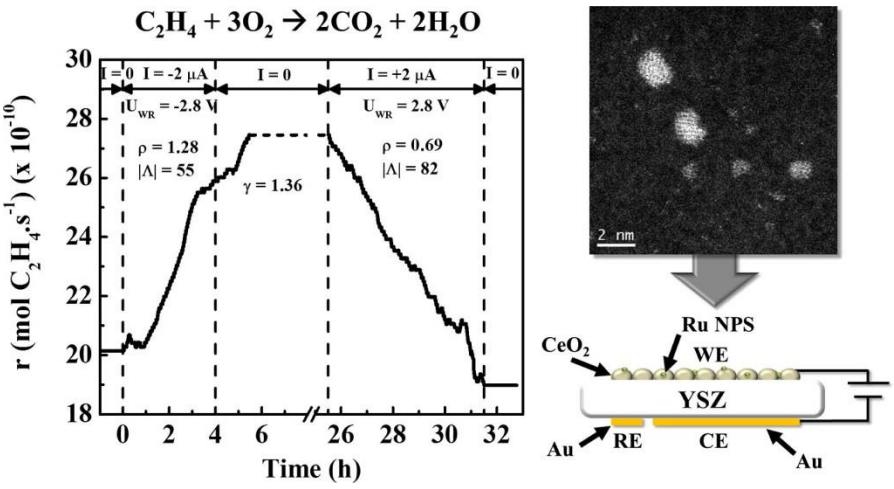

6.1 Introduction

Electrochemical promotion of catalysis (EPOC) is a promising method for enhancing catalytic activity through the application of a small electrical stimulus between the catalyst-working and counter electrode deposited on a solid electrolyte [14,20,140]. The electronic properties of the catalyst can be modified resulting in a change in catalytic activity. In the case of yttria-stabilized zirconia (YSZ) as a solid electrolyte, the addition or removal of O^{2-} species on the catalyst surface can be controlled in situ depending on the specified reaction

conditions. Fully reversible and ‘‘permanent’’ or ‘‘persistent’’ EPOC has been reported for more than 70 various catalytic systems [14]. In reversible EPOC experiments, the reaction rate returns to its initial value after the electrical stimulus is interrupted. For permanent EPOC (P-EPOC), the reaction rate remains at a higher value than the initial open circuit value [145,224]. Despite receiving much attention, this phenomenon has not yet reached commercial application. One of the main technical factors preventing such development is the use of thick film catalysts with low surface areas and high material costs [29]. The first step towards an alternative cell to accommodate high surface area catalysts was pioneered by Marwood, in the 1990s, where it was proposed that EPOC could be achieved through an isolated catalyst surrounded by two gold electrodes between which current passed [156,181]. Since then, several studies have expanded on this idea of a bipolar configuration, for example, sputtering a Pt catalyst between a comb-like gold electrode configuration [161,162]. Kambolis et al. [180] also demonstrated the feasibility of electropromoting a highly dispersed (~15%), Pt nanoparticle (average size: 8 nm) catalyst for the oxidation of propane. A 38% enhancement of the catalytic rate was observed with apparent Faradaic efficiency values up to 85.

Ceria (CeO_2) is a mixed ionic-electronic conducting (MIEC) material that conducts O^{2-} ions due to oxygen vacancies in the crystallographic structure in addition to conducting electrons at elevated temperatures. Furthermore, due to its non-stoichiometry, CeO_2 has the ability to undergo conversion between Ce^{4+} and Ce^{3+} quite easily [227]. These properties make the use of ceria-containing catalysts of interest for many applications, including soot removal from diesel engine exhaust [231], catalyst additives in combustion processes [232], and as a solid oxide electrolyte for fuel cells [233]. In heterogeneous catalysis, Pt group metals deposited on CeO_2 show a metal-support interaction (MSI) effect associated with charge transfer between the two solids that are in contact [234–236]. In EPOC studies, using a MIEC can also ensure electrical connectivity between highly dispersed nanoparticle catalysts [180]. EPOC studies using CeO_2 as an interlayer include those performed by Jiménez-Borja et al. [179,237] that compared both Pd/YSZ and Pd/CeO_2/YSZ electrocatalytic systems for the oxidation of methane and Petrolekas et al. [230] where a Pt/CeO_2 system was studied for ethylene oxidation. The presence of the CeO_2 interlayer was found to improve the supply of oxygen ions to the catalyst surface.

In this study, electrochemical enhancement of catalytic activity of a nano-sized ruthenium catalyst, with an average size of 1.1 nm, for ethylene oxidation was investigated. Ru nanoparticles, synthesized using a modified polyol reduction method, were supported on CeO_2 resulting in a 1 wt% Ru loading (RuNPs/CeO_2) (i.e., typical in heterogeneous catalysis studies). The highly dispersed RuNPs/CeO_2 catalyst powder was supported on a YSZ solid electrolyte in order to apply polarization. In this study, the effect of the partial pressure of ethylene with constant partial pressure of oxygen, temperature, and passed positive and negative current on the catalytic activity of the RuNPs/CeO_2 catalyst, as well as the role of the cerium redox state in the observed persistent effect are explored. XPS analysis of the catalyst before and after electrochemical enhancement of catalytic activity was used to determine any changes in the redox state of cerium. In addition, the catalytic properties of the RuNPs/CeO_2 catalyst is compared to that of larger Ru particles supported on CeO_2, prepared by the conventional method of thermally decomposing a precursor salt (TD-Ru/CeO_2) (same metal loading) and blank CeO_2, both supported on a YSZ solid electrolyte.

6.2 Materials and Methods

6.2.1 Synthesis of Ceria-supported Ru Nanoparticles

Ruthenium nanoparticles deposited on CeO_2 (Ru NPs/CeO_2) were synthesized using a modified polyol reduction method [68]. A colloid of Ru nanoparticles was synthesized in 50 mL of ethylene glycol (anhydrous 99.8% Sigma Aldrich), starting by adding 0.15 g RuCl (Alfa Aesar, 99.99% metals basis) precursor salt; then a volume of NaOH (EM Science, ACS grade) dissolved in ethylene glycol is added for a total concentration of 0.08 M. The salt solution was stirred for 30 min at room temperature and subsequently refluxed for 3 h at 160°C. The initial solution pH was 10 and after reflux, it dropped to 7. The resulting colloidal solution is deposited on CeO_2 (Alfa Aesar, specific surface area ~30–40 $m^2 \cdot g^{-1}$) at room temperature by mixing CeO_2 (1 g) in deionized water (25 mL) and adding an appropriate volume of colloid (5 mL, concentration of Ru = 2 mg/mL) for a desired metal loading of 1 wt%. The solution is stirred for 48 h at room temperature; then the supported nano-particles were extensively washed three times with deionized water (18 MΩ·cm) and separated by centrifugation. Finally, the supported nanoparticles were dried in air at 40–60°C for 48 h.

6.2.2 Preparation of Electrochemical Cells

To prepare the electrochemical cells, RuNPs/CeO_2, Ru particles (via thermal-decomposition) over CeO_2 (TD-Ru/CeO_2), or CeO_2 alone was deposited on one side of a masked YSZ disk as the working electrode along with inert gold counter and reference electrodes on the opposite side. YSZ powder (TOSOH, specific surface area ~13 $m^2 \cdot g^{-1}$, average size of 0.3 μm) containing 8 mol% yttria was used to form electrolyte disks (18 mm diameter and 1 mm thickness) by a known procedure [228]. The counter and reference electrodes were deposited by applying gold paste (C2090428D4, Gwent Group, CAS: 98-55-5) followed by annealing at 500°C for 1 h.

In order to deposit the RuNPs/CeO_2 catalyst-working electrode, a solution of 1 wt% RuNPs/CeO_2 powder and ethanol was prepared. Approximately 0.2 g of RuNPs/CeO_2 was dispersed in 2 mL of ethanol via sonication. The solution was then deposited until the desired loading was obtained (0.10 mg $Ru \cdot cm^{-2}$) (i.e., 10–15 times), drying at 60°C for 30 min between depositions. Finally, the catalyst was calcined in a mixture of O_2 (3 kPa) and He (balance) at 350°C for 1 h.

The TD-Ru/CeO_2 catalyst-working electrode was prepared in two steps. It should be noted, this method is commonly used in many EPOC studies; therefore was used as a comparison for this study [153,160,224,238]. First, approximately 0.2 g of CeO_2 powder was dissolved in 2 mL of ethanol via sonication for 10 min at room temperature. The solution was then deposited (10 μL at a time; drying at 60°C for 30 min between depositions) until the desired loading was obtained (9.9 mg CeO_2) (i.e., 10–15 times). The desired loading was in accordance with the mass of CeO_2 present in the nanoparticle catalyst. Next, the thermally-decomposed Ru particles were prepared by first dissolving 0.025 g $RuCl_2$ salt (via sonication for 10 min) in a 1 mL solution of isopropanol (Acros Organics, 99.5%) and deionized water (1:1 by volume) with a metal concentration of 0.12 M. The solution was pipetted, 10 μL at a time, onto the masked YSZ disk containing the CeO_2 layer, drying in air at 80°C for 30 min. The sample was then calcined in air at 500°C for 1 h. This procedure was repeated 8 times until desired metal loading (i.e., 10 mg Ru) was achieved for the same metal loading as the RuNPs/CeO_2 working electrode. Finally, the sample was reduced under hydrogen at 450°C for 4 h.

For further comparison, an electrochemical cell was prepared containing only a CeO_2 catalyst-working electrode. As in the first step of the thermally-decomposed Ru particles, a solution of CeO_2 powder and ethanol is prepared. Then a desired loading of 9.9 mg of CeO_2 was deposited and the catalyst was calcined in air at 350°C for 1 h to be consistent with the initial state of the nanoparticle catalyst.

6.2.3 Catalyst Characterization

The unsupported and supported nanoparticle catalysts were characterized by scanning transmission electron microscopy (STEM) to (1) determine the size distribution of the catalysts, and (2) directly image the catalyst on the ceria support both before and after electrochemical enhancement of catalytic activity. In both cases, the specimens were prepared by sonicating the catalyst powders in ethanol. For the case of after electrochemically enhanced catalytic measurements, the catalyst was scraped, using a spatula, from the surface of the YSZ in order to dissolve the powder in ethanol via sonication. One drop of the solution was then placed onto a STEM support grid and dried in air. For the first experiment (1), STEM micrographs of unsupported colloidal Ru nanoparticles were deposited directly on a carbon film (Ted Pella, ultrathin Carbon film on a holey carbon film), and for the second experiment (2), ceria-supported Ru nanoparticles were deposited on a lacey-carbon support film (Ted Pella). The analysis was performed on a FEI Titan^3 80-300 microscope operated at 300 kV and equipped with a CEOS aberration corrector for the probe forming lens, a monochromated field-emission gun, and an EDAX energy dispersive X-ray (EDX) spectrometer. High-angle annular dark-field (HAADF) imaging was used to image the Ru catalyst on the CeO_2 support. In this imaging mode, an electron probe is scanned over a specimen in a raster pattern while a detector collects electrons scattered at high angles over an annulus on the diffraction plane. By setting a high inner collection angle (60 mrad), ADF imaging provides a contrast sensitive to the atomic number Z. To determine the particle size distribution, Image J software was used, measuring at least 750 particles.

Two-wire in-plane resistance measurements of an as-prepared RuNPs/CeO_2 catalyst-electrode (as deposited on the YSZ electrolyte) were carried out under an O_2 (3 kPa) and He (balance) environment, allowing the catalyst to stabilize for 1 h. A multimeter (Agilent

model U1272A) was used to measure the resistance across two contacts attached on either side of the catalyst-electrode (5 mm apart). From these measurements, electrical resistances of 1.2 MΩ·cm, 0.5 MΩ·cm, and 0.2 MΩ·cm were determined at 350, 375 and 400°C, respectively.

X-ray photoelectron spectroscopy (XPS) characterization was carried out so as to study the chemical state of the ceria support before and after electrochemical enhancement of catalytic activity of the RuNPs/CeO_2 catalyst. These measurements were conducted using a KRATOS Axis Ultra DLD with a Hybrid lens mode at 140 W and pass energy 20 eV using a monochromatic Al Kα. The electrocatalytic cells were mounted on a copper tape so as to avoid charging effects. The binding energy (BE) scale was corrected using the C1S peak at 284.6 eV. The accuracy of measurement of the binding energy is ±0.1 eV while that of FWHM ±0.05 eV. The analysis of the O1s spectra was performed using a fitting routine that divided each spectrum into individual mixed Gaussian–Lorentzian peaks.

It should be noted that ceria can be found in two stable stoichiometries: (a) cerium dioxide (CeO_2, Ce^{4+}) characterized by unoccupied 4f states ($4f^0$) and (b) cerium trioxide (Ce_2O_3, Ce^{3+}) with a $4f^1$ configuration. To this point, it should be mentioned that X-ray irradiation during the XPS measurement can cause the reduction of Ce^{4+} to Ce^{3+}, as discussed in the literature [239–241]. Rama Rao and Shripathi [239] proposed that the reduction takes place through the dissociation of hydroxyl groups present on the surface of ceria. On the other hand, Paparazzo [240], in a previous study, attributed the Ce^{4+} reduction to a locally intense heating of the sample. Though, after further studies, an ‘‘internal’’ mechanism was suggested [241] according to which the Auger decay of core holes causes the creation of holes in the valence band region which are followed by electron shake-up transition leading to the occupancy of antibonding orbitals. During this process, two holes are created in the valence band that subsequently causes the scission of two Ce-O bonds, thus resulting in an oxygen deficiency.

Therefore, in order to avoid the reduction of the cerium oxide due to the presence of the samples under UHV conditions and under X-ray irradiation, which could cause the deduction of incorrect conclusions, both samples (i.e., as-prepared and after electrochemical

enhancement of catalytic activity) were treated in exactly the same way. Both samples were introduced and remained in the UHV chamber for about 2 h while the measurement took place over a period of about 1.5 h.

6.2.4 Catalytic Measurements

Catalytic studies were carried out at atmospheric pressure in a plug flow-type reactor [225]. The electrochemical cell was placed in contact with gold current collectors allowing the gas flow to pass over the catalyst. A potentiostat/galvanostat (PARSTAT 2263) was used to polarize the cell for a desired duration and constant current while measuring the catalyst potential (U_{WR}). The reaction gases were C_2H_4 (Linde, 0.5% C_2H_4 in He), O_2 (Linde, 20.9% O_2 in He), and pure He (Linde, 99.997% He) as a carrier gas. The gas composition of 0.005–0.03 kPa C_2H_4, 3 kPa O_2 and He balance was controlled by mass flow controllers (MKS, 1259C and 1261C Series). The overall flow rate was held constant at 6 $L \cdot h^{-1}$. The product gases were analyzed with an on-line CO gas analyzer (Horiba,VA-3000).

To evaluate the effect of EPOC, three parameters were calculated, the rate enhancement ratio (ρ) [14], defined as,

$$\rho = r/r_0 \qquad \textbf{6-1}$$

Apparent Faradaic efficiency (Λ), for an O^{2-} conducting system,

$$\Lambda = (r - r_0)/(I/2F) \qquad \textbf{6-2}$$

and the permanent rate enhancement ratio (γ), for the case of P-EPOC [139],

$$\gamma = r_p/r_0 \qquad \textbf{6-3}$$

where r_0 is the open-circuit catalytic rate (mol $C_2H_4 \cdot s^{-1}$) and r is the catalytic rate (mol $C_2H_4 \cdot s^{-1}$) under closed-circuit conditions, r_p is the catalytic rate (mol $C_2H_4 \cdot s^{-1}$) at the new steady-state value after current interruption, I is the current (A) and F is Faraday's constant (96,485 $C \cdot mol^{-1}$). It should be noted that the enhancement is considered to be the effect of electrochemical promotion only when $|\Lambda| > 1$, meaning non-Faradaic enhancement.

6.3 Results and Discussion

6.3.1 Characterization

STEM characterization was carried out for the colloidal and CeO_2-supported RuNPs and TD-Ru. EDX was also used to confirm the presence of Ru on the supported catalyst. Figure 6-1 shows representative STEM micrographs and a corresponding size distribution for the colloidal Ru nanoparticles. It is evident that well-defined and fairly uniformly sized Ru nanoparticles were achieved. From the STEM images, an average Ru particle size was found to be 1.1 nm.

Figure 6-2 presents STEM images of the Ru nanoparticles deposited on a ceria support, both before (a and b) and after (c and d) electrochemically enhanced catalytic measurements. Because of the relatively high Z number of the support, Ru catalysts are more easily imaged when located on the edge of the CeO_2 particles, but some catalyst particles are also observed in regions where the support is very thin. These bright features observed in the STEM images were confirmed to be Ru catalyst using spatially-resolved energy dispersive X-ray (EDX) spectroscopy (Figure 6-2e and f). On the as-prepared catalyst specimen, several sub-2 nm particles (a) were observed with a few larger ones (b) which were attributed to aggregation during deposition. The nanoparticles after electrochemically enhanced catalytic measurements showed more aggregation than the as-prepared catalyst, resulting in particles that were typically around 5 nm (c), with some that were occasionally even larger (d).

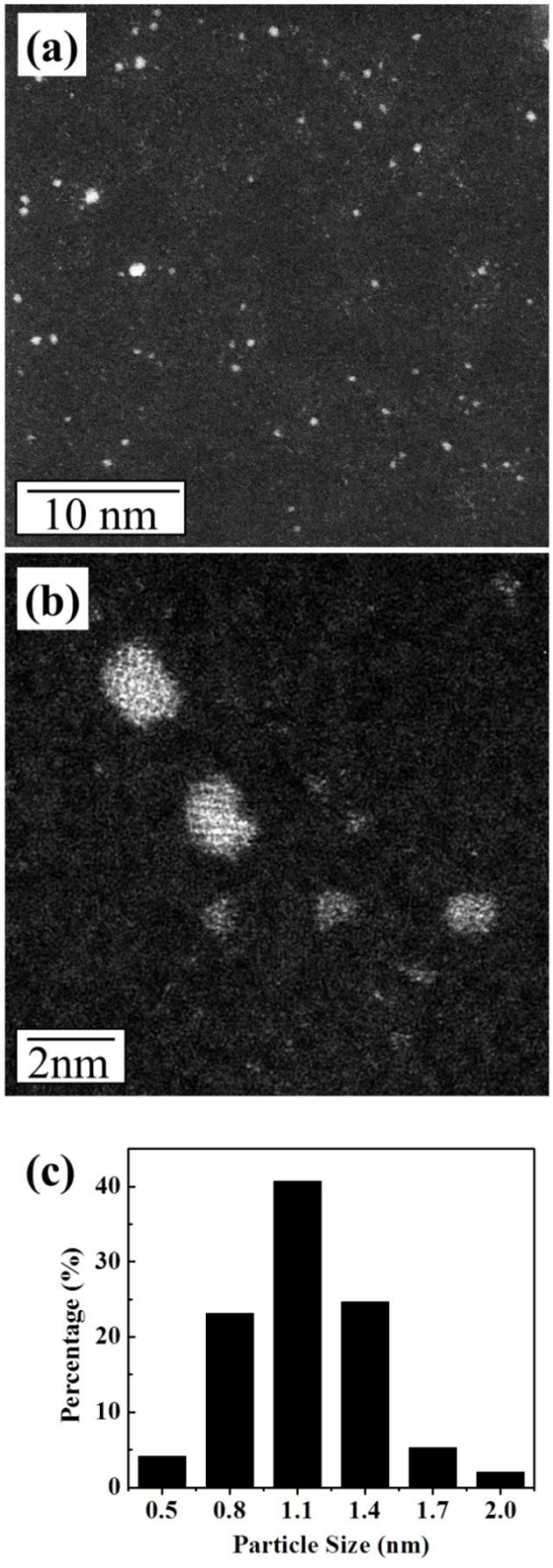

Figure 6-1: ADF-STEM images of colloidal Ru nanoparticles deposited on a thin carbon film (a, b); and (c) corresponding histogram.

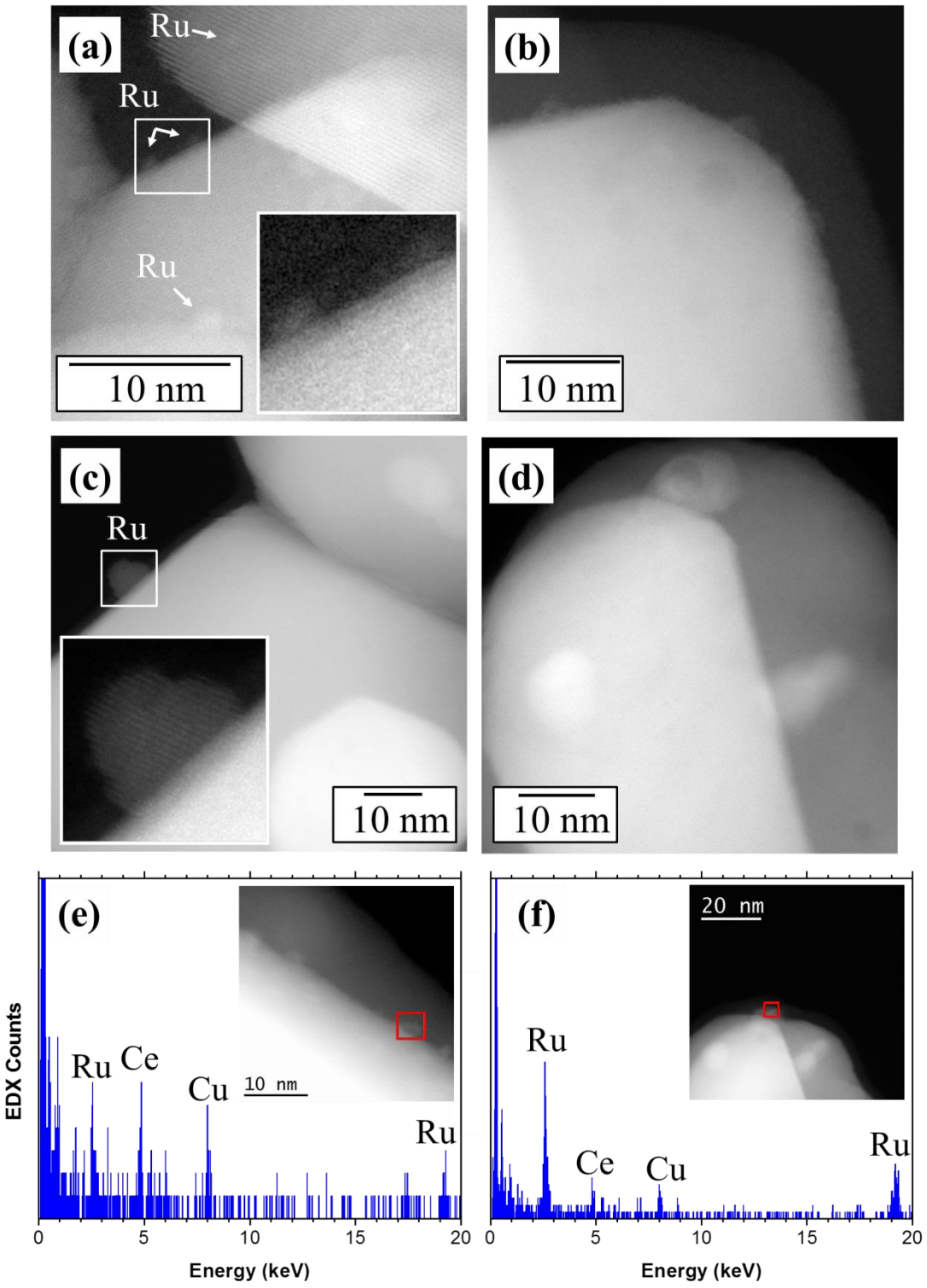

Figure 6-2: HAADF-STEM images of RuNPs/CeO_2 as-prepared (a and b); and after electrochemically enhanced catalytic measurement (c and d). Energy dispersive X-ray spectra acquired over the region labelled by a square on the inset images for RuNPs/CeO_2 as-prepared (e) and after electrochemical enhancement of catalytic activity (f).

Figure 6-3 shows representative STEM images of the thermally-decomposed Ru particles supported on ceria showing particles ranging from 2 to 25 nm. This demonstrates that the TD-Ru/CeO_2 catalyst consists of larger particles in comparison to the RuNPs/CeO_2 catalyst (average size = 1.1 nm) as well as having a much broader range.

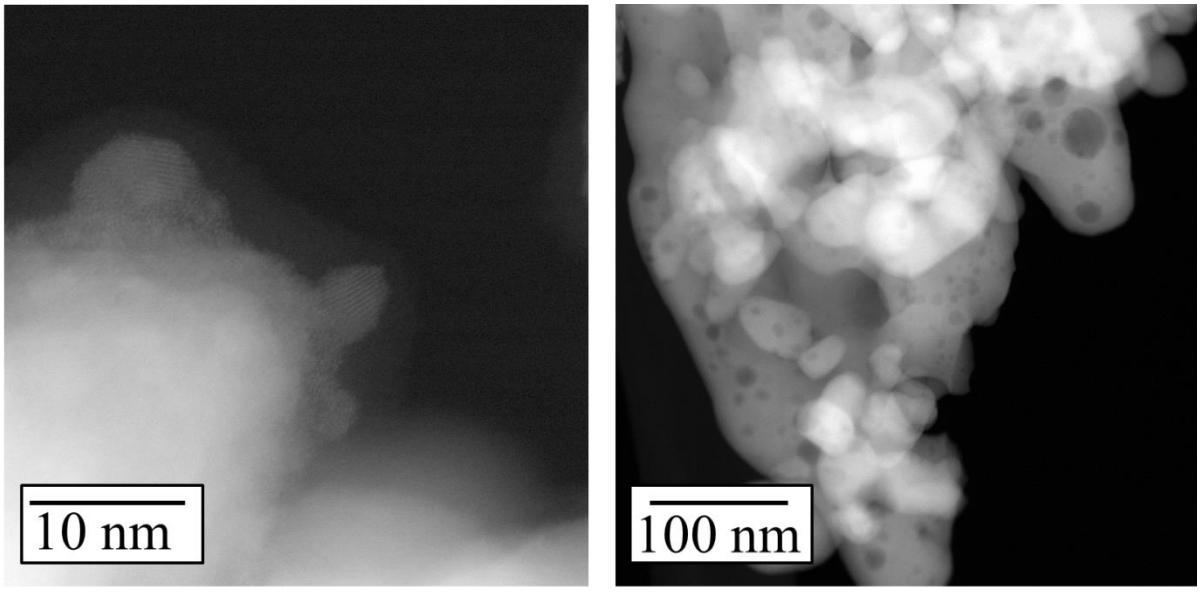

Figure 6-3: HAADF-STEM images of TD-Ru/CeO_2 after electrochemical enhancement of catalytic activity.

6.3.2 Catalytic Studies

The complete oxidation of ethylene has been used as a model reaction to study the electrochemical promotion for many years [14,15,24,141]. This model reaction was chosen to carry out promotion studies over the RuNPs/CeO_2, TD-Ru/CeO_2 and CeO_2 catalysts. It should be noted that several electrochemical cells using the same RuNPs/CeO_2 catalyst were prepared to complete this study.

6.3.2.1 Open Circuit Catalytic Activity

Before the application of electrochemical polarization to the cells, the catalytic performance under open-circuit conditions was determined. For a constant partial pressure of oxygen (3 kPa), a forward (i.e., increasing partial pressure of ethylene) and reverse (i.e., decreasing partial pressure of ethylene) scan (0.005–0.03 kPa) was carried out at 350°C allowing the reaction to stabilize for 1 h between each partial pressure. These results are shown in Figure

6-4. From these results partial pressures less than 0.012 kPa of C_2H_4, corresponding to conversions <30%, were chosen to carry out the EPOC studies.

A comparison of the open circuit catalytic activity between the three catalysts – RuNPs/CeO_2, TD-Ru/CeO_2 and CeO_2 is presented in Figure 6-4a. It can be seen that the catalytic activity is the highest for the CeO_2-supported nanoparticles (RuNPs/CeO_2), while the TD-Ru/CeO_2 and CeO_2 by itself show much lower activity. These results show that the Ru nanoparticles are the catalytically active phase for the selected reaction since blank CeO_2 is not as active; therefore, it is the interaction between these two materials that is causing such performance. A similar increase in the catalytic performance with the addition of a low loading of Pt nanoparticles was observed previously[180]. Furthermore, the size of the Ru particles is a factor in the performance as the TD-Ru/CeO_2 did not show much higher catalytic activity compared to the blank CeO_2. This observation is attributed to a stronger metal-support interaction between the Ru nanoparticles and CeO_2 compared to that of the particles deposited through thermal-decomposition. These results correspond with the size dependence on catalytic activity and metal-support interaction of Pt nanoparticles supported on YSZ previously shown [102].

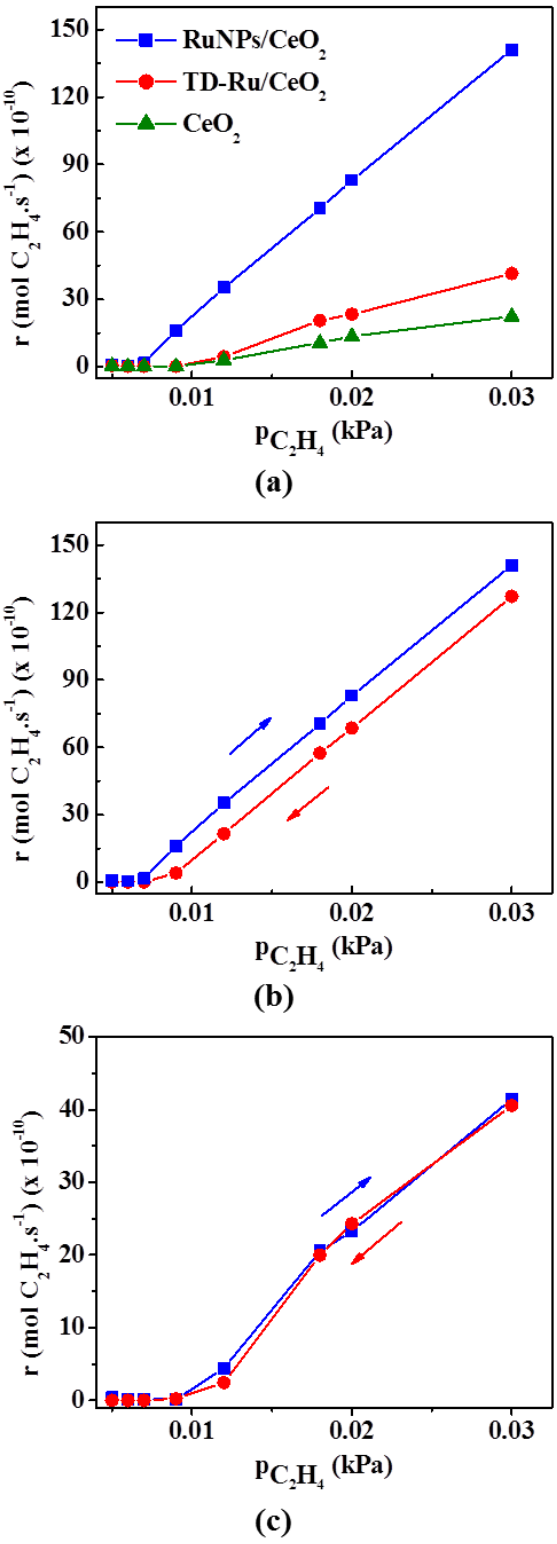

Figure 6-4: Catalytic performance for complete oxidation of ethylene over (a) all three catalysts, (b) Ru NPs/CeO_2 (forward and reverse) and (c) TD-Ru/CeO_2 (forward and reverse), with varying partial pressure of ethylene and constant oxygen partial pressure (3 kPa) under open circuit conditions at 350°C.

As can be seen in Figure 6-4b, a slight hysteresis was observed for the catalytic activity of the RuNPs/CeO_2 catalyst while, for the TD-Ru/CeO_2 (Figure 6-4c) and CeO_2 (not shown) catalysts, there was no hysteresis observed. Similar observations were discussed for a Rh film deposited on a TiO_2 interlayer [242,243]. The observed hysteresis may be attributed to either nanoparticle agglomeration or to the partial reduction of ruthenium oxide particles as the concentration of ethylene was increased, resulting in a higher catalytic activity curve in the forward direction. While in the reverse direction, as the concentration of ethylene is decreased, the partially-reduced ruthenium oxide was not oxidized as easily, resulting in a lower catalytic activity curve. Furthermore, at higher p_{C2H4}, nanoparticle poisoning (coking) to some extent may take place. It is difficult to distinguish between each effect because all three factors may explain the lower reaction rates in the reverse scan. Furthermore, due to the presence of smaller particles in the RuNPs/CeO_2 catalyst compared to the TD-Ru/CeO_2 catalyst, the partial reduction of the ruthenium oxide was more easily achieved resulting in less of a hysteresis effect for the TD-Ru/CeO_2 catalyst.

6.3.2.2 Effect of Polarization

The effect of negative polarization for all three catalysts was determined by passing -2 μA (U_{WR} = -6.8 V) at a partial pressure of ethylene of 0.012 kPa at 350°C. Under cathodic polarization three electrochemical processes are expected to take place simultaneously: (i) reduction of gas phase oxygen at the three-phase boundary, i.e., catalyst/solid-electrolyte/gas, (ii) CeO_2 reduction, and (iii) RuO_x reduction [244]. An enhancement in catalytic activity was only observed for the RuNPs/CeO_2 catalyst (shown in Figure 6-5a). A slightly higher current (-5μA, U_{WR} = -6.5 V) was then required at 375°C to electropromote the RuNPs/CeO_2 catalyst (Figure 6-5b).

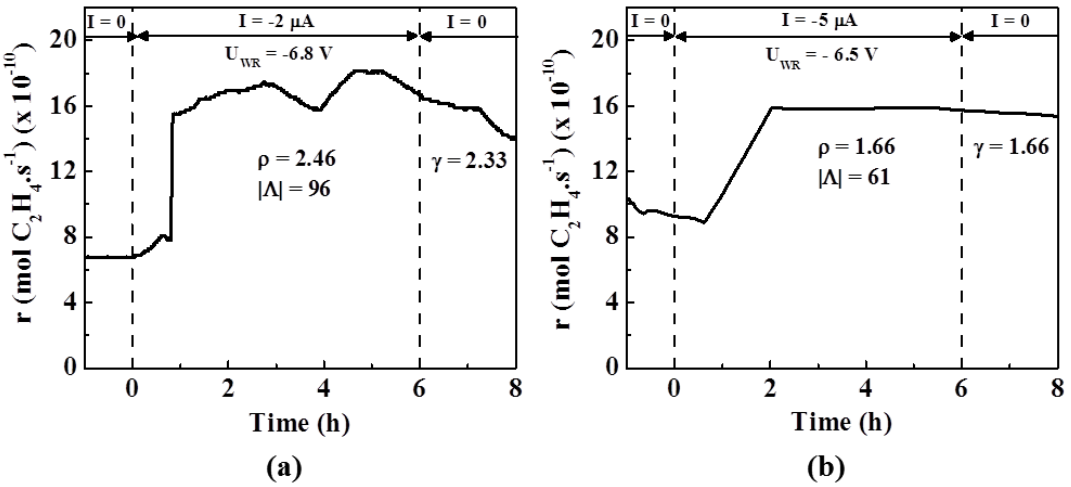

Figure 6-5: Transient effect of current application for C_2H_4 oxidation over RuNPs/CeO_2 on YSZ electrolyte at (a) 350°C for a current of -2 µA (U_{WR} = -6.8 V); and (b) 375°C for a current of -5 µA (U_{WR} = -6.5 V) for 6 hours (0.012 kPa C_2H_4).

A rate enhancement ratio of 2.46 and a Faradaic efficiency of 96 were observed when passing a current of -2 µA at an ethylene partial pressure at 0.012 kPa at 350°C (Figure 6-5a). Furthermore, a higher current at 375°C resulted in a rate enhancement ratio of 1.66 and a Faradaic efficiency of 61. It is worth noting that negative current application resulted in an initial slow increase in the reaction rate followed by an abrupt increase after approximately 1 h. These results indicate that there is a delay between the electrochemical and catalytic process. Additionally, as can be observed in Figure 6-5a, after approximately 3 h of passing negative current, the catalytic rate shows a gradual decline for about 1 h; then proceeds to gradually increase to an even higher rate than before the decline. Finally, this decline is observed again near the interruption of the current. It is possible that this instability is caused by the ability of CeO_2 to convert easily between Ce^{4+} and Ce^{3+} resulting in a change of metal-support interaction between CeO_2 and Ru which can alter the catalytic rate. On the one hand, since RuO_x is a better catalyst for ethylene oxidation than Ru metal, the increase in the reaction rate due to RuO_x reduction was ruled out[238,245]. On the other hand, CeO_2 is a MIEC and is easily reduced from Ce^{4+} to Ce^{3+} oxidation state; therefore partial reduction of ceria to CeO_{2-x} may be responsible for the observed increase in the catalytic rate of ethylene oxidation. As was shown earlier[246,247], the reduced ceria has higher ionic (O^{2-}) conductivity due to the larger amount of lattice defects, i.e., oxygen vacancies and Ce^{3+} ions. In the first hour (Figure 6-5), the partial reduction of CeO_2 to CeO_{2-}

$_x$ may take place. The reduced CeO_{2-x} enhances catalytic activity of Ru nanoparticles towards ethylene oxidation.

Furthermore, it was also observed that the catalytic rate remained in the enhanced state, at both conditions, even after current interruption resulting in a permanent enhancement ratio of 2.33 and 1.66 for a current of -2 μA and -5 μA, respectively. The effect of temperature and the observed permanent enhancement will be discussed in more detail later. An interesting point to note is that there was a longer persistent effect observed when passing a higher current.

As stated, the effect of polarization was not observed for the TD-Ru/CeO_2 or the CeO_2 catalysts (results are not shown). These results show that Ru particle size and metal-support interaction (MSI) between CeO_2 and the Ru particles plays a key role in the oxidation of ethylene at both open and closed circuit conditions. The catalytic activity of CeO_2 alone could not be enhanced by polarization. Furthermore, the TD-Ru/CeO_2 catalytic activity could not be enhanced plausibly due to either the large Ru particle size and size distribution or difference in the synthesis method, resulting in a weaker interaction with the CeO_2 support. It has been shown previously that MSI becomes stronger as the metal particle size decreases [102]. It is important to note, that previous EPOC studies of RuO_2 catalysts using the method of thermal-decomposition have been successful in enhancing the catalytic activity through polarization; however, the metal loading was much higher, 1–3 mg Ru/cm^2 in comparison to 0.10 mg Ru/cm^2 in this study, resulting in a continuous RuO_2 film and not isolated nanoparticles [160,224,238].

6.3.2.3 Effect of Temperature for RuNPs/CeO_2

To determine the effect of temperature on the extent of electrochemical catalytic enhancement over the RuNPs/CeO_2 catalyst, -2 μA was passed for 6 h at three different temperatures – 350, 375 and 400°C. Figure 6-6 shows this effect with regards to the rate enhancement ratio and Faradaic efficiency.

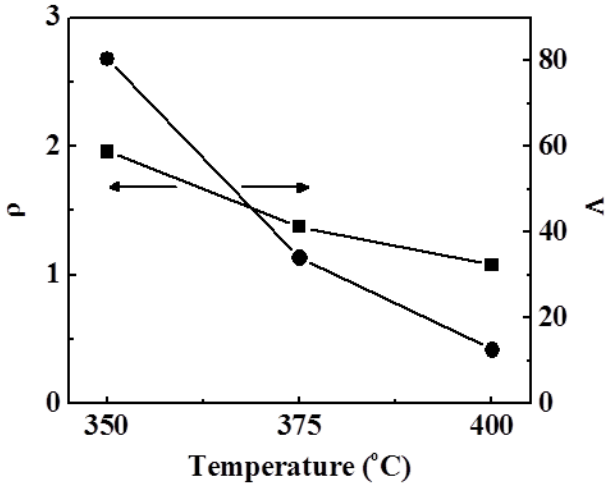

Figure 6-6: Effect of temperature on rate enhancement ratio (ρ) and Faradaic efficiency (Λ) when passing a current of -2 μA for 6 hours for C_2H_4 oxidation over RuNPs/CeO_2 on YSZ electrolyte (0.012 kPa C_2H_4).

Overall, it can be seen that electrochemical promotion was observed for all three temperatures since all Faradaic efficiencies are greater than 1. The highest rate enhancement ratio was obtained at a temperature of 350°C ($\rho \approx 2$), while increasing temperature showed a decrease in the rate enhancement ratio. As temperature increases, the open circuit catalytic rate increases as well, while the change in catalytic rate ($r - r_0$), due to polarization, decreases with increasing temperature; therefore, leading to a decrease in the ρ and Λ values. Similar observations have also been reported previously [160,179] where an optimal temperature for electrochemical promotion was determined. One study showed an optimal enhancement in catalytic activity at 350°C for a thermally-decomposed RuO_2 film on a YSZ monolith. It was explained that at a lower temperature the influence of EPOC was not as apparent due to a lower amount of current passed, while at higher temperatures, the enhancement reaches a maximal values leading to a decrease in the EPOC effect [160].

6.3.2.4 Persistent Effect due to Polarization

The effect of both negative and positive polarization was investigated and its relationship to the observed persistent effect. Figure 6-7 shows, for a constant partial pressure of oxygen (3 kPa), the effect of applying ±2 μA for 0.012 kPa C_2H_4 (Figure 6-7).

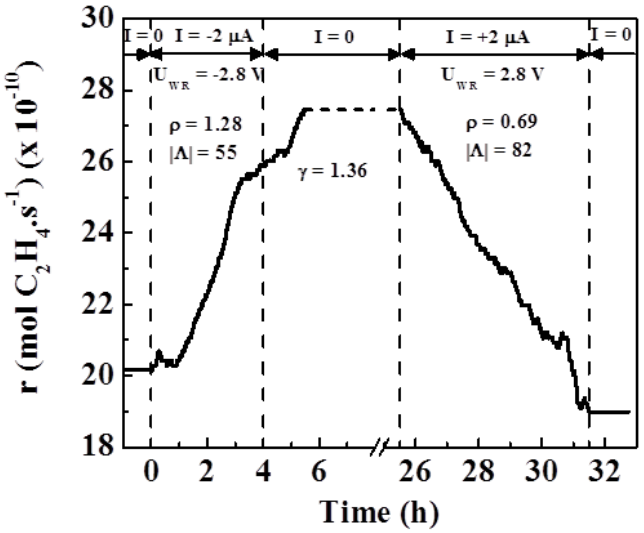

Figure 6-7: Transient effect of current application for C_2H_4 oxidation over Ru/CeO_2 on YSZ electrolyte at 350°C when passing a current of -2 µA (U_{WR} = -2.8 V) for 4 hours and +2 µA (U_{WR} = 2.8 V) for 6 hours (0.012 kPa C_2H_4).

It is evident that there is a pronounced effect of both negative and positive polarization. A rate enhancement ratio of 1.28 was observed when passing a current of -2 µA at a partial pressure of C_2H_4 of 0.012 kPa. The Faradaic efficiency was found to be 55, indicating that the catalytic activity is 55 times higher than predicted by Faraday's law. As shown in Figure 6-5, again, negative current resulted in an initial slow increase in the reaction rate followed by a rapid increase after 1 h (Figure 6-7). After current interruption, the catalytic rate remained in the enhanced state and continued to increase before reaching a new steady state. Moreover, by applying a positive current (+2 µA up to 6 h), this permanent effect was completely reversed.

Due to the observed ''permanent'' effect after passing a current of -2 µA for 0.012 kPa C_2H_4, the catalytic performance under open-circuit conditions was evaluated after 72, 96, and 144 h after current interruption (Figure 6-8). Note that ''open circuit'' indicates the catalytic rate before polarization.

It is evident that the catalyst has been permanently altered through the application of a negative current, with a more pronounced effect at low partial pressures of C_2H_4. It is proposed that partial reduction of CeO_2 might be responsible for the observed enhancement in reaction rate. It is has been shown previously that the catalytic activity of an Au catalyst

supported on reduced Ce_2O_3 exhibits much higher catalytic activity, due to stronger metal-support interaction, compared to that supported on CeO_2[104]. Catalytic activity of a metal-ceria system is directly related to the number of oxygen vacancies in the crystal structure; therefore, through the application of negative polarization, the following reaction could take place.

$$CeO_2 + 2xe^- \rightarrow CeO_{2-x} + xO^{2-} \qquad \textbf{6-4}$$

where Ce^{4+} is electroreduced to a lower valence state due to the removal of oxygen species from its structure. Through the partial reduction of CeO_2, more oxygen vacancies in the ceria interlayer are formed causing a stronger metal-support interaction and resulting in an increase in the catalytic activity of Ru nanoparticles [227]. A similar relationship was observed by Jiménez-Borja et al. [179] during the enhancement in catalytic activity of a Pd/CeO_2/YSZ catalyst. As seen in Figure 6-7, under negative polarization, initially a small increase in the reaction rate is observed due to the slow rate of the reaction (Eq. 6-4). The rate limiting step of (Eq. 6-4) is the diffusion of O^{2-} from CeO_2 to YSZ solid electrolyte. Under positive polarization for up to 6 h or open circuit operation for up to 144 h, the partially reduced ceria is oxidized and the opposite diffusion process of O^{2-} from YSZ to CeO_2 takes place. The latter leads to the catalytic rate decrease down to the initial rate values or even lower (Figure 6-8); however, this could be explained by the nanoparticle agglomeration as confirmed by STEM (Figure 6-2c and d). These results demonstrate the role of the MIEC interlayer, CeO_{2-x}, and its enhanced interaction with Ru upon electrochemical reduction of ceria. A similar persistent effect was observed for a IrO_2–TiO_2 catalyst [223]. It was found that the more TiO_2 present, the longer it took for the catalytic activity to return to its initial value.

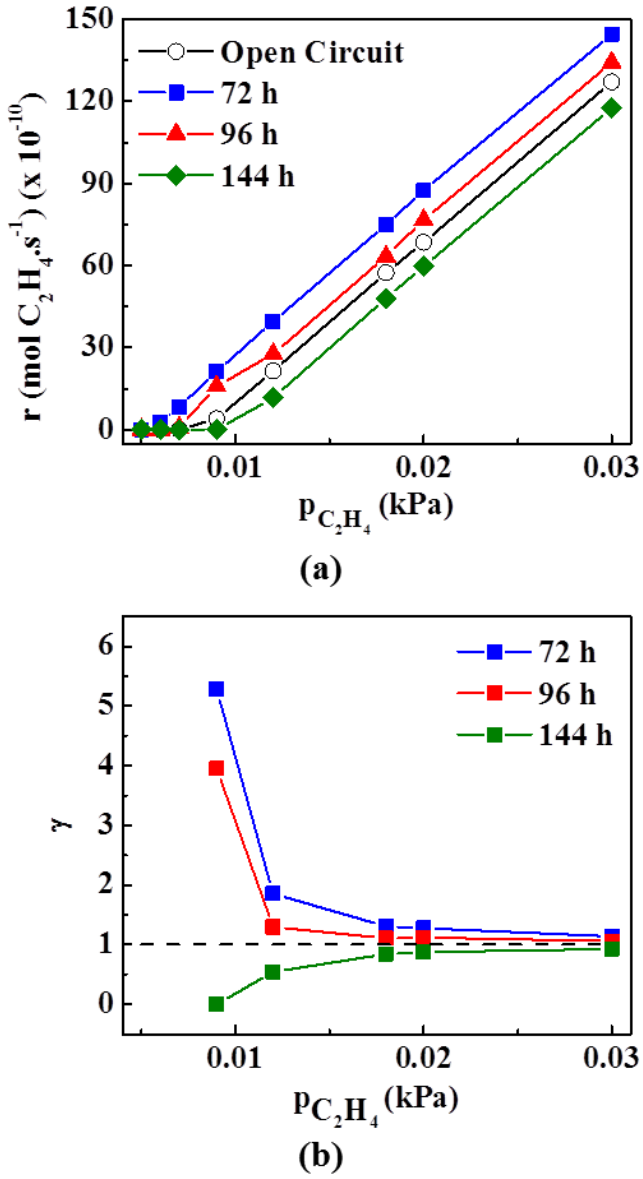

Figure 6-8: Persistent effect observed for the (a) catalytic rate and (b) permanent rate enhancement ratio after negative polarization (-2 μA, 4 hours) for complete oxidation of ethylene over Ru/CeO_2 with varying partial pressure of ethylene and constant oxygen partial pressure (3 kPa) under open circuit conditions at 350°C.

6.3.3 XPS Analysis of RuNPs/CeO_2 Before and After Electrochemical Enhancement

XPS results are discussed only qualitatively since the O abundance and the chemical state of cerium can be influenced by the exposure of the samples to the atmosphere and/or the Ultra High Vacuum/X-ray exposure as was mentioned above. In order to eliminate these effects, the two samples (before and after electrochemical enhancement of catalytic activity under negative polarization) were prepared and treated exactly in the same way. Figure 6-9a

presents the wide XPS scan for an as-prepared RuNPs/CeO_2 on YSZ sample (lower spectra) and after the catalytic measurements under negative polarization, i.e., when RuNPs/CeO_2 reaches the highest electrochemical enhancement in the catalytic rate (upper spectra).

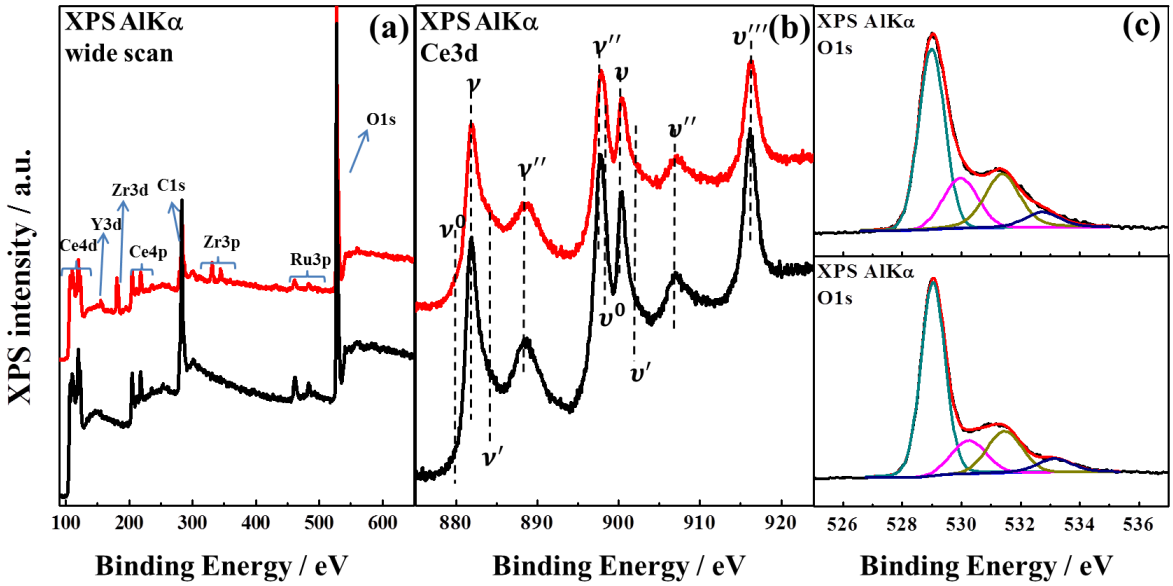

Figure 6-9: Wide scan (a), Ce3d (b) and O1s (c) XPS spectra of the RuNPs/CeO_2 on YSZ sample before (lower spectra) and after electrochemical enhancement of catalytic activity (upper spectra).

In the case of the as-prepared sample only ruthenium, cerium, oxygen and carbon are detected. The absence of signal due to yttrium and zirconium, both in the wide scan but also to the corresponding energy windows, denotes that the RuNPs/CeO_2 overlayer is homogeneous and its thickness is high enough (>10 nm). On the other hand, after the electrochemically enhanced catalytic measurements were performed, Zr and Y are also detected. This means that, after the electrochemically enhanced catalytic measurements, the layer of CeO_2 is ‘‘damaged’’, thus revealing the substrate (YSZ).

At this point, it cannot be excluded that the catalytic measurements caused the RuNPs/CeO_2 to diffuse into the YSZ matrix. In this way, the substrate is revealed leading to the detection of the characteristic XPS peaks of yttrium and zirconium. The Ru3p peak of the as-prepared sample (as shown in Appendix, Figure A-2) and the sample after the catalytic measurements (not shown here) are detected at 462.7 eV ($Ru3p_{3/2}$). The peak is rather wide with a full width at half maximum (FWHM) around 4.3 eV and is attributed to ruthenium atoms in RuO_2[248]. The existence of RuO_2 is further supported by the analysis of the O1s spectra.

In Figure 6-9b, the Ce3d spectra of the as-prepared sample (lower spectra) and after the electrochemically enhanced catalytic measurements (upper spectra) are presented. The intensity of the Ce3d spectra after the electrochemically enhanced catalytic measurement shows a decrease of about 30%. This supports the fact that the thickness and/or the uniformity of the ceria overlayer were affected by the catalytic measurements. The Ce3d XPS spectra is rather complex due to the existence of six different peaks corresponding to Ce^{4+} and four peaks corresponding to Ce^{3+}. The complexity of the Ce3d spectra arises from electron correlation phenomena that cause changes on both the initial state and the final state of the photoemission process. These phenomena involve the hybridization of spatially extended valence band O2p orbitals with the Ce4f orbitals.

In the following discussion the nomenclature proposed by Burroughs et al.[249] was chosen. In order of increasing binding energy, the $3d_{5/2}$ components that are attributed to Ce^{4+} are labeled as v, v'' and v''' while the $3d_{3/2}$ components are denoted as u, u'' and u'''. The v'''/u''' high binding energy doublet at around 897.8 and 916.1 eV is attributed to the final state of Ce(IV)$3d^9 4f^0 O2p^6$. The doublet v''/u'' at 888.5 and 906.9 eV is originated from the state of Ce(IV)$3d^9 4f^1 O2p^5$ while the doublet v/u at about 882.2 and 900.9 eV correspond to the state of Ce(IV)$3d^9 4f^2 O2p^4$. On the other hand, the characteristic doublets due to Ce_2O_3 are labeled as v^0 and v' ($3d_{5/2}$ component) and u^0 and u' ($3d_{3/2}$ component). The deconvolution of the O1s XPS peak reveals the existence of four components at 529 (O^I), 530.2 (O^{II}), 531.4 (O^{III}) and 533.1 eV (O^{IV}). The% relative intensity of the O1s components is O^I:O^{II}:O^{III}:O^{IV} = 60.7:14.4:18.2:6.7. The O^I and O^{III} are attributed to oxygen atoms in ceria and in OH groups, respectively. The O^{IV} component is attributed to water molecules on the oxide surface and structure but can be also related to C–O–H or C–O–C groups due to contamination [250]. The O^{II} is characteristic of RuO_2 [251]. Using the XPS intensities of O^{II} and Ru3p3/2, and the corresponding atomic sensitivity factors, the atomic ratio of O^{II}/Ru was calculated to be 2.3 which is close to the theoretical value of 2.

In order to identify any changes that can be attributed to the electrochemically enhanced catalytic measurements the two spectra of Ce3d were normalized relative to the signal of v''', that is the only peak in which the signal is not affected by the presence of Ce^{3+}. The normalized spectra are presented in Figure 6-10.

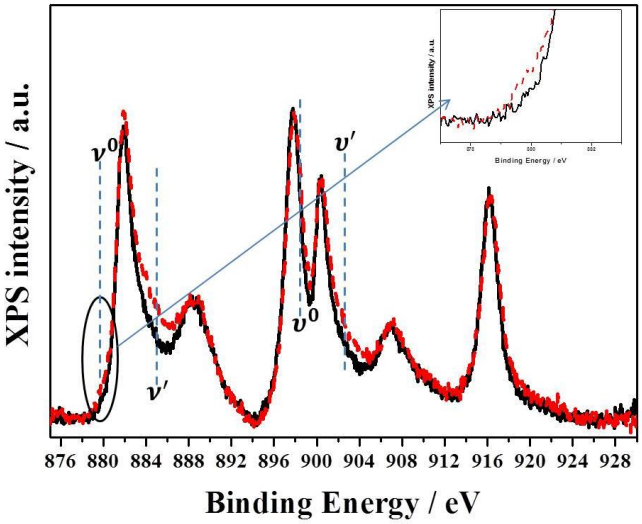

Figure 6-10: Comparison of the Ce3d XPS spectra of the RuNPs/CeO_2 on YSZ sample before (black solid line) and after the catalytic measurements under negative polarization (red dotted line).

As it can be seen, small changes are detected at around 880.5 eV and 885.8 eV, where the Ce^{3+} peaks ($3d_{5/2}$) are detected, accompanied by changes in the energy region where their corresponding $3d_{3/2}$ components are detected around 899 and 903.6 eV, respectively. The appearance of these changes can be attributed to a partial reduction of Ce^{4+} to Ce^{3+} during the catalytic experiments. The changes are rather limited, but this is expected due to the fact that previous studies have shown that the reduction observed for nanoceria is lower compared to micro-ceria [252]. The corresponding O1s spectra of the sample after catalytic measurements (Figure 6-9c, upper spectra) shows the existence of, again, four components at similar BEs compared to the spectra of the sample before. The % relative intensity of the four components is now O^{I}:O^{II}:O^{III}:O^{IV} = 51.5:18.9:23.1:6.5. The observed decrease of the O^{I} is relevant to the decrease of the intensity of the Ce3d. To this point, it should be mentioned that the signal of oxygen might also be influenced due to the exposure of the samples to the atmosphere and the introduction in the ultra-high vacuum chamber during the XPS measurements. Additionally, after the electrochemically enhanced catalytic measurements, the reveal of the YSZ substrate further affects the signal of the O1s peak; thus making it rather difficult, at this point, the attribution of the observed changes to the decrease of the O(I) peak or an increase in the other peaks.

The XPS results of the as-prepared sample and after electrochemical enhancement of catalytic activity show that a small increase of the signal to the energy regions that the Ce^{3+}

peaks are detected. These changes support the results of the catalytic measurements in which a partial reduction of Ce^{4+} to Ce^{3+} occurs.

6.4 Conclusions

In the present work, electrochemically enhanced metal-support interaction (MSI) between highly dispersed Ru nanoparticles and CeO_2 support was demonstrated for the complete oxidation of ethylene. Ru nanoparticles were supported on CeO_2, a MIEC (1 wt% Ru/CeO_2) and interfaced with YSZ, an O^{2-} conductor. Both negative and positive polarization (±2 μA and -5 μA) showed a pronounced effect on the catalytic rate of the RuNPs/CeO_2 catalysts. The catalytic enhancement was attributed to the partial electroreduction of CeO_2. This reduction of ceria, after negative polarization, was confirmed through XPS analysis by comparing of an as-prepared sample with an electrochemically promoted RuNPs/CeO_2, i.e., after passing negative current for 6 h and when the closed-circuit reaction rate was at the highest state. Partially reduced CeO_{2-x} and Ru nanoparticles are proposed to form a stronger metal-support interaction which could result in the observed higher catalytic activity. The reduction process of ceria is a limiting step in the enhancement of the catalytic activity of ethylene oxidation over the RuNPs/CeO_2/YSZ system. As the reaction temperature increases from 350 to 400°C, the open circuit catalytic rate increases from ~9 x 10^{-10} mol $C_2H_4 \cdot s^{-1}$ to ~17 x 10^{-10} mol $C_2H_4 \cdot s^{-1}$, while the change in catalytic rate ($r - r_0$), as a result of passing current at p_{C2H4} = 0.012 kPa, decreases with increasing temperature, leading to a decrease in the rate enhancement ratio, ρ, from 2.0 to 1.1 at 350 and 400°C, respectively. Once electrochemically promoted, a ‘‘permanent’’ or ‘‘persistent’’ catalytic rate enhancement was observed. The catalytic rate returned to its initial unpromoted state either under anodic polarization for up to 6 h or after the open-circuit catalyst operation for up to 144 h due to slow CeO_{2-x} oxidation. Overall, this study shows the feasibility of applying the concept of electrochemical promotion to highly-dispersed heterogeneous catalysts and feasibility of in-situ modification of MSI effect.

Chapter 7: Quantifying Metal Support Interaction in Ceria-supported Pt, PtSn and Ru Nanoparticles using Electrochemical Technique

Dole, H.A.E., Costa, A.C.G.S.A., Couillard, M., Baranova, E.A. Journal of Catalysis, ***333,*** *40-50 (2016).*

Electrochemical promotion and metal–support interaction (MSI) have long been viewed as two separate phenomena; however, more recently it has been shown that, functionally, for ionic and mixed ionic–electronic conducting materials, both are linked by the transfer of ionic species at the interfaces. The purpose of this study was to exhibit a relationship between these two concepts through the use of an electrochemical technique to evaluate CeO_2-supported Pt- and Ru-based nanoparticles. The presence of ceria was found to increase the reaction rate when compared to free-standing Pt and Ru nanoparticles with the metal–support interaction rate enhancement ratios, ρ_{MSI}, up to 14. Polarization measurements established that higher exchange current density, i_0, values correspond to lower open circuit catalytic rates. An apparent self-induced Faradaic efficiency was proposed and determined for each catalyst; lowest value ($|\Lambda_{MSI}| \approx 20$) was found for free-standing nanoparticles, while highest value ($|\Lambda_{MSI}| = 1053$) corresponded to 1 wt% Pt-1/CeO_2.

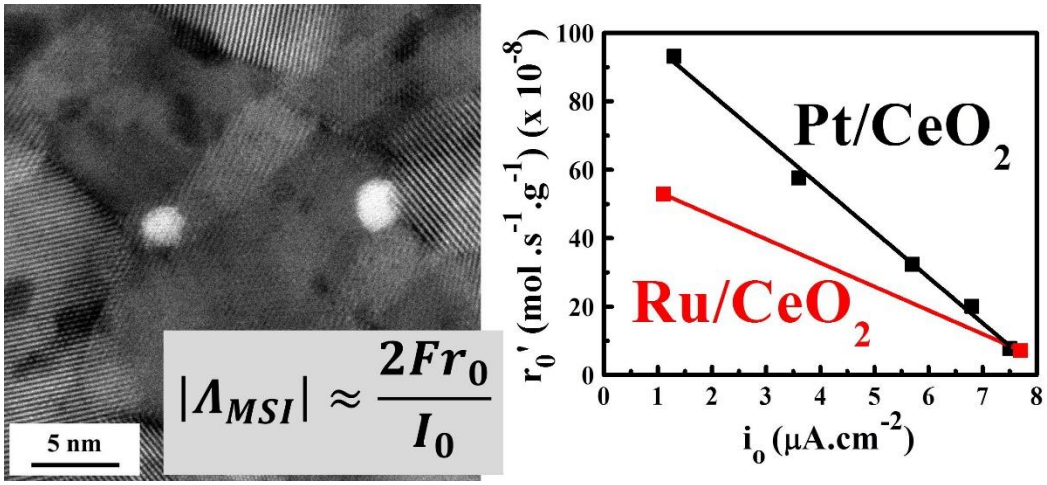

7.1 Introduction

For many years, the concepts of electrochemical promotion of catalysis (EPOC) and metal–support interaction (MSI) were deemed as two separate phenomena. However, in the last two decades, it has been shown that they are very closely related, through the phenomenon of backspillover-spillover of promoting species, for ionic (doped zirconia and ceria) and mixed ionic–electronic conducting (MIEC) supports (CeO_2, TiO_2, etc.) [14,32,109,223]. The difference between the two phenomena has been shown to be only operational. It has been

said that EPOC is electrochemically controlled MSI; likewise, MSI is considered as self-induced EPOC [14]. EPOC does have, however, an operational advantage of in situ control of the promoting species through the application of an electrical stimulus between a catalyst-working electrode and an inert counter electrode. On the other hand, the extent of the MSI effect mostly depends on the difference in work function of the two materials. It should be noted that, in both cases, two competing reactions are occurring – electrocatalytic (i.e., reacting with O^{2-} from the support) and catalytic (i.e., reacting with adsorbed O^{2-}) oxidation. The extent to which these reactions take place depends on several factors, including temperature, type of material, particle size and dispersion, ionic conductivity, and gas phase composition [16,106,116].

In order to evaluate the EPOC phenomenon, two parameters can be determined, rate enhancement ratio, ρ and an apparent Faradaic efficiency, Λ. Equation 7-1 shows Λ for O^{2-} conducting systems under closed circuit, applying a potential across the electrochemical cell [14],

$$\Lambda = (r - r_0)/(I/2F) \qquad \textbf{7-1}$$

where r is the closed circuit catalytic rate ($mol \cdot s^{-1}$), r_0 is the open circuit catalytic rate ($mol \cdot s^{-1}$), I is the current (A), and F is Faraday's constant (96 485 $C \cdot mol^{-1}$). A reaction is said to exhibit the EPOC effect when $|\Lambda| > 1$ (i.e., a non-Faradaic enhancement) [14]. Likewise, as proposed previously [14,20], the apparent Faradaic efficiency can also usually be estimated for any catalytic reaction using equation 7-2,

$$|\Lambda| \approx 2Fr_0/I_0 \qquad \textbf{7-2}$$

where I_0 is the exchange current (A); defined as the current in the absence of an electrical stimulus or a measure of the electrocatalytic activity at the three phase boundary (tpb). I_0 is known to predict the expected magnitude of Λ in EPOC studies. It is said that lower I_0 values, i.e., interface is more polarizable, are required in order to obtain high values of Λ, i.e., a strong EPOC effect [175].

Furthermore, the rate enhancement ratio (ρ) in conventional EPOC studies [14] is defined as,

$$\rho = r/r_0 \quad \textbf{7-3}$$

where r is the closed circuit catalytic rate ($mol \cdot s^{-1}$) and r_0 is the open circuit catalytic rate ($mol \cdot s^{-1}$). Similarly, in pioneering work by Nicole et al. [223], where the influence of adding TiO_2 to a IrO_2 catalyst was observed, the following relationship (Eq. 7-4) was defined as a promotional (metal-support interaction) rate enhancement ratio (ρ_{MSI}),

$$\rho_{MSI} = r/r_u \quad \textbf{7-4}$$

where r is the catalytic rate of the promoted catalyst ($mol \cdot s^{-1}$) and r_u is the catalytic rate of the unpromoted catalyst ($mol \cdot s^{-1}$).

Typically, EPOC experiments are carried out using a continuous film catalyst [141,225]; however, more recently, implementing nanocatalysts through the use of MIEC materials [180,229] has made it possible to reduce the amount of metal catalyst required, while maintaining the electrical conductivity of the electrode needed to complete the electrochemical cell. CeO_2 is one MIEC material that has been used for this purpose as it conducts O^{2-} ions due to oxygen vacancies in the crystallographic structure as well as conducts electrons at elevated temperatures. Additionally, due to its non-stoichiometry, CeO_2 has the ability to undergo conversion between Ce^{4+} and Ce^{3+} quite easily [109,227]. In heterogeneous catalysis, this reducibility and presence of oxygen vacancies are the reasons ceria is considered an "active support", as it has been shown to greatly influence the rate of various oxidation reactions, in comparison to "inert" non-reducible supports such as gamma alumina [253,254]. These properties play a significant role in the interaction with the supported metal nanoparticles. Specifically, this MSI effect has been shown previously for YSZ- and CeO_2-supported Pt systems for oxidation reactions [102,106,234]. It is said that the $O^{\delta-}$ ions from the support backspillover onto the catalyst, due to a difference in work function between the metal and support, forming what is called an effective double layer, resulting in enhanced catalytic activity. This enhancement is attributed to the $O^{\delta-}$ ions acting

as sacrificial promoters on the catalyst surface, which has been termed self-induced electrochemical promotion [109,115].

Recently, a study of Pt nanoparticles supported on YSZ, ZrO_2 and SiO_2 demonstrated, through the use of isotopic oxygen, a further understanding of the role of O^{2-} species present in the catalyst support [106]. It was shown that predominately the lattice oxygen species reacted with the propane for the Pt/YSZ catalyst, while the gas phase oxygen reacted predominately with propane for Pt/ZrO_2 and Pt/SiO_2. Therefore, in the presence of O^{2-}-conducting supports, the absorption of gas-phase oxygen is strongly inhibited by the backspillover of the promoting species. The participation of these O^{2-} species in reacting with the oxidizable reactants (e.g., C_3H_6 or C_2H_4) is referred to as the "sacrificial promoter" type mechanism [109,225].

In the present work, very small (average sizes: 1 – 4 nm), ceria-supported Pt- and Ru-based nanoparticle (typical state-of-the-art heterogeneous catalysts) for the complete oxidation of ethylene were studied using a combined electrochemical and catalytic approach. To this end, the free-standing (colloidal) Pt and Ru, and ceria-supported Pt/CeO_2, $Pt_{50}Sn_{50}/CeO_2$, and Ru/CeO_2 catalysts were incorporated in a solid-electrolyte (i.e., YSZ) electrochemical cell. First, the open circuit catalytic activity with varying partial pressure of reactants and temperature was evaluated, then electrochemical characterization of free-standing and CeO_2-supported Pt, PtSn and Ru nanoparticles was carried out using steady-state polarization measurements. The effect of temperature and particle size, as well as the role of ceria as a support and addition of tin to Pt ($Pt_{50}Sn_{50}/CeO_2$), on the electrochemical response was studied. The electrochemical data (i.e., the exchange current density) was correlated with the catalytic rate of ethylene oxidation for each catalyst.

7.2 Materials and Methods

7.2.1 Synthesis of Free-standing Nanoparticles

Platinum, ruthenium, and platinum-tin nanoparticles (Pt-1, Pt-2, Ru, $Pt_{50}Sn_{50}$) were first synthesized using a polyol reduction method [68]. To synthesize the Pt-1 and Pt-2 only colloids, 0.12 g $PtCl_4$ (Alfa Aesar, 99.99% metals basis) precursor salt was dissolved in 25 mL and 95 mL, respectively, of ethylene glycol (anhydrous 99.8% Sigma Aldrich); then a

volume of NaOH (EM Science, ACS grade) dissolved in ethylene glycol was added for a total concentration of 0.06 M or 0.2 M (indicated as Pt-1 and Pt-2, respectively), depending on the desired crystallite size (3.8 and 1.6 nm, respectively, as determine from XRD [255]). Likewise, the colloid of Ru nanoparticles (indicated as Ru) was synthesized in 50 mL of ethylene glycol, starting by adding 0.15 g $RuCl_3$ (Alfa Aesar, 99.99% metals basis) with a concentration of 0.08 M of NaOH. The $Pt_{50}Sn_{50}$-1 colloid was synthesized by dissolving both $PtCl_4$ and $SnCl_2$ (Acros Organics, 98% anhydrous) salts (50:50, Pt:Sn molar ratio) in ethylene glycol with a concentration of 0.08 M of NaOH (indicated as $Pt_{50}Sn_{50}$). The salt solutions were stirred for 30 minutes at room temperature and subsequently refluxed for 3 hours at 160°C. The initial solution pH was 10 and after reflux, it dropped to pH 7-8.

7.2.2 Deposition of Nanoparticles on CeO_2 Support

For the supported catalysts (Pt-1/CeO_2, Pt-2/CeO_2, Ru/CeO_2, and $Pt_{50}Sn_{50}$/CeO_2), the synthesized colloidal solution was deposited on CeO_2 (Alfa Aesar, specific surface area ~30-40 $m^2 \cdot g^{-1}$) at room temperature by mixing CeO_2, deionized water and an appropriate volume of the colloid for a desired metal loading of 1 wt% or 5 wt% . The solution was stirred for 48 h at room temperature; then the supported nanoparticles were extensively washed three times with deionized water (18 MΩ·cm) and separated by centrifugation. Finally, the supported nanoparticles were dried in air using a freeze dryer for 3-4 h. The catalysts studied in this work are summarized in Table 7-1.

Table 7-1: Summary of electrochemical characterization of nano-catalysts.

Catalyst	Average Particle Size (from STEM) (nm)	Nominal Metal Loading (%)	Exchange Current Density, i_o ($\mu A/cm^2$) at 350°C	Self-induced Faradaic Efficiency, Λ_{MSI}
Pt-1 (colloid)	3.8*	N/A	7.5	20
1 wt% Pt-1/CeO_2	3.0	1	1.3	1053
5 wt% Pt-1/CeO_2	3.0	5	6.8	57
5 wt% Pt-2/CeO_2	1.4	5	5.7	110
1 wt% $Pt_{50}Sn_{50}$/CeO_2	1.9	1	3.6	327
Ru (colloid)	1.1	N/A	7.7	18
1 wt% Ru/CeO_2	1.1	1	1.1	927

*crystallite size from XRD

7.2.3 Preparation of Electrochemical Cells

To prepare the electrochemical cells, the colloids (Pt-1 or Ru), supported powders (1 wt% Pt-1/CeO_2, 5 wt% Pt-1/CeO_2, 5 wt% Pt-2/CeO_2, 1 wt% Ru/CeO_2, and 1 wt% $Pt_{50}Sn_{50}$/CeO_2) or CeO_2 alone, were deposited on one side of a masked YSZ disk as the working electrode along with inert gold counter and reference electrodes on the opposite side. YSZ powder (TOSOH, specific surface area ~13 $m^2 \cdot g^{-1}$, average size of 0.3 μm) containing 8 mol% yttria was used to form solid electrolyte disks (18 mm diameter and 1 mm thickness) by a known procedure[228]. The counter and reference electrodes were deposited by applying gold paste (C2090428D4, Gwent Group, CAS: 98-55-5) followed by annealing at 500°C for 1 h.

The colloid was deposited directly onto the YSZ disk at the desired loading (0.10 mg metal$\cdot cm^{-2}$); however, in order to deposit the supported powders as the catalyst-working electrode, a solution of catalyst powder and ethanol was first prepared. Approximately 0.2 g of powder was dispersed in 2 mL of ethanol via sonication. The slurry was then deposited until the desired loading was obtained (0.10 mg metal$\cdot cm^{-2}$). It should be noted that the same metal loading on the electrode resulted in different thickness of the catalyst layer and amount of ceria, i.e., 9.9 mg $CeO_2 \cdot cm^{-2}$ or 1.9 mg $CeO_2 \cdot cm^{-2}$ for the 1 wt% and 5 wt% metal loading catalysts, respectively. After deposition, the catalyst layer was dried at 60°C for 30 min between depositions. Finally, the catalyst was calcined in a mixture of O_2 (3 kPa) and He (balance) at 350°C for 1 h.

7.2.4 Catalyst Characterization

X-ray diffraction (XRD) measurements of colloidal Pt nanoparticles (Pt-1, Pt-2) were carried out on a Rigaku Ultima-IV diffractometer using a Cu Kα X-ray source, 40 kV, 44 mA in order to determine the crystallite size of Pt-based nanoparticles. The crystallite size analysis of the Pt nanoparticles was based on the full-width at half maximum (FWHM) and full-width at ¾ maximum (FW¾M) of the Pt(111) peak and determined using the Debye formula for scattering by randomly oriented molecules. Further details of the procedure carried out and the resulting diffraction patterns can be found in a previous study [255]. A similar procedure was carried out for the $Pt_{50}Sn_{50}$ colloid where the Pt(111) peak was analyzed.

Further characterization of the colloidal and supported particles was performed using scanning transmission electron microscopy (STEM) and transmission electron microscopy

(TEM) to determine the size distribution and uniformity of the deposited particles. TEM micrographs of colloidal Pt nanoparticles (Pt-1 (colloid)) were obtained using JEOL JEM 2100F FETEM operating at 200 kV. Additional details of this characterization can be found in a previous study [255]. The STEM analysis was done for the Ru colloid and supported Pt and Ru particles using a FEI Titan3 80-300 microscope operated at 300 kV. Details of this procedure are discussed previously [229].

Two-wire in-plane resistance measurements of the catalyst-electrodes (as deposited on the YSZ electrolyte) for the free-standing Pt-1 and the supported 1 wt% Pt-1/CeO_2, 5 wt% Pt-1/CeO_2, and $Pt_{50}Sn_{50}/CeO_2$ were carried out under an O_2 (3 kPa) and He (balance) environment, allowing the catalyst to stabilize for 30 mins. A multimeter (Agilent model U1272A) was used to measure the resistance across two contacts attached on either side of the catalyst-electrode (6 mm apart). The measurements were taken at 350, 400, and 450°C. From these measurements, electrical resistances for Pt-1 colloid were determined to be 1.5 MΩ·cm, 0.6 MΩ·cm, and 0.1 MΩ·cm, respectively; 1 wt% Pt-1/CeO_2 to be 3.3 MΩ·cm, 0.9 MΩ·cm, and 0.2 MΩ·cm, respectively; 5 wt% Pt-1/CeO_2 to be 5.3 MΩ·cm, 1.5 MΩ·cm, and 0.2 MΩ·cm, respectively; and 1 wt% $Pt_{50}Sn_{50}/CeO_2$ to be 1.7 MΩ·cm, 0.5 MΩ·cm, and 0.1 MΩ·cm. Similar measurements were performed for the 1 wt% Ru/CeO_2 catalyst in a previous study[229] showing comparable resistances to the 1 wt% and 5 wt% Pt-1/CeO_2 catalysts. Relatively, the thickness of the catalyst layer (i.e., the difference between 1 wt% and 5 wt%) and presence of CeO_2 does not seem to be significant in this case. Therefore, the effect of the catalyst layer thickness on the polarization curve measurements is considered insignificant.

7.2.5 Catalytic and Electrocatalytic Measurements

Catalytic and electrochemical studies were carried out at atmospheric pressure in a single-chamber capsule reactor (SCCR), which is described elsewhere [244]. In short, for polarization measurements, the electrochemical cell was placed in contact with gold current collectors (gold mesh) that were mechanically pressed onto the surface of the catalyst-electrode on one side of YSZ, and onto the surface of counter and reference electrodes on the other side of YSZ disk. This current collector arrangement ensured good electrical contact from the top of the supported and free-standing nanoparticles, as well as allowed the gas

flow to pass over the catalyst. The electrochemical cell was enclosed in a tight-fit ceramic (McMaster-Carr, Mycalex) capsule that was held together with two metal clamps (Omega Engineering, Nichrome wire, Ni80/Cr20). Both the ceramic capsule and metal clamps were mechanically stable and chemically inert in the temperature range of interest. Once assembled, the capsule sits on top of a glass inner tube where the Au current collectors, enclosed in YSZ tubes (to ensure no electrical contact between the wires), are fed to the base of the reactor [244]. A potentiostat/galvanostat (Arbin Instruments, MSTAT) was used to polarize the cell for a desired duration and constant potential while measuring the current. The reaction gases were C_2H_4 (Linde, 0.5% C_2H_4 in He), O_2 (Linde, 20.9% O_2 in He), and pure He (Linde, 99.997% He) as a carrier gas. The gas composition of C_2H_4, O_2 and He was controlled by mass flow controllers (MKS, 1259C and 1261C Series). The overall flow rate was held constant at 6 $L \cdot h^{-1}$. The product gases were analyzed with an on-line CO_2 gas analyzer (Horiba, VA-3000). All open circuit catalytic studies (except the effect of temperature; 0.012 kPa C_2H_4, 3 kPa O_2, He balance) were carried out at a constant partial pressure of oxygen (3 kPa) and varying partial pressure of ethylene (0.009 – 0.018 kPa) through a forward (i.e., increasing partial pressure of ethylene) and reverse (i.e., decreasing partial pressure of ethylene) scan at 350°C allowing the reaction to stabilize for 1 h between each partial pressure. Electrochemical studies were carried out in a 0.012 kPa C_2H_4 and 3 kPa O_2 mixture and 3 kPa O_2 phase only; no difference in performance was determined (See Appendix, Figure A-1), indicating that O_2 evolution and O_2 reduction are the main reactions of the anodic and cathodic processes, respectively. Polarization curves were obtained through the application of potentials to the working-catalyst electrode vs. pseudo-reference electrode (U_{wr}) ($O^{2-}/½O_2$) from -5 to +5 V, while measuring the current passing through the cell and cell potential (U_{cell}). Using the anodic (positive potential) data, Tafel plots (See Appendix, Figure A-4) were used to determine the exchange current density (i_o).

7.3 Results and Discussion

7.3.1 Catalyst Characterization

XRD measurements were carried out to determine the average crystallite size of the Pt-based colloidal nanoparticles (Pt-1, Pt-2, and $Pt_{50}Sn_{50}$) and whether the bimetallic catalyst showed the presence of alloying. The XRD patterns for the Pt-only nanoparticles have been reported

in a previous study (Pt-1: 3.8 nm; Pt-2: 1.6 nm)[255]. Figure 7-1 shows the diffraction pattern for the $Pt_{50}Sn_{50}$ colloid; showing a full-range scan (Figure 7-1a) and focused on the Pt(111) peak (Figure 7-1b).

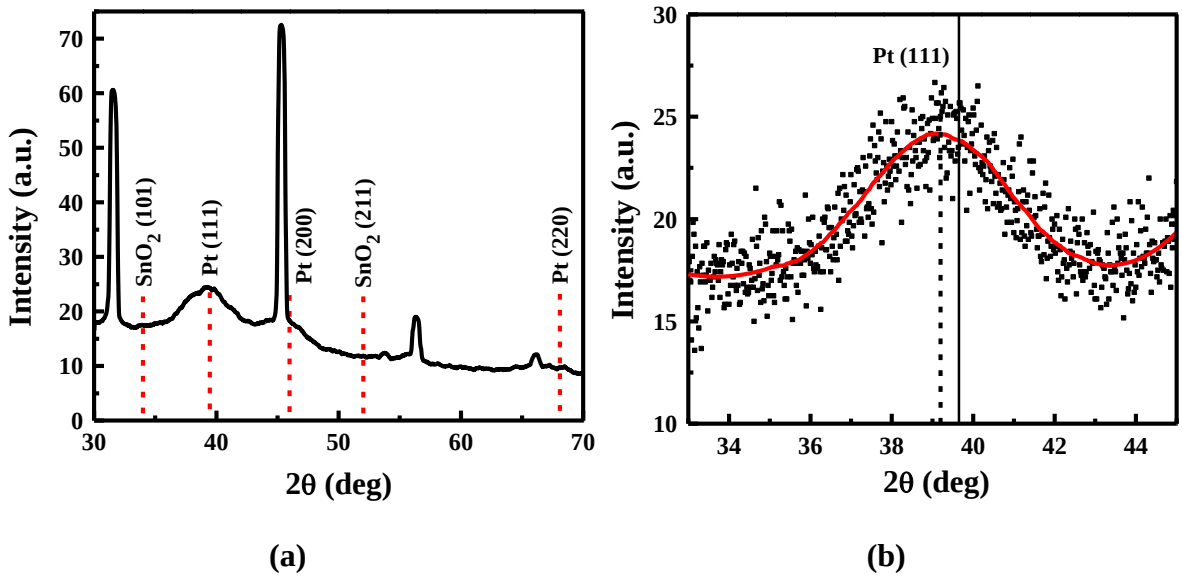

Figure 7-1: XRD pattern of $Pt_{50}Sn_{50}$ colloid (a) full scan; (b) focused to Pt(111) peak.

From the full-range scan, Pt peaks at approximately 40, 46, and 68°2θ were observed that correspond to face-centered-cubic crystal planes (111), (200), and (220), respectively. The sharp peaks around 32, 45, 56 °2θ are due to crystalline NaCl present as a result of the synthesis procedure [70]. There is no or little presence of reflections at 34 and 52°2θ, corresponding to the crystalline-phase of SnO_2, indicating possible alloying between Pt and Sn. Fitting a third order polynomial to the top of the Pt(111) peak, $2\theta_{MAX}$ was determined to be 39.2° (dashed line in Figure 7-1b). As shown previously, a shift in $2\theta_{MAX}$ can be attributed to alloy formation as well as to the small particle size effect [70]. The shift from bulk Pt (39.76°) can account for the particle size effect; however, the shift from pure Pt nanoparticles (solid line in Figure 7-1b) of similar size (39.65°) [70] demonstrates alloying between the Pt and Sn particles. Similar results were found for Pt_7Sn_3 catalysts prepared with NaOH concentrations lower than 0.15 M in a previous study [71].

TEMs carried out for the Pt colloids showed a uniform distribution of the particles, as shown previously [255]. Similarly, STEMs of the supported Ru catalyst (1 wt% Ru/CeO_2) were shown previously [229], resulting in an average particle size of 1.1 nm. Representative

images of the Ru colloidal nanoparticles, as well as the supported Pt-based nanoparticles, are shown in Figure 7-2. Average particle sizes are summarized in Table 7-1.

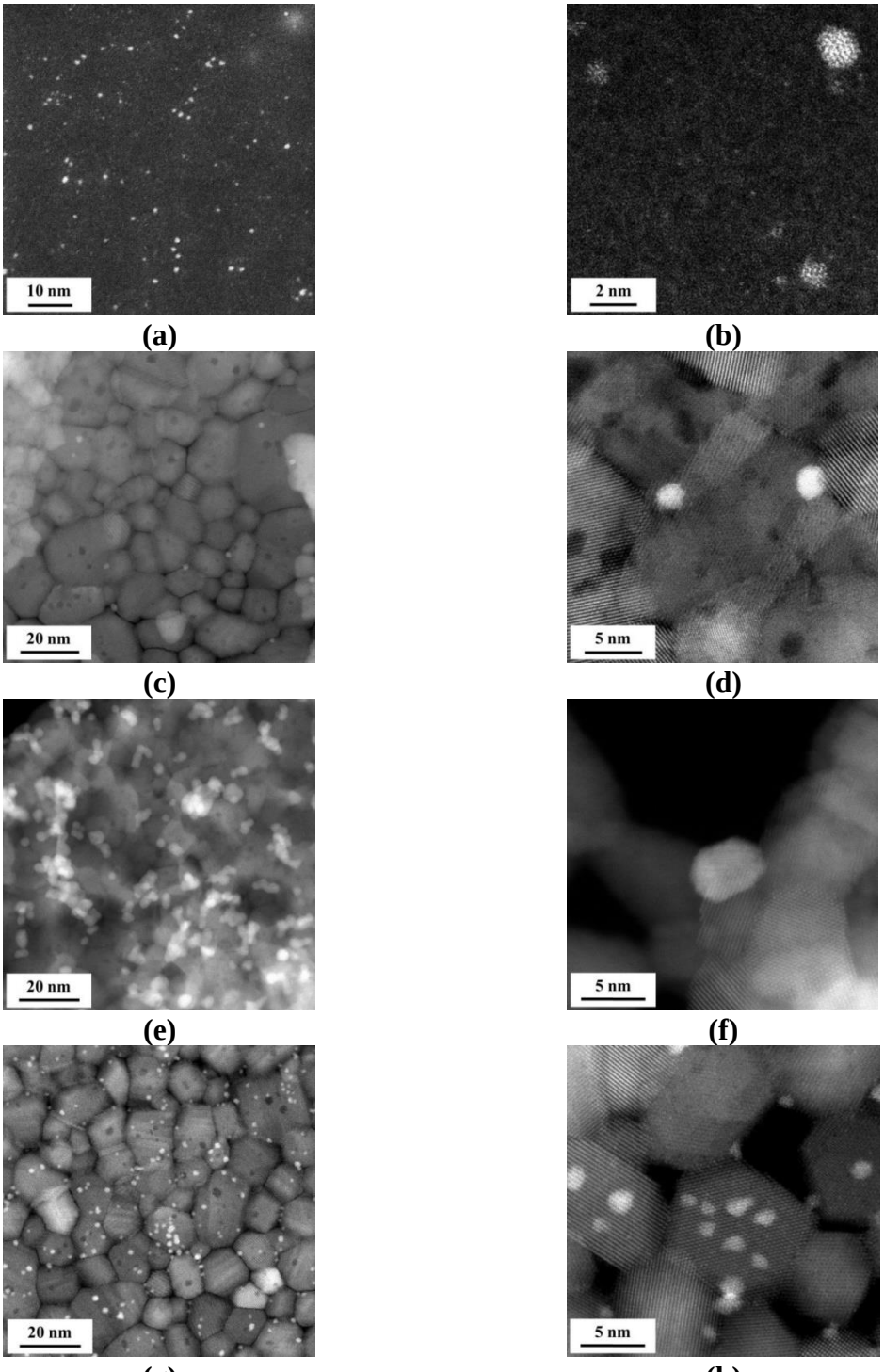

Figure 7-2: STEM images of (a and b) Ru (colloid); (c and d) 1 wt% $Pt_{50}Sn_{50}/CeO_2$; (e and f) 5 wt% Pt-1/CeO_2; (g and h) 5 wt% Pt-2/CeO_2.

7.3.2 Catalytic and Polarization Studies

The complete oxidation of ethylene has been used as a model reaction to study electrochemical promotion for many years [14,15,141]. This model reaction was chosen to carry out the following catalytic and electrochemical studies over the free-standing and supported catalysts. Temperature (50 – 350°C) and partial pressure of ethylene (0.009 – 0.018 kPa C_2H_4) were varied in order to evaluate the open circuit catalytic rate of each catalyst. The electrochemical responses of the electrocatalytic cells in the SCCR were determined through the application of potentials to working-catalyst electrode vs. pseudo-reference electrode (U_{wr}) ($O^{2-}/½O_2$) from -5 to +5 V, while measuring the current passing through the cell and cell potential (U_{cell}). Knowing the catalyst-working electrode has a geometric area of 1 cm^2, the current density was calculated for each cell. Polarization curves showing current density versus U_{wr} were used to evaluate the electrochemical performance of each catalyst (as discussed in further sections). Using the anodic (positive potential) data, Tafel plots (See Appendix, Figure A-4) were plotted to determine the exchange current density (i_o) for each one.

7.3.2.1 Effect of Temperature

To evaluate the effect of temperature on the catalytic activity, a forward and reverse scan at a constant partial pressure of C_2H_4 (0.012 kPa) and oxygen (3 kPa) was carried out. Figure 7-3a shows, as a representation, the forward and reverse catalytic rate of 1 wt% Pt-1/CeO_2 over a temperature range from 50 to 350°C. A comparison of the forward scans for all catalysts is shown in Figure 7-3b.

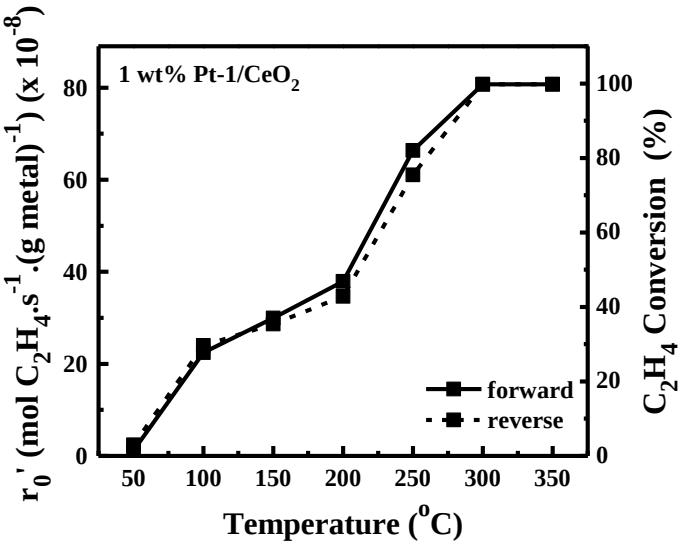

(a)

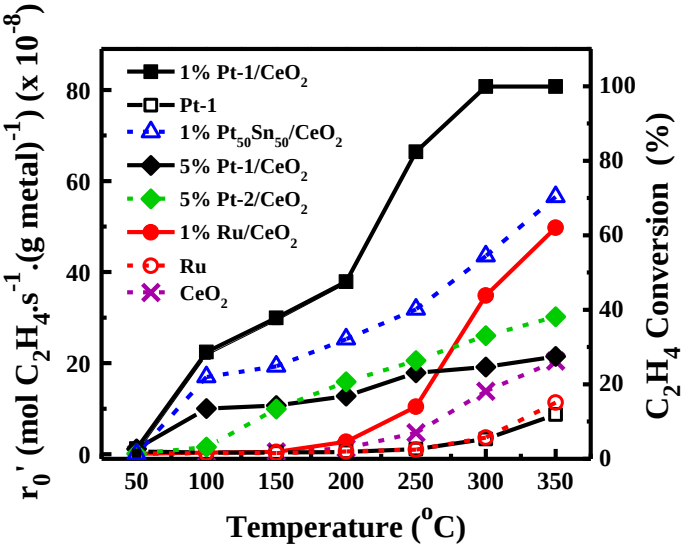

(b)

Figure 7-3: Open circuit catalytic rates (r_0) of (a) 1 wt% Pt-1/CeO_2 (forward and reverse scans); (b) all catalysts (forward scans) from 50-350°C (0.012 kPa C_2H_4, 3 kPa O_2, balance He; total flow: 6 $L \cdot h^{-1}$).

In Figure 7-3a, it is evident that as the temperature is increased, the catalytic rate increases, reaching a maximum rate at 300°C. No significant hysteresis effect was observed between the forward and reverse scans indicating that the nanoparticles are stable on the support in the corresponding temperature range. It should be noted that, even though maximum conversion for Pt-1/CeO_2 was achieved at 300°C, a temperature of 350°C was chosen to carry out the electrochemical studies as it was required for the YSZ electrolyte to be ionically conductive.

From the comparison of all catalysts in Figure 7-3b, it was found that 1 wt% Pt-1/CeO_2 reached the highest catalytic rate, followed by 1 wt% Ru/CeO_2, while the free-standing (Pt-1, Ru) and CeO_2 alone showed low catalytic rates. These results demonstrate the synergistic effect of supporting the metal nanoparticles on a MIEC material such as CeO_2, which was as expected from previous studies [16,102,234,253,254]. Overall, similar catalytic rates were obtained for 1 wt% $Pt_{50}Sn_{50}/CeO_2$, 5 wt% Pt-1/CeO_2 and 5 wt% Pt-2/CeO_2, however the rates deviated as the temperature approached 350°C. This could be attributed to the increase in ion conducting of the support with increasing temperature, allowing the O^{2-} ions to influence the catalytic rate. It is interesting to note that the 1 wt% $Pt_{50}Sn_{50}/CeO_2$ catalyst had less mass of Pt present compared to all other Pt catalysts; however, still demonstrated good performance. The role of the O^{2-} ions as well as the addition of Sn will be further discussed along with the following results obtained from this study.

The electrochemical response of the Pt-1 and 1 wt% Pt-1/CeO_2 cells was determined at three different temperatures: 350, 375 and 400ºC. The results for the 1 wt% Pt-1/CeO_2 catalyst are shown as a representation of the effect (Figure 7-4a). In Figure 7-4a, the current increase in the anodic (positive) region corresponds to oxygen evolution reaction, whereas the negative current growth in the cathodic region is due to oxygen reduction reaction at the three-phase boundary (tpb). It should be noted that for all catalysts, the magnitude of the current density in oxygen only (p_{O_2}= 3 kPa) and in the reaction mixture (p_{O_2} =3 kPa, p_{CH_4} = 0.012 kPa) was identical (See Appendix, Figure A-1) indicating that oxygen evolution/reduction is a dominant reaction, while contribution of ethylene oxidation is negligible. As the temperature is increased, the current density is increased due to the enhancement of the reaction rate of both anodic and cathodic processes at tpb, in addition to the increased ion conductivity of YSZ.

From the exchange current densities (i_0) obtained from the polarization curves at different temperatures, Arrhenius plots, using the following general relationship (Eq. 7-5), were constructed for Pt-1 (colloid) and 1 wt% Pt-1/CeO_2 (Figure 7-4b).

$$\ln\left(i_0(\mu A \cdot cm^{-2})\right) = -E_a/R \cdot 1/T + \ln A \qquad \textbf{7-5}$$

E_a is the apparent activation energy (J·mol^{-1}), R is the gas constant (8.314 J·mol^{-1}K^{-1}), T is the temperature (K), and A is the pre-exponential factor.

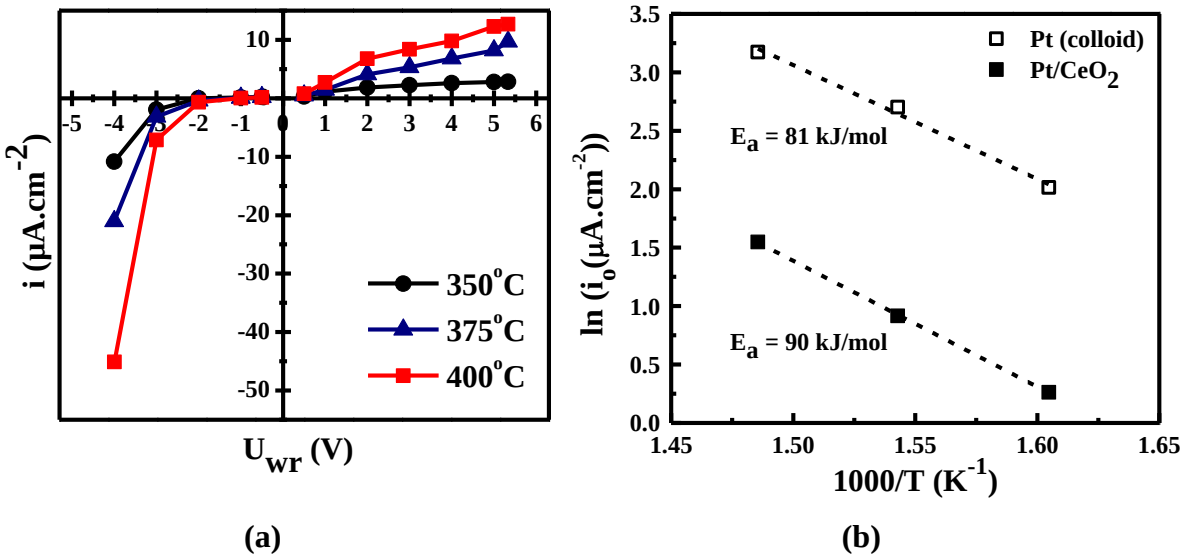

Figure 7-4: Temperature effect shown through (a) steady-state polarization curves for 1 wt% Pt-1/CeO_2; (b) Arrhenius plots of Pt-1 (colloid) and 1 wt% Pt-1/CeO_2 (3 kPa O_2, balance He; total flow: 6 L·h^{-1}).

From Figure 7-4b, the apparent activation energies of Pt-1 and 1 wt% Pt-1/CeO_2 were calculated to be 81 and 90 kJ/mol, respectively. Compared to a previous study for complete oxidation of ethylene over thick Pt films (159-188 kJ/mol[20]), the values obtained in this study are approximately half. This may be due to the difference in catalyst structure (i.e., thick continuous metal film compared to highly-dispersed metal nanoparticles). The smaller, dispersed particles allow for easier transport of O^{2-} species to the tpb sites. Furthermore, in the same previous study [20], similar activation energy values were found for all Pt catalysts tested even though the exchange current densities were different; as was the case in the present study.

7.3.2.2 Pt and Ru Nanocatalysts: Role of CeO_2 and Addition of Tin

Due to its oxygen vacancies and ability to easily convert between Ce^{4+} and Ce^{3+}, ceria has been shown to influence the catalytic activity of several metal nanoparticle catalysts [234,253,256–258]. Therefore, to determine the role of CeO_2 on the catalytic activity of the Pt and Ru nanoparticles, the catalytic rates of supported and free-standing Pt and Ru, as well as different metal loadings of Pt were compared (Figure 7-5a and b). Moreover, it has also been shown that the presence of a second metal can change the catalytic properties of a

catalyst due to the alloy formation and the synergetic effect between two metals[259]; therefore, the effect of adding Sn to Pt to form a bimetallic catalyst (1 wt% $Pt_{50}Sn_{50}/CeO_2$) was studied (Figure 7-5b). In addition, the electrochemical response of all catalysts was evaluated by means of steady-state polarization curves (Figure 7-5c and d).

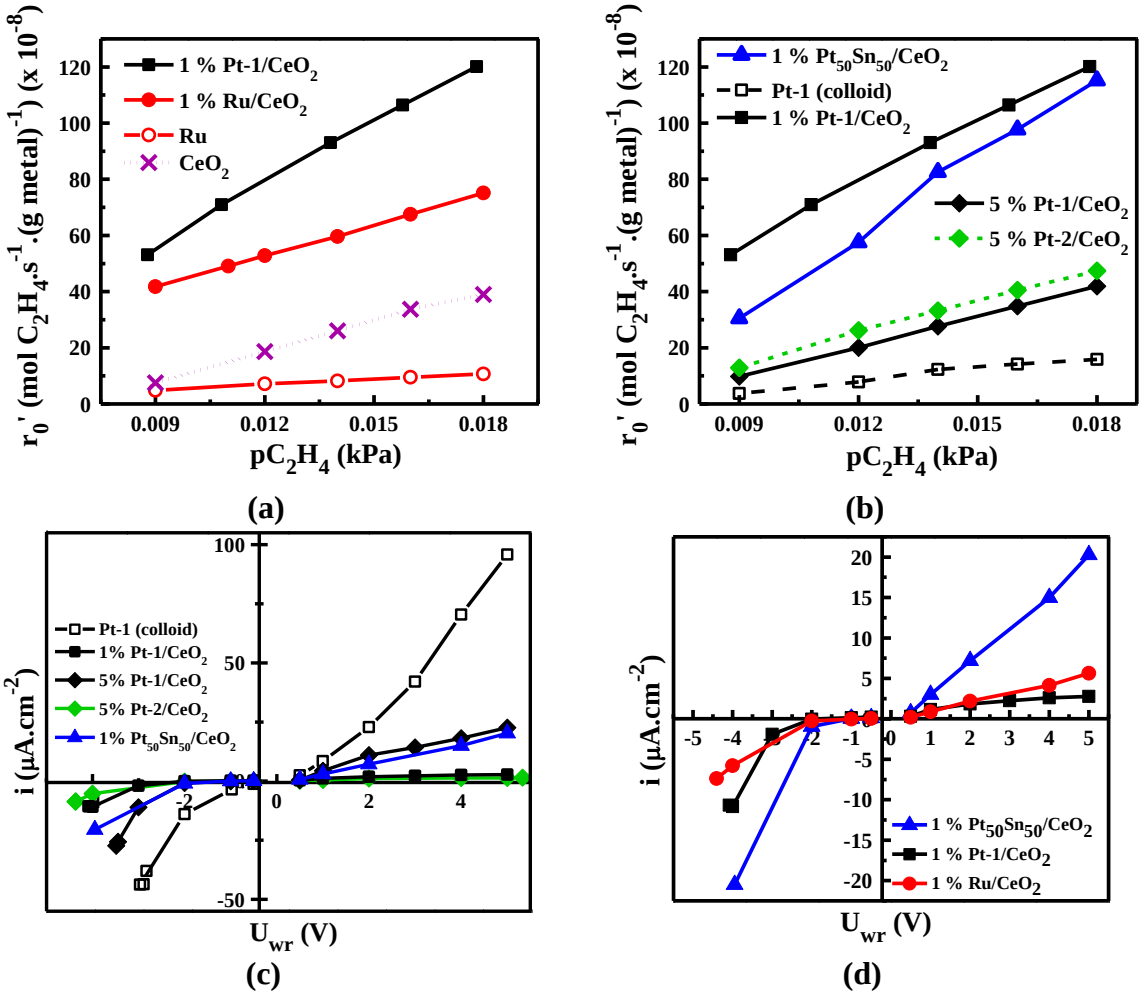

Figure 7-5: Comparison of free-standing and supported catalysts through open circuit catalytic rates (r_0) (forward scans) of (a) Ru- and Pt-based catalysts comparison between the free-standing and ceria-supported catalyst, (b) Pt-based catalysts; and steady-state polarization curves of (c) Pt-based catalysts; (d) 1 wt% $Pt_{50}Sn_{50}$, Pt-1, and Ru supported on CeO_2 at 350°C (3 kPa O_2, balance He; total flow: 6 $L \cdot h^{-1}$).

As shown in Figure 7-5a and b, the catalytic performance of the 1 wt% Pt-1/CeO_2 and 1 wt% Ru/CeO_2 have a much higher catalytic rate compared to the free-standing nanoparticles (Pt-1 and Ru, respectively) and CeO_2 support alone. It is also shown in Figure 7-5b that 1 wt% Pt-1/CeO_2 is more active than 5 wt% Pt-1/CeO_2, indicating that the presence of a higher amount of CeO_2 (thicker catalyst layer on YSZ) enhances the catalytic activity of the supported Pt nanoparticles (1 wt%: 9.9 mg $CeO_2 \cdot cm^{-2}$; 5 wt%: 1.9 mg $CeO_2 \cdot cm^{-2}$).

Therefore, the addition of ceria increases the rate of both Pt and Ru nanoparticles due to an electronic interaction between the metal and the support. The difference in the metal-support work function (electrochemical potential of electrons) between Pt (φ_{Pt}= 5.93 eV) [260], Ru (φ_{Ru}= 4.71 eV) [260] and CeO_2 (φ_{CeO_2}= 4.69eV) [261] would cause a charge transfer ($O^{\delta-}$) from ceria to Pt and Ru nanoparticles. This ion backspillover to Pt and Ru active surface promotes the ethylene oxidation reaction by modifying the adsorption strength of the reactants, similarly to the closed circuit state in the EPOC studies [14]. In addition, in agreement with the previous studies [73,262], the supported Pt nanoparticles have a higher catalytic activity than the Ru/CeO_2 catalyst, because Pt is a superior catalysts for the complete oxidation of ethylene and possibly due to the lower work function difference between Ru and CeO_2.

Figure 7-5b compares the reaction rate of 1 wt% $Pt\text{-}1/CeO_2$ and bimetallic 1 wt% $Pt_{50}Sn_{50}/CeO_2$. It can be seen that the addition of tin decreases the reaction rate; however, the comparison becomes advantageous per mass activities (See Appendix, Figure A-5), which represents an advantage for practical applications. As previously reported, the presence of Sn can be responsible for the partial reduction of ceria [259]. The catalytic rates of 1 wt% $Pt\text{-}1/CeO_2$ is higher than 1 wt% $Pt_{50}Sn_{50}/CeO_2$; however, the $Pt_{50}Sn_{50}/CeO_2$ catalyst shows higher activity than the 5 wt% Pt/CeO_2 catalysts. This enhanced activity could be attributed to the electronic interaction between Pt and Sn in the alloy and/or partial reduction of ceria, as proposed previously [229], resulting in a stronger metal-support interaction between the ceria and the bimetallic catalyst. This partial reduction can be attributed to the slight difference in work function between Sn [260] and CeO_2 [261]: φ_{Sn} = 4.42 eV and φ_{CeO_2}= 4.69 eV. This could explain the resulting similar catalytic activity per mass of Pt of the 1 wt% $Pt_{50}Sn_{50}/CeO_2$ catalyst compared to that of 1 wt% Pt/CeO_2.

Furthermore, as shown in previous studies [116,255], ethylene has been known to be structure sensitive; therefore, particle size has a strong effect on catalytic activity. This is shown by the higher catalytic rate of 5 wt% $Pt\text{-}1/CeO_2$ (1.6 nm) compared to 5 wt% $Pt\text{-}1/CeO_2$ (3.8 nm).

In Figure 7-5c, it was observed that during polarization, a higher electrochemical response was measured for the free-standing (colloid) in comparison to the supported catalysts. Using the Tafel plots, the exchange current densities (i_o) of all catalysts have been determined. Table 7-1 reports values of 1.3, 5.7, 6.8 and 7.5 $\mu A/cm^2$ for 1 wt% Pt-1/CeO_2, 5 wt% Pt-2/CeO_2, 5 wt% Pt-1/CeO_2, and Pt-1 (colloid), respectively; therefore, showing the higher rate for the Pt colloid. It is possible that since there is no CeO_2 present in the catalyst-working electrode for the colloid, there are more available tpb sites, resulting in a higher electrochemical rate; therefore, indicating that the electrocatalytic reaction is more dominant causing lower overall catalytic activity (Figure 7-5a). With a higher exchange current density, the electrocatalytic reaction becomes more dominant than the catalytic reaction. On the other hand, with a low exchange density, the catalytic reaction becomes dominant [160,229]. This difference in exchange current densities for the two different metal loadings is attributed to the increased resistance in the presence of higher total mass of CeO_2 (i.e., in the 1 wt% catalysts) compared to that of the 5 wt% catalysts; resulting in less tpb sites for the O^{2-} species to be available. It should be noted that agglomeration for the 5 wt% Pt-1/CeO_2 catalyst was observed (Figure 7-2e); therefore, resulting in a reduction of tpb sites. Similarly, the 5 wt% Pt-1/CeO_2 showed a higher electrochemical response compared to 5 wt% Pt-2/CeO_2, which could also be attributed to more resistance of CeO_2. Since the particles are smaller for the 5 wt% Pt-1/CeO_2 catalyst, there should be more tpb sites; however, the presence of CeO_2 adds more resistance than that of the 5 wt% Pt-1/CeO_2 catalysts, as the particles are in more intimate contact with the CeO_2.

In general, the electrochemical rate (Figure 7-5c and d) of 1 wt% $Pt_{50}Sn_{50}/CeO_2$ was observed to be higher than the electrochemical rate of 1 wt% Pt-1/CeO_2. The corresponding exchange current densities were determined to be 1.3 $\mu A/cm^2$ for 1 wt% Pt-1/CeO_2 and 3.6 $\mu A/cm^2$ for 1 wt% $Pt_{50}Sn_{50}/CeO_2$ (Table 7-1); thus confirming the slightly higher electrochemical rate of the $Pt_{50}Sn_{50}$-1/CeO_2 catalyst. This difference could be attributed to the fact that the addition of Sn may assist the oxygen evolution reaction at the tpb in a similar way as in aqueous electrocatalytic studies [71].

7.3.3 Relating Catalytic Activity and Electrochemical Behaviour

Knowing the exchange current, the following relationship (Eq. 7-6) (adapted from that proposed previously (Eq. 7-2) in EPOC theory [14]) was used to determine the magnitude of the self-induced Faradaic efficiency (Λ_{MSI}),

$$|\Lambda_{MSI}| \approx 2Fr_0/I_0 \qquad \textbf{7-6}$$

where F is Faraday's constant (96 485 C·mol^{-1}), r_0 is the open circuit catalytic rate (mol·s^{-1}) at a specific temperature, and I_0 is the exchange current (A). These results are summarized in Table 7-1.

From the values obtained, it can be seen that there are three levels of magnitude for the catalysts tested (1 wt% catalysts > 5 wt% catalysts > colloids). It is said that highly polarizable catalysts are required to obtain large Faradaic efficiencies; therefore, 1 wt% Pt-1/CeO_2, 1 wt% $Pt_{50}Sn_{50}/CeO_2$ and 1 wt% Ru/CeO_2 are more polarizable than the other catalysts studied. This could be attributed to the influence of CeO_2 through its oxygen storage capacity. The presence of CeO_2 allows for more readily available O^{2-} species at the tpb to participate in enhancing the catalytic reaction rather than only being consumed in the electrocatalytic reaction.

Based on the catalytic and electrochemical results, a preliminary relationship between the open circuit catalytic rate (normalized for the mass of Pt or Ru) of the Pt- and Ru- based nano-catalyst systems and their corresponding electrochemical responses was determined (Figure 7-6a). Additionally, as defined previously by Vayenas and co-workers[14], the rate enhancement ratio for MSI (ρ_{MSI}) was established for 1 wt% Pt-1/CeO_2, 5 wt% Pt-1/CeO_2, and 1 wt% $Pt_{50}Sn_{50}/CeO_2$ with respect to the Pt-1 (colloid), and 1 wt% Ru-1/CeO_2 with respect to Ru (colloid) (Figure 7-6b) using equation 7-4, where r corresponds to the promoted catalytic rate (i.e., for 1 wt% Pt-1/CeO_2, 5 wt% Pt-1/CeO_2, 1 wt% $Pt_{50}Sn_{50}/CeO_2$, and 1 wt% Ru/CeO_2) and r_u corresponds to the unpromoted catalytic rate (i.e., for Pt-1 (colloid) and Ru-1 (colloid)). It should be noted that the catalytic rates are normalized for the mass of Pt or Ru, respectively.

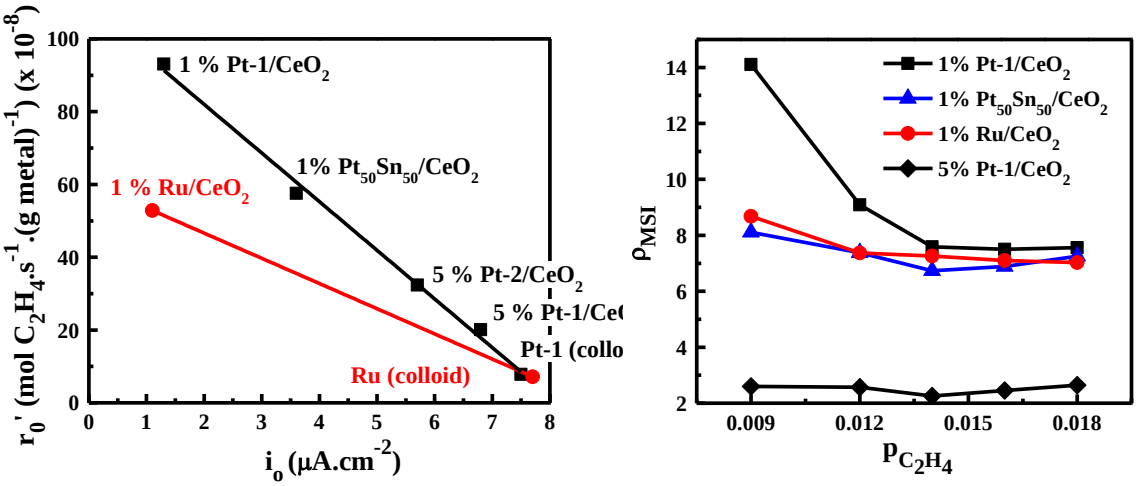

(a) (b)

Figure 7-6: Open circuit (350°C; total flow: 6 L·h^{-1}) (a) relationship between the normalized catalytic rate (r_0) (0.012 kPa C_2H_4, 3 kPa O_2, balance He) and the exchange current density (i_o) of colloidal and supported (1 wt%) catalysts; (b) metal-support interaction rate enhancement ratio (ρ_{MSI}) over range of C_2H_4 partial pressures (3 kPa O_2 and He balance) of supported catalysts.

As can be seen (Figure 7-6a), it was found that the catalytic rate for each metal decreases with increasing exchange current density, due to the competition between the electrocatalytic and catalytic oxidation reactions. A higher exchange current density indicates that the electrocatlytic reaction is more dominant; resulting in the O^{2-} species being consumed in the electrochemical reaction at the tpb without significant backspillover of ion promoters to the gas exposed catalytic active sites. Therefore, the catalytic reaction is not subject to a promotional effect. The obtained relationship is in excellent agreement with the classical EPOC relationship (Eq. 7-2) that was verified for numerous catalytic systems, reactions and solid electrolytes [14].

Previously, it has been shown that certain metal-support combinations can reach a promoted state that is equivalently to that of the electrochemically promoted state [223]. This could be the case for the supported Pt catalysts as a result of the MSI; while the supported Ru catalyst has not reached that point yet. This could explain why it was possible to alter the MSI between the Ru nanoparticles and CeO_2 in a previous study [229].

Figure 7-6b shows that the metal-support interaction rate enhancement ratios for the 1 wt% Pt-1/CeO_2, 5 wt% Pt-1/CeO_2, 1 wt% $Pt_{50}Sn_{50}$/CeO_2, and 1 wt% Ru/CeO_2 catalysts are all greater than 1, indicating the enhancement is a result of the interaction between the metal and support. In general, the rate enhancement ratio is greater, at lower $p_{C_2H_4}$, for 1 wt% Pt-

1/CeO_2 compared to 1 wt% Ru/CeO_2 and $Pt_{50}Sn_{50}$/CeO_2 which is then significantly greater than Ru/CeO_2. This can be attributed to the stronger metal-support interaction of the Pt with CeO_2 in comparison to Ru. Similarly, the enhancement of 1 wt% Pt-1/CeO_2 is much greater than that of 5 wt% Pt-1/CeO_2 which could be a result of a greater mass presence of CeO_2 or higher particle dispersion in the 1 wt% catalyst causing a stronger interaction. Furthermore, ρ_{MSI} appears to be effected by the partial pressure of C_2H_4 for the 1 wt% Pt-1/CeO_2 catalyst, but not significantly for the 5 wt% Pt-1/CeO_2, 1 wt% $Pt_{50}Sn_{50}$/CeO_2, and 1wt% Ru/CeO_2 catalysts. It is said that the adsorption of electropositive species (i.e., C_2H_4) can cause a decrease in the work function. Since the work functions of Ru and CeO_2 are close in value, the adsorption of C_2H_4 may not have a significant effect in changing the work function due to this interaction, resulting in the same enhancement ratio for the partial pressure range observed. However, Pt and CeO_2 have a much greater difference in work function, which could mean that it is vulnerable to a change in work function that C_2H_4 would impose; therefore, altering the extent of enhancement in the catalytic activity. The difference between the 1 wt% Pt-1/CeO_2 and 1 wt% $Pt_{50}Sn_{50}$/CeO_2 catalysts at lower partial pressures could be a result of the influence of Sn. With less C_2H_4 present, the partial reduction of CeO_2, with the influence of Sn, may happen to a lesser extent. This would result in a weaker interaction between the Pt and CeO_2 and a lower rate enhancement ratio.

7.4 Conclusions

A combination of open circuit catalytic and electrochemical measurements was used to evaluate and understand the catalytic performance of highly dispersed Pt- and Ru-based, free-standing and CeO_2-supported catalysts with regards to metal-support interaction and the effect of O^{2-} ions from the support. The presence of CeO_2 was shown to play a significant role in increasing the catalytic activity of Pt and Ru nanoparticles. It was observed that the Pt and Ru colloids had similar catalytic performance (~3 – 16 × 10^{-8} mol C_2H_4·(g metal)$^{-1}$·s^{-1}); however, when supported on CeO_2, the Pt nano-catalyst had higher catalytic activity (53 – 120 × 10^{-8} mol C_2H_4·(g metal)$^{-1}$·s^{-1}) than the supported Ru catalyst (41 – 75 × 10^{-8} mol C_2H_4·(g metal)$^{-1}$·s^{-1}). Furthermore, the addition of Sn was shown to help in a promoting the catalytic activity (per mass of Pt) of the CeO_2-supported Pt catalyst (15 – 58 × 10^{-8} mol C_2H_4·(g Pt)$^{-1}$·s^{-1}) through what is thought to be the partial reduction of ceria. Both of these

observed enhancements in catalytic activity are attributed to a stronger interaction between the metal catalyst and support and are shown through the observed MSI rate enhancement ratios of ~8 – 14 for 1 wt% Pt-1/CeO_2, ~8 for 1 wt% Ru/CeO_2, ~ 8 for 1 wt% $Pt_{50}Sn_{50}$/CeO_2, and ~3 for 5 wt% Pt-1/CeO_2. The parameter of an apparent self-induced Faradaic efficiency was proposed to quantify the MSI effect for the first time. The calculated values showed orders of magnitude difference between the colloids ($|\Lambda_{MSI}| \approx 18 – 20$), 5 wt% catalysts ($|\Lambda_{MSI}| \approx 57 – 110$), and 1 wt% catalysts ($|\Lambda_{MSI}| \approx 327 – 1053$). Finally, a preliminary relationship was established between the catalytic rate and electrochemical response (i.e., exchange current density) for the Pt- and Ru-based catalytic systems; indicating that the lattice O^{2-} species play a key role in the overall catalytic activity of the nano-catalysts supported on active conductive supports. Further research into this intriguing area and studies of other nano-structured catalysts and reactions are required.

Chapter 8: Ethylene oxidation in an oxygen deficient environment: Why ceria is an active support?

Dole, H.A.E., Baranova, E.A. ChemCatChem DOI: 10.1002/cctc.201600142.

Pt/CeO_2, Ru/CeO_2, Ir/CeO_2 and corresponding free-standing nanoparticles (Pt. Ru, and Ir) were evaluated for their performance for the complete oxidation of ethylene in the presence and absence of oxygen. The lattice oxygen and storage capability of CeO_2 was found to have a significant influence on the interaction with the supported metal nanoparticles causing different catalytic behaviours in the absence of oxygen. Overall, Ru/CeO_2 was found to have superior stability in comparison to Ir/CeO_2 and Pt/CeO_2, resulting in transient promotional rate enhancement ratio (ρ_{MSI}) values reaching 200 in the first 25 min. These results were attributed to the oxygen adsorption strength of the metal and the corresponding interaction with CeO_2. A proposed relationship between ρ_{MSI} and the O^{2-} consumed from the support is discussed, which was suggested as a possible tool to estimate the extent of MSI. In general, it was found that an increase in ρ_{MSI} corresponded to an increase in O^{2-} consumed.

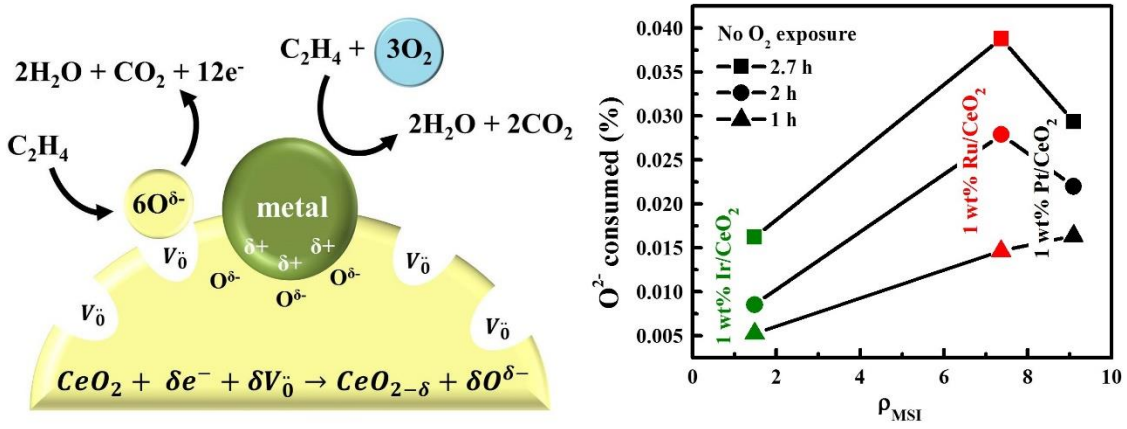

8.1 Introduction

The concept of metal-support interaction (MSI) has been studied by many research groups in order to determine the effect that the support, especially "active" supports, has on the supported metal catalyst for several different reactions [31,32,263,264]. More specifically, Tauster et al. [30,31] deemed the term strong metal-support interaction (SMSI) after it was observed that TiO_2 as a support has a great effect on the catalytic properties of Pt. This was attributed to the presence of the migration of reduced titanium oxide onto the metal surface

[31]. The pioneering work by Nicole et al. [223] also observed an enhanced effect from adding TiO_2 to CeO_2, which led to the introduction of the following relationship (Eq. 8-1), referred to as the promotional (MSI) rate enhancement ratio (ρ_{MSI}),

$$\rho_{MSI} = r/r_u \quad \textbf{8-1}$$

where r is the catalytic rate of the promoted catalyst ($mol \cdot s^{-1}$) and r_u is the catalytic rate of the unpromoted catalyst ($mol \cdot s^{-1}$). This relationship was adapted from the rate enhancement ratio (ρ) that was established for the phenomenon of electrochemical promotion of catalysis (EPOC) [14]; the electrochemically controlled addition or removal of ionic promoters from the support. From the results obtained by Nicole et al. [223] and the development of this relationship (Eq. 8-1), it was concluded that the well-known concepts of EPOC and MSI are functionally equivalent for IrO_2 and Rh catalysts supported on YSZ, TiO_2 and TiO_2-doped supports even if an external electrical circuit is required for the former and spontaneous charge transfer occurs in the latter. A similar conclusion was also obtained in a previous study for Pt/CeO_2, Ru/CeO_2 and $PtSn/CeO_2$ catalysts for the complete oxidation of ethylene [265].

In conventional EPOC studies, an apparent Faradaic efficiency (Λ) is used to evaluate whether the catalytic enhancement is non-Faradaic in the presence of an electrical stimuli (i.e., $|\Lambda| > 1$). It has also been shown that Λ can usually be estimated for any catalytic reaction using equation 2 when the exchange current (I_0) is known, as follows,

$$|\Lambda| \approx 2Fr_0/I_0 \quad \textbf{8-2}$$

where F is Faraday's constant (96 485 $C \cdot mol^{-1}$) and r_0 is the open circuit catalytic rate ($mol \cdot s^{-1}$). In relation to MSI, a self-induced Faradaic efficiency (Λ_{MSI}) was proposed (Eq. 8-3) previously to determine the magnitude of non-Faradaic behaviour caused by self-induced backspillover-spillover of the O^{2-} ions from the catalyst support [265].

$$|\Lambda_{MSI}| \approx 2Fr_0/I_0 \quad \textbf{8-3}$$

More recently, the term electronic metal-support interaction (EMSI) [33–37] has been used to describe the influence of the d-orbital electrons on the interaction between the metal and

support. It has been shown that platinum group metals, when in contact with ceria, disturb the electronic band structure of ceria [34,35]; however, without exchanging any surface chemical species, unlike what is proposed for SMSI. This electronic effect has also been referred to previously as the junction effect theory [33], which relates metals having high work functions with metal oxides with high band gap in terms of the presence of a new equilibrium being established by the re-distribution of electrons between the oxide conduction band and Fermi level of the metal.

The electrons that are re-distributed are said to come from the ionization of the oxygen vacancies [33]. In the case of CeO_2, a material that easily converts between Ce^{3+} and Ce^{4+} and is known for its oxygen storage capability (OSC) [266–269], the interaction with the supported metals is greatly influenced, especially in the case of oxidation reactions [106,269,270]. The involvement of the lattice oxygen from the support in the reaction mechanism has been termed as a Mars van-Krevelen type reaction [270,271].

Furthermore, it has been shown previously that depending on the oxygen mobility in the support, different reaction pathways can occur with the gaseous hydrocarbon (in this case, C_2H_4):

(i) gaseous oxygen reacts with C_2H_4 through catalytic oxidation (Eq. 8-4),

$$C_2H_4 + 3O_2 \rightarrow 2H_2O + 2CO_2 \quad \textbf{8-4}$$

(ii) lattice oxygen (O^{2-}) reacts with C_2H_4 through electrochemical oxidation at the three-phase boundary (tpb), i.e., O^{2-}_{tpb} and/or C_2H_4 reaction with ionic "sacrificial" promoters adsorbed at the catalyst surface, i.e., $O^{2-}_{catalyst}$ (Eq. 8-5),

$$C_2H_4 + 6O^{2-} \rightarrow CO_2 + 2H_2O + 12e^- \quad \textbf{8-5}$$

with the corresponding partial reduction of CeO_2 at the cathode (Eq. 8-6),

$$CeO_2 + \delta e^- + \delta V_{\ddot{0}} \rightarrow CeO_{2-\delta} + \delta O_0^* \quad \textbf{8-6}$$

giving the overall reaction (Eq. 8-7):

$$\delta C_2H_4 + 12CeO_2 + 12\delta V_{\ddot{0}} \rightarrow CeO_{2-\delta} + \delta O_0^* \quad \textbf{8-7}$$

This observation of mobile oxygen from the support material has been confirmed through isotopic oxygen studies for catalytic systems involving conductive supports (i.e., YSZ, CeO_2) in comparison to non-conductive supports (i.e., SiO_2, ZrO_2, Al_2O_3), which do not show lattice oxygen mobility [106,221,266].

An alternate approach for confirming the role of the lattice oxygen has been carried out previously by measuring the catalytic performance in the absence of gaseous oxygen [73,103,271,272]. This implies that only the O^{2-} from the support can react with the hydrocarbon in an electrochemical reaction. It was found that the support with higher ionic conductivity (i.e., samarian-doped ceria (SDC) compared to ceria or YSZ) showed higher catalytic activity in the absence of oxygen for both ethylene and carbon monoxide oxidation [103]. A similar observation was determined for CeO_2 catalysts containing various metal loadings of SnO_2 for the complete oxidation of CO [271]. In the absence of oxygen, the CeO_2-supported SnO_2 catalysts showed higher catalytic activity than CeO_2 alone, which is as expected since SnO_2 is known to partially reduce ceria [259].

The following study investigates the role of lattice oxygen and OSC of CeO_2 and its influence on the interaction with and behaviour of the supported metal nanoparticles. Three different supported metal catalysts as well as their corresponding free-standing metal catalysts – Pt/CeO_2 and Pt, Ru/CeO_2 and Ru, and Ir/CeO_2 and Ir, were evaluated for their catalytic performance for the complete oxidation of ethylene at 350°C. Depending on the experiment performed, the effect on the catalytic rate in the presence or absence of oxygen or ethylene was determined. It should be noted that to the authors' knowledge, this is the first time Ir/CeO_2 and Ir catalysts have been used for the complete oxidation of ethylene. Previous studies have only shown its catalytic performance for steam reforming of ethanol [267,273–275].

8.2 Materials and Methods

8.2.1 Synthesis of Pt, Ru and Ir Nanoparticles

Platinum, ruthenium, and iridium nanoparticles were first synthesized using the polyol reduction method [68]. To synthesize the Pt colloid, 0.12 g $PtCl_4$ (Alfa Aesar, 99.99% metals basis) precursor salt was dissolved in 25 mL of ethylene glycol (anhydrous 99.8% Sigma

Aldrich); then a volume of NaOH (EM Science, ACS grade) dissolved in ethylene glycol was added for a total concentration of 0.06 M. Likewise, the colloids of Ru and Ir nanoparticles were synthesized in 50 mL of ethylene glycol, starting by adding 0.15 g $RuCl_3$ (Alfa Aesar, 99.99% metals basis) and 0.10 g of $H_2IrCl_6 \cdot xH_2O$ (Aldrich, 99.98% metals basis), respectively, with a NaOH concentration of 0.08 M. The salt solutions were stirred for 30 minutes at room temperature and subsequently refluxed for 2-3 hours at 160°C. The initial solution pH was 10 and after reflux, it dropped to 8.

8.2.2 Deposition of Nanoparticles on CeO_2 Support

For the supported catalysts (Pt/CeO_2, Ru/CeO_2, and Ir/CeO_2), the synthesized colloidal solution was deposited on CeO_2 (Alfa Aesar, specific surface area ~30-40 $m^2 \cdot g^{-1}$) at room temperature by mixing CeO_2, deionized water and an appropriate volume of the colloid for a desired metal loading of 1 wt%. The solution was stirred for 48 hours at room temperature; then the supported nanoparticles were extensively washed three times with deionized water (18 MΩ·cm) and separated by centrifugation. Finally, the supported nanoparticles were dried in air using a freeze dryer for 3-4 hours.

8.2.3 Deposition of Catalyst on YSZ disk

To prepare the catalyst for evaluation, the colloids (Pt, Ru, Ir) or supported powders (1 wt% Pt/CeO_2, 1 wt% Ru/CeO_2, and 1 wt% Ir/CeO_2), was deposited on a YSZ disk (Figure 8-1) having a geometric surface area of 1 cm^2. YSZ powder (TOSOH, specific surface area ~13 $m^2 \cdot g^{-1}$, average size of 0.3 μm) containing 8 mol% yttria was used to form electrolyte disks (18 mm diameter and 1 mm thickness) by a known procedure [228]. The colloid was deposited directly onto the YSZ disk at the desired loading; however, in order to deposit the supported powders, a solution of catalyst powder and ethanol was first prepared. Approximately 0.2 g of powder was dispersed in 2 mL of ethanol via sonication. The solution was then deposited until the desired loading was obtained (0.10 mg metal·cm^{-2} corresponding to 9.9 mg $CeO_2 \cdot cm^{-2}$), drying at 60°C for 30 minutes between depositions. Finally, the catalyst was calcined in a mixture of O_2 (3 kPa) and He (balance) at 350°C for 1 hour.

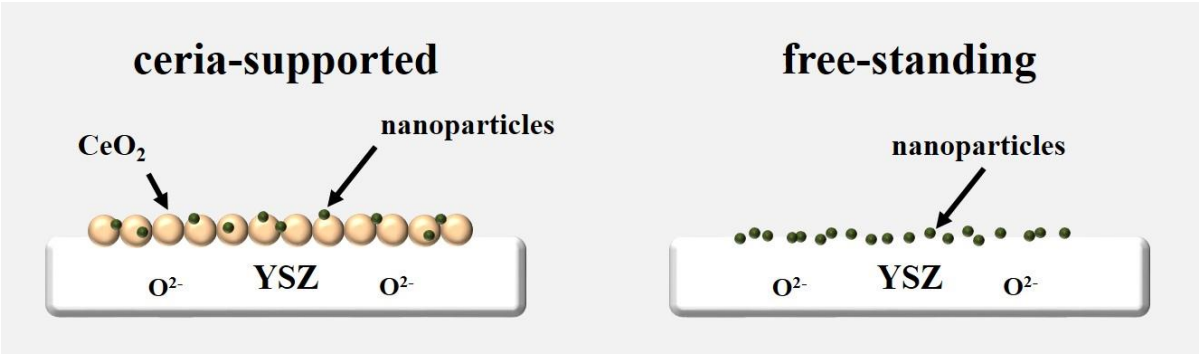

Figure 8-1: Schematic of catalytic evaluation cell.

8.2.4 Catalyst Characterization

Characterization of the free-standing and supported particles was performed using both annular dark-field scanning transmission electron microscopy (ADF-STEM) and transmission electron microscopy (TEM) to determine the size distribution and uniformity of the deposited particles. TEM micrographs of the free-standing Pt nanoparticles were obtained using JEOL JEM 2100F FETEM operating at 200 kV. The ADF-STEM analysis was performed for the free-standing Ru and Ir nanoparticles and supported Pt, Ru and Ir using a FEI Titan^3 80-300 microscope operated at 300 kV and equipped with a CEOS aberration corrector for the probe forming lens and a monochromated field-emission gun. Due to the very small size of the nanoparticles studied, ADF-STEM was used instead of conventional TEM to achieve a higher sensitivity in the micrographs. Previously, this technique has been shown to be able to obtain images of a single atom [276]. Additional details of these characterizations can be found in previous studies [229,255,265]. ImageJ software was used to determine the particle size distribution of at least 200 nanoparticles.

8.2.5 Catalytic Measurements

Catalytic studies were carried out at atmospheric pressure in a single-chamber capsule reactor (SCCR) [244]. The reaction gases were C_2H_4 (Linde, 0.5% C_2H_4 in He), O_2 (Linde, 20.9% O_2 in He), and pure He (Linde, 99.997% He) as a carrier gas. The gas composition of C_2H_4, O_2 and He was controlled by mass flow controllers (MKS, 1259C and 1261C Series). The overall flow rate was held constant at 6 $L \cdot h^{-1}$. The product gases were analyzed with an on-line CO_2 gas analyzer (Horiba, VA-3000). The catalytic studies in the presence of oxygen were carried out at a constant partial pressure of oxygen (3 kPa) and varying partial pressure of ethylene (0.009 – 0.018 kPa) through a forward (i.e., increasing partial pressure of

ethylene) and reverse (i.e., decreasing partial pressure of ethylene) scan at 350°C, allowing the reaction to stabilize for 1 hour between each partial pressure. In the absence of oxygen or ethylene, the catalytic studies were carried out at corresponding constant partial pressures of 0.012 kPa C_2H_4 or 3 kPa O_2, and He balance at 350°C.

8.3 Results and Discussion

8.3.1 Catalyst Characterization

TEM and ADF-STEM characterization of the Pt and Ru catalysts were shown previously, showing a uniform distribution of particles [229,255,265], resulting in an average particle size of approximately 3.0 nm and 1.1 nm, respectively. ADF-STEM images of the free-standing Ir nanoparticles and 1 wt% Ir/CeO_2 are shown in Figure 8-2. An average particle size for both free-standing Ir and Ir/CeO_2 was found to be 1.0 nm; thus showing no significant agglomeration during the deposition on CeO_2.

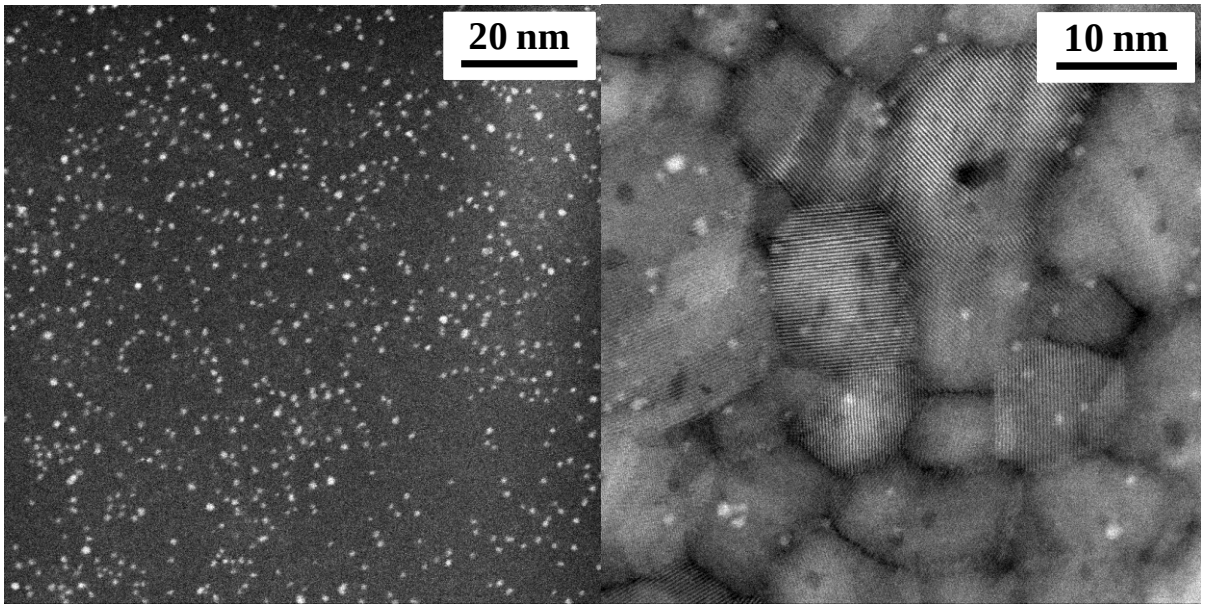

Figure 8-2: ADF-STEM micrographs of (a) free-standing Ir nanoparticles and (b) 1 wt% Ir/CeO_2.

8.3.2 Catalytic Studies in the Presence of Gaseous Oxygen

The complete oxidation of ethylene was chosen as a model reaction for this study. Each catalyst was exposed to the gas mixture at a constant partial pressure of O_2 (3 kPa), varying partial pressure of C_2H_4 with He to balance (as shown in Figure 8-3a). Furthermore, as defined previously by Vayenas and co-workers [14], the rate enhancement ratio for MSI

(ρ_{MSI}) was established for Pt/CeO_2 with respect to the Pt, Ru/CeO_2 with respect to Ru, and Ir/CeO_2 with respect to Ir (Figure 8-3b) using equation 8-1, where r corresponds to the promoted catalytic rate (i.e., for Pt/CeO_2, Ru/CeO_2 and Ir/CeO_2) and r_u corresponds to the unpromoted catalytic rate (i.e., for Pt, Ru and Ir).

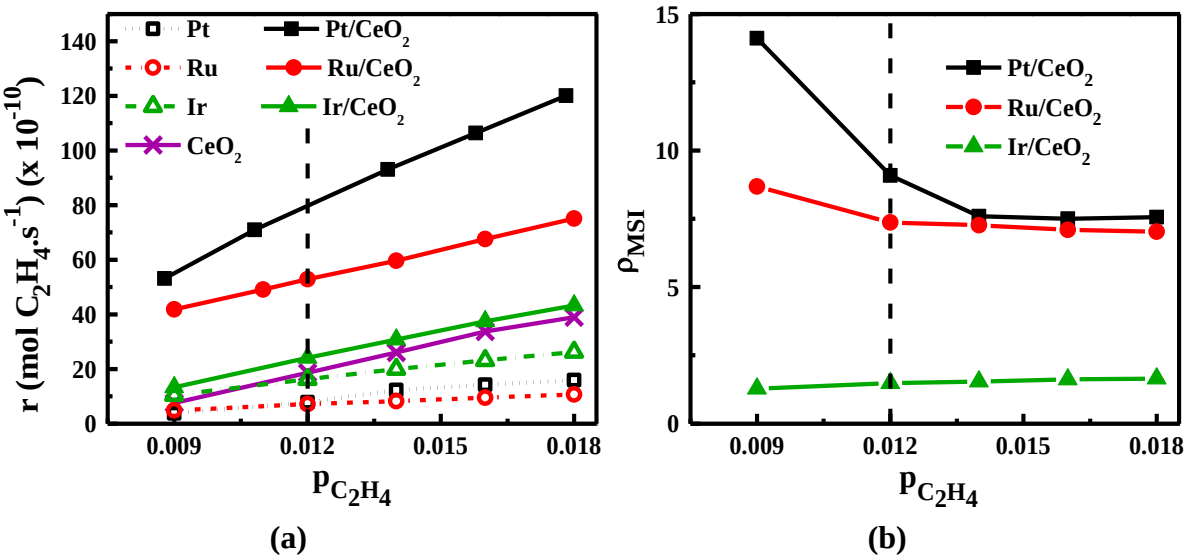

Figure 8-3: Comparison of free-standing and supported catalysts through (a) catalytic rates (forward scans) and (b) metal-support interaction rate enhancement ratio (ρ_{MSI}) with varying ethylene partial pressure at 350°C (3 kPa O_2, balance He; total flow: 6 L·h^{-1}) (dashed lines: reaction condition for further evaluation).

It is evident that the free-standing nanoparticle catalysts (Pt, Ru, Ir) have lower catalytic activity in comparison to their corresponding CeO_2-supported catalysts. This is expected due to an interaction between the metal and support likely caused by the difference in metal-support work function between Pt (φ_{Pt}= 5.93 eV) [260], Ru (φ_{Ru}= 4.71 eV) [260] or RuO_x (φ_{RuO_2}= 4.6 eV) [277], Ir (φ_{Ir}= 5.76 eV) [260] or IrO_x (φ_{IrO_2}= 4.23 eV) [278], and CeO_2 (φ_{CeO_2}= 4.69eV) [261]. In addition, the CeO_2-supported Pt nanoparticles have a higher catalytic activity than the Ru/CeO_2 catalyst, because Pt is known to be a highly active catalyst for the complete oxidation of ethylene [73,262] and possibly due to the lower work function difference between Ru and CeO_2. A higher work function difference is said to lower the barrier for the formation of oxygen vacancies, causing the CeO_2 to become more reducible [34] which results in higher activity as shown previously [229]. However, the Ir/CeO_2 catalyst shows the lowest activity of the supported catalysts, even though there is a larger difference in work function between Ir and CeO_2 compared to Ru and CeO_2. This is

likely due to the presence of IrO_x (φ_{IrO_2}= 4.23 eV) [278] rather than metallic Ir on the CeO_2 (φ_{CeO_2}= 4.69eV) [261] support; therefore, in this case, CeO_2 has a higher work function than IrO_x causing a weaker interaction and lower catalytic activity. Similar low catalytic activity of Ir/CeO_2 was found in a previous study for ethanol steam reforming where the activation energy was found to be much higher (58 kJ/mol) for Ir/CeO_2 in comparison to Pt/CeO_2 (18 kJ/mol) [273].

Recently, Acerbi et al. [37] discussed the interaction of precious metals with CeO_2 using what is called the d-band center model. Three properties are identified which are shown to influence the ability for a surface to make and break adsorbate bonds; two of which are the degree of filling of the d-bands and the position of the d-band centres. For the case of the degree of filling, Pt ($[Xe]4f^{14}5d^{9}6s^{1}$) has more electrons in its d-band compared to both Ru ($[Kr]4d^{7}5s^{1}$) and Ir ($[Xe]\ 4f^{14}5d^{7}6s^{2}$), thus resulting in an easier ability to make and break bonds causing the higher catalytic activity. Similarly, Pt has a lower d-band center (~ -2.2 eV) [37,279], relative to the Fermi level, in comparison to Ru (~ -1.4 eV) [37,279], indicating weaker bonding with the adsorbate which results in higher catalytic activity. Contrary to this, the d-band center of Ir (~ - 2.1 eV) [279], relative to the Fermi level, is similar to that of Pt; however, it has been shown by O_2 reduction that the oxygen adsorption strength to Ir is much stronger in comparison to Pt [279]. The higher adsorption strength causes high coverage of oxygen on the surface which slowly desorbs, resulting in lower catalytic activity; thus confirming the likely presence of IrO_x.

Figure 8-3b shows the metal-support interaction rate enhancement ratio for all three catalysts. Firstly, these results show that CeO_2 has a significant role in the catalytic activity of the metal catalysts, as all of the ρ_{MSI} values are greater than 1. In general, it is shown, through higher rate enhancement ratios, that Pt has a stronger interaction with CeO_2 compared to Ru and an even stronger interaction compared to Ir. This can be attributed to the difference in electronic nature of the interaction of these metals with CeO_2. Further investigation into this interaction is shown and discussed in the following sections.

8.3.3 Catalytic Studies in the Absence of Gaseous Oxygen

8.3.3.1 Stability of Pt, Ru and Ir Nanocatalysts in the Absence of Oxygen

Each catalyst was evaluated for its performance in the absence of oxygen in the gas feed. The catalyst was allowed to stabilize in the reaction mixture (0.012 kPa C_2H_4, 3 kPa O_2 and He balance) for at least 2 hours (Time: 0-0.75 h interval in Figure 8-4a); then the oxygen supply was stopped while maintaining the same partial pressure of C_2H_4 (Time: 0.75 – 3.5 h interval in Figure 8-4a). Figure 4a compares the stability of all catalysts, supported and freestanding, in the absence of oxygen up to approximately 2.5 hours, while Figure 8-4b shows the change in the promotional rate enhancement ratio (ρ_{MSI}) (i.e., supported vs. free-standing) for the first 25 minutes in the absence of oxygen. It should be noted that after 25 minutes, ρ_{MSI} approaches infinity due to the diminishing catalytic rate of the free-standing nanoparticles.

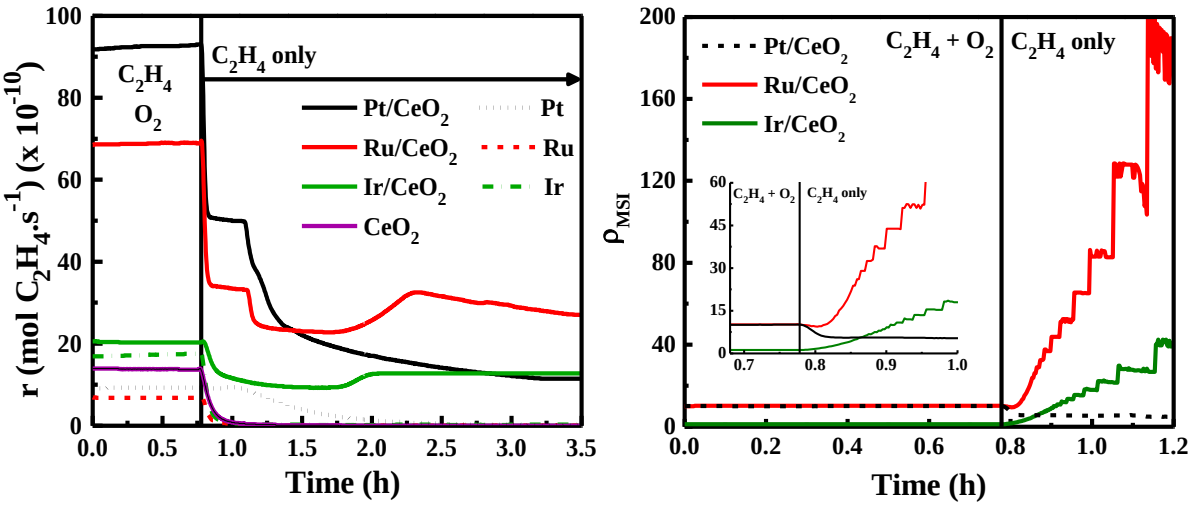

Figure 8-4: Transient C_2H_4 oxidation (a) reaction rate over free-standing and supported catalysts and (b) rate enhancement ratio in the presence and absence of oxygen at 350°C (0.012 kPa C_2H_4, 3 kPa O_2, balance He; total flow: 6 L·h^{-1}). Inset shows focused area of the first 20 min in the absence of O_2.

In the first 0.75 h, two reactions occur; between molecular oxygen and ethylene (Eq. 8-4) and electrochemically between $O^{\delta-}$ and C_2H_4 at the tpb, together with the backspillover of $O^{\delta-}$ to the catalyst surface (Eq. 8-5). In the absence of oxygen (> 0.75 h), only the electrochemical reaction (Eq. 8-5) takes place, which is accompanied by the partial reduction of ceria. As was shown previously, Pt nanoparticles prepared by the polyol method are mostly metallic [96,255], whereas Ru and Ir nanoparticles are present as oxides [146,229].

Consequently, their reduction can take place in the absence of molecular oxygen. As can be seen (Figure 8-4a), in general, the free-standing nanoparticles (Pt, Ru, Ir) as well as CeO_2 alone, have almost an immediate decline in the catalytic rate. The CeO_2-supported catalysts, on the other hand, show different behaviours. In the absence of oxygen, the catalytic rate of the Pt/CeO_2 and Ru/CeO_2 catalysts decline by about 60%, reaching a plateau that remains for about half an hour; Ir/CeO_2 does not show this behaviour. The observed plateau is attributed to the reaction of ethylene with the readily available surface lattice oxygen ions from ceria. After the plateau, Pt/CeO_2 activity declines gradually and reaches the steady-state after 3 h that is characterized by 8 times lower reaction rate than in the presence of oxygen. The continuous decline in the reaction rate is due to the consumption of surface lattice oxygen ions from ceria, as well as due to catalyst surface poisoning by carbon deposition as was shown earlier [103,116] and will be discussed in section 8.3.4. The deposited carbon is oxidized by O^{2-} :

$$C + 2O^{2-} \rightarrow CO_2 + 4e^- \qquad \textbf{8-8}$$

However, deposited carbon will block active catalytic sites and render them unavailable for C_2H_4 adsorption and reaction.

Furthermore, for Ru/CeO_2 (after the plateau at 1.25 h) and for Ir/CeO_2, an initial decline in the rate is observed which then increases within the following hour, and finally slowly declines once again. During the initial decline, oxygen ions from ceria surface are consumed via the electrochemical reaction (Eq. 8-5) and at the same time IrO_x and RuO_x are becoming reduced [146,229]. Then at ~1.75 h the reaction rate starts increasing, because more catalyst surface sites become available for ethylene adsorption and reaction with the lattice oxygen, however because O^{2-} continues to be depleted from CeO_2 the reaction rate declines again. As it was shown previously, backspillover of oxygen results in the partial reduction of CeO_2, resulting in enhanced catalytic activity [229]; hence the temporary increase in the catalytic rate for Ru/CeO_2 and Ir/CeO_2. Overall, the stability of Ru/CeO_2, in the absence of oxygen, is higher (61% decline after 3.5 h) than for ceria-supported Pt (88%) and Ir (37%), and it appears to be the superior catalyst, with Pt/CeO_2 and Ir/CeO_2 reaching a similar stability after approximately 2.5 hours.

This difference in behaviour of the Pt/CeO_2 catalyst compared to Ru/CeO_2 and Ir/CeO_2 is also evident in terms of ρ_{MSI} in the absence of oxygen (Figure 8-4b). The rate enhancement for both Ru/CeO_2 and Ir/CeO_2 initially increases, more rapidly for Ru/CeO_2, in the absence of oxygen, while the rate enhancement of Pt/CeO_2 slowly decreases. Again, these results are attributed to the weaker oxygen adsorption strength of Pt compared to that of Ru and Ir. The O^{2-} ions are immediately consumed at the tpb instead of migrating onto the catalyst surface which cause promotion of the catalytic performance. Furthermore, previously, it has been shown that certain metal-support combinations can reach a promoted state that is equivalently to that of the electrochemically promoted state [223]. This could be the case for the supported Pt catalysts as a result of the MSI with CeO_2; that is, in the absence of oxygen, the catalytic properties of Pt cannot be further enhanced. While it may be that the supported Ru and Ir catalysts have not reached this point yet; hence the significant increase in ρ_{MSI} when gaseous oxygen is removed.

8.3.3.2 Role of the Oxygen Storage Capacity of CeO_2

To gain further insight in the role of the OSC of CeO_2 and its relation to the supported metal catalyst, transient interval experiments were performed. Each catalyst was exposed to alternating reaction gas (0.012 kPa C_2H_4, 3 kPa O_2 and He balance) and absence of oxygen (0.012 kPa C_2H_4 and He balance) conditions every 2 hours, as shown in Figure 8-5. Overall, each catalyst demonstrated repeatable and reversible behaviour in the presence and absence of oxygen. This is as expected as ceria is known to easily convert between Ce^{3+} and Ce^{4+} due to the small electric potential of oxygen (i.e., 1.7 V) between this redox couple [280].

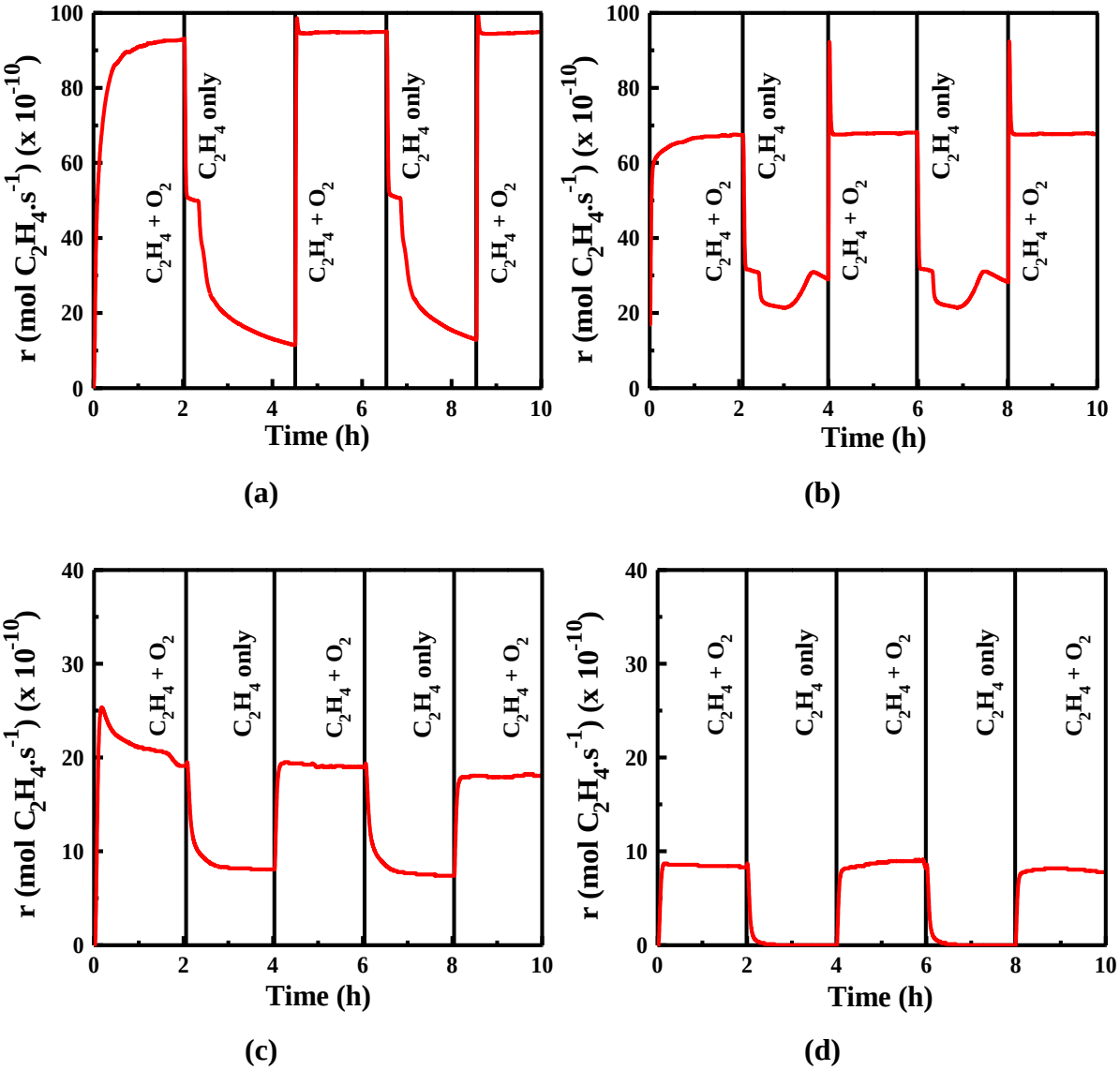

Figure 8-5: Catalytic rate in the absence of oxygen for 2 hour intervals for (a) Pt/CeO_2; (b) Ru/CeO_2; (c) Ir/CeO_2; (d) Ru colloid at 350°C (0.012 kPa C_2H_4, 3 kPa O_2, balance He; total flow: 6 L·h^{-1}).

In comparison to each other, different behaviour was observed in the absence of oxygen for each catalyst (as shown in Figure 8-5). These different behaviours are due to the adsorption strength of oxygen on the catalyst surface as well their individual interaction with CeO_2, as discussed previously. In terms of oxygen storage, it is evident from these results that the oxygen in the support can be replenished in the 2 h exposure interval in the reaction gases. This is as expected, as CeO_2 is known be able to convert between Ce^{3+} and Ce^{4+} quite easily [109,227]. To further investigate this oxygen storage capability of CeO_2, the percent O^{2-} consumed was calculated for each catalyst over different durations in the absence of oxygen

(Figure 8-6). A preliminary relationship between the O^{2-} consumed (in the absence of oxygen) and the promotional rate enhancement (in the presence of oxygen) was established.

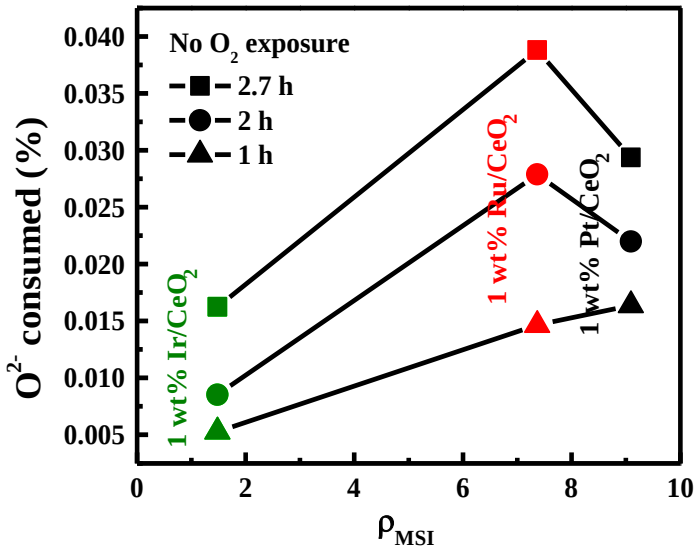

Figure 8-6: Consumption of O^{2-} ions in the absence on gaseous oxygen at various durations over 1 wt% Pt/CeO_2, Ru/CeO_2 and Ir/CeO_2 at 350°C (0.012 kPa C_2H_4, balance He; total flow: 6 $L \cdot h^{-1}$).

In general, it was determined that as the promotional rate enhancement ratio increased, the percent O^{2-} consumed increased. This is as expected due to the promotional effects of backspillover of O^{2-} species onto the surface of catalysts. Therefore, it is possible that by estimating the amount of O^{2-} consumed, the extent of MSI could be predicted. Moreover, as the exposure duration was increased, more O^{2-} ions from the support should be available to migrate to the surface of the catalyst; therefore, resulting in an increase in the percent O^{2-} consumed. This was the case for Ru/CeO_2 and Ir/CeO_2; however not for the Pt/CeO_2 catalyst. After 1 hour in the absence of oxygen, the percent O^{2-} consumed did not increase for Pt/CeO_2 according to the expected trend. These results are attributed to possible carbon deposition, more specially at the tpb, causing a decrease in available O^{2-} species to react with the C_2H_4. This rationale is discussed further as follows.

8.3.4 Ethylene Cracking and Carbon Formation

In order to examine the different behaviours observed of each catalyst and OSC of CeO_2 further, transient experiments in the absence of both O_2 and C_2H_4 individually were carried out. These experiments also explored this possibility in the absence of oxygen. It has been

shown previously that deposition of carbon on Group VIII metal catalysts can occur through the Boudouard reaction (i.e., CO disproportionation) [281–283], methane decomposition [282], or ethylene cracking [284]. In applications, such as fuel cells [285], carbon deposition has been identified as one of the main reasons for electrode degradation. Furthermore, in the absence of oxygen, for ionically conductive (i.e., SDC, CeO_2, YSZ) supports, carbon deposition has been proposed to be a possibility [103,283], while for non-ionically conductive (Al_2O_3) supports , no significant carbon deposition was observed [282]. For ionically conductive supports, it is said that the deposited carbon can be oxidized by the O^{2-} ions from the support material. Previously, this occurrence of oxidation was shown to be possible for CeO_2 for soot oxidation [286]. Since the O^{2-} ions can react with the carbon, in order to determine the presence of deposited carbon, a carbon balance can be performed by observing the production of CO_2.

Each catalyst was stabilized in the reaction gas (0.012 kPa C_2H_4, 3 kPa O_2 and He balance) for 2 hours, then alternating between C_2H_4 or O_2 (He balance) only environments for 1 hour (Figure 8-7).

It is evident that similar behaviour was observed in the absence of oxygen (as in Figure 8-5); however, the interesting part is the behaviour in the subsequent absence of ethylene and absence of oxygen. In the absence of ethylene, the catalytic rate decreases towards zero; however, in the subsequent presence of ethylene and absence of oxygen, the catalytic rate behaviour is repeated. The catalytic rate for Pt/CeO_2 (Figure 8-7a) and Ru/CeO_2 (Figure 8-7b) return to the same plateau state shown before (Figure 8-4 and Figure 8-5), while the free-standing nanoparticles do not (i.e., Ru (Figure 8-6d), Pt and Ir). In addition, Ir/CeO_2 shows again the slight decline, increase, then decline in the catalytic rate in the absence of oxygen. These observations emphasize the involvement of the adsorbed surface and lattice oxygen in the oxidation of the gaseous ethylene. After being exposed to gaseous oxygen, the surface lattice oxygen is slowly released resulting in the plateau for Pt/CeO_2 and Ru/CeO_2. Similarly, the temporary increase in catalytic rate is again observed for the Ir/CeO_2 catalyst, but not the Ru/CeO_2 due to the shorter absence of oxygen compared to in Figure 8-5b.

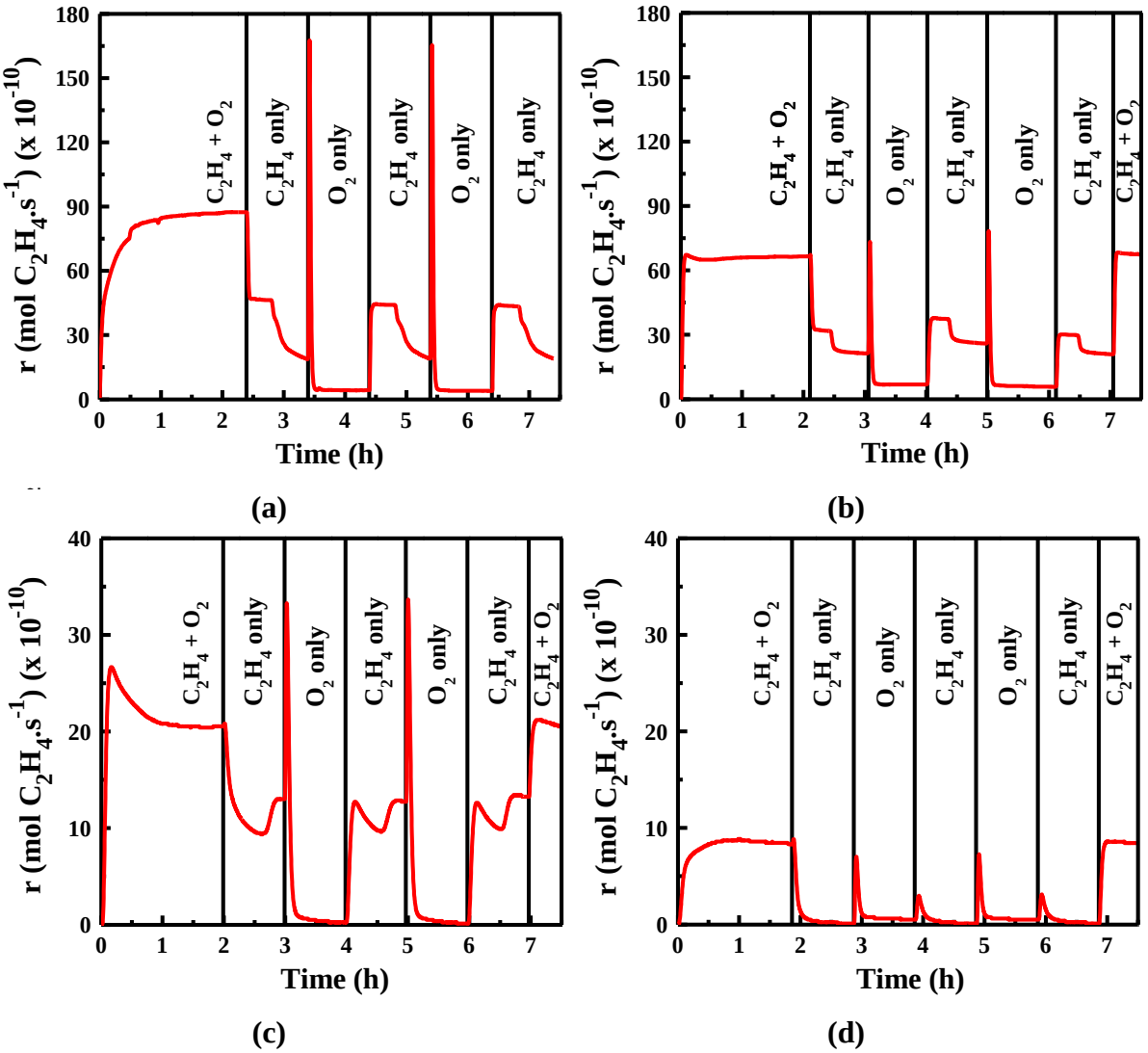

Figure 8-7: Catalytic rate in the absence of ethylene and oxygen for 1 hour intervals for (a) Pt/CeO_2; (b) Ru/CeO_2; (c) Ir/CeO_2; (d) Ru colloid at 350°C (0.012 kPa C_2H_4, 3 kPa O_2, balance He; total flow: 6 L·h^{-1}).

In order to determine possible carbon formation, a carbon balance was carried out for each catalyst at the CO_2 peaks formed (Figure 8-7) once only oxygen was introduced into the system. The following trend was observed: Pt/CeO_2 (-120%) >> Pt (-35%) > Ir/CeO_2 (-16%) ≈ Ru/CeO_2 (-15%) >> Ru (+2%) > Ir (+10%). A negative percentage value indicates that more CO_2 was produced than theoretically possible from the catalytic oxidation of ethylene; indicating possible carbon deposition [286]. A positive percentage value indicates that less CO_2 was produced than theoretically possible; therefore, the observed peak is less likely caused by carbon deposition but rather adsorbed CO_2 from the oxidation of ethylene being desorbed. It is well studied, especially for fuel cells, that Pt is poisoned my carbonaceous species, specifically CO; therefore, explaining the higher deposition of carbon on the Pt

catalysts [287,288]. The similar behaviour between Ir/CeO_2 and Ru/CeO_2 could be due to their common formation of oxides more readily than Pt; allowing for less deposition of carbon as the surface is already covered by oxygen species [279].

Further investigation into the possibility of carbon deposition was conducted through transient interval experiments in the absence of C_2H_4 or O_2, individually, where the exposure to ethylene (i.e., in the absence of O_2) was varied (Figure 8-8). It is evident for Pt/CeO_2 (Figure 8-8a) that as the exposure to ethylene was increased, the peak (indicated by *) height increased, suggesting the deposition of carbon; however, this increase was not observed for Ru/CeO_2 (Figure 8-8b) or free-standing Ru (Figure 8-8c).

From the results shown in Figure 8-8, the peak maximum (mol $C_2H_4 \cdot s^{-1}$) was determined, as well as the area under each peak (mol C_2H_4) which was used to determine the possible moles of carbon formed (shown in Figure 9). The overall increasing trend for Pt/CeO_2, but not for Ru/CeO_2 or Ru colloid, for both moles of carbon and peak maximum, with C_2H_4 exposure time is more apparent.

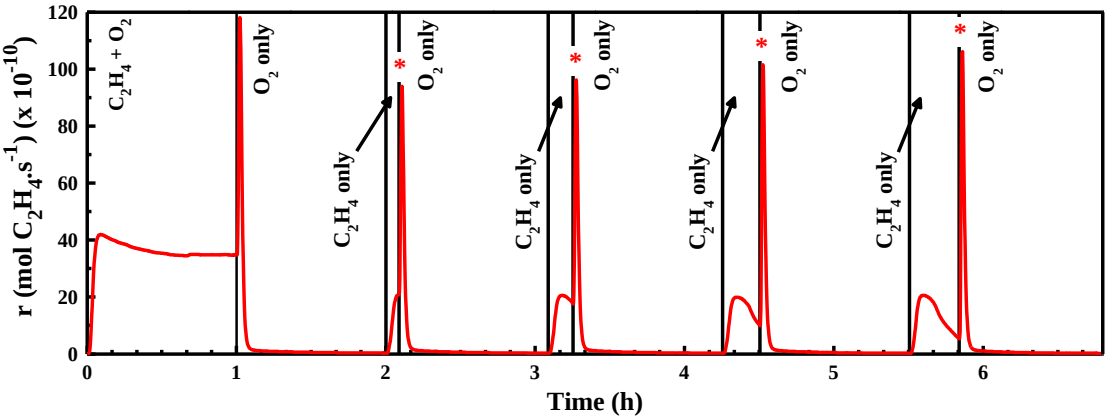

(a)

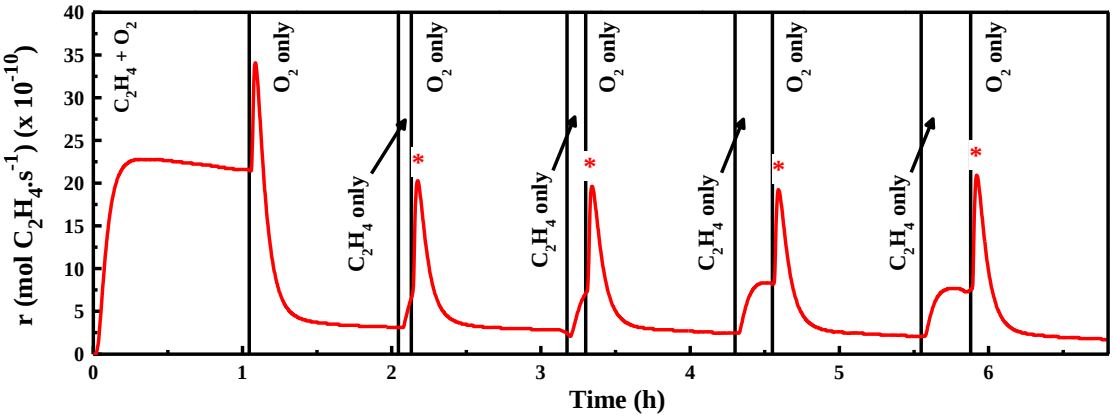

(b)

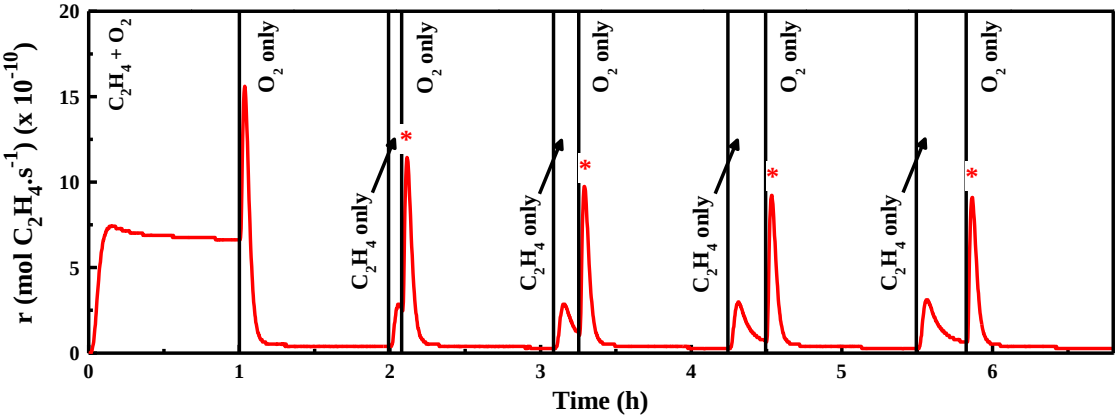

(c)

Figure 8-8: Catalytic rate in the absence of oxygen for varying intervals (5, 10, 15, 20 minutes) and absence of ethylene for a constant duration for (a) Pt/CeO_2; (b) Ru/CeO_2; (c) Ru colloid at 350°C (0.012 kPa C_2H_4, 3 kPa O_2, balance He; total flow: 6 $L \cdot h^{-1}$).

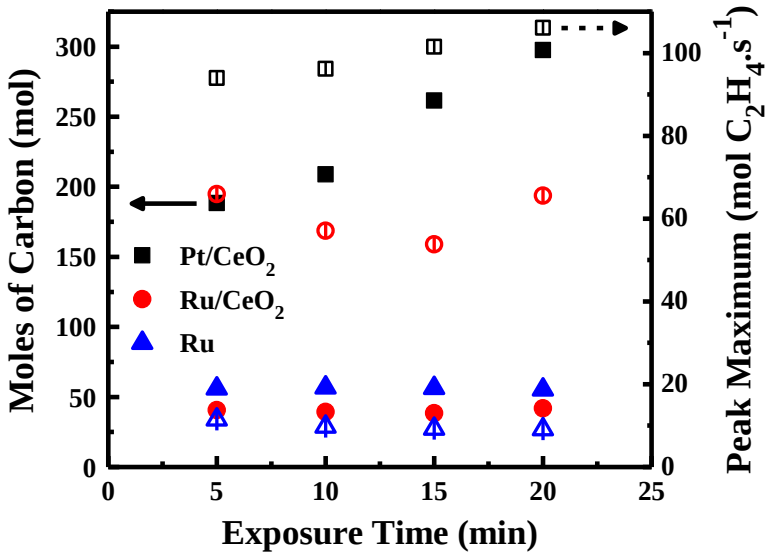

Figure 8-9: Summary of the possible moles of carbon formed (solid symbols) and peak maximums (dashed symbols) with respect to ethylene exposure time for Pt/CeO_2, Ru/CeO_2 and Ru colloid.

8.4 Conclusion

Three different highly-dispersed CeO_2-supported (Pt/CeO_2, Ru/CeO_2, and Ir/CeO_2) and free-standing (Pt, Ru, and Ir) nano-catalysts were evaluated for their catalytic performance in the presence and absence of oxygen. It was evident that the CeO_2 support greatly enhanced the catalytic rate of each metal catalyst in comparison to its corresponding free-standing catalyst: Pt/CeO_2 > Ru/CeO_2 > Ir/CeO_2 > CeO_2 > Ir > Pt > Ru. In the absence of oxygen, it was found that the storage capability of CeO_2 assisted in the overall stability of the metal nano-catalysts; however, different behaviours were observed for each catalyst. Both the catalytic rates of the Pt/CeO_2 and Ru/CeO_2 catalysts declined slightly, reaching a plateau that remained for about half an hour; Ir/CeO_2 did not show this plateau. The catalytic rate then gradually declined; however, in the case of both Ru/CeO_2 and Ir/CeO_2, the catalytic rate increased within the following hour, and then finally slowly declined again. These observations were attributed to increase in available active sites for C_2H_4 adsorption of Ir and Ru in comparison to Pt and its effect on the electronic interaction with the CeO_2 support. As a result, in the absence of oxygen, Ru/CeO_2 demonstrated to have superior activity compared to Ir/CeO_2 and Pt/CeO_2. A relationship between the promotional rate enhancement ratio (ρ_{MSI}) and the O^{2-} consumed from the support was proposed, which was suggested as a possible tool to estimate the extent of MSI. In general, it was found that an increase in ρ_{MSI}

corresponded to an increase in O^{2-} consumed, as expected. However, this was not the case for Pt/CeO_2, where carbon deposition was found, inhibiting the available active catalytic sites where C_2H_4 can be adsorbed. Overall, these results show the significant impact that the interaction of the metal and support can have on its catalytic performance, especially in the case of "active" supports such as CeO_2 and confirm the important role of backspillover of $O^{\delta-}$. Quantifying this influence could help in the design of catalysts for a specific purpose.

Chapter 9: Conclusions and Recommendations

Highly-dispersed nano-catalysts were studied with regards to the concepts of metal-support interaction (MSI) and electrochemical promotion of catalysis (EPOC) in order to improve the catalytic performance for the oxidation of various volatile organic compounds (VOCs). The overall objective was to study MSI and EPOC separately; then to determine a connection between these two phenomena. It has been said that EPOC and MSI are closely related and this project has furthered understanding this notion.

In order to achieve the overall objective, several sub-objectives were executed. Firstly, nanoparticle catalysts (Au, Pt, Ru, Ir, PtSn) were synthesized having average particle sizes in the range of less than 10 nm. The synthesis of these nano-catalysts was carried out using a polyol method, as discussed in Chapters 4-8. The first study (Chapter 3), however, demonstrated a modified synthesis method for Au nanoparticles using a stabilizing polymer, which resulted in particles with an average size greater than 10 nm. The synthesized nano-catalysts were supported on different materials, including γ-Al_2O_3 (non-ionically conductive), YSZ (ionically conductive), and CeO_2 (mixed ionic-electronic conductive, MIEC).

The supported and free-standing nano-catalysts were evaluated for their catalytic performance for different VOC oxidation reactions to better understand the concept of MSI. YSZ was shown to be a promising catalyst support for both Au and Pt nanoparticles for the reaction of CO oxidation (Chapter 3) and toluene oxidation (Chapter 4), respectively. Due to the larger size of the Au nanoparticles resulting in lower catalytic performance, and corresponding difficulty to remove the stabilizing polymer, these nano-catalysts were not studied further. The YSZ-supported Pt nano-catalysts demonstrated a higher reaction rate compared to a γ-Al_2O_3-supported Pt nano-catalyst for the oxidation of toluene, despite the lower dispersion of the nanoparticles on YSZ. These findings were attributed to a stronger MSI between Pt and YSZ due to the ionic conductivity of YSZ and presence of oxygen vacancies. Overall, it was evident that the support material significantly influences the catalytic activity of the supported metal.

In order to study the highly-dispersed nano-catalysts with regards to the concept of EPOC, a reactor setup was developed and the form of the catalyst was adjusted. A single-chamber capsule reactor (SCCR) was designed to allow for easy assembly and disassembly as well as improved current collection in comparison to the plug flow (PF)-type reactor. Open circuit experiments were carried out to show that similar catalytic performance was achieved for the SCCR compared to the PF-type. Therefore, the feasibility of this new reactor design was deemed acceptable for the application of the concept of electrochemical promotion to highly-dispersed heterogeneous catalysts.

Even though YSZ proved to be a promising catalyst support, this material was not adequate for a catalyst-working electrode for the electrochemical cell since it is not electrically conductive. Therefore, a similar ionic (i.e., O^{2-}) conducting material (i.e., CeO_2) that also possessed electrical conductivity properties was used instead as a catalyst support. Before applying the concept of EPOC, the open circuit heterogeneous catalytic performance of the CeO_2-supported catalysts was evaluated which showed that CeO_2 plays a key role in enhancing the performance of the metal catalyst (Chapters 6-8). This was determined by comparing the supported and free-standing metal catalysts for the complete oxidation of ethylene.

By implementing CeO_2 as a support material for the Ru nano-catalysts, EPOC was successfully applied to highly-dispersed catalysts (Chapters 5 and 6). It was shown that both negative and positive polarization (± 2 μA and -5 μA) resulted in a pronounced effect on its catalytic rate. The catalytic enhancement, as a result of negative polarization, was attributed to the partial electroreduction of CeO_2 which was confirmed through XPS analysis. Partially reduced CeO_{2-x} and Ru nanoparticles was proposed to form a stronger metal-support interaction. As a result, the connection between EPOC and MSI was further investigated.

Chapter 7 discussed a combination of open circuit catalytic and electrochemical measurements which was used to evaluate and understand the catalytic performance of Pt- and Ru-based, free-standing and CeO_2-supported catalysts with regards to MSI and electrochemical movement of O^{2-} ions from the support. The addition of Sn was also shown to help in a promoting the catalytic activity of the CeO_2-supported Pt catalyst through what is thought to be the partial reduction of ceria. Both of these observed enhancements in catalytic

activity are attributed to a stronger interaction between the metal catalyst and support. Through this study, the parameter of an apparent self-induced Faradaic efficiency ($|\Lambda_{MSI}|$) was proposed to quantify the MSI effect for the first time. In addition, a preliminary relationship was established between the catalytic rate and electrochemical response (i.e., exchange current density) for the Pt- and Ru-based catalytic systems; indicating that the lattice O^{2-} species play a key role in the overall catalytic activity of the nano-catalysts supported on active conductive supports.

Finally, three different highly-dispersed CeO_2-supported (Pt/CeO_2, Ru/CeO_2, and Ir/CeO_2) and free-standing (Pt, Ru, and Ir) nano-catalysts were evaluated for their catalytic performance in the presence and absence of oxygen in order to determine the influence of the oxygen storage capability of CeO_2. In the absence of oxygen, it was found that the storage capability assisted in the overall stability of the metal nano-catalysts; however, different behaviours were observed for each catalyst. The difference was attributed to the oxygen adsorption strength on Ir, Ru, and Pt and its effect on the electronic interaction with the CeO_2 support. From this study, a preliminary relationship between the promotional rate enhancement ratio (ρ_{MSI}) and the O^{2-} consumed from the support was proposed, which was suggested as a possible tool to estimate the extent of MSI. Overall, these results showed the significant impact that the interaction of the metal and support can have on its catalytic performance, especially in the case of "active" supports such as CeO_2. Quantifying this influence could help in the design of catalysts for a specific purpose

From this project, it is evident that further research into this intriguing area of EPOC and MSI would be recommended. Evaluating other metal nanoparticle catalysts, possibly less expensive, non-precious metals, would prove to be valuable to further understanding the relationship between MSI and EPOC, as well as for implementing EPOC for highly-dispersed catalysts. Similarly, it would be beneficial to study other O^{2-}-conducting MIEC materials as supports (e.g., samarium-doped ceria or titania), to determine the validity of the proposed relationship for different combinations of metals and support materials. As well, electron donor promotor supports (e.g., Na^+, K^+) should be considered in order to determine the influence of the type of promoter species on the MSI and movement of ions from the support.

In this study, model reactions were used to evaluate the catalytic performance. This was done in order to simplify the interpretation of the behaviour of the different catalysts. Once the fundamental connection of these phenomena are understood and quantified, it would be useful and more practical to involve a more complex or realistic reaction mixture. Therefore, the applicability of such techniques and catalysts to commercial applications could be assessed.

Furthermore, a recent study by Jiménez-Borja et al. [289] demonstrated the applicability of modelling the kinetics of the catalytic oxidation of CH_4 in order to determine the likely mechanism of the adsorbed species. A relationship between the mechanism and the electrochemical promotion was also proposed. Just as this project demonstrated a fundamental connection between MSI and EPOC through carrying out experiments, using this type of modelling could be beneficial in quantifying this relationship in a more efficient manner.

Finally, experimentally, two challenges encountered through this project included physical instability of the catalyst in the electrochemical cell, as well as fragile gold wires for the current collectors in the new reactor design. It is recommended that the method for depositing the supported catalysts on the YSZ disc be improved to ensure good adhesion to the disc surface; however, without introducing any or minimal interference to the performance of the catalyst. Due to the prototype nature of the newly designed reactor, it is recommended that overall improvements should be performed in the future to obtain the complete potential ease of the design. However, of main concern is the fragility of the gold wires which could be addressed by either increasing the thickness of the wires or enclosing them in a more stable arrangement.

References

[1] R.T. Burnett, S. Cakmak, M.E. Raizenne, D. Stieb, R. Vincent, D. Krewski, et al., The association between ambient carbon monoxide levels and daily mortality in Toronto, Canada., J. Air Waste Manage. Assoc. 48 (1998) 689–700.

[2] R.T. Burnett, J. Brook, A. Environment, E. Canada, T. Dann, C. Delocla, et al., Association between Particulate- and Gas-Phase Components of Urban Air Pollution and Daily Mortality in Eight Canadian Cities, Inhal. Toxicol. 12 (2000) 15–39.

[3] D. Stieb, M. Doiron-Smith, J.R. Brook, R.T. Burnett, T. Dann, A. Mamedov, et al., Air Pollution and Disability Days in Toronto: Results from the National Population Health Survey, Environ. Res. 89 (2002) 210–219.

[4] K.Y. Fung, I.N. Luginaah, K.M. Gorey, Impact of air pollution on hospital admissions in Southwestern Ontario, Canada: generating hypotheses in sentinel high-exposure places, Environ. Heal. 6 (2007) 18–25.

[5] S. Cakmak, R. Dales, J. Leech, L. Liu, The influence of air pollution on cardiovascular and pulmonary function and exercise capacity: Canadian Health Measures Survey (CHMS)., Environ. Res. 111 (2011) 1309–1312.

[6] H. Chen, M.S. Goldberg, R.T. Burnett, M. Jerrett, A.J. Wheeler, P.J. Villeneuve, Long-term exposure to traffic-related air pollution and cardiovascular mortality, Epidemiology. 24 (2013) 35–43.

[7] S.C. Kim, W.G. Shim, Catalytic combustion of VOCs over a series of manganese oxide catalysts, Appl. Catal. B Environ. 98 (2010) 180–185.

[8] N. Kamiuchi, T. Mitsui, N. Yamaguchi, H. Muroyama, T. Matsui, R. Kikuchi, et al., Activation of Pt/SnO_2 catalyst for catalytic oxidation of volatile organic compounds, Catal. Today. 157 (2010) 415–419.

[9] Z. Abbasi, M. Haghighi, E. Fatehifar, S. Saedy, Synthesis and physicochemical characterizations of nanostructured Pt/Al_2O_3-CeO_2 catalysts for total oxidation of VOCs., J. Hazard. Mater. 186 (2011) 1445–1454.

[10] S. Bensaid, F. A. Deorsola, D. Fino, N. Russo, After-treatment of household wood-fired stove emissions: From catalyst formulation to full-scale system, Catal. Today. 197 (2012) 76–89.

[11] P. Gawade, A.-M.C. Alexander, R. Clark, U.S. Ozkan, The role of oxidation catalyst in dual-catalyst bed for after-treatment of lean burn natural gas exhaust, Catal. Today. 197 (2012) 127–136.

[12] J.R. Theis, R.W. McCabe, The effects of high temperature lean exposure on the subsequent HC conversion of automotive catalysts, Catal. Today. 184 (2012) 262–270.

[13] M.F. Weilenmann, P. Soltic, S. Hausberger, The cold start emissions of light-duty-vehicle fleets: A simplified physics-based model for the estimation of CO(2) and pollutants., Sci. Total Environ. 444 (2013) 161–176.

[14] C.G. Vayenas, S. Bebelis, C. Pliangos, S. Brosda, D. Tsiplakides, Electrochemical Activation of Catalysis: Promotion, Electrochemical Promotion, and Metal-Support Interactions, Kluwer Academic/Plenum Publishers, New York, 2001.

[15] C.G. Vayenas, S. Bebelis, S. Ladas, Dependence of catalytic rates on catalyst work function, Nature. 343 (1990) 625–627.

[16] C. Vayenas, S. Brosda, C. Pliangos, Rules and Mathematical Modeling of Electrochemical and Chemical Promotion 1. Reaction Classification and Promotional Rules, J. Catal. 203 (2001) 329–350.

[17] S. Brosda, C.G. Vayenas, Rules and Mathematical Modeling of Electrochemical and Classical Promotion 2. Modeling, J. Catal. 208 (2002) 38–53.

[18] S. Brosda, C. Vayenas, J. Wei, Rules of chemical promotion, Appl. Catal. B Environ. 68 (2006) 109–124.

[19] I.V. Yentekakis, C.G. Vayenas, The Effect of Electrochemical Oxygen Pumping on the Steady-State and Oscillatory Behavior of CO Oxidation on Polycrystalline Pt, J. Catal. 111 (1988) 170–188.

[20] S. Bebelis, C.G. Vayenas, Non-Faradaic Electrochemical Modification of Catalytic Activity 1. The Case of Ethlyene Oxidation of Pt, J. Catal. 118 (1989) 125–146.

[21] C.A. Cavalca, G. Larson, C.G. Vayenas, G.L. Haller, Electrochemical Modification of CH_3OH Oxidation Selectivity and Activity on a Pt Single-Pellet Catalytic Reactor, J. Phys. Chem. 97 (1993) 6115–6119.

[22] S.G. Neophytides, C.G. Vayenas, TPD and Cyclic Voltammetric Investigation of the Origin of Electrochemical Promotion in Catalysis, J. Phys. Chem. 99 (1995) 17063–17067.

[23] G. Pacchioni, F. Illas, S. Neophytides, C.G. Vayenas, Quantum-Chemical Study of Electrochemical Promotion in Catalysis, J. Phys. Chem. 100 (1996) 16653–16661.

[24] C.G. Vayenas, S. Bebelis, Electrochemical promotion of heterogeneous catalysis, Catal. Today. 51 (1999) 581–594.

[25] C. Vayenas, S. Brosda, C. Pliangos, The double-layer approach to promotion, electrocatalysis, electrochemical promotion, and metal–support interactions, J. Catal. 216 (2003) 487–504.

[26] A. Piram, X. Li, F. Gaillard, C. Lopez, A. Billard, P. Vernoux, Electrochemical promotion of environmental catalysis, Ionics (Kiel). 11 (2005) 327–332.

[27] A. de Lucas-Consuegra, F. Dorado, C. Jiménez-Borja, J.L. Valverde, Electrochemical promotion of Pt impregnated catalyst for the treatment of automotive exhaust emissions, J. Appl. Electrochem. 38 (2008) 1151–1157.

[28] A. Toghan, L.M. Rösken, R. Imbihl, The electrochemical promotion of ethylene oxidation at a Pt/YSZ catalyst., Chemphyschem. 11 (2010) 1452–1459.

[29] D. Tsiplakides, S. Balomenou, Milestones and perspectives in electrochemically promoted catalysis, Catal. Today. 146 (2009) 312–318.

[30] S.J. Tauster, S.C. Fung, R.L. Garten, Strong metal-support interactions. Group 8 noble metals supported on titanium dioxide, J. Am. Chem. Soc. 100 (1978) 170–175.

[31] S.J. Tauster, Strong Metal-Support Interactions, Acc. Chem. Res. 20 (1987) 389–394.

[32] C.G. Vayenas, Promotion, electrochemical promotion and metal-support interactions: Their common features, Catal. Letters. 143 (2013) 1085–1097.

[33] J.C. Frost, Junction effect interactions in methanol synthesis catalysts, Nature. 334 (1988) 577–580.

[34] N. Acerbi, S.C. Tsang, S. Golunski, P. Collier, A practical demonstration of electronic promotion in the reduction of ceria coated PGM catalysts., Chem. Commun. (Camb). (2008) 1578–1580.

[35] N. Acerbi, S. Golunski, S.C. Tsang, H. Daly, C. Hardacre, R. Smith, et al., Promotion of ceria catalysts by precious metals: Changes in nature of the interaction under reducing and oxidizing conditions, J. Phys. Chem. C. 116 (2012) 13569–13583.

[36] C.T. Campbell, Catalyst–support interactions: Electronic perturbations, Nat. Chem. 4 (2012) 597–598.

[37] N. Acerbi, S.C.E. Tsang, G. Jones, S. Golunski, P. Collier, Rationalization of interactions in precious metal/ceria catalysts using the d-band center model, Angew. Chemie - Int. Ed. 52 (2013) 7737–7741.

[38] J.A. Dumesic, G.W. Huber, M. Boudart, Introduction, in: G. Ertl (Ed.), Handb. Heterog. Cataysis, 2nd ed., Weinheim : Wiley-VCH, Chichester, 2008: pp. 1–15.

[39] D.M. Mattox, Introduction, in: Handb. Phys. Vap. Depos. Process. Film Form. Adhes. Surf. Prep. Contam. Control, Noyes Publications, New Jersey, 1998: pp. 29–55.

[40] M. Fee, S. Ntais, A. Weck, E. A. Baranova, Electrochemical behavior of silver thin films interfaced with yttria-stabilized zirconia, J. Solid State Electrochem. 18 (2014) 2267–2277.

[41] A.C. Junes, M.L. Hitchman, Chapter 1 Overview of Chemical Deposition Vapor Deposition, in: Chem. Vap. Depos. Precursors, Process. Appl., Royal Society of Chemistry, Cambridge, UK, 2009: pp. 1–36.

[42] T.-S. Oh, S.M. Haile, Electrochemical behavior of thin-film Sm-doped ceria: insights from the point-contact configuration, Phys. Chem. Chem. Phys. 17 (2015) 13501–13511.

[43] N. Pinna, M. Knez, Atomic lay deposition of nanostructured materials, Wiley-VCH Verlag & Co, Weinheim, Germany, 2011.

[44] M. a. Mamun, D. Gu, H. Baumgart, A. A. Elmustafa, Nanomechanical properties of platinum thin films synthesized by atomic layer deposition, Surf. Coatings Technol. 265 (2015) 185–190.

[45] W. Li, M. Comotti, F. Schuth, Highly reproducible syntheses of active Au/TiO2 catalysts for CO oxidation by deposition–precipitation or impregnation, J. Catal. 237 (2006) 190–196.

[46] M. Alcala, C. Real, Synthesis based on the wet impregnation method and characterization of iron and iron oxide-silica nanocomposites, Solid State Ionics. 177 (2006) 955–960.

[47] T. Mitsui, K. Tsutsui, T. Matsui, R. Kikuchi, K. Eguchi, Support effect on complete oxidation of volatile organic compounds over Ru catalysts, Appl. Catal. B Environ. 81 (2008) 56–63.

[48] M.A. Fortunato, D. Aubert, C. Capdeillayre, C. Daniel, A. Hadjar, A. Princivalle, et al., Dispersion measurement of platinum supported on Yttria-Stabilised Zirconia by pulse H_2 chemisorption, Appl. Catal. A Gen. 403 (2011) 18–24.

[49] J.A. Toledo-Antonio, C. Ángeles-Chávez, M.A. Cortés-Jácome, I. Cuauhtémoc-López, E. López-Salinas, M. Pérez-Luna, et al., Highly dispersed Pt–Ir nanoparticles on titania nanotubes, Appl. Catal. A Gen. 437-438 (2012) 155–165. http://linkinghub.elsevier.com/retrieve/pii/S0926860X12003869 (accessed June 9, 2013).

[50] J. Radnik, L. Wilde, M. Schneider, M.-M. Pohl, D. Herein, Influence of the precipitation agent in the deposition-precipitation on the formation and properties of Au nanoparticles supported on Al_2O_3., J. Phys. Chem. B. 110 (2006) 23688–23693.

[51] A. Sandoval, A. Gómez-Cortés, R. Zanella, G. Díaz, J.M. Saniger, Gold nanoparticles: Support effects for the WGS reaction, J. Mol. Catal. A Chem. 278 (2007) 200–208.

[52] A. Sandoval, A. Aguilar, C. Louis, A. Traverse, R. Zanella, Bimetallic Au–Ag/TiO_2 catalyst prepared by deposition–precipitation: High activity and stability in CO oxidation, J. Catal. 281 (2011) 40–49.

[53] K. Qian, L. Luo, H. Bao, Q. Hua, Z. Jiang, W. Huang, Catalytically active structures of SiO_2-supported Au nanoparticles in low-temperature CO oxidation, Catal. Sci. Technol. 3 (2013) 679–687.

[54] X. Bokhimi, R. Zanella, V. Maturano, A. Morales, Nanocrystalline Ag, and Au–Ag alloys supported on titania for CO oxidation reaction, Mater. Chem. Phys. 138 (2013) 490–499.

[55] H. Liang, J.M. Raitano, G. He, A.J. Akey, I.P. Herman, L. Zhang, et al., Aqueous co-precipitation of Pd-doped cerium oxide nanoparticles: chemistry, structure, and particle growth, J. Mater. Sci. 47 (2011) 299–307.

[56] K. Petcharoen, A. Sirivat, Synthesis and characterization of magnetite nanoparticles via the chemical co-precipitation method, Mater. Sci. Eng. B. 177 (2012) 421–427.

[57] A.P. Kumar, B.P. Kumar, A.B.V.K. Kumar, B.T. Huy, Y.-I. Lee, Preparation of palladium nanoparticles on alumina surface by chemical co-precipitation method and catalytic applications, Appl. Surf. Sci. 265 (2013) 500–509.

[58] I. Sharifi, H. Shokrollahi, Structural, Magnetic and Mössbauer evaluation of Mn substituted Co–Zn ferrite nanoparticles synthesized by co-precipitation, J. Magn. Magn. Mater. 334 (2013) 36–40.

[59] S. Wang, H. Yang, L. Feng, S. Sun, J. Guo, Y. Yang, et al., A simple and inexpensive synthesis route for $LiFePO_4$/C nanoparticles by co-precipitation, J. Power Sources. 233 (2013) 43–46.

[60] D.M. Fernandes, R. Silva, A.A.W. Hechenleitner, E. Radovanovic, M.A.C. Melo, E.A.G. Pineda, Synthesis and characterization of ZnO, CuO and a mixed Zn and Cu oxide, Mater. Chem. Phys. 115 (2009) 110–115.

[61] E.V. Gopalan, P.A. Joy, I.A. Al-Omari, D.S. Kumar, Y. Yoshida, M.R. Anantharaman, On the structural, magnetic and electrical properties of sol–gel derived nanosized cobalt ferrite, J. Alloys Compd. 485 (2009) 711–717.

[62] M. Aziz, S. Saber Abbas, W.R. Wan Baharom, Size-controlled synthesis of SnO_2 nanoparticles by sol–gel method, Mater. Lett. 91 (2013) 31–34.

[63] K.M. Batoo, M.-S.A. El-sadek, Electrical and magnetic transport properties of Ni–Cu–Mg ferrite nanoparticles prepared by sol–gel method, J. Alloys Compd. 566 (2013) 112–119.

[64] C. Liu, X. Wu, T. Klemmer, N. Shukla, X. Yang, D. Weller, et al., Polyol Process Synthesis of Monodispersed FePt Nanoparticles., J. Phys. Chem. B. 108 (2004) 6121–6123.

[65] C. Bock, C. Paquet, M. Couillard, G. a Botton, B.R. MacDougall, Size-selected synthesis of PtRu nano-catalysts: reaction and size control mechanism., J. Am. Chem. Soc. 126 (2004) 8028–37.

[66] B. Wiley, T. Herricks, Y. Sun, Y. Xia, Polyol Synthesis of Silver Nanoparticles: Use of Chloride and Oxygen to Promote the Formation of Single-Crystal, Truncated Cubes and Tetrahedrons, Nano Lett. 4 (2004) 1733–1739.

[67] T. Herricks, J. Chen, Y. Xia, Polyol Synthesis of Platinum Nanoparticles: Control of Morphology with Sodium Nitrate, Nano Lett. 4 (2004) 2367–2371.

[68] E.A. Baranova, C. Bock, D. Ilin, D. Wang, B. Macdougall, Infrared spectroscopy on size-controlled synthesized Pt-based nano-catalysts, Surf. Sci. 600 (2006) 3502–3511.

[69] B.K. Park, S. Jeong, D. Kim, J. Moon, S. Lim, J.S. Kim, Synthesis and size control of monodisperse copper nanoparticles by polyol method, J. Colloid Interface Sci. 311 (2007) 417–24.

[70] E.A. Baranova, Y. Le Page, D. Ilin, C. Bock, B. MacDougall, P.H.J. Mercier, Size and composition for 1–5nm Ø PtRu alloy nano-particles from Cu Kα X-ray patterns, J. Alloys Compd. 471 (2009) 387–394.

[71] E.A. Baranova, T. Amir, P.H.J. Mercier, B. Patarachao, D. Wang, Y. Page, Single-step polyol synthesis of alloy Pt_7Sn_3 versus bi-phase Pt/SnO_x nano-catalysts of controlled size for ethanol electro-oxidation, J. Appl. Electrochem. 40 (2010) 1767–1777.

[72] R.J. Isaifan, H.A.E. Dole, E. Obeid, L. Lizarraga, E.A. Baranova, P. Vernoux, Catalytic CO Oxidation over Pt nanoparticles prepared from the Polyol Reduction Method Supported on Yttria-Stabilized Zirconia, Electrocatal. 5, ECS Trans. 35 (2011) 43–57.

[73] R.J. Isaifan, E.A. Baranova, Effect of ionically conductive supports on the catalytic activity of platinum and ruthenium nanoparticles for ethylene complete oxidation, Catal. Today. (2015) 107–113.

[74] S.H. Overbury, L. Ortiz-soto, H. Zhu, B. Lee, M.D. Amiridis, S. Dai, Comparison of Au catalysts supported on mesoporous titania and silica : investigation of Au particle size effects and metal-support interactions, Catal. Letters. 95 (2004) 99–106.

[75] Z. Wang, B. Li, M. Chen, W. Weng, H. Wan, Size and support effects for CO oxidation on supported Pd catalysts, Sci. China Chem. 53 (2010) 2047–2056.

[76] K. Kimura, H. Einaga, Y. Teraoka, Preparation of highly dispersed platinum catalysts on various oxides by using polymer-protected nanoparticles, Catal. Today. 164 (2011) 88–91.

[77] R.A. van Santen, Chemical basis of metal catalyst promotion, Surf. Sci. 251/252 (1991) 6–11.

[78] G. Ertl, S.B. Lee, M. Weiss, Adsorption of Nitrogen on Potassium Promoted Fe(111) and (100) Surfaces, Surf. Sci. 114 (1982) 527–545.

[79] T. Bécue, R.J. Davis, J.M. Garces, Effect of Cationic Promoters on the Kinetics of Ammonia Synthesis Catalyzed by Ruthenium Supported on Zeolite X, J. Catal. 179 (1998) 129–137.

[80] O. Shekhah, W. Ranke, R. Schlogl, Styrene synthesis: in situ characterization and reactivity studies of unpromoted and potassium-promoted iron oxide model catalysts, J. Catal. 225 (2004) 56–68.

[81] X.M. Zhu, M. Schön, U. Bartmann, A.C. van Veen, M. Muhler, The dehydrogenation of ethylbenzene to styrene over a potassium-promoted iron oxide-based catalyst: a transient kinetic study, Appl. Catal. A Gen. 266 (2004) 99–108.

[82] I. V Yentekakis, R.M. Lambert, M.S. Tikhov, M. Konsolakis, V. Kiousis, Promotion by Sodium in Emission Control Catalysis : A Kinetic and Spectroscopic Study of the Pd- Catalyzed Reduction of NO by Propene, J. Catal. 176 (1998) 82–92.

[83] I.. Yentekakis, M. Konsolakis, R.. Lambert, N. Macleod, L. Nalbantian, Extraordinarily effective promotion by sodium in emission control catalysis: NO reduction by propene over Na-promoted Pt/γ-Al_2O_3, Appl. Catal. B Environ. 22 (1999) 123–133.

[84] M. Konsolakis, N. Macleod, J. Isaac, I.V. Yentekakis, R.M. Lambert, Strong Promotion by Na of Pt/γ-Al_2O_3 Catalysts Operated under Simulated Exhaust Conditions, J. Catal. 193 (2000) 330–337.

[85] C. Pliangos, C. Raptis, T. Badas, D. Tsiplakides, C.. Vayenas, Electrochemical promotion of a classically promoted Rh catalyst for the reduction of NO, Electrochim. Acta. 46 (2000) 331–339.

[86] N. Ibrahim, D. Poulidi, I.S. Metcalfe, The role of sodium surface species on electrochemical promotion of catalysis in a Pt/YSZ system: The case of ethylene oxidation, J. Catal. 303 (2013) 100–109.

[87] M.O. Özbek, R.A. van Santen, The Mechanism of Ethylene Epoxidation Catalysis, Catal. Letters. 143 (2013) 131–141.

[88] M. Konsolakis, I.V. Yentekakis, The Reduction of NO by Propene over Ba-Promoted Pt/γ-Al_2O_3 Catalysts, J. Catal. 198 (2001) 142–150.

[89] B.P.C. Hereijgers, B.M. Weckhuysen, Selective Oxidation of Methanol to Hydrogen over Gold Catalysts Promoted by Alkaline-Earth-Metal and Lanthanum Oxides., ChemSusChem. 2 (2009) 743–748.

[90] P. Nagaraju, N. Lingaiah, P.S. Sai Prasad, V. Narayana Kalevaru, A. Martin, Preparation, characterization and catalytic properties of promoted vanadium phosphate catalysts, Catal. Commun. 9 (2008) 2449–2454.

[91] P. Rodriguez, Y. Kwon, M.T.M. Koper, The promoting effect of adsorbed carbon monoxide on the oxidation of alcohols on a gold catalyst, Nat. Chem. 4 (2012) 177–182.

[92] Y.J. Tong, Unconventional promoters of catalytic activity in electrocatalysis., Chem. Soc. Rev. 41 (2012) 8195–8209.

[93] G.M. Schwab, J. Block, W. Muller, D. Schultze, Zur Natur der katalytischen Verst€arker-Wirkung, Naturwissenschaften. 44 (1957) 582–584.

[94] G.M. Schwab, J. Block, D. Schultze, Kontaktkatalytische Verst€arkung durch dotierte Tr€ager, Angew. Chem. 71 (1958) 101–104.

[95] A. Lewera, L. Timperman, A. Roguska, N. Alonso-Vante, Metal-Support Interactions between Nanosized Pt and Metal Oxides (WO_3 and TiO_2) Studied Using X-ray Photoelectron Spectroscopy, J. Phys. Chem. C. 115 (2011) 20153–20159.

[96] S. Ntais, R.J. Isaifan, E.A. Baranova, An X-ray photoelectron spectroscopy study of platinum nanoparticles on yttria-stabilized zirconia ionic support : Insight into metal support interaction, Mater. Chem. Phys. 148 (2014) 673–679.

[97] M. Jin, J.-N. Park, J.K. Shon, J.H. Kim, Z. Li, Y.-K. Park, et al., Low temperature CO oxidation over Pd catalysts supported on highly ordered mesoporous metal oxides, Catal. Today. 185 (2012) 183–190.

[98] I.S. Metcalfe, S. Sundaresan, Oxygen transfer between metals and oxygen-ion conducting supports, AIChE J. 34 (1988) 195–208.

[99] W.-P. Dow, T.-J. Huang, Effects of Oxygen Vacancy of Yttria-Stabilized Zirconia Support on Carbon Monoxide Oxidation over Copper Catalyst, J. Catal. 147 (1994) 322–332.

[100] W.-P. Dow, Y.-P. Wang, T.-J. Huang, Yttria-Stabilized Zirconia Supported Copper Oxide Catalyst I. Effect of Oxygen Vacancy of Support on Copper Oxide Reduction, J. Catal. 160 (1996) 155–170.

[101] W.-P. Dow, T.-J. Huang, Yttria-Stabilized Zirconia Supported Copper Oxide Catalyst II. Effect of Oxygen Vacancy of Support on Catalytic Activity for CO Oxidation, J. Catal. 160 (1996) 171–182.

[102] R.J. Isaifan, H.A.E. Dole, E. Obeid, L. Lizarraga, P. Vernoux, E.A. Baranova, Metal-Support Interaction of Pt Nanoparticles with Ionically and Non-Ionically Conductive Supports for CO Oxidation, Electrochem. Solid-State Lett. 15 (2012) E14–E17.

[103] R.J. Isaifan, E.A. Baranova, Catalytic electrooxidation of volatile organic compounds by oxygen-ion conducting ceramics in oxygen-free gas environment, Electrochem. Commun. 27 (2013) 164–167.

[104] J.B. Park, J. Graciani, J. Evans, D. Stacchiola, S. Ma, P. Liu, et al., High catalytic activity of $Au/CeO_x/TiO_2(110)$ controlled by the nature of the mixed-metal oxide at the nanometer level., Proc. Natl. Acad. Sci. U. S. A. 106 (2009) 4975–4980.

[105] C. Jiménez-Borja, F. Matei, F. Dorado, J.L. Valverde, Characterization of Pd catalyst-electrodes deposited on YSZ: Influence of the preparation technique and the presence of a ceria interlayer, Appl. Surf. Sci. 261 (2012) 671–678.

[106] M.A. Fortunato, A. Princivalle, C. Capdeillayre, N. Petigny, C. Tardivat, C. Guizard, et al., Role of Lattice Oxygen in the Propane Combustion Over Pt/Yttria-Stabilized Zirconia : Isotopic Studies, Top. Catal. 57 (2014) 1277–1286.

[107] H.A.E. Dole, R.J. Isaifan, F.M. Sapountzi, L. Lizarraga, D. Aubert, A. Princivalle, et al., Low Temperature Toluene Oxidation Over Pt Nanoparticles Supported on Yttria Stabilized-Zirconia, Catal. Letters. 143 (2013) 996–1002.

[108] N. Toshima, Chapter 17: Inorganic Nanoparticles for Catalysis, in: C. Altavilla, E. Ciliberto (Eds.), Inorg. Nanoparticles Synth. Appl. Perspect., CRC Press, Boca Raton, FL, USA, 2010: pp. 475–505.

[109] P. Vernoux, L. Lizarraga, M.N. Tsampas, F.M. Sapountzi, A. De Lucas-Consuegra, J.-L. Valverde, et al., Ionically Conducting Ceramics as Active Catalyst Supports., Chem. Rev. 113 (2013) 8192–8260.

[110] H. Sato, Some Theoretical Aspects of Solid Electrolytes, in: S. Geller (Ed.), Solid Electrolytes, Springer Berlin Heidelberg, Berlin, 1977: pp. 3–39.

[111] V.S. Bagotsky, Nonaqueous Electrolytes, in: Fundam. Electrochem., 2nd ed., John Wiley & Sons Ltd., Hoboken, 2006: pp. 127–137.

[112] L. Heyne, Electrochemistry of Mixed Ionic-Electronic Conductors, in: S. Geller (Ed.), Solid Electrolytes, Springer Berlin Heidelberg, Berlin, 1977: pp. 169–221.

[113] U. Stimming, T. Hengyong, V.S. Bagotsky, Solid-State Electrochemistry, in: Fundam. Electrochem., 2nd ed., John Wiley & Sons Ltd., Hoboken, 2006: pp. 419–447.

[114] A.V. Chadwick, S.L.P. Savin, Ion-Conducting Nanocrystals: Theory, Methods, and Applications, in: V.V. Kharton (Ed.), Solid State Electrochem. Fundam. Mater. Their Appl., Wiley-VCH Verlag GmbH & Co. KGaA, betz-druck GmbH, 2009: pp. 79–132.

[115] P. Vernoux, M. Guth, X. Li, Ionically Conducting Ceramics as Alternative Catalyst Supports, Electrochem. Solid-State Lett. 12 (2009) E9–E11.

[116] R.J. Isaifan, S. Ntais, M. Couillard, E.A. Baranova, Size-dependent activity of Pt/yttria-stabilized zirconia catalyst for wireless electrooxidation of ethylene and carbon monoxide in oxygen free environment, J. Catal. 324 (2015) 32–40.

[117] M. Stoukides, C. Vayenas, The Effect of Electrochemical Oxygen Pumping on the Rate and Selectivity of Ethylene Oxidation on Polycrystalline, J. Catal. 70 (1981) 137–146.

[118] C. Vayenas, The double-layer approach to promotion, electrocatalysis, electrochemical promotion, and metal–support interactions, J. Catal. 216 (2003) 487–504.

[119] C. Pliangos, C. Raptis, I. Bolzonella, C. Comninellis, C.G. Vayenas, Electrochemical Promotion of Conventional and Bipolar Reactor Configurations for NO Reduction, Ionics (Kiel). 8 (2002) 372–382.

[120] C.G. Vayenas, S. Ladas, S. Bebelis, I.. V. Yentekakis, S. Neophytides, J. Yi, et al., Electrochemical Promotion in Catalysis: Non-Faradaic Electrochemical Modification of Catalytic Activity, Electrochim. Acta. 39 (1994) 1849–1855.

[121] C.G. Vayenas, I.V. Yentekakis, S. Bebelis, S.G. Neophytides, In-situ controlled promotion of catalyst surfaces via solid electrolytes - the NEMCA effect, Phys. Chem. Chem. Phys. 99 (1995) 1393–1401.

[122] G. Vayenas, S.I. Bebelis, Electrochemical promotion, Solid State Ionics. 94 (1997) 267–277.

[123] I. Metcalfe, Electrochemical Promotion of Catalysis I: Thermodynamic Considerations, J. Catal. 199 (2001) 247–258.

[124] I. Metcalfe, Electrochemical Promotion of Catalysis II: The Role of a Stable Spillover Species and Prediction of Reaction Rate Modification, J. Catal. 199 (2001) 259–272.

[125] A. Katsaounis, Electrochemical promotion of catalysis (EPOC) perspectives for application to gas emissions treatment, Glob. Nest J. 10 (2008) 226–236.

[126] D. Tsiplakides, S. Balomenou, Electrochemical promoted catalysis: Towards practical utilization, Chem. Ind. Chem. Eng. Q. 14 (2008) 97–105.

[127] C.G. Vayenas, C.G. Koutsodontis, Non-Faradaic electrochemical activation of catalysis., J. Chem. Phys. 128 (2008) 182506.

[128] N.A. Anastasijevic, NEMCA—From discovery to technology, Catal. Today. 146 (2009) 308–311.

[129] R. Imbihl, Electrochemical promotion of catalytic reactions, Prog. Surf. Sci. 85 (2010) 241–278.

[130] A. Katsaounis, Recent developments and trends in the electrochemical promotion of catalysis (EPOC), J. Appl. Electrochem. 40 (2010) 885–902.

[131] I. Garagounis, V. Kyriakou, C. Anagnostou, V. Bourganis, I. Papachristou, M. Stoukides, Solid Electrolytes: Applications in Heterogeneous Catalysis and Chemical Cogeneration, Ind. Eng. Chem. Res. 50 (2011) 431–472.

[132] C.G. Vayenas, Bridging electrochemistry and heterogeneous catalysis, J. Solid State Electrochem. 15 (2011) 1425–1435.

[133] C.G. Vayenas, Electrochemical Activation of Catalysed Reactions, in: R.W. Joyner, R.A. van Santen (Eds.), Elem. React. Steps Heterog. Catal., 398th ed., Springer Netherlands, Netherlands, 1993: pp. 73–92.

[134] G. Foti, I. Bolzonella, C. Comninellis, Electrochemical promotion of catalysis, in: C.G. Vayenas, B.E. Conway, R.E. White (Eds.), Mod. Asp. Electrochem., 36th ed., Plenum Press, New York, 2003: pp. 191–254.

[135] R.M. Lambert, Electrochemical and Chemical Promotion by Alkalis with Metal Films and Nanoparticles, in: A. Wieckowski, E.R. Savinova, C.G. Vayenas (Eds.), Catal. Electrocatal. Nanoparticle Surfaces, Marcel Dekker, Inc., New York, 2003: pp. 583–612.

[136] C.G. Vayenas, C. Pliangos, S. Brosda, D. Tsiplakides, Promotion, Electrochemical Promotion, and Metal-Support Interactions: The Unifying Role of Spillover, in: A. Wieckowski, E.R. Savinova, C.G. Vayenas (Eds.), Catal. Electrocatal. Nanoparticle Surfaces, Marcel Dekker, Inc., New York, 2003: pp. 667–744.

[137] C. Jiménez-Borja, A. de Lucas-Consuegra, J.L. Valverde, F. Dorado, A. Caravaca, J. González-Cobos, One of the Recent Discoveries in Catalysis: The Phenomenon of Electrochemical Promotion, in: J.C. Taylor (Ed.), Adv. Chem. Res., 14th ed., Nova Publishers, New York, 2012: pp. 99–132.

[138] H.L. Skriver, N.M. Rosengaard, Surface energy and work function of elemental metals, Phys. Rev. B. 46 (1992) 7157–7168.

[139] J. Nicole, D. Tsiplakides, S. Wodiunig, C. Comninellis, Activation of Catalyst for Gas-Phase Combustion by Electrochemical Pretreatment, J. Electrochem. Soc. 144 (1997) L312–L314.

[140] C.G. Vayenas, S. Bebelis, S. Neophytides, Non-Faradaic Electrochemical Modification of Catalytic Activity, J. Phys. Chem. 92 (1988) 5083–5085.

[141] C. Koutsodontis, A. Katsaounis, J.C. Figueroa, C. Cavalca, C. Pereira, C.G. Vayenas, The effect of catalyst film thickness on the electrochemical promotion of ethylene oxidation on Pt, Top. Catal. 39 (2006) 97–100.

[142] I.V. Yentekakis, S. Bebelis, Study of the NEMCA Effect in a Single-Pellet Catalytic Reactor, J. Catal. 137 (1992) 278–283.

[143] S. Brosda, T. Badas, C.G. Vayenas, Study of the Mechanism of the Electrochemical Promotion of Rh/YSZ Catalysts for C_2H_4 Oxidation Via AC Impedance Spectroscopy, Top. Catal. 54 (2011) 708–717.

[144] E. Varkaraki, J. Nicole, E. Plattner, C. Comninellis, C.G. Vayenas, Electrochemical promotion of IrO_2 catalyst for the gas phase combustion of ethylene, J. Appl. Electrochem. 25 (1995) 978–981.

[145] J. Nicole, C. Comninellis, Electrochemical promotion of IrO_2 catalyst activity for the gas phase combustion of ethylene, J. Appl. Electrochem. 28 (1998) 223–226.

[146] D. Tsiplakides, J. Nicole, C.G. Vayenas, C. Comninellis, Work Function and Catalytic Activity Measurements of an IrO2 Film Deposited on YSZ Subjected to In Situ Electrochemical Promotion, J. Electrochem. Soc. 145 (1998) 905–908.

[147] A.C. Kaloyannis, C.A. Pliangos, D.T. Tsiplakides, I. V. Yentekakis, S.G. Neophytides, S. Bebelis, et al., Electrochemical promotion of catalyst surfaces deposited on ionic and mixed conductors, Ionics (Kiel). 1 (1995) 414–420.

[148] D. Poulidi, M.A. Castillo-del-Rio, R. Salar, A. Thursfield, I.S. Metcalfe, Electrochemical promotion of catalysis using solid-state proton-conducting membranes, Solid State Ionics. 162-163 (2003) 305–311.

[149] D. Poulidi, G.C. Mather, C.N. Tabacaru, A. Thursfield, I.S. Metcalfe, Electrochemical promotion of a platinum catalyst supported on the high-temperature proton conductor $La_{0.99}Sr_{0.01}NbO_{4-\delta}$, Catal. Today. 146 (2009) 279–284.

[150] I.V. Yentekakis, G. Moggridge, C.G. Vayenas, R.M. Lambert, In Situ Controlled Promotion of Catalyst Surfaces via NEMCA: The Effect of Na on the Pt-Catalyzed CO Qxidation, J. Catal. 146 (1994) 292–305.

[151] R.M. Lambert, I.R. Harkness, I. V. Yentekakis, C.G. Vayenas, Electrochemical promotion in emission control catalysis, Ionics (Kiel). 1 (1995) 29–31.

[152] F. Dorado, A. de Lucas-Consuegra, C. Jiménez, J.L. Valverde, Influence of the reaction temperature on the electrochemical promoted catalytic behaviour of platinum impregnated catalysts for the reduction of nitrogen oxides under lean burn conditions, Appl. Catal. A Gen. 321 (2007) 86–92.

[153] F. Dorado, A. de Lucas-Consuegra, P. Vernoux, J.L. Valverde, Electrochemical promotion of platinum impregnated catalyst for the selective catalytic reduction of NO by propene in presence of oxygen, Appl. Catal. B Environ. 73 (2007) 42–50.

[154] A. de Lucas-Consuegra, F. Dorado, J.L. Valverde, R. Karoum, P. Vernoux, Electrochemical activation of Pt catalyst by potassium for low temperature CO deep oxidation, Catal. Commun. 9 (2008) 17–20.

[155] D. Tsiplakides, S.G. Neophytides, O. Enea, M. Jaksic, C.G. Vayenas, Nonfaradaic Electrochemical Modification of the Catalytic Activity of Pt-Black Electrodes Deposited on Nafion 117 Solid Polymer Electrolytes, J. Electrochem. Soc. 144 (1997) 2072–2078.

[156] M. Marwood, C.G. Vayenas, Electrochemical Promotion of a Dispersed Platinum Catalyst, J. Catal. 178 (1998) 429–440.

[157] C. Jiménez-Borja, B. Delgado, L.F. Díaz-Díaz, J.L. Valverde, F. Dorado, Enhancing the combustion of natural gas by electrochemical promotion of catalysis, Electrochem. Commun. 23 (2012) 9–12.

[158] N. Li, F. Gaillard, Catalytic combustion of toluene over electrochemically promoted Ag catalyst, Appl. Catal. B Environ. 88 (2009) 152–159.

[159] D. Theleritis, S. Souentie, A. Siokou, A. Katsaounis, C.G. Vayenas, Hydrogenation of CO_2 over Ru/YSZ Electropromoted Catalysts, ACS Catal. 2 (2012) 770–780.

[160] S. Wodiunig, F. Bokeloh, J. Nicole, C. Comninellis, Electrochemical Promotion of RuO_2 Catalyst Dispersed on an Yttria-Stabilized Zirconia Monolith, Electrochem. Solid-State Lett. 2 (1999) 281–283.

[161] C. Xia, M. Hugentobler, Y. Li, G. Foti, C. Comninellis, W. Harbich, Electrochemical promotion of CO combustion over non-percolated Pt particles supported on YSZ using a novel bipolar configuration, Electrochem. Commun. 13 (2010) 99–101.

[162] C. Xia, M. Hugentobler, C. Comninellis, W. Harbich, Quantifying electrochemical promotion of induced bipolar Pt particles supported on YSZ, Electrochem. Commun. 12 (2010) 1551–1554.

[163] E.I. Papaioannou, S. Souentie, F.M. Sapountzi, A. Hammad, D. Labou, S. Brosda, et al., The role of TiO_2 layers deposited on YSZ on the electrochemical promotion of C_2H_4 oxidation on Pt, J. Appl. Electrochem. 40 (2010) 1859–1865.

[164] R. Karoum, V. Roche, C. Pirovano, R.-N. Vannier, A. Billard, P. Vernoux, CGO-based electrochemical catalysts for low temperature combustion of propene, J. Appl. Electrochem. 40 (2010) 1867–1873.

[165] S. Souentie, L. Lizarraga, E.I. Papaioannou, C.G. Vayenas, P. Vernoux, Permanent electrochemical promotion of C_3H_8 oxidation over thin sputtered Pt films, Electrochem. Commun. 12 (2010) 1133–1135.

[166] L. Lizarraga, S. Souentie, L. Mazri, A. Billard, P. Vernoux, Investigation of the CO oxidation rate oscillations using electrochemical promotion of catalysis over sputtered-Pt films interfaced with YSZ, Electrochem. Commun. 12 (2010) 1310–1313.

[167] L. Lizarraga, M. Guth, A. Billard, P. Vernoux, Electrochemical catalysis for propane combustion using nanometric sputtered-deposited Pt films, Catal. Today. 157 (2010) 61–65.

[168] A. Hammad, S. Souentie, E.I. Papaioannou, S. Balomenou, D. Tsiplakides, J.C. Figueroa, et al., Electrochemical promotion of the SO_2 oxidation over thin Pt films interfaced with YSZ in a monolithic electropromoted reactor, Appl. Catal. B Environ. 103 (2011) 336–342.

[169] E.A. Baranova, A. Thursfield, S. Brosda, G. Fóti, C. Comninellis, C.G. Vayenas, Electrochemical Promotion of Ethylene Oxidation over Rh Catalyst Thin Films Sputtered on YSZ and TiO_2/YSZ Supports, J. Electrochem. Soc. 152 (2005) E40–E49.

[170] S. Balomenou, D. Tsiplakides, A. Katsaounis, S. Thiemann-Handler, B. Cramer, G. Foti, et al., Novel monolithic electrochemically promoted catalytic reactor for environmentally important reactions, Appl. Catal. B Environ. 52 (2004) 181–196.

[171] S. Balomenou, D. Tsiplakides, A. Katsaounis, S. Brosda, A. Hammad, G. Foti, et al., Monolithic electrochemically promoted reactors: A step for the practical utilization of electrochemical promotion, Solid State Ionics. 177 (2006) 2201–2204.

[172] C. Koutsodontis, A. Hammad, M. Lepage, Y. Sakamoto, G. Fóti, C.G. Vayenas, Electrochemical Promotion of NO Reduction by C_2H_4 in Excess O_2 Using a Monolithic Electropromoted Reactor and Pt–Rh Sputtered Electrodes, Top. Catal. 50 (2008) 192–199.

[173] V. Roche, R. Revel, P. Vernoux, Electrochemical promotion of YSZ monolith honeycomb for deep oxidation of methane, Catal. Commun. 11 (2010) 1076–1080.

[174] A. Lintanf, Pt/YSZ electrochemical catalysts prepared by electrostatic spray deposition for selective catalytic reduction of NO by C_3H_6, Solid State Ionics. 178 (2008) 1998–2008.

[175] C.G. Vayenas, S. Bebelis, I. V. Yentekakis, H.-G. Lintz, Non-faradaic electrochemical modification of catalytic activity: A status report, Catal. Today. 11 (1992) 303–442.

[176] E.A. Baranova, A. Thursfield, S. Brosda, G. Fóti, C. Comninellis, C.G. Vayenas, Electrochemically Induced Oscillations of C_2H_4 Oxidation Over Thin Sputtered Rh Catalyst Films, Catal. Letters. 105 (2005) 15–21.

[177] E.A. Baranova, G. Fóti, H. Jotterand, C. Comninellis, Electrochemical modification of the catalytic activity of TiO_2/YSZ supported rhodium films, Top. Catal. 44 (2007) 355–360.

[178] I. Constantinou, D. Archonta, S. Brosda, M. Lepage, Y. Sakamoto, C. Vayenas, Electrochemical promotion of NO reduction by C_3H_6 on Rh catalyst-electrode films supported on YSZ and on dispersed Rh/YSZ catalysts, J. Catal. 251 (2007) 400–409.

[179] C. Jiménez-Borja, F. Dorado, A. de L.-Consuegra, J.M. G.-Vargas, J.L. Valverde, Electrochemical Promotion of CH4 Combustion over a Pd/CeO2-YSZ Catalyst, Fuel Cells. 11 (2011) 131–139.

[180] A. Kambolis, L. Lizarraga, M.N. Tsampas, L. Burel, M. Rieu, J.-P. Viricelle, et al., Electrochemical promotion of catalysis with highly dispersed Pt nanoparticles, Electrochem. Commun. 19 (2012) 5–8.

[181] M. Marwood, Electrochemical Promotion of Electronically Isolated Pt Catalysts on Stabilized Zirconia, J. Catal. 168 (1997) 538–542.

[182] S. Balomenou, G. Pitselis, D. Polydoros, A. Giannikos, A. Vradis, A. Frenzel, et al., Electrochemical promotion of Pd , Fe and distributed Pt, Solid State Ionics. 137 (2000) 857–862.

[183] D. Poulidi, G. Mather, I. Metcalfe, Wireless electrochemical modification of catalytic activity on a mixed protonic–electronic conductor, Solid State Ionics. 178 (2007) 675–680.

[184] D. Poulidi, A. Thursfield, I.S. Metcalfe, Electrochemical promotion of catalysis controlled by chemical potential difference across a mixed ionic-electronic conducting ceramic membrane – an example of wireless NEMCA, Top. Catal. 44 (2007) 435–449.

[185] D. Poulidi, I.S. Metcalfe, Comparative studies between classic and wireless electrochemical promotion of a Pt catalyst for ethylene oxidation, J. Appl. Electrochem. 38 (2008) 1121–1126.

[186] M. Haruta, Catalysis of gold nanoparticles deposited on metal oxides, Surf. Sci. 6 (2002) 102–115.

[187] M. Haruta, When gold is not noble: catalysis by nanoparticles., Chem. Rec. 3 (2003) 75–87.

[188] M. Haruta, Gold as a Novel Catalyst in the 21st Century: Preparation, Working Mechanism and Applications, ChemInform. 35 (2004) 27–36.

[189] J.-D. Grunwaldt, C. Kiener, C. Wögerbauer, A. Baiker, Preparation of Supported Gold Catalysts for Low-Temperature CO Oxidation via “Size-Controlled” Gold Colloids, J. Catal. 181 (1999) 223–232.

[190] N. Lopez, On the origin of the catalytic activity of gold nanoparticles for low-temperature CO oxidation, J. Catal. 223 (2004) 232–235.

[191] E.D. Park, J.S. Lee, Effects of Pretreatment Conditions on CO Oxidation over Supported Au Catalysts, J. Catal. 186 (1999) 1–11.

[192] F. Boccuzzi, Au/TiO_2 Nanosized Samples: A Catalytic, TEM, and FTIR Study of the Effect of Calcination Temperature on the CO Oxidation, J. Catal. 202 (2001) 256–267.

[193] H.S. Subbarao, E C, Maiti, Solid Electrolytes with Oxygen Ion Conduction, Solid State Ionica. 11 (1984) 317–338.

[194] W. Heller, T.L. Pugh, "Steric" stabilization of colloidal solutions by adsorption of flexible macromolecules, J. Polym. Sci. 47 (1960) 203–217.

[195] M.Y. Han, C.H. Quek, W. Huang, C.H. Chew, L.M. Gan, A Simple and Effective Chemical Route for the Preparation of Uniform Nonaqueous Gold Colloids, Chem. Mater. 11 (1999) 1144–1147.

[196] J. Wagner, J.M. Köhler, Continuous synthesis of gold nanoparticles in a microreactor, Nano Lett. 5 (2005) 685–91.

[197] H. Hirai, Formation and Catalytic Functionality of Synthetic Polymer-Noble Metal Colloid, J. Macromol. Sci. Part A - Chem. A13 (1979) 633–649.

[198] T. Ashida, K. Miura, T. Nomoto, S. Yagi, H. Sumida, G. Kutluk, et al., Synthesis and characterization of Rh(PVP) nanoparticles studied by XPS and NEXAFS, Surf. Sci. 601 (2007) 3898–3901.

[199] Y. Leng, K. Sato, J.-G. Li, T. Ishigaki, M. Iijima, H. Kamiya, et al., Iron nanoparticles dispersible in both ethanol and water for direct silica coating, Powder Technol. 196 (2009) 80–84.

[200] L. Prati, G. Martra, New Gold Catalysts for Liquid Phase Oxidation, Gold Bull. 32 (1999) 96–101.

[201] X. Zuo, H. Liu, M. Liu, Asymmetric Hydrogenation of alpha-Ketoesters over Finely Dispersed Polymer-stabilized Platinum Clusters, Tetrahedron Lett. 39 (1998) 1941–1944.

[202] J. Ayache, L. Beaurier, J. Boumendil, G. Ehret, D. Laub, Chapter 5 Replica Technique, in: Sample Prep. Handb. Transm. Electron Microsc., 1st ed., Springer, 2010: pp. 229–256.

[203] M. Boudart, Catalysis by Supported Metals *, Adv. Catal. 20 (1969) 153–166.

[204] M. Valden, X. Lai, D. Goodman, Onset of catalytic activity of gold clusters on titania with the appearance of nonmetallic properties, Science. 281 (1998) 1647–1650.

[205] C.T. Campbell, G. Ertl, H. Kuipers, J. Segner, A molecular beam study of the catalytic oxidation of CO on a Pt(111) surface, J. Chem. Phys. 73 (1980) 5862.

[206] X. Su, P.S. Cremer, Y.R. Shen, G.A. Somorjai, High-Pressure CO Oxidation on Pt(111) Monitored with Infrared−Visible Sum Frequency Generation (SFG), J. Am. Chem. Soc. 119 (1997) 3994–4000.

[207] K.R. McCrea, J.S. Parker, G.A. Somorjai, The Role of Carbon Deposition from CO Dissociation on Platinum Crystal Surfaces during Catalytic CO Oxidation: Effects on Turnover Rate, Ignition Temperature, and Vibrational Spectra, J. Phys. Chem. B. 106 (2002) 10854–10863.

[208] S. Arrii, F. Morfin, A.. J. Renouprez, J.L. Rousset, Oxidation of CO on gold supported catalysts prepared by laser vaporization: direct evidence of support contribution, J. Am. Chem. Soc. 126 (2004) 1199–1205.

[209] E. Quinet, L. Piccolo, H. Daly, F.C. Meunier, F. Morfin, A. Valcarcel, et al., H_2-induced promotion of CO oxidation over unsupported gold, Catal. Today. 138 (2008) 43–49.

[210] R.J.H. Grisel, B.E. Nieuwenhuys, Selective Oxidation of CO, over Supported Au Catalysts, J. Catal. 199 (2001) 48–59.

[211] M. Lamallem, H. El Ayadi, C. Gennequin, R. Cousin, S. Siffert, F. Aïssi, et al., Effect of the preparation method on Au/Ce-Ti-O catalysts activity for VOCs oxidation, Catal. Today. 137 (2008) 367–372.

[212] S. Benard, M. Ousmane, L. Retailleau, A. Boreave, P. Vernoux, A. Giroir-Fendler, Catalytic removal of propene and toluene in air over noble metal catalyst, Can. J. Civ. Eng. 36 (2009) 1935–1945.

[213] T. Masui, H. Imadzu, N. Matsuyama, N. Imanaka, Total oxidation of toluene on Pt/CeO_2-ZrO_2-Bi_2O_3/gamma-Al_2O_3 catalysts prepared in the presence of polyvinyl pyrrolidone., J. Hazard. Mater. 176 (2010) 1106–1109.

[214] F. Diehl, J. Barbier Jr., D. Duprez, I. Guibard, G. Mabilon, Catalytic oxidation of heavy hydrocarbons over Pt/Al_2O_3. Influence of the structure of the molecule on its reactivity, Appl. Catal. B Environ. 95 (2010) 217–227.

[215] V.P. Santos, S. A. C. Carabineiro, P.B. Tavares, M.F.R. Pereira, J.J.M. Órfão, J.L. Figueiredo, Oxidation of CO, ethanol and toluene over TiO_2 supported noble metal catalysts, Appl. Catal. B Environ. 99 (2010) 198–205.

[216] M. Paulis, H. Peyrard, M. Montes, Influence of Chlorine on the Activity and Stability of Pt/Al_2O_3 Catalysts in the Complete Oxidation of Toluene, J. Catal. 199 (2001) 30–40.

[217] L.F. Liotta, Catalytic oxidation of volatile organic compounds on supported noble metals, Appl. Catal. B Environ. 100 (2010) 403–412.

[218] K. Bendahou, L. Cherif, S. Siffert, H.L. Tidahy, H. Benaïssa, A. Aboukaïs, The effect of the use of lanthanum-doped mesoporous SBA-15 on the performance of Pt/SBA-15 and Pd/SBA-15 catalysts for total oxidation of toluene, Appl. Catal. A Gen. 351 (2008) 82–87.

[219] N. Radic, B. Grbic, A. Terlecki-Baricevic, Kinetics of deep oxidation of n-hexane and toluene over Pt/Al_2O_3 catalysts, Appl. Catal. B Environ. 50 (2004) 153–159.

[220] X. Li, F. Gaillard, P. Vernoux, Investigations under real operating conditions of the electrochemical promotion by O_2 temperature programmed desorption measurements, Top. Catal. 44 (2007) 391–398.

[221] M.N. Tsampas, F.M. Sapountzi, A. Boréave, P. Vernoux, Isotopical labeling mechanistic studies of electrochemical promotion of propane combustion on Pt/YSZ, Electrochem. Commun. 26 (2013) 13–16.

[222] A. Wieckowski, E.R. Savinova, C.G. Vayenas, eds., Catalysis and electrocatalysis at nanoparticle surfaces, Marcel Dekker, Inc., New York, 2001.

[223] J. Nicole, D. Tsiplakides, C. Pliangos, X.E. Verykios, C. Comninellis, C.G. Vayenas, Electrochemical Promotion and Metal–Support Interactions, J. Catal. 204 (2001) 23–34.

[224] S. Wodiunig, V. Patsis, C. Comninellis, Electrochemical promotion of RuO2 - catalysts for the gas phase combustion of C_2H_4, Solid State Ionics. 137 (2000) 813–817.

[225] P. Vernoux, F. Gaillard, L. Bultel, E. Siebert, M. Primet, Electrochemical Promotion of Propane and Propene Oxidation on Pt/YSZ, J. Catal. 208 (2002) 412–421.

[226] D. Tsiplakides, S. Balomenou, A. Katsaounis, D. Archonta, C. Koutsodontis, C.G. Vayenas, Electrochemical promotion of catalysis: mechanistic investigations and monolithic electropromoted reactors, Catal. Today. 100 (2005) 133–144.

[227] A. Trovarelli, ed., Catalysis by Ceria and Related Materials, Imperial College Press, London, 2002.

[228] I.R. Gibson, G.P. Dransfield, J.T.S. Irvine, Sinterability of commercial 8 mol % yttria-stabilized zirconia powders and the effect of sintered density on the ionic conductivity, J. Mater. Sci. 33 (1998) 4297–4305.

[229] H.A.E. Dole, L.F. Safady, S. Ntais, M. Couillard, E.A. Baranova, Electrochemically enhanced metal-support interaction of highly dispersed Ru nanoparticles with a CeO2 support, J. Catal. (2014).

[230] P.D. Petrolekas, S. Balomenou, C.G. Vayenas, Electrochemical Promotion of Ethylene Oxidation on Pt Catalyst Films Deposited on CeO_2, J. Electrochem. Soc. 145 (1998) 1202–1206.

[231] J. Lahaye, S. Boehm, P. Chambrion, P. Ehrburger, Influence of Cerium Oxide on the Formation and Oxidation of Soot, Combust. Flame. 104 (1996) 199–207.

[232] W. Liu, M. Flytzani-Stephanopoulos, Total Oxidation of Carbon Monoxide and Methane over Transition Metal-Fluorite Oxide Composite Catalysts II. Catalyst Characterization and Reaction Kinetics, J. Catal. 153 (1995) 317–332.

[233] M. Sahibzadab, B.C.H. Steelea, K. Zheng, R.A. Rudkin, I.S. Metcalfe, Development of solid oxide fuel cells based on a $Ce(Gd)O_2$-X electrolyte film for intermediate temperature operation, Catal. Today. 38 (1997) 459–466.

[234] D.R. Mullins, K.Z. Zhang, Metal – support interactions between Pt and thin film cerium oxide, Surf. Sci. 513 (2002) 163–173.

[235] S. Penner, D. Wang, R. Podloucky, R. Schlogl, K. Hayek, Rh and Pt nanoparticles supported by CeO_2: Metal–support interaction upon high-temperature reduction observed by electron microscopy, Phys. Chem. 6 (2004) 5244–5249.

[236] A. Bruix, J. A Rodriguez, P.J. Ramírez, S.D. Senanayake, J. Evans, J.B. Park, et al., A new type of strong metal-support interaction and the production of H2 through the transformation of water on $Pt/CeO_2(111)$ and $Pt/CeO(x)/TiO_2(110)$ catalysts., J. Am. Chem. Soc. 134 (2012) 8968–8974.

[237] C. Jiménez-Borja, F. Dorado, A. de Lucas-Consuegra, J.M. García-Vargas, J.L. Valverde, Complete oxidation of methane on Pd/YSZ and Pd/CeO_2/YSZ by electrochemical promotion, Catal. Today. 146 (2009) 326–329.

[238] I. Constantinou, I. Bolzonella, C. Pliangos, C. Comninellis, C.G. Vayenas, Electrochemical promotion of RuO_2 catalysts for the combustion of toluene and ethylene, Catal. Letters. 100 (2005) 125–133.

[239] M.V. Rama Rao, T. Shripathi, Photoelectron spectroscopic study of X-ray induced reduction of CeO_2, J. Electron Spectrosc. 87 (1997) 121–126.

[240] E. Paparazzo, XPS Studies of Damage Induced by X-ray Irradiation on CeO_2 Surfaces, Surf. Sci. Lett. 234 (1990) L253 – L258.

[241] E. Paparazzo, G.M. Ingo, N. Zacchetti, X-ray induced reduction effects at CeO_2 surfaces: An x-ray photoelectron spectroscopy study, J. Vac. Sci. Technol. A Vacuum, Surfaces, Film. 9 (1991) 1416 – 1420.

[242] E.A. Baranova, G. Fóti, C. Comninellis, Promotion of Rh catalyst interfaced with TiO_2, Electrochem. Commun. 6 (2004) 170–175.

[243] E.A. Baranova, G. Fóti, C. Comninellis, Current-assisted activation of Rh/TiO_2/YSZ catalyst, Electrochem. Commun. 6 (2004) 389–394.

[244] H.A.E. Dole, L.F. Safady, S. Ntais, M. Couillard, E.A. Baranova, Improved Catalytic Reactor for the Electrochemical Promotion of Highly Dispersed Ru Nanoparticles with CeO_2 support, ECS Trans. 61 (2014) 65–74.

[245] S. Wodiunig, C. Comninellis, Electrochemical Promotion of RuO_2 Catalysts for the Gas Phase Combustion of C_2H_4, J. Eur. Ceram. Soc. 19 (1999) 931–934.

[246] F. Vasiliu, V. Parvulescu, C. Sarbu, Trivalent Ce_2O_3 and CeO_{2-x} intermediate oxides induced by laser irradiation of CeO_2 powders, J. Mater. Sci. 29 (1994) 2095–2101.

[247] J.J. Plata, A.M. Marquez, J.F. Sanz, Transport Properties in the CeO_{2-x} (111) Surface : From Charge Distribution to Ion-Electron Collaborative Migration, J. Phys. Chem. C. 117 (2013) 25497–25503.

[248] E. Monyoncho, S. Ntais, F. Soares, T. Woo, E.A. Baranova, Promoting Ethanol Electrooxidation on Pd with Ru in Alkaline Media, ACS Catal. (n.d.).

[249] P. Burroughs, A. Hamnett, A.F. Orchard, G. Thornton, Satellite Structure in the X-ray Photoelectron Spectra of some Binary and Mixed Oxides of Lanthanum and Cerium, J. Chem. Soc. - Dalt. Trans. (1976) 1686 – 1698.

[250] A. Siokou, S. Ntais, V. Dracopoulos, S. Papaefthimiou, G. Leftheriotis, P. Yianoulis, Substrate related structural, electronic and electrochemical properties of evaporated CeO_x ion storage layers, Thin Solid Films. 514 (2006) 87–96.

[251] J.Y. Shen, A. Adnot, S. Kaliaguine, An ESCA study of the interaction of oxygen with the surface of ruthenium, Appl. Surf. Sci. 51 (1991) 47–60.

[252] L. Qiu, F. Liu, L. Zhao, Y. Ma, J. Yao, Comparative XPS study of surface reduction for nanocrystalline and microcrystalline ceria powder, Appl. Surf. Sci. 252 (2006) 4931–4935.

[253] M. Cargnello, V.V.T. Doan-Nguyen, T.R. Gordon, R.E. Diaz, E.A. Stach, R.J. Gorte, et al., Control of metal nanocrystal size reveals metal-support interface role for ceria catalysts., Science. 341 (2013) 771–773.

[254] T. Bunluesin, E.S. Putna, R.J. Gorte, A comparison of CO oxidation on ceria-supported Pt, Pd, and Rh, Catal. Letters. 41 (1996) 1–5.

[255] R.J. Isaifan, S. Ntais, E.A. Baranova, Particle size effect on catalytic activity of carbon-supported Pt nanoparticles for complete ethylene oxidation, Appl. Catal. A Gen. 464-465 (2013) 87–94.

[256] H. Cordatos, T. Bunluesin, J. Stubenrauch, J.M. Vohs, R.J. Gorte, Effect of Ceria Structure on Oxygen Migration for Rh/Ceria Catalysts, J. Phys. Chem. 100 (1996) 785–789.

[257] G.S. Zafiris, R.J. Gorte, Evidence for Low-Temperature Oxygen Migration from Ceria to Rh, J. Catal. 139 (1993) 561–567.

[258] A. Bruix, A. Migani, G.N. Vayssilov, K.M. Neyman, J. Libuda, F. Illas, Effects of deposited Pt particles on the reducibility of CeO_2(111)., Phys. Chem. Chem. Phys. 13 (2011) 11384–11392.

[259] J.C. Serrano-Ruiz, A. Sepúlveda-Escribano, F. Rodríguez-Reinoso, D. Duprez, Pt–Sn catalysts supported on highly-dispersed ceria on carbon, J. Mol. Catal. A Chem. 268 (2007) 227–234.

[260] W.M. Haynes, ed., Electron Work Function of the Elements, in: Handb. Chem. Phys., 95 th, CRC Press/Taylor and Francis, Boca Raton, FL, USA, 2014: pp. 12–124.

[261] S.S. Warule, N.S. Chaudhari, B.B. Kale, K.R. Patil, P.M. Koinkar, M.A. More, et al., Organization of cubic CeO_2 nanoparticles on the edges of self assembled tapered ZnO nanorods via a template free one-pot synthesis: significant cathodoluminescence and field emission properties, J. Mater. Chem. 22 (2012) 8887.

[262] N. Cant, W.K. Hall, Catalytic oxidation II. Silica supported noble metals for the oxidation of ethylene and propylene, J. Catal. 16 (1970) 220–231.

[263] R. Malathi, R. Madhusudhan, R.P. Viswanath, Metal-support interaction in mixed oxide supports, Stud. Surf. Sci. Catal. 113 (1998) 957–962.

[264] M. Cargnello, P. Fornasiero, R.J. Gorte, Opportunities for Tailoring Catalytic Properties Through Metal-Support Interactions, Catal. Letters. 142 (2012) 1043–1048.

[265] H.A.E. Dole, A.C.G.S.A. Costa, M. Couillard, E.A. Baranova, Quantifying metal support interaction in ceria-supported Pt, PtSn and Ru nanoparticles using electrochemical technique, J. Catal. 333 (2016) 40–50.

[266] P. Lakshmanan, F. Averseng, N. Bion, L. Delannoy, J.-M. Tatibouët, C. Louis, Understanding of the oxygen activation on ceria- and ceria/alumina-supported gold catalysts: a study combining 18O/16O isotopic exchange and EPR spectroscopy, Gold Bull. 46 (2013) 233–242.

[267] W. Cai, F. Wang, C. Daniel, A.C. van Veen, Y. Schuurman, C. Descorme, et al., Oxidative steam reforming of ethanol over Ir/CeO_2 catalysts: A structure sensitivity analysis, J. Catal. 286 (2012) 137–152.

[268] S. Lin, L. Yang, X. Yang, R. Zhou, Redox behavior of active PdOx species on (Ce,Zr)xO_2–Al_2O_3 mixed oxides and its influence on the three-way catalytic performance, Chem. Eng. J. 247 (2014) 42–49.

[269] M.M. Pakulska, C.M. Grgicak, J.B. Giorgi, The effect of metal and support particle size on NiO/CeO_2 and NiO/ZrO_2 catalyst activity in complete methane oxidation, Appl. Catal. A Gen. 332 (2007) 124–129.

[270] H.-H. Liu, Y. Wang, A.-P. Jia, S.-Y. Wang, M.-F. Luo, J.-Q. Lu, Oxygen vacancy promoted CO oxidation over Pt/CeO_2 catalysts: A reaction at $Pt–CeO_2$ interface, Appl. Surf. Sci. 314 (2014) 725–734.

[271] A. Vasile, V. Bratan, C. Hornoiu, M. Caldararu, N.I. Ionescu, T. Yuzhakova, et al., Electrical and catalytic properties of cerium – tin mixed oxides in CO depollution reaction, Appl. Catal. B, Environ. 140-141 (2013) 25–31.

[272] F. Esch, S. Fabris, L. Zhou, T. Montini, C. Africh, P. Fornasiero, et al., Electron Localization Determines Defect Formation on Ceria Substrates, Science (80-.). 309 (2005) 752–755.

[273] F. Wang, W. Cai, C. Descorme, H. Provendier, W. Shen, C. Mirodatos, et al., From mechanistic to kinetic analyses of ethanol steam reforming over Ir/CeO_2 catalyst, Int. J. Hydrogen Energy. 39 (2014) 18005–18015.

[274] W. Cai, F. Wang, E. Zhan, A. Vanveen, C. Mirodatos, W. Shen, Hydrogen production from ethanol over Ir/CeO_2 catalysts: A comparative study of steam reforming, partial oxidation and oxidative steam reforming, J. Catal. 257 (2008) 96–107.

[275] J.-Y. Siang, C.-C. Lee, C.-H. Wang, W.-T. Wang, C.-Y. Deng, C.-T. Yeh, et al., Hydrogen production from steam reforming of ethanol using a ceria-supported iridium catalyst: Effect of different ceria supports, Int. J. Hydrogen Energy. 35 (2010) 3456–3462.

[276] M. Couillard, G. Radtke, A.P. Knights, G. A. Botton, Three-dimensional atomic structure of metastable nanoclusters in doped semiconductors, Phys. Rev. Lett. 107 (2011) 1–4.

[277] A.J. Hartmann, M. Neilson, R.N. Lamb, K. Watanabe, J.F. Scott, Ruthenium oxide and strontium ruthenate electrodes for ferroelectric thin-films capacitors, Appl. Phys. A Mater. Sci. Process. 70 (2000) 239–242.

[278] B.R. Chalamala, R.H. Reuss, K.A. Dean, E. Sosa, D.E. Golden, Field emission characteristics of iridium oxide tips, J. Appl. Phys. 91 (2002) 6141–6146.

[279] F.H.B. Lima, J. Zhang, M.H. Shao, K. Sasaki, M.B. Vukmirovic, E.A. Ticianelli, et al., Catalytic activity - d-band center correlation for the O_2 reduction reaction on platinum in alkaline solutions, J. Phys. Chem. C. 111 (2007) 404–410.

[280] L. Fan, K. Fujimoto, Reaction Mechanism of Methanol Synthesis from Carbon Dioxide and Hydrogen on Ceria-Supported Palladium Catalysts with SMSI Effect, J. Catal. 172 (1997) 238–242.

[281] K. Nagaoka, K. Seshan, K. Aika, J.A. Lercher, Carbon Deposition during Carbon Dioxide Reforming of Methane—Comparison between Pt/Al_2O_3 and Pt/ZrO_2, J. Catal. 197 (2001) 34–42.

[282] J.B. Claridge, M.L.H. Green, S.C. Tsang, A.P.E. York, A.T. Ashcroft, P.D. Battle, A study of carbon deposition on catalysts during the partial oxidation of methane to synthesis gas, Catal. Letters. 22 (1993) 299–305.

[283] P.E. Nolan, D.C. Lynch, A.H. Cutler, Carbon deposition and hydrocarbon formation on group VIII metal catalysts, J. Phys. Chem. B. 102 (1998) 4165–4175.

[284] S.M. Davis, F. Zaera, B.E. Gordon, G.A. Somorjal, Radiotracer and Thermal Desorption Studies of Dehydrogenation and Atmospheric Hydrogenation of Organic Fragments Obtained from [14C]Ethylene Chemisorbed over Pt(l11) Surfaces, J. Catal. 92 (1985) 240–246.

[285] S. Park, R.J. Gorte, J.M. Vohs, Applications of Heterogeneous Catalysis in the Direct Oxidation of Hydrocarbons in a Solid-Oxide Fuel Cell, Appl. Catal. A Gen. 200 (2000) 55–61.

[286] E. Obeid, L. Lizarraga, M.N. Tsampas, A. Cordier, A. Boréave, M.C. Steil, et al., Continuously regenerating Diesel Particulate Filters based on ionically conducting ceramics, J. Catal. 309 (2014) 87–96.

[287] H. Igarashi, T. Fujino, M. Watanabe, Hydrogen electro-oxidation on platinum catalysts in the presence of trace carbon monoxide, J. Electroanal. Chem. 391 (1995) 119–123.

[288] F. Bortoloti, A.C. Garcia, A.C.D. Angelo, Electronic effect in intermetallic electrocatalysts with low susceptibility to CO poisoning during hydrogen oxidation, Int. J. Hydrogen Energy. 40 (2015) 10816–10824.

[289] C. Jiménez-Borja, B. Delgado, F. Dorado, J.L. Valverde, Experimental data and kinetic modeling of the catalytic and electrochemically promoted CH_4 oxidation over Pd catalyst-electrodes, Chem. Eng. J. 225 (2013) 315–322.

Appendix: Supplementary Material

Several experimental methods and characterization techniques were used during this project. The experimental methods include synthesizing the nano-catalysts, preparing the electrochemical cells, and evaluating the catalytic and electrocatalytic performance of the catalysts. X-ray diffraction (XRD) and transmission electron microscopy (TEM) were used to characterize the physical properties of the nano-catalysts. Other characterization techniques used throughout the project included X-ray photoelectron spectroscopy (XPS), inductively-coupled plasma optical emission spectroscopy (ICP-OES), and CO titration. Details of each of these techniques are summarized in each corresponding chapter; however, further explanation and supporting information for some of the techniques are shown as follows.

A.1 Catalytic Measurements

The catalytic activity measurements (Chapter 3, 4) of the supported nano-catalysts are carried out at atmospheric pressure in a continuous flow U-tube reactor (Figure A-1).

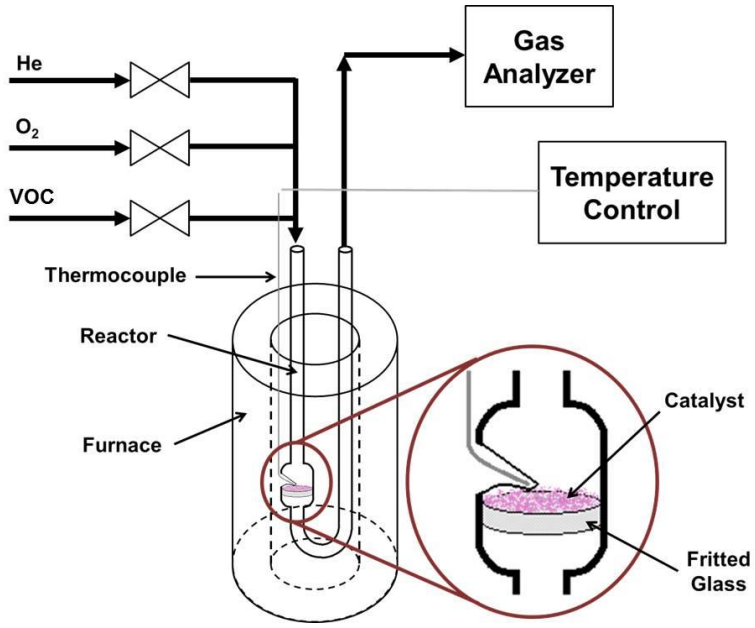

Figure A-1: Schematic of the continuous flow U-tube reactor.

In order to evaluate the performance of each nano-catalyst, several calculations are performed, including reactant conversion (X_R) (i.e., R = CO, C_2H_4, or C_7H_8), turnover frequency (*TOF*), and activation energy (E_a). The reactant conversion is calculated as a basic evaluation of the catalytic

performance of a catalyst and is calculated for CO (Eq. A-1), C_2H_4 (Eq. A-2) and C_7H_8 (Eq. A-3), assuming complete oxidation, with the respective equations,

$$X_{CO}(\%) = \frac{[CO_2]_{out}}{[CO]_{out} + [CO_2]_{out}} \times 100\% \quad \textbf{A-1}$$

$$X_{C_2H_4}(\%) = \frac{[CO_2]_{out}/2}{[C_2H_4]_{in}} \times 100\% \quad \textbf{A-2}$$

$$X_{C_7H_8} = \frac{[CO_2]_{out}}{7 \cdot [C_7H_8]_{out} + [CO_2]_{out}} \times 100\% \quad \textbf{A-3}$$

Note: equations were adapted to fit the gas analysis equipment available for each reaction

where $[S]_i$ represents the concentration of the corresponding gas species which was measured in the inlet or outlet of the reactor system.

Another common form of representing catalytic performance is through the *TOF* (s^{-1}) of the reactant species. This parameter evaluates the units of reactant species that is converted over a period of time and calculated using equation A-4,

$$TOF = \frac{r_0}{N_G} \quad \textbf{A-4}$$

where N_G is the moles of active metal species available (mol) (determined from the dispersion) and r_0 is the intrinsic catalytic rate ($mol \cdot s^{-1}$) which is calculated using equation A-5.

$$r_0 = TMF \cdot [R]_{in} \cdot X_R \quad \textbf{A-5}$$

where *TMF* represents the total molar flow rate ($mol \cdot s^{-1}$) (adjusted for room temperature), and $[R]_{in}$ is the concentration of the reactant gas species in the inlet of the reactor (mol frac).

Finally, the activation energy for the initial activity of each nano-catalyst is determined to evaluate the energy required for the oxidation reaction to occur (below 20% conversion). Using the following Arrhenius equation (Eq. A.6),

$$ln\, r_0 = -\frac{E_a}{R} \cdot \frac{1}{T} + \ln k \qquad \textbf{A-6}$$

where R is the universal gas constant (8.314 $J \cdot mol^{-1} \cdot K^{-1}$), T is the reaction temperature (K) corresponding to the catalytic rate (r_0), and k is the rate constant (which is not calculated for the purpose of these experiments), ln r_0 vs. 1/T is plotted and a linear relationship is fitted to the data to obtain the slope. The activation energy (E_a, in $J \cdot mol^{-1}$) is then determined by multiplying the slope by $-R$.

A.2 Dispersion Measurements: CO Titration

Supported Pt nano-catalysts were subject to dispersion testing using an established CO titration method[175]. This method is used to determine the amount of active metal available by the adsorption of CO, assuming that only one CO molecule adsorbs on one Pt atom. In short, a known mass of catalyst is placed in the continuous flow U-tube reactor (Figure A-1) which is heated in helium to a temperature in which adsorption of CO is considered adequate. In order to saturate the surface of the Pt nanoparticles, CO (1% in helium) is fed into the system for a specified time. Next, pure helium is purged through the system for a determined time period in order to remove any gaseous CO. Finally, pure oxygen is fed to react with the adsorbed CO molecules to produce CO_2 which is measured by an on-line CO_2 gas analyzer. This procedure is repeated for several different helium purge durations. By plotting the moles of CO_2 produced versus the helium purge time and extrapolating to a purge time of zero, the maximum moles of CO_2 that can be produced can be determined. Assuming every mole of CO_2 produced corresponds to one mole of active Pt and knowing the total mass of Pt present, the dispersion can be calculated using equation A-7.

$$Dispersion\ (\%) = \frac{moles\ of\ active\ metal\ sites}{moles\ of\ metal\ in\ reactor} \times 100\% \qquad \textbf{A-7}$$

The moles of metal in the reactor is calculated using equation A-8.

$$moles\ of\ metal\ in\ reactor = \frac{mass\ of\ catalyst\ added\ to\ reactor \times metal\ loading\ fraction}{molar\ mass\ of\ metal} \qquad \textbf{A-8}$$

The moles of active metal sites is determined by plotting ln N_{CO_2} versus He Purge Time, where N_{CO_2} is the moles of CO_2 produced and is calculated as follows.

$$N_{CO_2} = \frac{area\ under\ peak\ (ppm.min) \times flow of\ O_2(mol/min)}{10^6 ppm} \times \frac{CO_2}{O_2} stoichiometric\ ratio \qquad \textbf{A-9}$$

A.3 Carbon Balance for Toluene Oxidation

In order to determine whether complete toluene oxidation was occurring during the experiments, a carbon balance was calculated for each temperature (Table A-1). It is noted, that a value greater than 5% was considered to be the presence of carbon deposition or the formation of other intermediates.

Table A-1: Representative carbon balance data from toluene oxidation experiments (first cycles shown).

Pt/γ-Al_2O_3		**Pt/YSZ2**	
Temperature (°C)	**Carbon Balance (%)**	**Temperature (°C)**	**Carbon Balance (%)**
22.3	9.4	22.8	52.9
21.8	4.4	27.1	36.9
21.8	2.1	48.5	100.0
22.0	0.3	59.0	1.9
34.8	-32.3	76.2	-44.9
48.8	-5.9	93.3	-9.7
70.8	-11.4	105.3	-8.9
80.9	6.5	118.1	-17.2
98.1	1.2	136.3	-1.3
115.1	5.0	153.3	14.7
130.5	6.9	169.2	22.4
144.2	17.1	184.5	21.9
157.6	17.4	199.1	12.6
171.4	2.7	227.6	8.9
186.6	2.5	240.0	6.7
202.4	2.0	250.6	7.4
219.4	0.9	239.2	6.6
236.7	0.0	228.5	6.9
251.8	-1.0		

A.4 X-ray Photoelectron Spectroscopy of Ru/CeO_2 Catalyst

XPS characterization was performed for the Ru/CeO_2 catalysts that was tested before and after polarization (Chapter 6). Figure A-2 shows the XPS spectra of the Ru3p peaks.

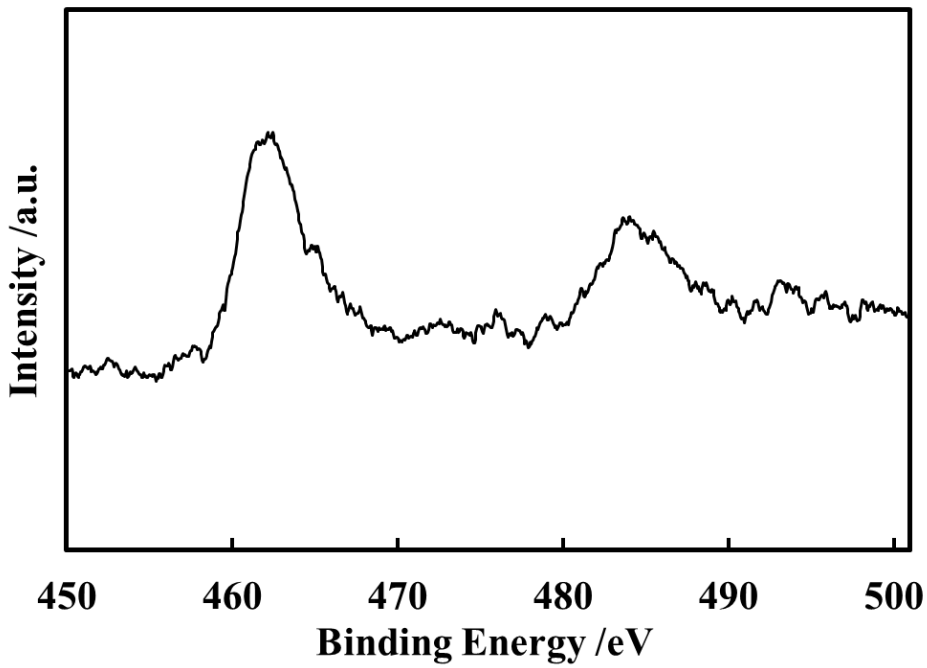

Figure A-2: Ru3p XPS spectra of the RuNPs/CeO_2 on YSZ sample before electrochemical enhancement of catalytic activity.

A.5 Polarization Curves and Tafel Plots

Validation of the applicability of equation 7-2 was carried out in the reaction mixture (C_2H_4 and O_2) and in the presence of only oxygen (helium carrier gas). Steady-state polarization curves are shown in Figure A-4 of the catalyst-working electrode potential (U_{wr}) versus current density (i) in the presence and absence of C_2H_4 for 1 wt% Pt-1/CeO_2; and 1 wt% $Pt_{50}Sn_{50}/CeO_2$.

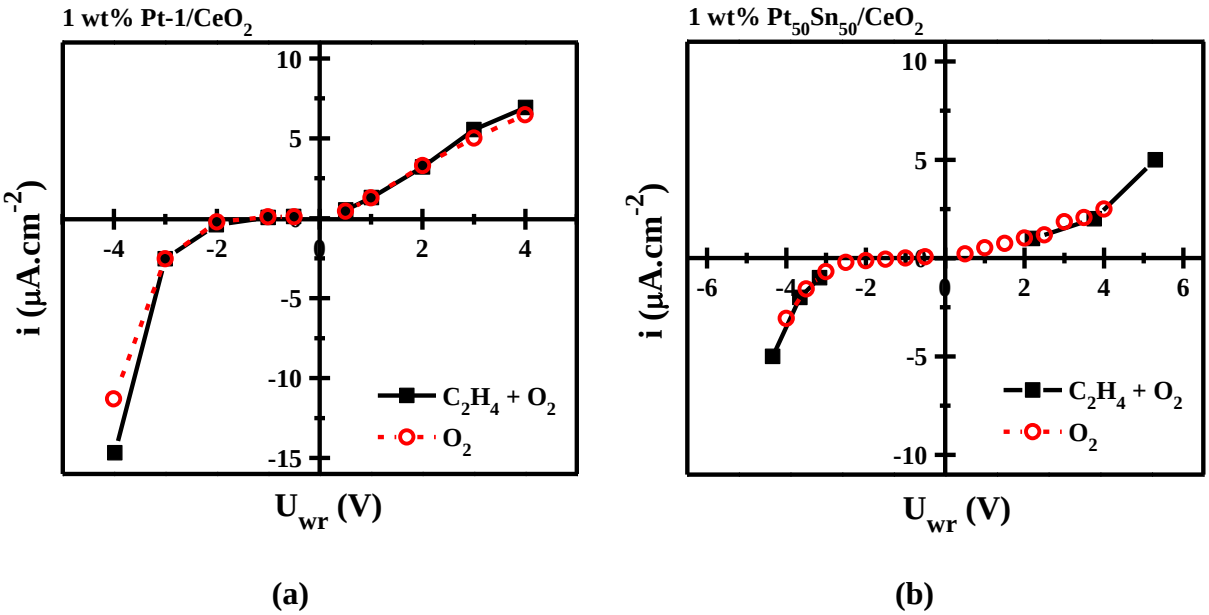

Figure A-3: Steady-state polarization curves for 1 wt% Pt-1/CeO_2 and 1 wt% $Pt_{50}Sn_{50}/CeO_2$ at 350°C (0.012 kPa C_2H_4, 3 kPa O_2, balance He; total flow: 6 L·h^{-1}).

Tafel plots using the anodic data of the steady-state polarization curves (U_{wr} – 0.5 – 5 V) were plotted to determine the exchange current density (i_0) for each catalysts. Representative plots of Pt-1 (colloid), 1 wt% Pt-1/CeO_2 and 1 wt% $Pt_{50}Sn_{50}$-1/CeO_2 are shown in Figure A-4. Exchange current densities were determined when U_{wr} = 0 (i.e., log i_0) using correlations of the linear segment of the Tafel plots.

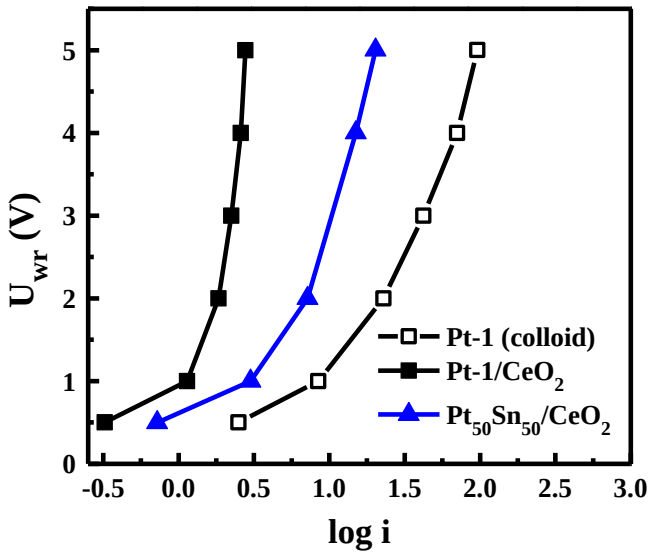

Figure A-4: Tafel plots of Pt-1 (colloid), 1 wt% Pt-1/CeO_2 and 1 wt% $Pt_{50}Sn_{50}$/CeO_2 (3 kPa O_2, balance He; total flow: 6 L·h^{-1}).

Open circuit catalytic rates, normalized for the mass of Pt, are shown to compare Pt-1 (colloid), 1 wt% Pt-1/CeO_2 and 1 wt% $Pt_{50}Sn_{50}$-1/CeO_2.

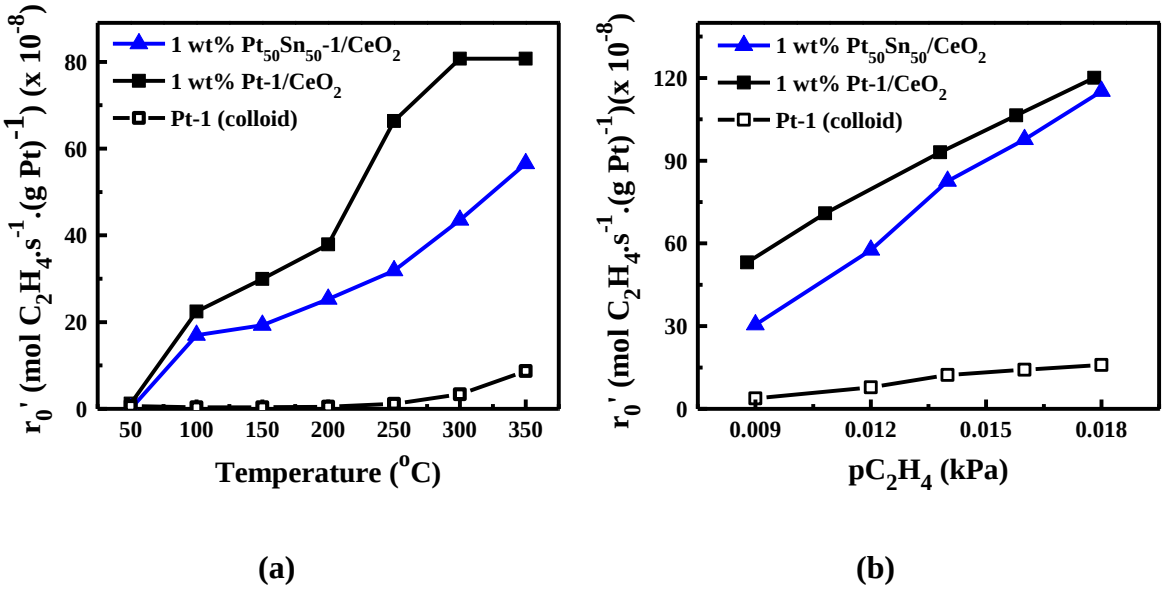

Figure A-5: Open circuit catalytic rates (r_0) (a) over a temperature range of 50 - 350°C (0.012 kPa C_2H_4, 3 kPa O_2, balance He) for Pt-1 (colloid), 1 wt% Pt-1/CeO_2 and 1 wt% $Pt_{50}Sn_{50}$-1/CeO_2; and (b) over a partial pressure of C_2H_4 of 0.009 – 0.018 kPa (3 kPa O_2, balance He; total flow: 6 $L \cdot h^{-1}$).